Structures Research Report 2008/51117

University of Florida
Civil and Coastal Engineering

GATOR Engineering
University of Florida
Civil and Coastal Engineering

Final Report **April 2008**

Development of Improved Bridge Design Provisions for Barge Impact Loading

Principal investigators:
Gary R. Consolazio, Ph.D.
Michael C. McVay, Ph.D.

Research assistants:
David R. Cowan
Michael T. Davidson
Daniel J. Getter

Department of Civil and Coastal Engineering
University of Florida
P.O. Box 116580
Gainesville, Florida 32611

Sponsor:
Florida Department of Transportation (FDOT)
Marcus H. Ansley, P.E. – Project manager

Contract:
UF Project No. 00051117
FDOT Contract No. BD-545 RPWO 29

DISCLAIMER

The opinions, findings, and conclusions expressed in this publication are those of the authors and not necessarily those of the State of Florida Department of Transportation.

1. Report No.	2. Government Accession No.	3. Recipient's Catalog No.
BD-545 RPWO 29		

4. Title and Subtitle	5. Report Date
Development of Improved Bridge Design Provisions for Barge Impact Loading	April 2008
	6. Performing Organization Code
	8. Performing Organization Report No.
7. Author(s)	
G. R. Consolazio, M.C. McVay	2008/51117
9. Performing Organization Name and Address	10. Work Unit No. (TRAIS)
University of Florida Department of Civil & Coastal Engineering P.O. Box 116580 Gainesville, FL 32611-6580	11. Contract or Grant No. BD-545 RPWO 29
12. Sponsoring Agency Name and Address	13. Type of Report and Period Covered
Florida Department of Transportation Research Management Center 605 Suwannee Street, MS 30 Tallahassee, FL 32301-8064	Final Report
	14. Sponsoring Agency Code

15. Supplementary Notes

16. Abstract

Current practice with regard to designing bridge structures to resist impact loads associated with barge collisions relies upon the use of the AASHTO bridge design specifications. The AASHTO barge impact design provisions, which employ a static analysis approach, were developed from pendulum impact testing of reduced scale barge models. However, research sponsored by the FDOT, both experimental and analytical in nature, has revealed that both the barge force-deformation relationships employed by AASHTO as well as the use of static analysis should be re-examined. Specifically, FDOT sponsored research has revealed that 1) the geometry of the impacted portion of a bridge pier can affect the magnitude of impact forces that are generated, and 2) substantial dynamic amplifications of pier design forces may arise under certain combinations of bridge configuration, soil condition, and barge impact condition. In the research reported on herein, high-resolution finite element models of jumbo hopper and tanker barges have been developed and analyzed to produce updated barge force-deformation relationships for use in bridge design. Additionally, new dynamic barge-impact analysis procedures—coupled vessel impact analysis (CVIA) and impact response spectrum analysis (IRSA)—have been developed. These procedures account for dynamic amplifications and may be used to quantify internal pier design forces under barge impact loading conditions.

17. Key Words	18. Distribution Statement
Vessel, barge, impact, collision, bridge pier, validation, crushing, deformation, finite element analysis, dynamic analysis, time-history analysis, response spectrum analysis, bridge design specifications	No restrictions.

19. Security Classif. (of this report)	20. Security Classif. (of this page)	21. No. of Pages	22. Price
Unclassified	Unclassified	256	

Form DOT F 1700.7 (8-72). Reproduction of completed page authorized

ACKNOWLEDGEMENTS

The authors would like to thank the Florida Department of Transportation (FDOT) for providing the funding that made this research project possible. The authors would also like to thank Mr. Henry T. Bollmann, P.E. (Florida Bridge Software Institute) and Mr. Michael A. Knott, P.E. (Moffatt & Nichol Engineers) for reading portions of this report, meeting with the authors, and providing valuable comments and suggestions.

EXECUTIVE SUMMARY

Current practice with regard to designing bridge structures to resist impact loads associated with barge collisions relies upon the use of the AASHTO bridge design specifications. The AASHTO barge impact design provisions, which employ a static analysis approach, were developed from pendulum impact testing of reduced scale barge models. However, past FDOT-sponsored research, both experimental and analytical in nature, has revealed that both the barge force-deformation relationships employed by AASHTO as well as the use of static analysis procedures should be re-examined. Specifically, the past research revealed that the geometry of the impacted portion of a bridge pier can affect the magnitude of impact forces that are generated and that substantial dynamic amplifications of pier design forces may arise under certain combinations of bridge configuration, soil condition, and barge impact condition. The research reported on herein was undertaken to develop improved models of barge and bridge behavior during collisions, and to develop improved collision analysis techniques. The research was divided into four key areas:

1. Investigation of barge bow crushing characteristics and the development of updated numerical models of barge crushing behavior
2. Development of simplified techniques for modeling multi-pier, multi-span bridge structures
3. Development of dynamic collision analysis techniques capable of accounting for dynamic amplifications
4. A parametric study in which seventeen different representative bridge configurations, sampled from throughout Florida, were analyzed using both static and dynamic analysis methods.

Findings and outcomes resulting from completion of these tasks included:

- High-resolution models of hopper and tanker barges were developed and subjected to crushing by flat-faced and round pier column impactors of various widths. Based on force-deformation results obtained from the high-resolution models, it has been concluded that barge bow crushing behavior does not vary substantially from one barge type to another and that barge crushing behavior may be adequately and conservatively modeled using an elastic, perfectly-plastic representation. These conclusions differ substantially from the current AASHTO provisions. Barge bow yield loads have also been found to be strongly dependent on the shape and size of the pier column, and not a function of the barge bow width, as the AASHTO provisions prescribe. Newly proposed barge bow force-deformation relationships have been developed in this report.
- A simplified bridge modeling technique—the one-pier two-span (OPTS) technique—has been developed that consists of the reduction (simplification) of a full-bridge model into a single pier model with two adjacent spans, springs, and lumped masses. The OPTS modeling technique retains appropriate analytical accuracy while simultaneously increasing modeling efficiency.

- Two numerical procedures for conducting dynamic analyses of barge impacts on bridge piers have been developed for use in design: the coupled vessel impact analysis (CVIA) method and the impact response spectrum analysis (IRSA) method. The CVIA method is a time-history analysis technique that has been shown to be the most accurate means currently available for assessing bridge pier response to barge collision loading in design applications. The IRSA method is a response spectrum analysis technique that amplifies and combines modal analysis data to predict approximate maximum dynamic design forces without the need for performing a time-history analysis. Both CVIA and IRSA account for dynamic amplifications and may be used to quantify internal pier design forces under barge impact loading conditions.
- A parametric study was performed in which 152 unique impact analyses were conducted: 38 static (AASHTO) and 114 dynamic (CVIA, IRSA). It was found that the IRSA analysis technique predicts suitably conservative measures of pier internal force in comparison to CVIA analysis; and that the dynamic analysis methods (CVIA and IRSA) conservatively predict dynamic amplification effects, when such effects are present, whereas the AASHTO static analysis method does not account for such effects.

TABLE OF CONTENTS

LIST OF FIGURES

LIST OF TABLES

CHAPTER 1
INTRODUCTION

1.1 Introduction

Bridge structures that span navigable waterways are inherently susceptible to vessel collision. In the United States, vessels operate on a vast network of coastal waterways and inland rivers, over which bridges span, to transport cargo between destinations. Many of these waterways have relatively shallow channels, and therefore are unable to accommodate large-draft vessels. For this reason, large-draft cargo ships are restricted to operation in deep water routes and ports. Barges, however, have a shallow draft, and are thus capable of operating on shallow coastal and inland waterways. Thus, heavily-loaded barge traffic routinely passes beneath highway bridge structures.

Vessel collisions on bridge structures may occur when vessels veer off-course, becoming aberrant. Factors that affect vessel aberrancy include adverse weather conditions, mechanical failures, and human error. It has been noted in the literature that, on average, at least one serious vessel collision occurs per year (Larsen 1993). During severe vessel collisions, significant lateral loads may be imparted to bridge structures. Engineers must therefore account for lateral vessel impact loads when designing bridge structures over navigable waterways. If such bridges cannot adequately resist impact loading, vessel collisions may result in failure and collapse of the bridge; leading to expensive repairs, extensive traffic delays, and potentially, human casualties.

1.2 Motivation

In 1980, the Sunshine Skyway Bridge over Tampa Bay was struck by a cargo ship, the Summit Venture, resulting in the collapse of a portion of the superstructure and thirty-five human casualties. Later, in 1988, prompted by the collapse of the Sunshine Skyway Bridge, a formal investigation was initiated to develop bridge design specifications for vessel collision. As a result, the American Association of State Highway and Transportation Officials (AASHTO) published the Guide Specification and Commentary for Vessel Collision Design of Highway Bridges in 1991 (AASHTO 1991). Additionally, similar provisions were incorporated in the AASHTO Load and Resistance Factor Design (LRFD) Specifications (AASHTO 1994) a few years later. Publication of these design specifications represented a major step in improving the safety of bridge structures.

At the time of the inception of the AASHTO vessel collision specifications, relatively few experimental studies had been conducted involving barge collisions. Thus, very little data was available for the development of the AASHTO specifications. The data upon which the AASHTO specifications were based came from a single experimental study conducted by Meier-Dörnberg during the 1980's in Germany (Meier-Dörnberg 1983). In these experiments, Meier-Dörnberg conducted pendulum drop-hammer impacts on reduced-scale European hopper barge bow models. Additionally, static load tests were also conducted on a similarly scaled barge bow model.

One of the major findings of this study was that no significant differences were observed between static and dynamic tests. Thus, relationships between barge kinetic energy, barge bow deformation, and static impact force were developed and recommended. With few modifications, the relationships developed by Meier-Dörnberg were ultimately adopted by

the AASHTO Specifications. Consequently, static loads are implicitly assumed to be sufficient in the prediction of structural capacity during a vessel collision.

Using reduced-scale models to describe a full-scale response may introduce an uncertainty in the accuracy of experimental results. This uncertainty is even more pronounced when full-scale experimental data are unavailable to validate results obtained from the reduced-scale models, as is the case with the Meier-Dörnberg data. Therefore, the AASHTO vessel collision specifications necessarily include the same degree of uncertainty given that the AASHTO provisions are directly based upon the Meier-Dörnberg results.

Particularly, the nature of the dynamic tests Meier-Dörnberg conducted precludes the presence of significant dynamic effects that are generated between the barge and bridge in a collision event. The interaction between the barge, bridge, and soil significantly affects the loads, displacements, and stresses generated. One setback of the Meier-Dörnberg experiments is the use of a pendulum drop-hammer. The interaction between the barge and the drop-hammer is not representative of barge-bridge-soil interaction. Additionally, for the Meier-Dörnberg study, the barge bow models were fixed in a stationary configuration, thereby simulating impacts on a rigid pier structure. Hence, the fixed condition of the barge bow models used in the Meier-Dörnberg study prevents dynamic interaction between the barge and drop-hammer. Use of static analysis and design procedures fails to account for important dynamic effects—such as inertial forces, damping forces, and rate effects—present in an impact event. Omission of dynamic effects from analysis procedures may result in a non-uniform margin of safety against failure in a dynamic impact event.

At the time that the AASHTO specifications were first published, typical analysis procedures use in bridge design practice were linear and static. Nonlinear and dynamic analyses required expensive, with respect to both cost and time, computational hardware and software. As a result, nonlinear dynamic analysis was primarily used in research, being too time-consuming for use in typical design practice. However, with technological advancements in both hardware and software over the past two decades, analysis techniques that were historically in the domain of research have now become commonplace in design. Nonlinear analysis techniques are now commonly used in design of bridge foundations. Additionally, dynamic analyses—either modal or time-history—are commonly employed in the design of structures to resist earthquake loads.

Given the limitations of the Meier-Dörnberg data, full-scale barge impact tests were initiated by the Florida Department of Transportation (FDOT) and researchers at the University of Florida (UF) in 2000 (Consolazio et al. 2006). The old St. George Island Causeway Bridge was scheduled for demolition and eventual replacement by a new structure. Located in the panhandle of Florida, approximately 5 miles east of Apalachicola, the bridge spanned, north to south, from Eastpoint to St. George Island. Due to environmental concerns, the alignment of the new replacement bridge deviated nearly 1500 ft from the old alignment in several locations, affording researchers the unique opportunity to conduct full-scale barge impact tests on the out-of-commission structure without endangering the new bridge.

During March and April of 2004, after the new St. George Island Causeway Bridge was opened to traffic, full-scale impact testing commenced. Two of the piers near the main navigation channel were selected for a total of fifteen impact tests. Instrumentation was installed on each pier, and during each test, barge impact forces, deformations, and decelerations; pier displacement and accelerations; and soil information were recorded. Once all of the experimental test data was reduced, analytical models of each pier were developed

and validated using the experimental results. Based on the data recorded and insights gained from full scale testing of the old St. George Island Causeway Bridge, it was possible to initiate the development of updated design provisions for bridge structures subjected to barge impact loading.

1.3 Objectives

The two primary objectives of this research were to develop: 1) improved methods for calculating maximum impact forces imparted to a bridge structure during a barge collision, and 2) improved procedures for determining corresponding bridge response to such loads. A major aspect of all of the proposed structural analysis methods is the ability to quantify important dynamic effects inherently present in a barge collision event. Most design provisions for impact loading use a static analysis to determine bridge response; however, these static methods fail to capture significant dynamic effects. Therefore, semi-empirical methods that can capture dynamic effects were developed as a part of this research, each providing a more sophisticated—yet still design-oriented (i.e., practical enough for use in bridge design)—impact analysis.

1.4 Scope of Work

- Characterize barge bow force-deformation relationships: It was discovered during St. George Island full-scale testing that in situations in which the barge bow undergoes significant plastic deformation, the maximum impact force that can be generated is limited by the load-carrying capacity of the barge. This implies that, as the barge bow crushes beyond yield and fracture, the impact force generated does not increase with further bow deformation. The relationships of Meier-Dörnberg and the AASHTO specifications, however, prescribe that the impact force increases monotonically with increasing barge bow deformation (crush depth). In this study, updated relationships between impact force and barge bow deformation for various barge types have been developed independently of the AASHTO relationship.
- Develop a simplified bridge modeling technique: Of particular importance during an impact event are the dynamic effects of the superstructure. Due to the large mass of the superstructure and its location relative to the impact point, the inertial effects associated with the superstructure contribute significantly to the response of the pier. Thus, in developing a numerical bridge model for impact analysis, it is imperative that the mass and stiffness of the superstructure be accurately represented. However, modeling of all the components (multiple spans, piers, and foundations) in typical bridges requires a large degree of complexity and a large number of degrees-of-freedom, making dynamic analysis of a full bridge model computationally expensive. Therefore, a simplified bridge modeling technique called the one-pier two-span (OPTS) model has been developed. The OPTS model is composed of the impact pier and two adjacent spans, with the remainder of the bridge modeled using springs and concentrated masses. The OPTS modeling technique will be shown to have similar accuracy to full bridge modeling, while requiring much shorter analysis times (i.e. the OPTS procedure is more computationally efficient).

- Develop dynamic analysis techniques for use in design: It was determined during St. George Island experimental testing that dynamic effects have a significant effect on pier response during a barge impact. Early in an impact event, inertial (mass-proportional) and damping (velocity-proportional) forces comprise more resistance to impact loading than the stiffness (displacement-proportional resistance). However, during later stages in an impact, it has been shown that inertial forces actually change directions, and drive the motion of the bridge, effectively becoming a source of loading on the structure. This complex interaction of dynamic forces cannot be adequately captured through the use of static analysis, and thus dynamic analysis is required. In this study, two dynamic analysis techniques were developed for use in design:
    a. Coupled vessel impact analysis (CVIA): A time-history analysis that permits interaction between a single degree-of-freedom barge model and a numerical bridge model.
    b. Impact response spectrum analysis (IRSA): A response spectrum analysis method that uses impact characteristics and dynamic structural characteristics (modal shapes and periods of vibration) to determine maximum dynamic forces in a bridge structure during an impact.
- Conduct a parametric study: A comprehensive parametric study was conducted using to evaluate the effectiveness of the proposed dynamic analysis methods for a variety of different bridge configurations. Construction drawings for a representative set of bridge structures within the state of Florida were obtained and used to develop numerical bridge models. Bridge structures selected were chosen based upon the following criteria: foundation type, pier size and strength, pier column size and geometry, and superstructure type.

CHAPTER 2
BACKGROUND

2.1 Vessel-Bridge Collision Incidents

Designing bridge structures that span over navigable bodies of water requires that careful consideration be given to the fact that cargo vessels may inadvertently collide with piers that support the bridge superstructure. Causes of such collisions often involve poor weather conditions, limited visibility, strong cross-currents, poor navigational aids, failure of mechanical equipment, and/or operator error. Worldwide, vessel impacts occur frequently enough that, on average, at least one serious collision occurs each year (Larsen 1993). Within the United States, a succession of incidents involving ships and barges impacting bridge structures clearly demonstrates that the potential for structural failure and loss of life exist.

One of the most catastrophic incidents of vessel-bridge collision in the United States was the 1980 collapse of the Sunshine Skyway Bridge, which spanned over Tampa Bay in Florida. Navigating in poor weather conditions and limited visibility, the cargo ship *Summit Venture* collided with one of the anchor piers of the bridge causing the collapse of almost 1300 ft. of bridge deck (Figure 2.1) and the loss of thirty-five lives. Due in large part to this incident, comprehensive guidelines for designing bridge structures to resist ship and barge collision loads were later published, in 1991, as the *AASHTO Guide Specification and Commentary for Vessel Collision Design of Highway Bridges* (AASHTO 1991).

Figure 2.1 Collapse of the Sunshine Skyway Bridge in Florida (1980)
after being struck by the cargo ship *Summit Venture*

While massive cargo ships clearly pose a significant threat to bridge structures, they are also limited in operation to relatively deep waterways. Consequently, ships pose significant risks primarily to bridges near major shipping ports. In contrast, multi-barge flotillas are able to operate in much shallower waterways and thus pose a risk to a greater number of structures. Considering that each individual barge within a flotilla might weigh as

much as fifty fully-loaded tractor-trailers, the potential damage that can be caused by barges striking bridge piers is clear.

In September 1993, a multi-barge tow navigating at night and in dense fog collided with the Big Bayou Canot railroad bridge near Mobile, Alabama resulting in a significant lateral displacement of the structure. Moments later, unaware that the bridge had just been struck by a barge, a passenger train attempted to cross the structure at 70 mph, resulting in catastrophic structural failure (Figure 2.2) and forty-seven fatalities (Knott 2000). In September 2001 a barge tow navigating near South Padre, Texas veered off course in strong currents and collided with piers supporting the Queen Isabella Causeway Bridge. As a result of this impact, three spans of the structure collapsed (Figure 2.3) and several people died (Wilson 2003). In May 2002, an errant barge tow struck a bridge on interstate I-40 near Webbers Falls, Oklahoma. On an average day, this structure carried approximately 20,000 vehicles across the Arkansas River. As a result of the impact, 580 ft. of superstructure collapsed (Figure 2.4), fourteen people died, and traffic had to be rerouted for approximately two months (NTSB 2004).

Figure 2.2 Failure of the Big Bayou Canot railroad bridge in Alabama (1993) after being struck by a barge flotilla

Figure 2.3 Collapse of the Queen Isabella Causeway Bridge in Texas (2001) after being struck by a barge flotilla

Figure 2.4 Collapse of an Interstate I-40 bridge in Oklahoma (2002)
after being struck by a barge flotilla
(Source: Oklahoma DOT)

2.2 Review of Experimental Vessel Impact Tests

Despite the significant number of vessel-bridge collisions that have occurred in recent decades, only a small number of instrumented experimental tests have ever been performed to quantify vessel impact loading characteristics. Generally, ship collision events have been studied to a much greater extent than have barge collisions. Two key ship collision studies form the basis for most current theories relating to ship impact loading. The first was conducted by Minorsky (1959) to analyze collisions with reference to protection of nuclear powered ships, and focused on predicting the extent of vessel damage sustained during a collision. A semi-analytical approach was employed using data from twenty-six actual collisions. From this data a relationship between the deformed steel volume and the absorbed impact energy was formulated. A second key ship collision study was that of Woisin (1976) which also focused on deformation of nuclear powered ships during collisions. Data were collected from twenty-four collision tests (Figure 2.5) of reduced-scale (1:7.5 to 1:12) ship-bow models colliding with ship-side-hull models. Relationships between impact energy, deformation, and force developed during this study were later used in the development of the AASHTO equations for calculating equivalent static ship impact forces (AASHTO 1991).

In terms of quantifying the characteristics of barge impact loads, as opposed to ship impact loads, one of the most significant experimental studies conducted to date is that of Meier-Dörnberg (1983). This research included both dynamic and static loading of reduced-scale (1:4.5 to 1:6) models of European Type IIa barges. In overall dimensions, European Type IIa barges are similar to the jumbo hopper barges commonly found in the U.S. barge fleet. All tests in the Meier-Dörnberg study were conducted on *partial* vessel models that consisted only of nose sections of barges. In conducting the dynamic tests in this study, the partial barge models were mounted in a stationary (fixed-boundary-condition) configuration and then struck by a falling impact pendulum hammer. The amount of impact energy imparted to the barge model during each test was dictated by the weight of the hammer and its drop height. Due to limitations of hammer drop height, repeated impacts were carried out on each partial barge model to accumulate both impact energy and impact damage (crushing

deformation). From the experimental data collected, Meier-Dörnberg developed relationships between kinetic impact energy, inelastic barge deformation, and force.

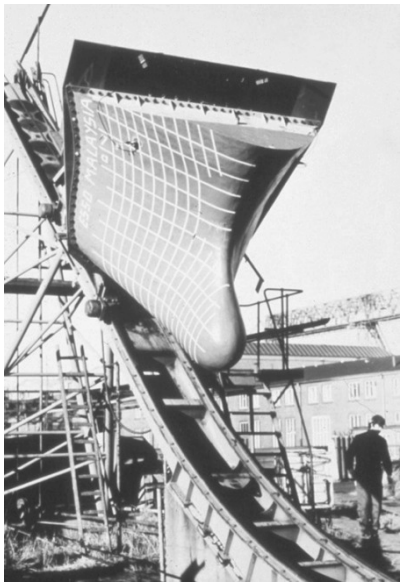

a) Ship bow model on inclined ramp prior to test

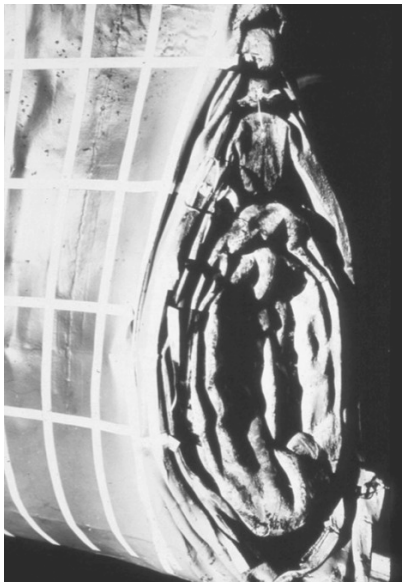

b) Permanent deformation of ship bow model after test

Figure 2.5 Reduced scale ship-to-ship collision tests conducted by Woisin (1976)

More recently, experimental studies have been conducted that overcome one of the key limitations of the Meier-Dörnberg study—i.e., the use of reduced-scale models. In 1989, Bridge Diagnostics, Inc. completed a series of *full-scale* tests for the U.S. Army Corps of Engineers that involved a nine-barge flotilla impacting lock gates at Lock and Dam 26 on the Mississippi river near Alton, Illinois (Goble 1990). Each of the impacts was performed at approximately 0.4 knots. Force, acceleration, and velocity time histories for the impacting barge were recorded using commercially available sensors such as strain gages and accelerometers. In addition, custom manufactured and calibrated load cells, developed by Bridge Diagnostics, were used to measure impact forces (Figure 2.6). Unfortunately, data obtained from this study are not directly applicable to bridge pier design because the system struck by the barge was a lock gate, not a bridge pier. Lock gates and bridge piers possess different structural characteristics which produce dissimilar impact loads. More importantly, the energy levels used during these tests were insufficient to cause significant inelastic barge deformation. Because inelastic barge deformations are common in head-on barge-pier collisions, and given that such deformations affect both barge stiffness and impact energy dissipation, data obtained from this set of tests are not directly applicable to bridge design.

Several years later, full-scale barge impact tests on concrete lock walls were conducted by the U.S. Army Corps of Engineers. In 1997, a 4-barge flotilla was used to ram a lock wall at Old Lock and Dam 2, located north of Pittsburgh, Pennsylvania (Patev and Barker 2003). These experiments (Figure 2.7) were conducted to measure the structural response of the lock wall at the point of impact and to quantify barge-to-barge lashing forces during impact. Strain gages were installed on the barge to record steel plate deformations at

the point of impact. An accelerometer was used to capture the overall acceleration history of the flotilla, and clevis pin load cells quantified lashing forces generated during impact. A total of thirty-six impact tests were successfully carried out on the lock wall.

a) Barge bow approaching lock gate

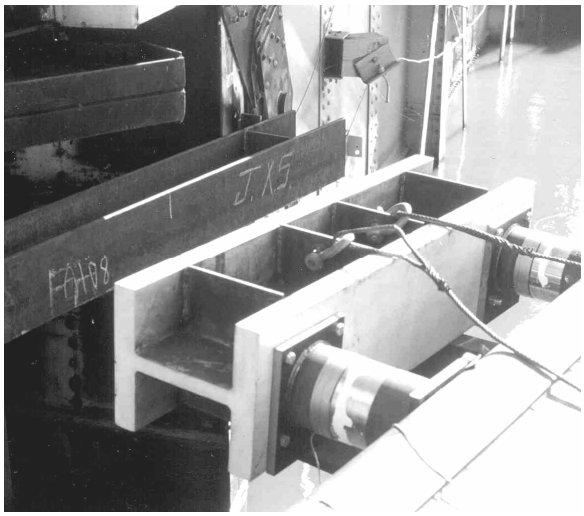

b) Load cells attached to barge bow

Figure 2.6 Instrumented full-scale barge-lock-gate collision tests
(Source: Bridge Diagnostics, Inc.)

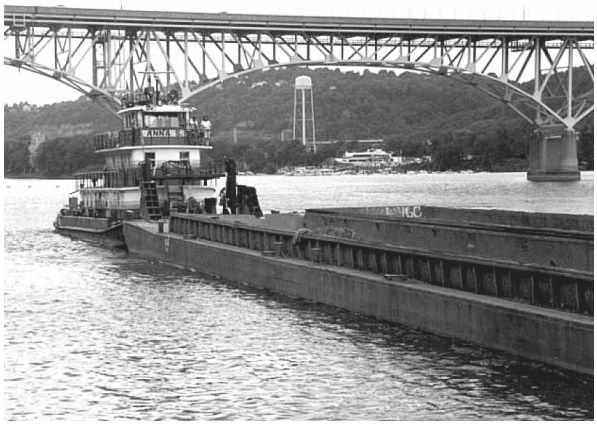

a) Push boat and 4-barge flotilla

b) Sensors at impact corner of barge

Figure 2.7 Instrumented 4-barge lock-wall collision tests
(Source: U.S. Army Corps of Engineers)

Following the 4-barge tests, larger impact experiments involving a 15-barge flotilla were initiated in December of 1998 at the decommissioned Gallipolis Lock at Robert C. Byrd Lock and Dam in West Virginia (Arroyo et al. 2003). In contrast to the 4-barge tests, one of the primary goals of the 15-barge tests was to recover time-histories of impact force

generated between the barge flotilla and the lock wall. To accomplish this goal, a load-measurement impact beam was affixed to the impact corner of the barge flotilla using two uniaxial high-capacity clevis-pin load cells (Figure 2.8). Additional instrumentation used during these tests included accelerometers, strain gages, water pressure transducers, and smaller capacity clevis-pin load cells that were installed in-line with the barge-to-barge cable lashings. In total, forty-four impact tests were successfully carried out on the lock wall.

In bridge pier design for barge collision loading, maximum impact forces are generally associated with head-on impact conditions, as opposed to oblique glancing blows of the type tested in the 4-barge and 15-barge tests performed by the Army Corps. Therefore, while the data collected during these tests could be useful in developing load prediction models for oblique side impacts on piers, the same data cannot be used to improve the AASHTO expressions for head-on impacts. Additionally, neither of the Army Corps test series involved dynamic vessel-pier-soil interactions or significant crushing deformation of the impacting barges. Data collected during the experimental tests were later used to develop several analytical methods for approximating impact load on structures based on the experimental test results (Patev 1999, Arroyo et al. 2003).

a) Push boat and 15-barge flotilla

b) Force measurement beam attached to barge with clevis-pin load cells

Figure 2.8 Instrumented 15-barge lock-wall collision tests
(Source: U.S. Army Corps of Engineers)

In 2004, full-scale experimental barge impact tests on piers of the old St. George Island Causeway Bridge (Consolazio et al. 2006) were conducted by the University of Florida (UF) and the Florida Department of Transportation (FDOT). The purpose of conducting these tests was to directly quantify barge impact loads and resulting pier, soil, and superstructure responses. The research revealed that the AASHTO static design forces currently employed in bridge design range broadly from being overly conservative in some cases to being unconservative (due to dynamic amplification effects) in other cases. This variability stems from differences in the dynamic characteristics of varying bridge types and in variations of design impact conditions. A detailed review of the St. George Island barge impact test program is provided in Chapter 3.

Researchers at the University of Kentucky (UK) conducted numerical finite element barge impact simulations to estimate forces imparted to bridge piers when impacted by a

barge flotilla (Yuan 2005a, Yuan et al. 2005b). High-resolution finite element models of a single jumbo hopper barge and of multi-barge flotillas were developed for the purpose of conducting collision analyses, using the finite element analysis code LS-DYNA (LSTC 2003), on bridge piers. From the analysis results, expressions were developed for predicting average barge impact force and duration of impact load. Additionally, the effects of pier shape and pier stiffness on barge impact force were investigated. A response spectrum analysis technique involving a four degree-of-freedom pier model subjected to a rectangular pulse impact load was also developed.

Researchers at the University of Texas (UTx) have recently investigated the AASHTO probabilistic analysis procedures for bridge impact design under vessel impact loading (Manuel 2006). Computer software has been developed to determine the annual frequency of collapse, facilitating the AASHTO probabilistic design procedure. Additionally, high resolution finite element simulations were conducted to determine impact forces imparted to a pier during an impact event, as well as providing guidance for calculating the ultimate lateral strength of the pier.

2.3 Design of Bridges According to the AASHTO Barge Impact Provisions

A pooled fund research program sponsored by eleven states and the Federal Highway Administration (FHWA) was initiated in 1988 to develop methods of safeguarding bridges against collapse when impacted by ships or barges. The findings of the research were adopted by AASHTO and published in the *Guide Specification and Commentary for Vessel Collision Design of Highway Bridges* and the *Load and Resistance Factor Design (LRFD) Specifications*. Provisions included in these publications serve as a nationally adopted basis for bridge design with respect to vessel collision loads. The provisions allow two approaches to collision resistant bridge design. Either the structure can be designed to withstand the vessel impact loads alone, or a secondary protection system can be designed that will absorb the vessel impact loads and prevent the bridge structure itself from being struck. In addition to providing design guidelines, the AASHTO provisions recommend methodologies for placement of the bridge structure relative to the waterway as well as specifications for navigational aids. Both are intended to reduce the potential risk of a vessel collision with the bridge. Nonetheless, for a wide ranging set of reasons—windy high-current waterways; adverse weather conditions; narrow or curved waterway geometry—most bridges that are accessible to barge impact will likely be struck at some point during their lifetime (Knott and Prucz 2000). With this in mind, all bridges that span navigable waterways need to be designed with due consideration being given to vessel impact loading.

The *AASHTO Guide Specification and Commentary for Vessel Collision Design of Highway Bridges* (1991) provides designers with three methods by which piers may be designed for direct impact loading: Methods I, II, and III. Method I uses a simple semi-deterministic procedure, calibrated to Method II criteria, for the selection of a design vessel. This method however, is less accurate than Method II, and as such, should not be used for complex structures. Method II uses a probability based method for selecting an impact design vessel. Method II is also more complicated than Method I; however, Method II is required if documentation on the acceptable annual frequency of collapse is necessary. Method III is a cost-effective vessel selection procedure that is permitted when compliance with acceptable annual frequency of collapse provisions are neither economically nor technically feasible. This method is typically used in evaluation of the vulnerability of existing bridges.

The first step in designing a bridge structure for barge impact loading is to determine the characteristics of the waterway over which the structure spans. Determination of waterway characteristics includes the geometric layout of the channel (including the centerline) beneath the bridge, the design water depth for each component, and the water currents parallel and perpendicular to the motion of the barge.

Next, impact vessel characteristics—such as, vessel type, size, cargo weight, typical speed, and annual frequency—must be determined based upon actual vessels traversing the design waterway. Furthermore, vessel characteristics must be calculated for waterway traffic in both directions along the channel. Using the characteristics of individual barges, the overall length (length-overall, LOA) of the barge tow must be calculated as the total length of the barge tow plus the length of the tow vessel (Figure 2.9).

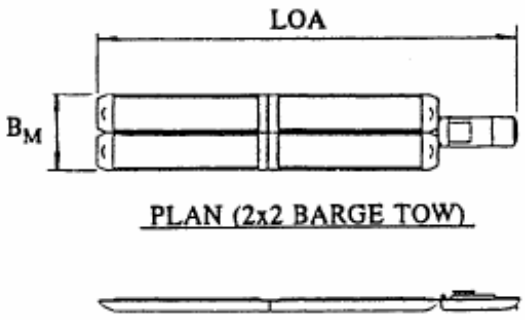

Figure 2.9 Barge tow configuration
(Source: AASHTO Figure 3.5.1-2)

The design impact velocity for each bridge element is calculated based upon the typical vessel transit speed, geometry of the channel, and overall length of the barge tow. The design velocity within the area extending from the centerline of the channel to the edge of the channel is the typical vessel transit speed (V_T) (Figure 2.10). From the edge of the channel (x_C) to a distance equal to three times the overall barge tow length ($3 \cdot \mathrm{LOA}$) from the centerline (x_L), the design speed linearly decreases to a minimum design speed (V_{min}). Beyond a distance of $3 \cdot \mathrm{LOA}$ from the channel centerline, the design speed is held constant at a minimum design impact speed that corresponds to the yearly mean current at that location.

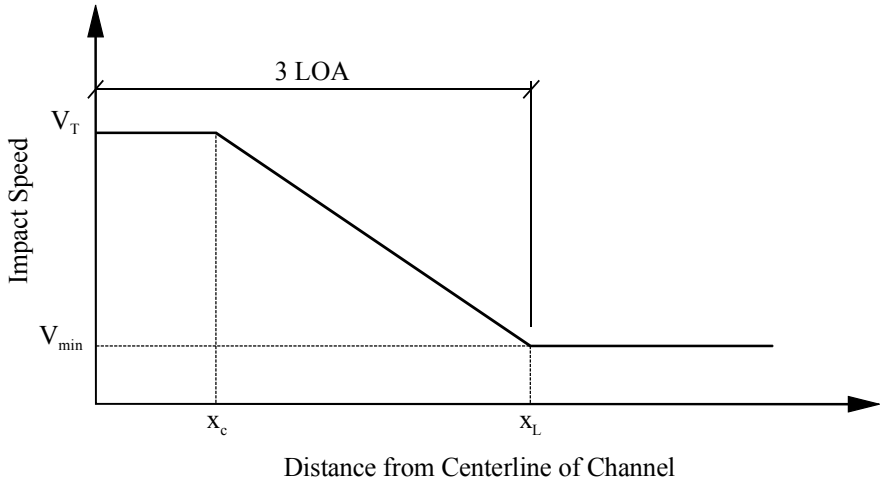

Figure 2.10 Design impact speed

Method II : Probability Based Analysis

AASHTO Method II design requires the designer to calculate the annual frequency of collapse resulting from vessel collisions as:

$$AF = N \cdot PA \cdot PG \cdot PC \tag{2.1}$$

where AF is the annual frequency of collapse, N represents the annual vessel frequency for each design element and vessel type and size, PA is the probability of vessel aberrancy, PG is the geometric probability of impact, and PC is the probability of collapse due to impact. The annual frequency of collapse must be calculated for each bridge element and each type and size of vessel. Summing up all of the individual annual frequencies of collapse yields the annual frequency of collapse for the total bridge. The annual frequency of collapse determined from this process is required to be less than or equal to an acceptable annual frequency of collapse that depends upon the importance of the bridge:

- For critical bridges $AF \leq 0.0001$ (i.e., a 1 in 10,000 probability of failure each year)
- For regular bridges $AF \leq 0.001$ (i.e., a 1 in 1000 probability of failure each year)

Probability of aberrancy (PA) represents the probability that a given vessel will deviate from its course, possibly endangering the bridge. Based upon the proposed bridge site, the most accurate determination of probability of aberrancy is determined from historical data on vessel aberrancy. However, if appropriate historical data are not available, AASHTO permits estimation of the probability of aberrancy:

$$PA = BR \cdot R_B \cdot R_C \cdot R_{XC} \cdot R_D \tag{2.2}$$

where BR is the base aberrancy rate (specified by AASHTO), R_B is the bridge location correction factor, R_C is the water current correction factor in the direction of barge travel, R_{XC} is the water current correction factor transverse to barge travel, and R_D is a vessel traffic density factor. The base aberrancy rate (BR) was determined from historical accident data

along several U.S. waterways. For barge traffic, the base aberrancy rate specified by AASHTO is 1.2×10^{-4} (i.e., 0.00012, or 1 aberrancy in every 8333 barge transits).

The bridge location correction factor (R_B) was implemented to account for the added difficulty in navigating a barge tow around a bend (Figure 2.11):

$$R_B = \begin{cases} 1.0 & \text{straight region} \\ 1.0 + \theta/90 & \text{transition region} \\ 1.0 + \theta/45 & \text{bend region} \end{cases} \tag{2.3}$$

where θ is the angle of the bend in degrees.

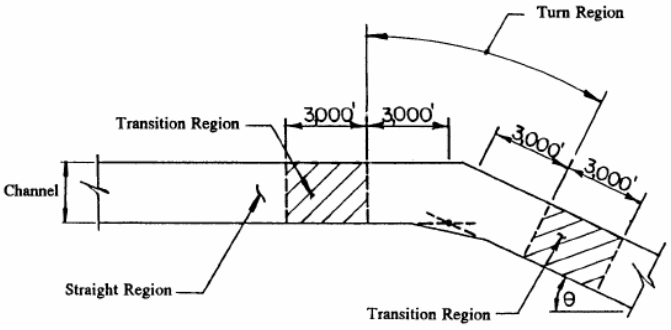

(a) Turn in channel

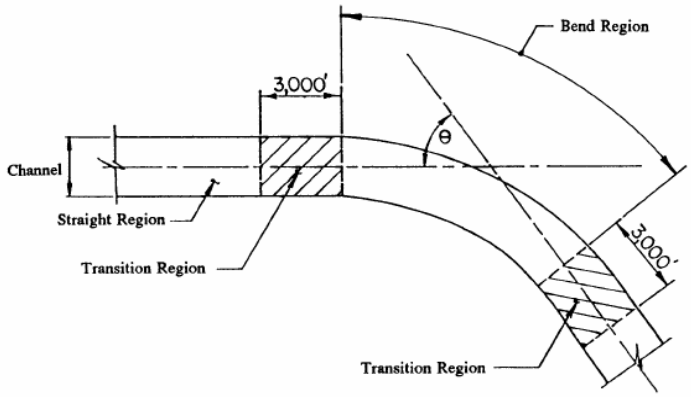

(b) Bend in channel

Figure 2.11 Bridge location correction factor
(Source: AASHTO Figure 4.8.3.2-1)

In order to account for the effects that water currents have on the navigation of a barge tow, correction factors for water currents both parallel (R_C) and transverse (R_{XC}) to the motion of the barge tow are required:

$$R_C = 1 + V_C/10 \tag{2.4}$$

$$R_{XC} = 1 + V_{XC} \tag{2.5}$$

where V_C and V_{XC} are the water current velocities parallel and transverse to the barge motion (in units of knots). Furthermore, depending upon the density of vessel traffic in the waterway, a vessel traffic density factor is used to modify the base aberrancy rate:

- Low density traffic: $R_D = 1.0$
- Average density traffic: $R_D = 1.3$
- High density traffic: $R_D = 1.6$

Geometric probability of impact is defined as the probability that a vessel will strike a bridge element once it has become aberrant. Based on historical barge collision data, AASHTO requires that a normal distribution be used to characterize the locations of aberrant vessels in relation to the centerline of the channel (Figure 2.12). The normal distribution is then used to determine the chance that a given bridge element will be struck by the aberrant barge. Furthermore, the mean value of the distribution is situated on the centerline of the channel and the standard deviation is assumed to be equal to the overall length of the barge tow (LOA). The effective width of impact for each bridge element is calculated as the width of the structural element plus half the width of the vessel on each side of the pier. Using this impact zone width, the geometric probability of impact is calculated as the area under the normal distribution curve that is bounded by the effective impact width and centered on the pier.

Assuming a bridge element is struck by an errant vessel, the probability that the element (e.g., a pier) will collapse must also be determined. AASHTO provides the following relationships for calculating the probability of collapse (PC) based upon the strength of the bridge element and the static vessel impact force that is applied to the element (Figure 2.13):

$$PC = \begin{cases} 0.1 + 9(0.1 - H/P) & \text{if } H/P < 0.1 \\ (1 - H/P)/9 & \text{if } 0.1 \le H/P < 1.0 \\ 0.0 & \text{if } H/P \ge 1.0 \end{cases} \tag{2.6}$$

In this equation, H is the ultimate strength of the pier element, and P is the design static vessel impact force.

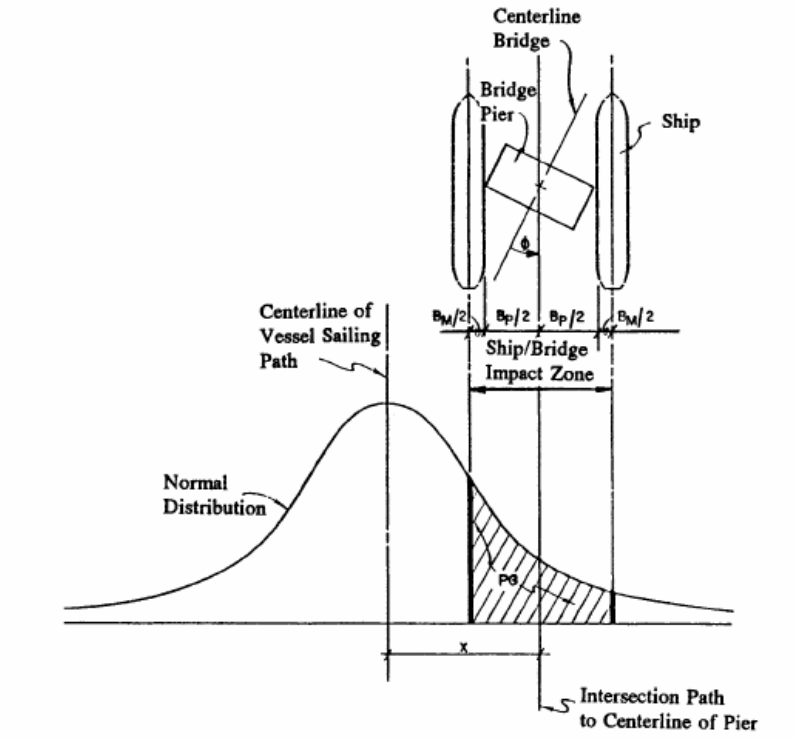

Figure 2.12 Geometric probability of collision
(Source: AASHTO Figure 4.8.3.3-1)

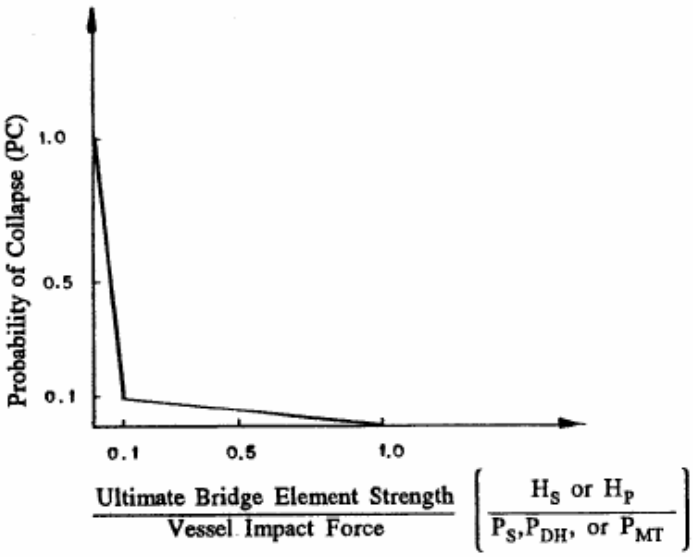

Figure 2.13 Probability of collapse distribution
(Source: AASHTO Figure 4.8.3.4-1)

Barge Impact Force Determination

The AASHTO specifications use a kinetic energy based method to determine the design impact load imparted to a bridge element. Using the total barge tow weight and design velocity determined for each bridge element (e.g., pier), the kinetic energy of the barge is computed as follows:

$$KE = \frac{C_H W V^2}{29.2} \tag{2.7}$$

where KE is the barge kinetic energy (kip-ft), C_H is the hydrodynamic mass coefficient, W is the weight of the vessel tow (in tones), and V is the design speed of the vessel tow (ft/sec). The hydrodynamic mass coefficient (C_H) is included to account for additional inertia forces caused by the mass of the water surrounding and moving with the vessel. Several variables may be accounted for in the determination of C_H: water depth, underkeel clearance, shape of the vessel, vessel speed, current velocity, direction of travel, and the cleanliness of the submerged portions of the hull. A simplified expression has been adopted by AASHTO in the case of a vessel moving in a forward direction at high velocity (the worst-case scenario). Under such conditions, the recommended procedure depends only on the underkeel clearances:

- For large underkeel clearances $(\geq 0.5 \text{ draft})$: $C_H = 1.05$
- For small underkeel clearances $(\leq 0.1 \text{ draft})$: $C_H = 1.25$

where the draft is the distance between the bottom of the vessel and the floor of the waterway. For underkeel clearances between the two limits cited above, C_H is estimated by linear interpolation.

Once the kinetic energy of the barge tow has been determined, a two-part empirical load-prediction model is used to determine the static-equivalent impact load. The first component of the model consists of an empirical relationship that predicts barge crush deformation (inelastic deformation) as a function of kinetic energy:

$$a_B = \left[\left(1 + \frac{KE}{5672}\right)^{1/2} - 1\right]\frac{10.2}{R_B} \tag{2.8}$$

where a_B is the depth (ft.) of barge crush deformation (depth of penetration of the bridge pier into the bow of the barge), KE is the barge kinetic energy (kip-ft), and $R_B = B_B/35$; where B_B is the width of the barge (ft). Figure 2.14 graphically illustrates Eqn. 2.8.

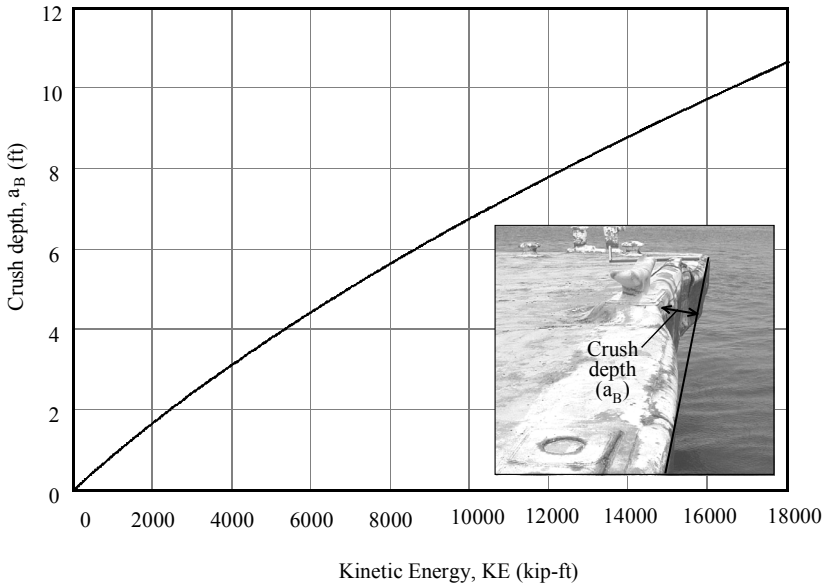

Figure 2.14 AASHTO relationship between kinetic energy and barge crush depth

The second component of the load prediction model consists of an empirical barge crush model that predicts impact load as a function of crush depth:

$$P_B = \begin{cases} 4112 a_B R_B & \text{if } a_B < 0.34 \\ (1349 + 110 a_B) R_B & \text{if } a_B \geq 0.34 \end{cases} \tag{2.9}$$

where P_B is the equivalent static barge impact load (kips) and a_B is the barge crush depth (ft). The AASHTO barge force-deformation relationship given in Eqn. 2.9 is illustrated in Figure 2.15. Furthermore, by combining Eqns. 2.8 and 2.9, a relationship between barge impact force and initial barge kinetic energy may be defined (Figure 2.16). As will be discussed in additional detail in Chapter 4, Eqns. 2.8 and 2.9 above were both adopted from research conducted by Meier-Dörnberg (1983).

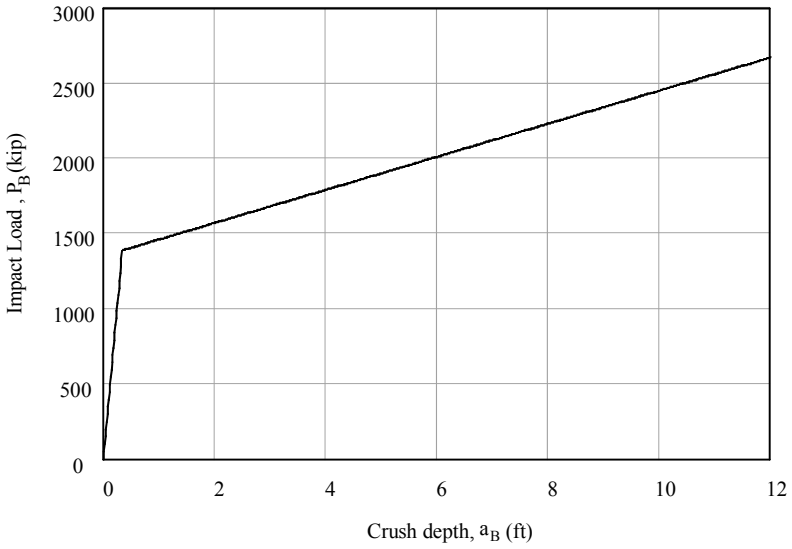

Figure 2.15 AASHTO relationship between barge crush depth and impact force

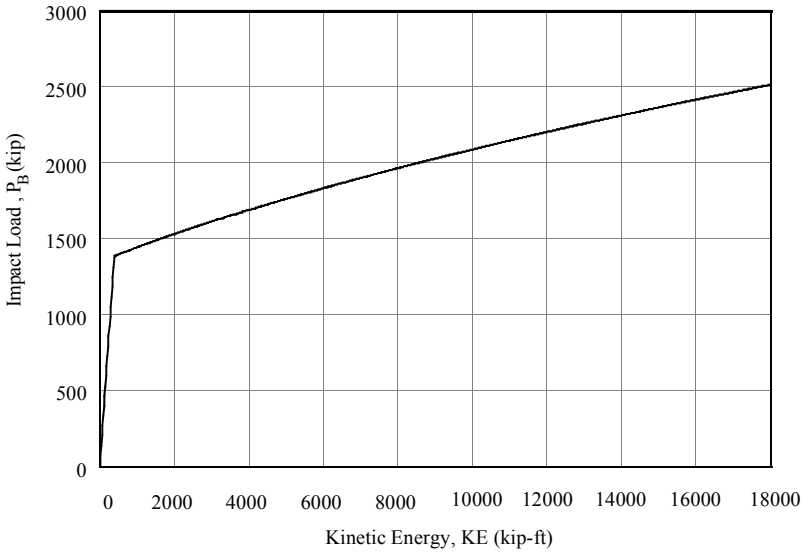

Figure 2.16 Relationship between kinetic energy and impact load

CHAPTER 3
SUMMARY OF FINDINGS FROM ST. GEORGE ISLAND BARGE IMPACT TESTING

3.1 Introduction

In 2004, the University of Florida (UF) and the Florida Department of Transportation (FDOT) conducted full-scale barge impact tests on the old St. George Island Causeway Bridge (Consolazio et al. 2006). Experimental results were obtained to quantify the loading and response of pier and bridge structures subjected to a barge impact. To compliment the physical testing, numerical finite element analysis (FEA) techniques were employed to aid in interpretation of experimental test data. Comparisons of measured experimental data and FEA results substantiated the validity of the experimental data and provided additional insights into the nature of pier response to barge impact loading.

3.2 Overview of Experimental Test Program

Impact tests were conducted on Piers 1 and 3 on the south side of the St. George Island Causeway Bridge, near the navigation channel (Figure 3.1). These piers were selected for the different structural configurations that they represented.

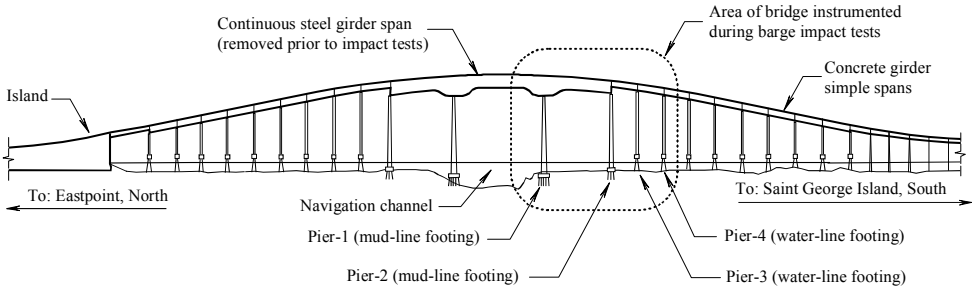

Figure 3.1 Overview of the layout of the bridge

Pier-1 (Figure 3.2), the more impact resistant pier, was a reinforced concrete pier composed of two pier columns, a pier cap, a shear wall for lateral resistance, and a massive concrete pile cap and tremie seal mud-line footing, all supported by forty HP 14x73 steel piles. This pier was adjacent to the navigation channel, and as such, was most prone to impact from an errant vessel. Therefore, Pier-1 was designed to be the most impact resistant pier supporting the bridge. From the perspective of the barge impact test program, Pier-1 was expected to be able to resist the highest loads as well as produce the largest amounts of barge bow deformation.

In contrast to Pier-1, Pier-3 (Figure 3.3) was a more flexible, less impact resistant reinforced concrete structure composed of two pier columns, a pier cap, and a shear strut for lateral resistance. Unlike the massive pile and cap foundation system supporting Pier-1, Pier-3 was supported by two small waterline pile caps, each on top of four 20 in. square prestressed concrete piles. Due to its flexibility, Pier-3 was not able to resist large impact forces. Pier-3, however, was selected to investigate the effects of low-energy impacts on

secondary support piers. Furthermore, it was anticipated that the barge would sustain negligible permanent barge bow deformations during impacts on Pier-3.

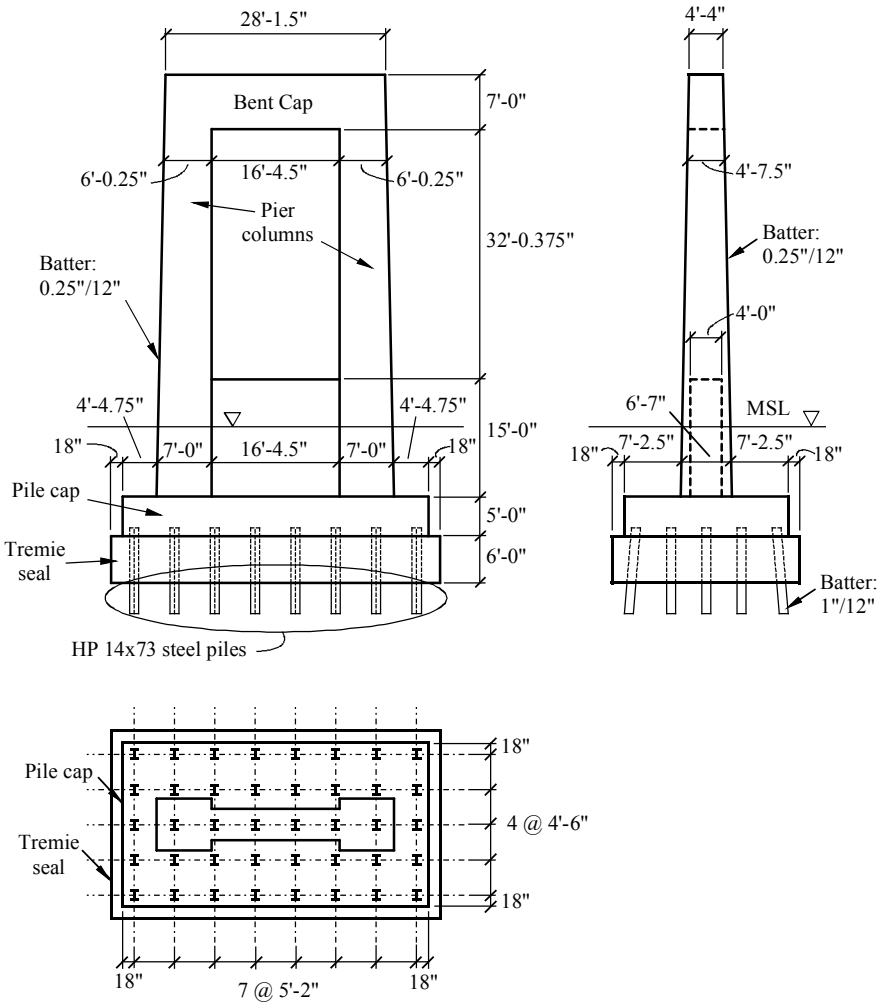

Figure 3.2 Schematic of Pier-1

The overall experimental test program was conducted in three distinct series, each with a different structural configuration. The first test series (Figure 3.4), denoted series P1, involved tests conducted on Pier-1 in isolation, with the primary objective of generating maximal impact loads and inelastic barge bow deformations. In order to achieve such loads and deformations, the mass of the barge was increased by placing two 55 ft. spans of concrete deck from a previously demolished section of the bridge on top of the barge, for a total barge-plus-payload weight of 604 tons. Impact speeds in series P1 varied from 0.75 knots 3.45 knots. Instrumentation used during test series P1 included load cells, accelerometers (on both the pier and the barge), displacement transducers, optical break beams (used to trigger the data acquisition (DAQ) system and provide precise barge velocity determination), and a pressure transducer (used to measure pressure changes in the water). See Consolazio et al. (2006) for a detailed discussion of the instrumentation systems used.

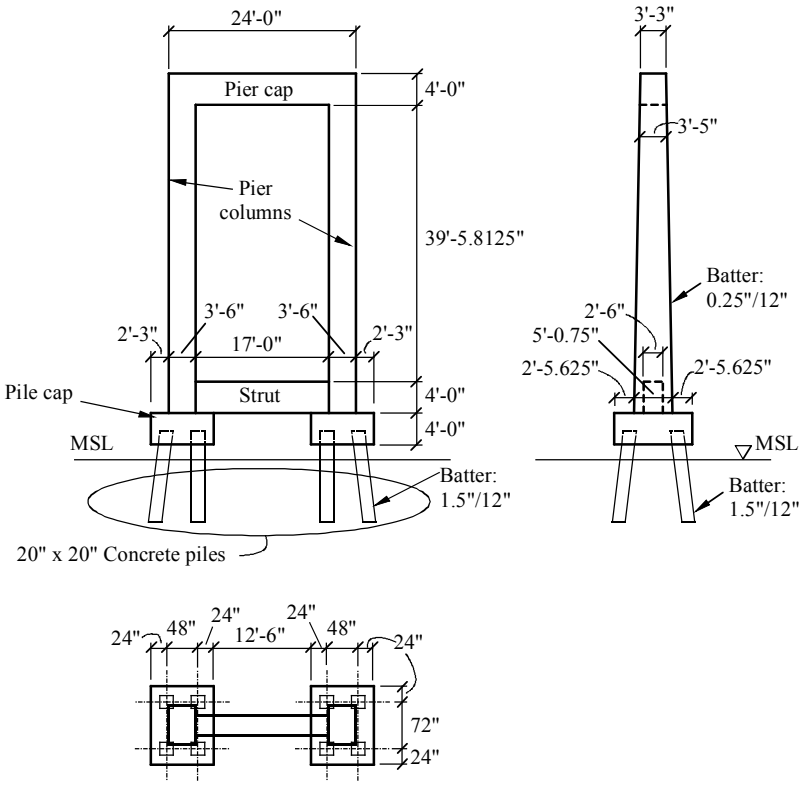

Figure 3.3 Schematic of Pier-3

Figure 3.4 Test barge with payload impacting Pier-1 in the series P1 tests

Upon completion of the series P1 tests, the payload spans on the test barge were removed (Figure 3.5a), restoring the empty barge weight to 275 tons. After removal of the payload spans from the barge, impact tests on Pier-3 began; the first series of which was denoted series B3. The B3 test series involved low-energy impacts on Pier-3 with superstructure spans still intact between piers 2, 3, 4, 5, and beyond (Figure 3.5b). Due to the relatively high flexibility of Pier-3, impact velocities were limited so as to avoid dislodging

the superstructure. With the reduced mass and lower velocities, the impact energies imparted to the pier during the B3 series of impacts were not substantial enough to generate noticeable permanent barge bow deformations. The instrumentation used during test series B3 included load cells, accelerometers (including the addition of accelerometers on the superstructure), displacement transducers, an optical break beam, and strain gages (attached to the piles).

(a) (b)

Figure 3.5 Series B3 tests: a) Empty test barge used in the series B3 tests, and b) Test barge impacting the bridge at Pier-3 during the series B3 tests

Following the B3 series tests, the superstructure connecting piers 2, 3, and 4 was removed, leaving Pier-3 isolated (Figure 3.6). Impact tests were then conducted on Pier-3 in isolation during tests series P3. The series P3 tests were very similar to the series B3 tests with respect to barge velocities and mass, instrumentation, and barge bow deformations. Data from the B3 and P3 series tests were used to compare the response of an isolated pier to a pier that is integrated within a bridge structure.

Figure 3.6 Pier-3 in isolation for the series P3 tests

A total of fifteen impact tests were conducted: eight in series P1, four in series B3, and three in series P3. Maximum allowable impact speeds for each series were governed by equipment limitations, weather conditions, and safety concerns. For additional details, see Consolazio et al. (2006).

Finite element models were developed using the pier analysis program, FB-MultiPier (2007), which was selected for its ability to model both dynamic behavior and material nonlinearity. A brief description of the finite element models is presented below, however, for a more detailed discussion see Consolazio et al. (2006) and McVay et al. (2005).

3.3 Overview of Analytical Research

3.3.1 FB-MultiPier Models

The FB-MultiPier Pier-1 model used frame elements to model the pier components, such as the columns, pier cap, shear wall, and piles; and shell elements to model the behavior of the cap and seal (Figure 3.7). Since shell elements were used to model the pile cap, the piles connected to the mid-plane of the cap. However, in the actual structure, the piles were embedded in both the 5 ft thick pile cap, and the 6 ft thick tremie seal. Within this embedment length, the piles were restrained against flexure. To correctly model this embedment, a network of cross bracing frame elements (Figure 3.7) was placed in the top 8.5 ft (half of the 5 ft cap plus the 6 ft seal) of the piles. The material behavior of all structural elements was chosen to be linear elastic because the physical tests were non-destructive in nature.

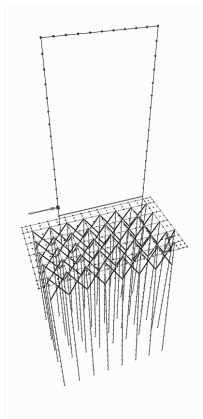

Figure 3.7 Pier-1 FB-MultiPier model

FB-MultiPier Pier-3 model

All structural components of Pier-3—pier columns, pier cap, shear strut, and piles—excluding the pile caps, were modeled using frame elements (Figure 3.8). As with Pier-1, the pile caps were modeled using shell elements at the mid-plane elevation of the caps. In the Pier-3 model, it was determined that additional elements were necessary to correctly model the shear strut behavior. As such, cross bracing was provided to stiffen the shear strut. Furthermore, though not monolithically cast together, the strut and the pile caps were cast such that they could come in contact during impact. Therefore, a strut was placed connecting

the pier column to the pile caps to model this added stiffness. Similar to the previous model, the material model chosen was linear elastic.

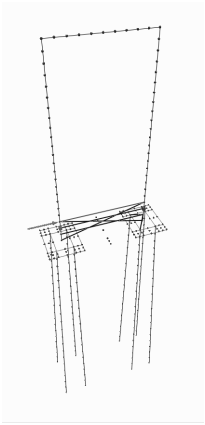

Figure 3.8 Pier-3 FB-MultiPier model

FB-MultiPier Bridge model

In addition to the Pier-3 model, a model of the bridge was also developed (Figure 3.9). This model included Piers 2, 3, 4, and 5 with superstructure elements connecting adjacent piers. Models of Piers 4 and 5 were developed from the Pier-3 model since these three piers have very similar structural layouts—with variation only in the height of the pier column. Pier-2 had a similar layout to Pier-1 in that it was composed of two pier columns, a pier cap, a shear wall, and a massive mudline footing with a pile cap resting on twenty-one steel H-piles. All elements of each pier were modeled using frame elements with the exception of the pile caps, which were modeled using shell elements. The superstructure was modeled using frame elements with cross-sectional properties calculated from the cross-sectional properties of the individual elements.

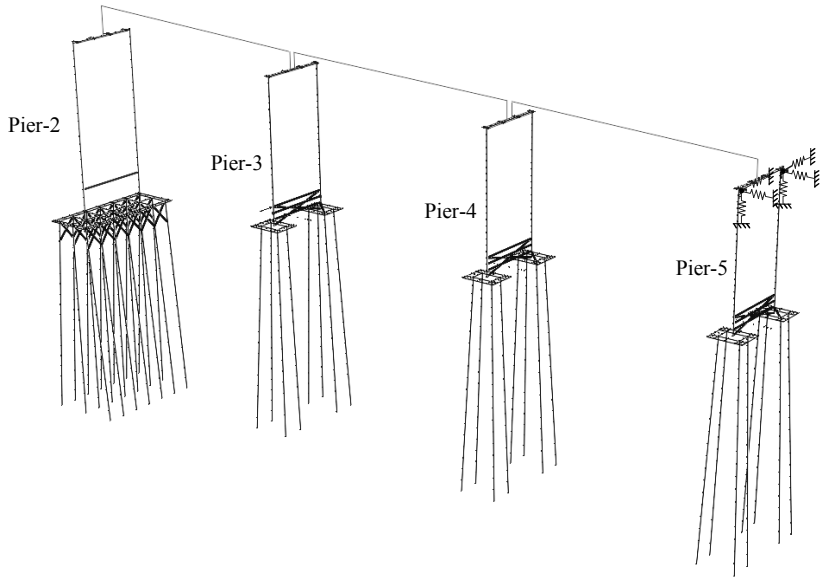

Figure 3.9 Bridge FB-MultiPier model

3.3.2 Finite Element Simulation of Models

In order to understand the sources of resistance that are mobilized during a barge impact scenario, it was imperative to quantify all of the forces acting on the structure. However, sensors installed on the piers were unable to measure all of the forces generated during the impact tests. Thus, using experimental data, the numerical models discussed previously were calibrated to yield responses similar (e.g. pier displacement) to those measured experimentally.

The general calibration procedure involved applying the impact loads measured from the experimental tests directly to the numerical models of the piers. Various parameters (e.g. soil properties) were then calibrated such that the numerical predictions of pier response—pier displacement, pile displacement, pile shears, pressure forces on the foundation, and other quantities (all discussed below)—agreed well with the measured experimental data. With confidence in the numerical models established, results from the analyses were then used to predict sources of resistance that could not be measured during the experimental tests.

This procedure was applied to three characteristic impact tests from the experimental program. Each test in the experimental study was given a four-character designation; the first two characters indicate the test series in which the impact tests were conducted, and the second two characters indicate the specific test within that series. The three tests analyzed are as follows: 1.) P1T7 (i.e. test series P1, test number 7) 2.) P3T3, and 3.) B3T4. These three tests represent some of the more severe impacts conducted. The remainder of this section focuses on results from dynamic analyses of these three tests. Specifically, the sources of resistances are broken down and compared to the impact force (as well as each other) during each simulation.

3.3.2.1 Impact test P1T7

Shown in Figure 3.10 is a schematic of Pier-1 with the forces acting upon the structure during test P1T7. Due to the embedment of the pier cap and tremie seal in the soil, a complex interaction—both static and dynamic—between the soil and the pier foundation occurred. Forces presented in the schematic that were experimentally measured—either directly or indirectly—include the impact force, inertia force, shear force in the instrumented pile, and the cap+seal passive+active pressure force. The experimentally measured impact load for test P1T7 was applied to the finite element model as an external force (Figure 3.10). Calibration of the model was then carried out to bring model and experimental results into agreement mainly through refinement of soil parameters.

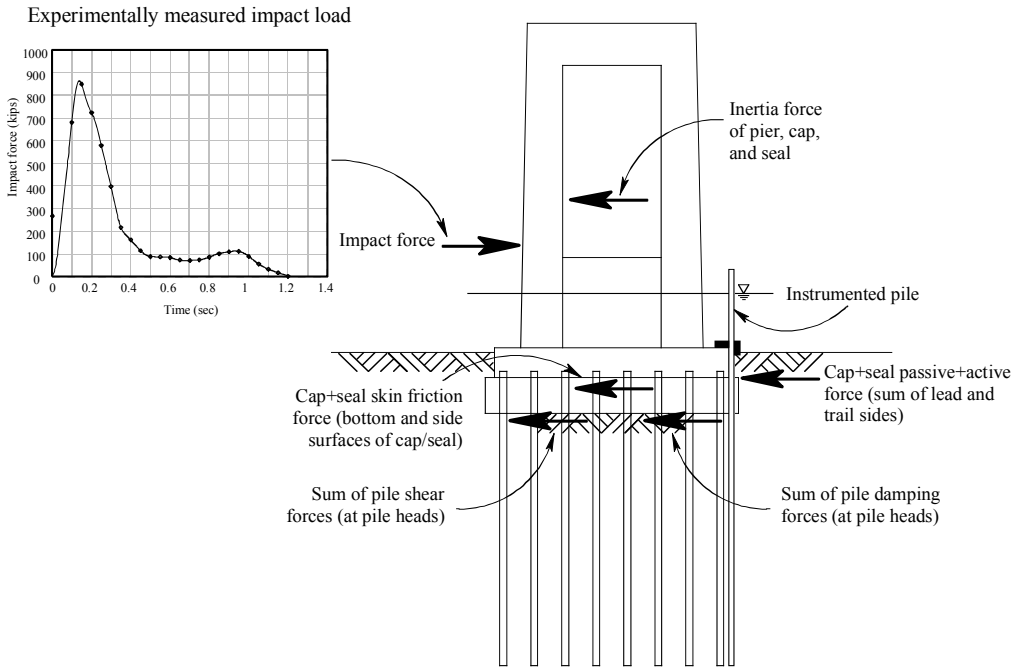

Figure 3.10 Schematic of forces acting on Pier-1

Figure 3.11a provides a comparison of all forces acting on the pier structure during the P1T7 impact, and Figure 3.11b compares the soil forces acting on the pile cap and tremie seal. Positive values correspond to forces acting in the directions indicated by the arrows shown in Figure 3.10. The effective load presented in these plots is a combination of the applied load and the negative portion of the inertial (acceleration-dependent) force. This approach was used because, as the inertial force changes from a positive value—representing a resistance to the motion of the pier—to a negative value, the force becomes a source of loading, further driving the motion of the pier.

Table 3.1 summarizes the maximum values of the five major forces acting on the pier, as presented in Figures 3.11. Examining the data presented in the table, it is evident that the inertial resistance is mobilized more rapidly than all other sources of resistance. Note that at the time at which the inertial resistance is fully mobilized (250 kips at 0.10 sec), the inertial resistance is approximately 40-percent of the applied load of 600 kips at the same point in time. Furthermore, the other three major sources of resistance indicated in Figure 3.11a are

all less than 200 kips. This indicates that at an early stage of an impact event, the mass properties of the pier structure comprise an important contribution to the total resistance developed.

Table 3.1 Summary of forces acting on the pier during test P1T7

Force	Approx. maximum (kips)	Time to peak (sec)
Applied loading	850	0.15
Inertial forces on the pier	250	0.10
Sum of pile shears	275	0.27
Pressure forces on cap+seal	200	0.20
Friction forces on cap+seal	500	0.25

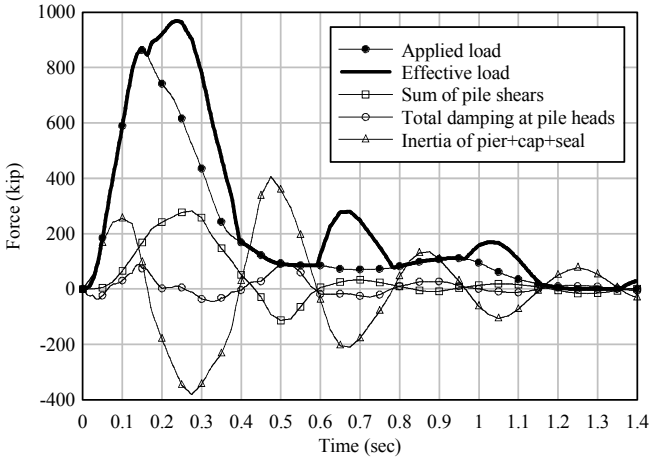

(a)

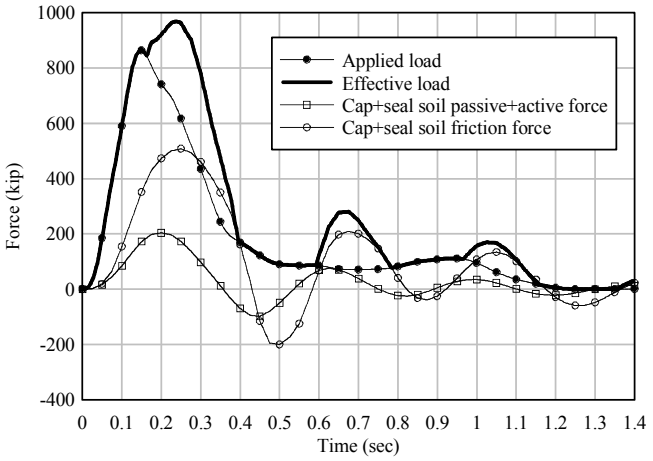

(b)

Figure 3.11 Resistance forces mobilized during tests P1T7: a) Forces acting on the pier structure, and b) Cap and seal pressure and friction forces

As the impact event continues, note that between 0.1 and 0.2 seconds, the inertial force has reversed direction, effectively providing an additional source of loading (Figure 3.11a). When combining this inertial load with the applied load, the effective load maximizes at approximately 970 kips at 0.25 sec. Comparing this value to the major sources of resistance present, it is apparent that the sum of the pile shears (an indication of the soil forces acting on the piles) constitutes only 30-percent of the total resistance, whereas the soil forces acting on the cap and seal constitute approximately 70-percent of the total resistance, thus indicating that the cap and seal forces have a major effect on the total resistance (Figure 3.11).

3.3.2.2 Impact test P3T3

Shown in Figure 3.12 is a schematic of Pier-3 with the forces acting upon the structure during test P3T3. One of the key differences between this test and test P1T7, is that the soil forces acting on the cap and seal during test P1T7 are not present in test P3T3, as the pile caps are above the mudline. Thus, looking at the forces acting on the pier structure, the interaction of Pier-3 with the surrounding soil was far less complex than that of Pier-1 and its surrounding soil. As with test P1T7, the experimentally measured P3T3 load history was applied dynamically to the structure (Figure 3.12). Furthermore, results from the calibrated P3T3 model agreed well with the results from the experimental test (Consolazio et al. 2006).

As with test P1T7, the inertial force acting on Pier-3 mobilizes earlier, reaching a maximum value of approximately 370 kips at 0.08 sec, than the sum of the pile shears, which maximizes at approximately 400 kips at 0.23 sec (Figure 3.13). Furthermore, this inertial resistance clearly dominates the total resistance of the pier at this early stage, representing approximately 75-percent of the total resistance at 0.08 sec. In contrast, the pile shears (slightly larger than 100 kips at 0.08 sec) only represent 25-percent of the total resistance. Clearly, inertial forces provide an important source of resistance early in the P3T3 test.

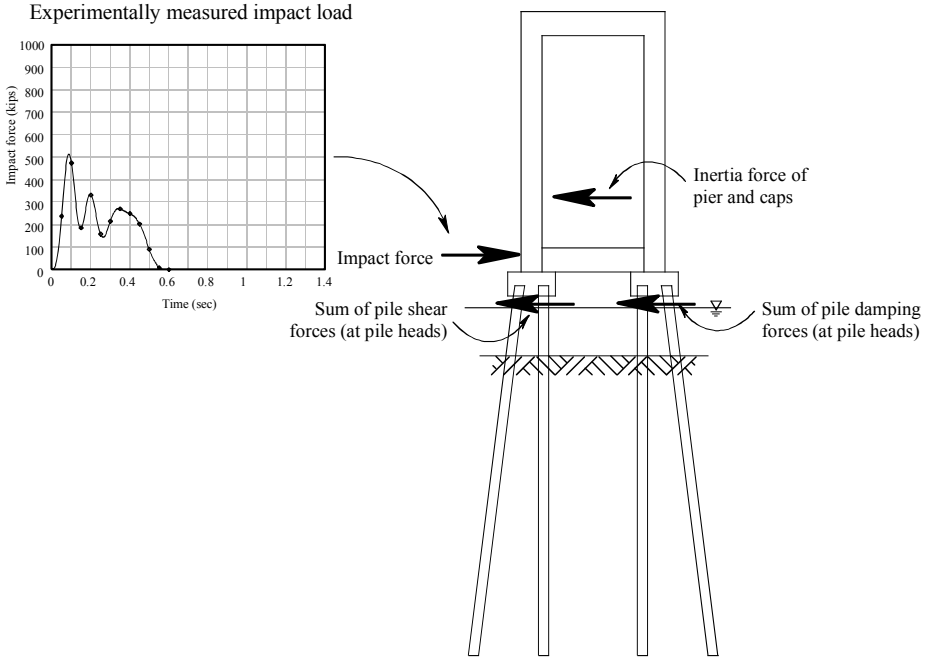

Figure 3.12 Schematic of forces acting on Pier-3

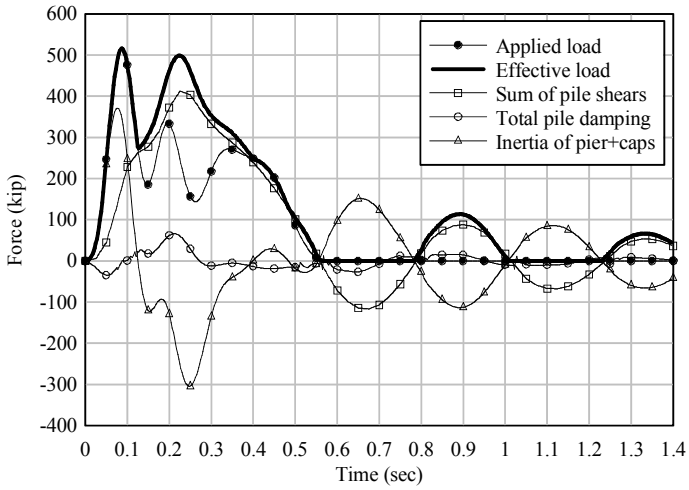

Figure 3.13 Resistance forces mobilized during tests P3T3

3.3.2.3 Impact test B3T4

Impact test B3T4 differed from tests P1T7 and P3T3 in that during test B3T4, portions of the superstructure connecting Pier-3 to adjacent piers were still intact. Comparing Figure 3.14 to Figure 3.12, it can be seen that the sources of resistance present in test B3T4 are the same as those in P3T3 with the addition of load transferring through shear in the superstructure bearings to the superstructure and adjacent piers. Using the bridge model discussed earlier, a dynamic FB-MultiPier analysis was conducted. As with tests P1T7 and P3T3, the experimentally measured B3T4 impact load was applied to Pier-3 in the numerical model (Figure 3.14).

Forces acting on the pier were extracted from the FB-MultiPier analysis of test B3T4, and are presented in Figure 3.15. Like previous tests, pier inertia forces mobilized earlier than any other forms of resistance, maximizing at 190 kips at approximately 0.08 seconds and accounting for approximately 70-percent of the 280-kip applied load at this point in time, thus clearly dominating the resistance early in the impact. As the pier displaces further, shear forces (representing static and dynamic resistance from the soil) start to mobilize, maximizing at about 260 kips at 0.20 seconds. Following the shear forces, forces in the bearing pads (representing resistance from adjacent piers) begin to mobilize, maximizing at 130 kips at approximately 0.16 seconds.

As with the P1T7 and P3T3 analyses, the inertia resistance quickly decreases, and changes to a form of loading when it becomes negative, further driving pier motion. When the bearing shear force decreases and becomes negative, it constitutes a form of loading on the structure that also drives the motion of the pier. To illustrate this concept, the magnitudes of the inertial force and the bearing shear force (when negative) are added to the applied load to form an effective load history (Figure 3.15). Note that from 0.25 to 0.50 seconds, this effective load is approximately equal to the shear in the piles (with the difference being attributable to structural damping), thus indicating that the effective load drives the motion of the pier, and the resistance to this motion is mobilized in the soil (acting through the pile shears).

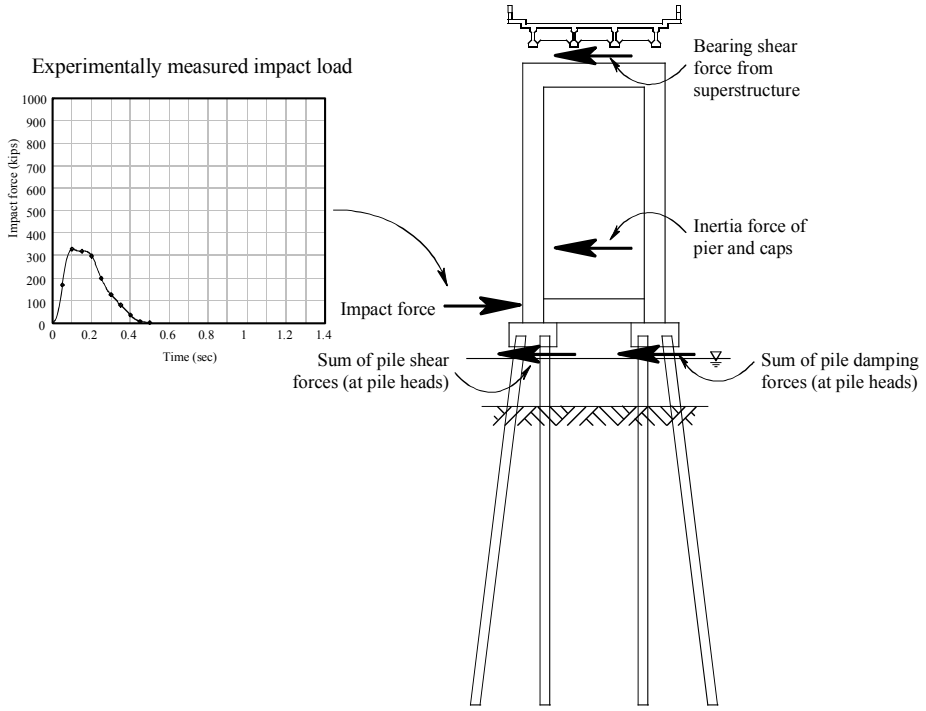

Figure 3.14 Schematic of forces acting on Pier-3 during test B3T4

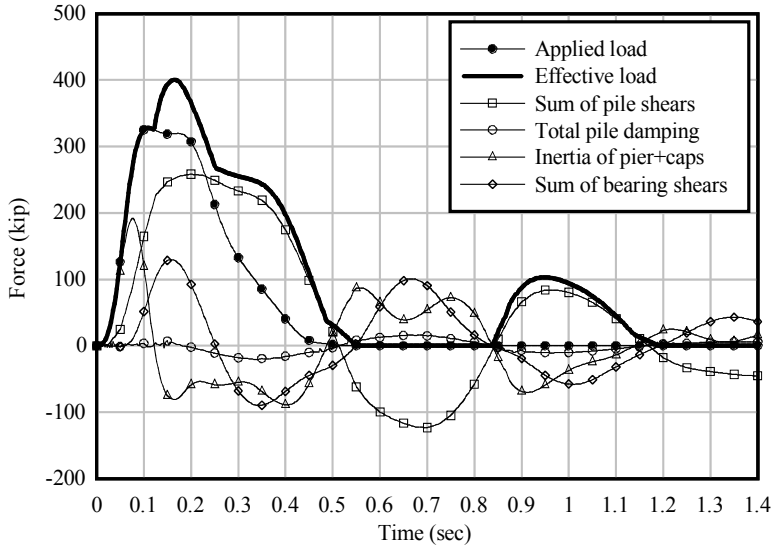

Figure 3.15 Resistance forces mobilized during tests B3T4

3.4 Comparison of Dynamic and Static Pier Response

Currently, design of bridges to resist barge impact load involves using an equivalent static load procedure—such as the method outlined in AASHTO—in which the calculated load is applied to a static pier model. However, as presented in the results outlined in

previous sections, dynamic effects (such as damping and inertial forces) constitute a significant source of resistance, and in some cases additional loading. In the present section, comparisons between static and dynamic analyses for each of the three tests simulated (i.e. P1T7, P3T3, and B3T4) are presented. Three separate analyses were conducted for each test: 1.) dynamic analysis using the experimentally measured load histories, 2.) static analysis using the peak load from the experimentally measured load histories applied statically, and 3.) static analysis using the AASHTO specified load based upon the initial impact energy measured for the tests. Each of these cases is summarized in Table 3.2. Comparisons of results for each of these three analyses provide insight into the level of safety present in static analysis procedures, such as the methods provided by AASHTO.

Table 3.2 Dynamic and static analysis cases

Case	Impact condition	Analysis type	Load description	Max. load (kip)	Pier/pile behavior	Soil behavior
A	P1T7	Dynamic	Time-varying P1T7	864	Linear	Nonlinear
B	P1T7	Static	Peak P1T7 load	864	Linear	Nonlinear
C	P1T7	Static	AASHTO	1788	Linear	Nonlinear
D	P3T3	Dynamic	Time-varying P3T3	516	Linear	Nonlinear
E	P3T3	Static	Peak P3T3 load	516	Linear	Nonlinear
F	P3T3	Static	AASHTO	398	Linear	Nonlinear
G	B3T4	Dynamic	Time-varying B3T4	328	Linear	Nonlinear
H	B3T4	Static	Peak B3T4 load	328	Linear	Nonlinear
I	B3T4	Static	AASHTO	276	Linear	Nonlinear

Cases A, D, and G in Table 3.2 represent dynamic analyses in which the time-varying experimentally measured loads are applied to the piers in tests P1T7, P3T3, and B3T4 respectively. For cases B, E, and H, the peak load from experimentally measured load histories (864 kips, 516 kips, and 328 kips for tests P1T7, P3T3, and B3T4 respectively) was applied to the structures statically. Finally, cases C, F, and I represent the cases in which the AASHTO equivalent static load is calculated from the measured impact energies (494 kip-ft, 108 kip-ft, and 75 kip-ft for experiments P1T7, P3T3, and B3T4 respectively), and then applied to the structure in a static manner. In each case, a hydrodynamic mass coefficient of 1.05—the value specified by AASHTO for large underkeel clearances (see Chapter 2, Section. 2.3)—was used. All dynamic effects (such as structural and soil damping, inertial effects, and cyclic degradation behavior) are absent in the static analysis for each model.

The experiments are broken down into two categories: 1.) high-energy impacts (those in which there is enough impact energy to produce significant plastic deformation of the barge bow), and 2.) low-energy impacts (those in which negligible plastic deformation of the barge bow is observed). The P1T7 experiment—along with the majority of the P1 series tests—falls into the former category, where as the P3 and B3 series tests fall into the latter.

Figure 3.16 presents key results for the foundation of each pier from each analysis. For the high-energy impact P1T7, a comparison between cases A and B shows that for the same peak load, the maximum dynamic pier displacement is 32-percent larger than the static displacement. Furthermore, as expected, the pile shears and moments are also larger for the dynamic analysis. This amplification in pier displacement, and ultimately response forces, indicates that inertial effects play an important role in driving the pier motion.

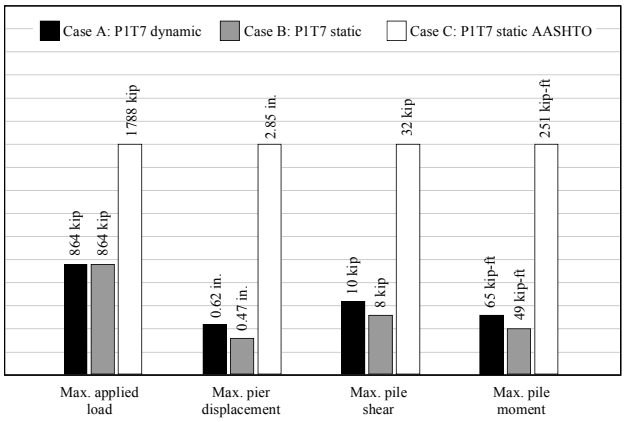

(a)

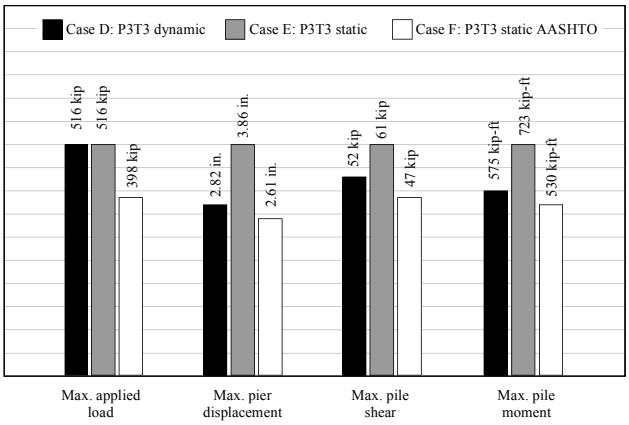

(b)

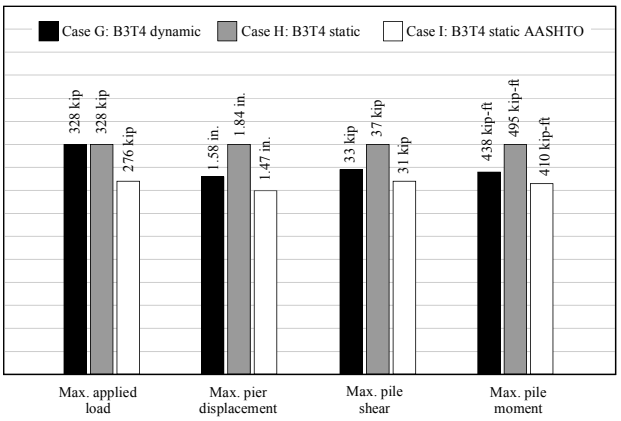

(c)

Figure 3.16 Comparison dynamic and static analysis results for foundation of pier: a) P1T4, b) P3T3, and c) B3T4

A comparison of the low-energy cases (cases D and E for test P3T3, and cases G and H for test B3T4) reveals trends opposite to those observed among the high-energy cases. The case D dynamic analysis yields a maximum displacement that is 27-percent smaller than that resulting from the case E static analysis. Likewise, with test B3T4, the case G dynamic analysis yields a maximum displacement that is 14-percent smaller than that obtained from the case H static analysis. For both tests, the predicted pile shears and moments exhibit a similar decrease in the dynamic cases, as is expected.

Including the AASHTO results (i.e. cases C, F, and I), it can be seen that for the high-energy impact of test P1T7, the AASHTO procedure predicts a load that is higher than the peak dynamic load. As a result, the predicted pier displacements from the AASHTO load case are 360-percent larger than the maximum dynamic pier displacement, and consequently, the resulting pile shears and moments are also much larger. In contrast, for cases F and I, the AASHTO procedure predicts loads that are smaller than the experimentally measured peak dynamic loads for tests P3T3 and B3T4 respectively. However, when resulting pier displacements and pile forces are compared, these quantities are only slightly smaller than the maximum dynamic quantities for the respective tests.

For the cases in which piers are in isolation, the column shears and moments are negligible for the static cases, as expected, considering the absence of restraint at the top of the pier. However, for the B3T4 cases, significant forces are developed in the columns in the static cases as load transfers to the superstructure. Thus, in Figure 3.17 the maximum applied loads, column shears and moments, and bearing shear forces are compared for cases G, H, and I. The column shear and moment, and the bearing shear force predicted for case H are 26, 27, and 28-percent of those predicted from the dynamic case; and those from case I are 20, 21, and 22-percent of the dynamic quantities. Given that demands on the foundation, such as pile shears and moments, are quite similar for the B3T4 cases, the disparity between the column force results of the static and dynamic cases is attributable to amplification factors from the inertia forces generated in the superstructure. Although momentary, the effects of these inertia forces can account for as much as 70 to 80-percent of the column forces generated. Thus, failure to account for dynamic restraint, in addition to the static resistance, at the top of a pier can lead to unconservative column design forces.

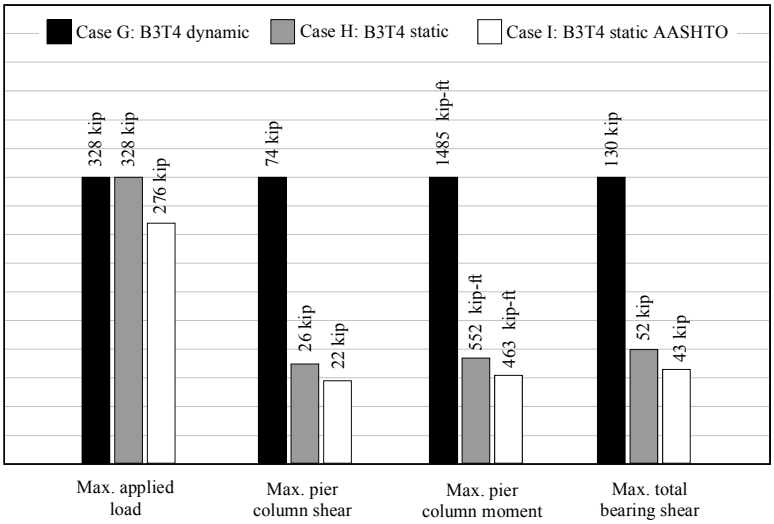

Figure 3.17 Comparison of dynamic and static analysis results for pier structure

3.5 Observations

Field testing of the old St. George Island Causeway Bridge was undertaken to investigate impact loads, as well as resulting pier responses, generated during barge-to-bridge collisions. Results from these experiments were then used to calibrate several finite element models, the results of which were used to interpret the experimental results, as well as identify sources of resistance that could not be measured during the experiments. Subsequently, the results from these analyses were used to conduct a preliminary assessment of the current AASHTO load determination procedure.

Results indicate that mass-proportional forces, known as inertial forces, constitute a significant source of resistance to the motion of a pier during the early stages of a barge impact. Inertial forces tend to mobilize earlier in an impact than static or damping forces (displacement and velocity-proportional forces respectively). However, as the pier reaches its peak velocity and begins to decelerate, these inertial forces change from a source of resistance (to pier motion) to an effective load that actually drives pier motion.

The effect of inertia forces is even more pronounced in the analysis of bridge structures, as opposed to isolated piers, as the inertial resistance and effective loading due to the presence of a superstructure can significantly increase the design forces in pier columns. Given the important influences that inertial forces have on structural response, it is recommended that dynamic analysis procedures, which are capable of accounting for such phenomena, be used in the design and assessment of bridges that may be subjected to vessel collision loading.

CHAPTER 4
BARGE BOW FORCE-DEFORMATION RELATIONSHIPS

4.1 Introduction

During a barge-bridge collision, the magnitude of impact force generated on the bridge structure is strongly related to the stiffness of the barge bow, among other factors. Barge bow stiffness in both the linear elastic and nonlinear inelastic ranges may be characterized by a nonlinear force-deformation relationship (also referred to as a barge crush-curve). In this chapter, the basis for the current AASHTO crush-curve is reviewed, and new crush-curves, based on work conducted in this study and in the prior St. George Island barge impact study, are proposed.

4.2 Review of the Current AASHTO Load Determination Procedure

As described in Chapter 2, barge impact load calculations per the current AASHTO specifications make use of an empirical load calculation procedure. The equivalent static load determination equations presented in Chapter 2 are based upon an experimental study conducted by Meier-Dörnberg (1983). As previously noted, Meier-Dörnberg conducted both static and dynamic impact tests on reduced-scale European Type IIa barge bow sections. The European type IIa barge is similar in size and configuration to the jumbo hopper barges widely used throughout the United States. Two dynamic tests, conducted using 2-ton pendulum hammers and two different shapes of impact head, were conducted on 1:4.5-scale stationary (i.e. fixed) barge bows. One dynamic test involved three progressive impacts using a cylindrical hammer with a diameter of 1.7 m (67.0 in), whereas the other involved three progressive impacts using a ninety-degree pointed hammer. A static test was also conducted on a 1:6 scale barge bow using a 2.3 m (90.6 in) hammer. Results obtained from the dynamics tests are shown in Figures 4.1a and b and results from the static test are shown in Figure 4.1c.

Using the experimental data collected, Meier-Dörnberg developed mathematical relationships between kinetic energy (E_B), inelastic barge deformation (a_B), and dynamic and static force (P_B and $\overline{P}_B$ respectively). These relationships are illustrated in Figure 4.2. As the figure suggests, no major differences were found between the magnitude of dynamic and static impact force. However, this fact is likely due to the stationary barge bow configuration used in the testing. Omission of a flexible impact target and the corresponding barge-pier interaction necessarily precludes the ability to measure and capture dynamic amplification effects.

Inelastic barge bow deformations were, however, measured in the Meier-Dörnberg study. Results showed that once the barge bow yielding was initiated, at approximately 4 in. of deformation (a_B), the stiffness of the bow diminishes significantly (see Figure 4.2). Additionally, Meier-Dörnberg recognized that inelastic bow deformations represent a significant form of energy dissipation.

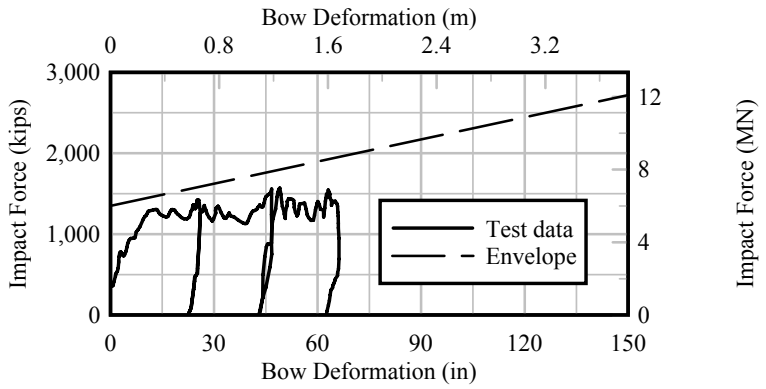

(a)

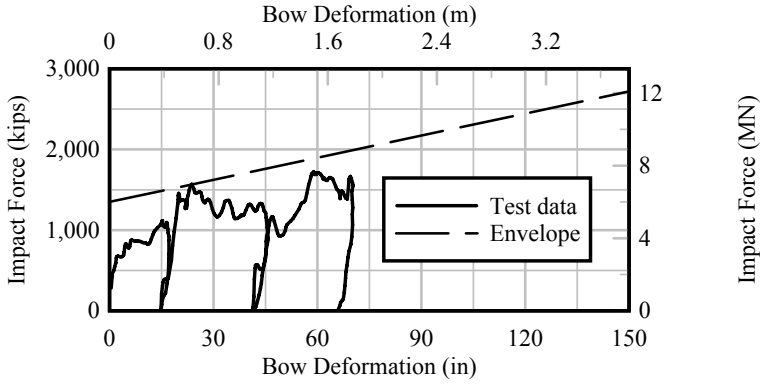

(b)

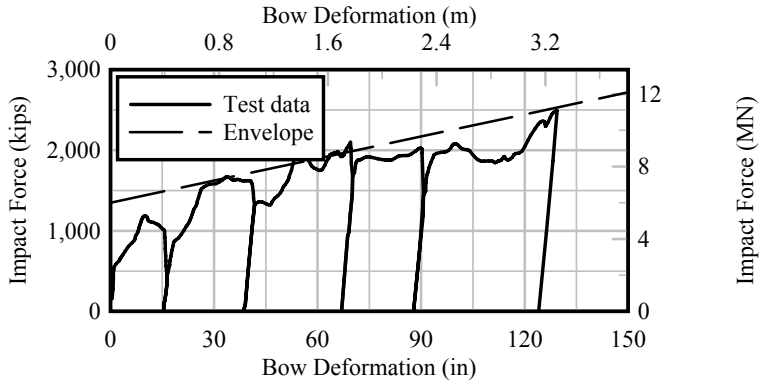

(c)

Figure 4.1 Force-deformation results obtained by Meier-Dörnberg (Adapted from Meier-Dörnberg 1983): a) Results from dynamic cylindrical impact hammer test, b) Results from dynamic 90° pointed impact hammer test, and c) Results from static impact hammer test

In the development of the AASHTO barge impact design provisions, the relationships between initial barge kinetic energy (KE), barge deformation (a_B) and equivalent static force (P_B) developed by Meier-Dörnberg, were adopted with minimal modifications:

$$KE = \frac{C_H W V^2}{29.2} \tag{4.1}$$

$$a_B = \left[\left(1 + \frac{KE}{5672}\right)^{1/2} - 1\right]\frac{10.2}{R_B} \tag{4.2}$$

$$P_B = \begin{cases} 4112 a_B R_B & \text{if } a_B < 0.34 \\ (1349 + 110 a_B) R_B & \text{if } a_B \geq 0.34 \end{cases} \tag{4.3}$$

In these equations, a_B is the depth of barge crush deformation (ft), KE is the barge kinetic energy (kip-ft), and $R_B = B_B/35$ where B_B is the width of the barge (ft). The only notable difference between the expressions developed by Meier-Dörnberg and the AASHTO expressions given above as Eqn. 4.1 - 4.3 is the use of a barge width correction factor (R_B). While the AASHTO specification utilizes the R_B term to reflect the influence of barge width, no such factor has been included to account for variations in either the size (width) or geometric shape of the bridge pier being impacted. In Figure 4.3, the AASHTO barge force-deformation relationship (crush-curve) given by Eqn. 4.3 is plotted for a hopper barge having a width B_B=35 ft and for a tanker barge having a width of B_B=50 ft.

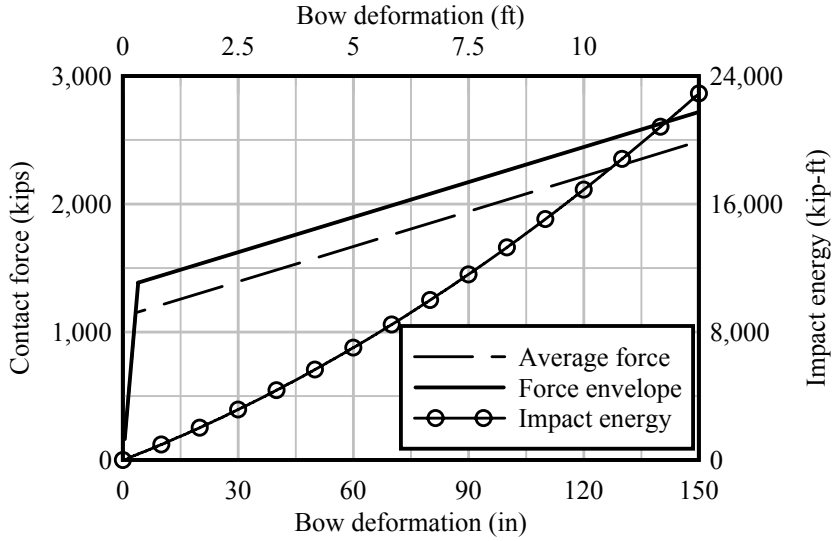

Figure 4.2 Relationships developed from experimental barge impact tests conducted by Meier-Dörnberg (1983) (Adapted from AASHTO 1991)

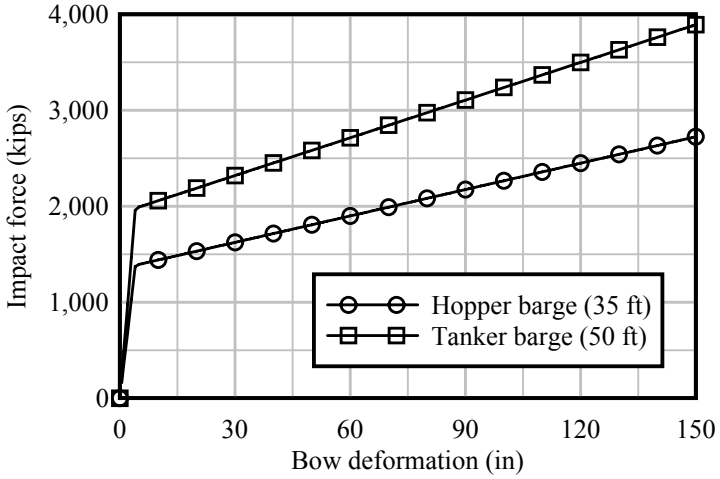

Figure 4.3 AASHTO barge force-deformation relationship for hopper and tanker barges

4.3 High-Fidelity Finite Element Barge Models

In this study, the development of updated barge bow force-deformation relationships was carried out by developing high-resolution finite element barge models. These models were created for the purpose of conducting quasi-static crushing analyses to obtain force-deformation data. The nonlinear explicit finite element code, LS-DYNA (LSTC 2003), was chosen to conduct the quasi-static barge crushing analyses. LS-DYNA is capable of analyzing large scale nonlinear plastic deformations associated with extreme levels of barge bow crush (up to 200 in); can account for global and local member buckling of barge bow components; and is capable of modeling contact not only between the barge and the bridge, but also between internal components within the barge itself.

Two distinct barge models were created: a jumbo hopper barge (Figure 4.4) and an oversize tanker barge (Figure 4.5). The jumbo hopper barge is the baseline vessel upon which the AASHTO barge impact provisions were based (AASHTO 1991) and is the most common type of barge found operating on the inland waterway system in the United States. Modeling and analysis of a jumbo hopper barge allows for direct comparisons between finite element analysis results and the current AASHTO barge impact design provisions. To ensure that adequate ranges of barge sizes and configurations were included in this study, the oversize tanker barge was also modeled and analyzed. Tanker barges are very commonly found operating on the inland waterway system and are considerably different from hopper barges in terms of geometric size and mass.

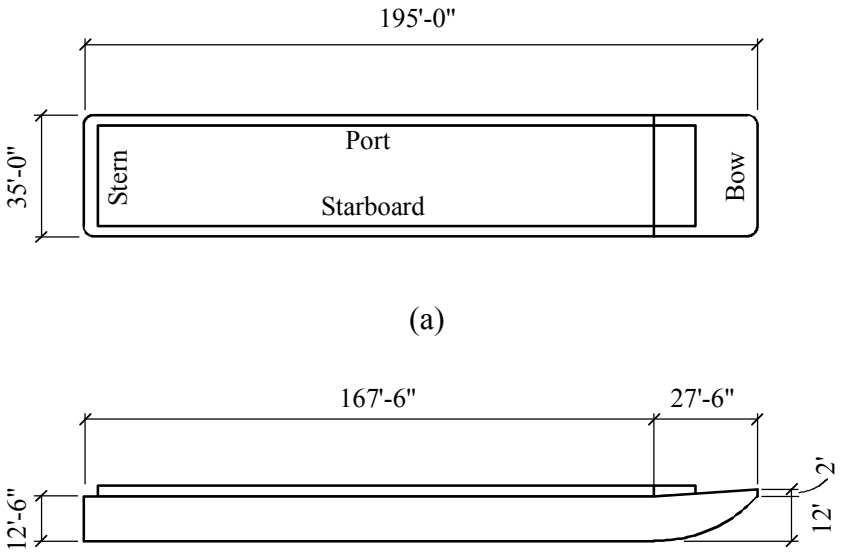

Figure 4.4 Hopper barge dimensions: a) Plan view, and b) Elevation

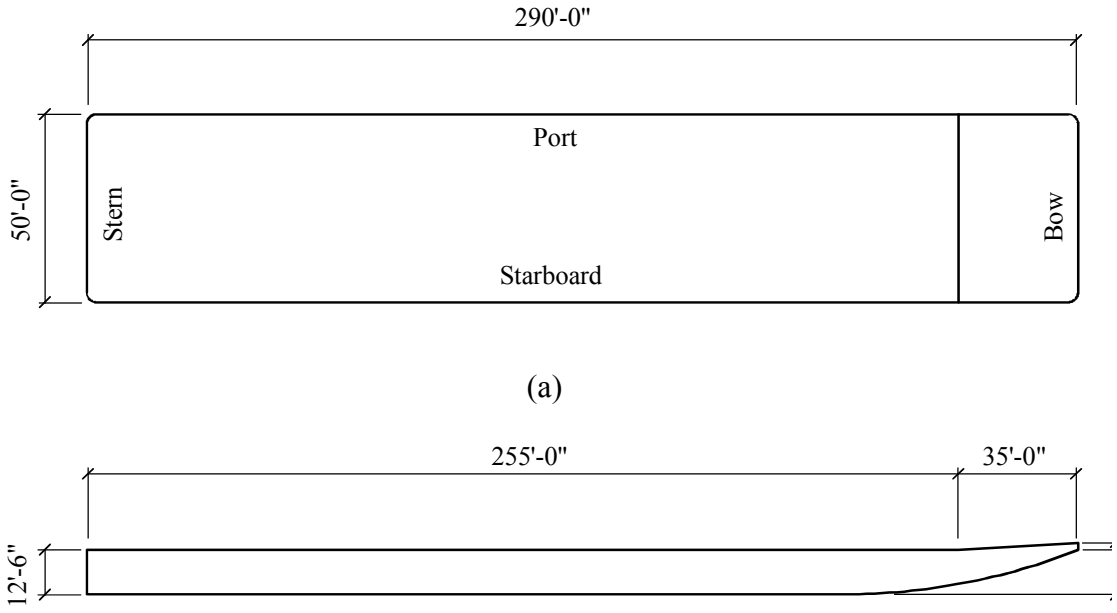

Figure 4.5 Tanker barge dimensions a) Plan view, and b) Elevation

4.3.1 Jumbo Hopper Barge Finite Element Model

For the purposes of generating a finite element model of a jumbo hopper barge, detailed structural plans were obtained from a barge manufacturer. From the point of view of structural configuration, the barge consists of two sections: 1.) the barge bow, and 2.) the hopper, or cargo area (Figure 4.6). Since the focus here is on characterizing the force-deformation relationship that is associated with the bow section of the barge, only this portion was included in the finite element model (Figure 4.7).

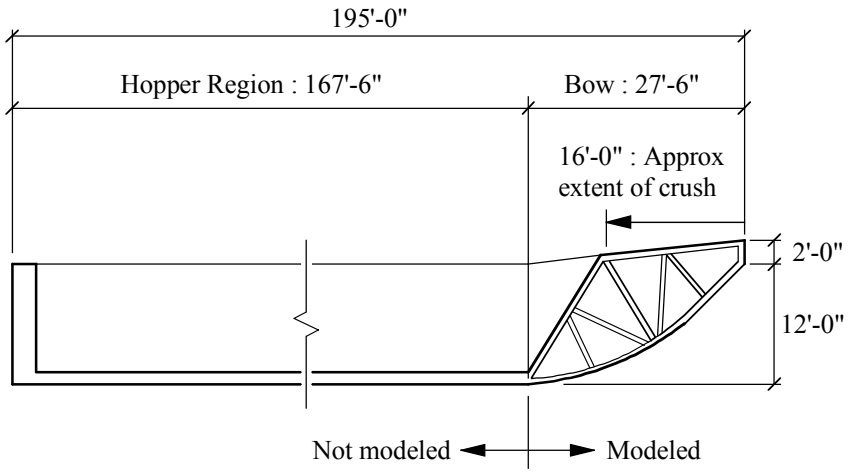

Figure 4.6 Hopper barge schematic

It is noted that the range of crush deformations simulated in this study (16 ft.) is greater than the range of deformations generated during the Meier-Dörnberg test program (which produced equivalent full-scale crush depths of less than approximately 12 ft). As will be shown later, peak force levels are generated at relatively low deformation levels, therefore modeling only the bow section of the barge is adequate.

Hopper barges are fabricated from steel plates and standard structural steel shapes (channels, angles, etc.) in both the bow and hopper regions. The bow of the hopper barge considered in this study is 27 ft - 6 in. long by 35 ft -0 in. wide, and is composed of fourteen internal rake trusses, transverse stiffening members, and several external hull plates of various thicknesses (Figure 4.7). Structural steel members are welded together with gusset plates to form the internal rake truss members (Figure 4.8).

All of the components in this model were modeled using four-node shell elements, mimicking the actual geometric shape of the barge members (Figure 4.7 and 4.8). With regard to modeling the rake trusses, the use of shell elements, as opposed to resultant beam elements, was necessary to capture buckling of the barge bow components. By using a high resolution mesh of shell elements, it was possible to capture not only global buckling, but also local buckling effects. Thus, special attention was given to the number of elements used to model the legs of the structural steel shapes, such that the legs could exhibit reverse curvature during buckling. Additionally, the use of shell elements to discretely model the internal structural members of the barge allows these components to exhibit a local material

failure, which is represented by element deletion in LS-DYNA. If resultant beam elements had been used to model the internal members, material failure and local buckling modes would have been absent from the simulations and the force-deformation data obtained would have been adversely affected.

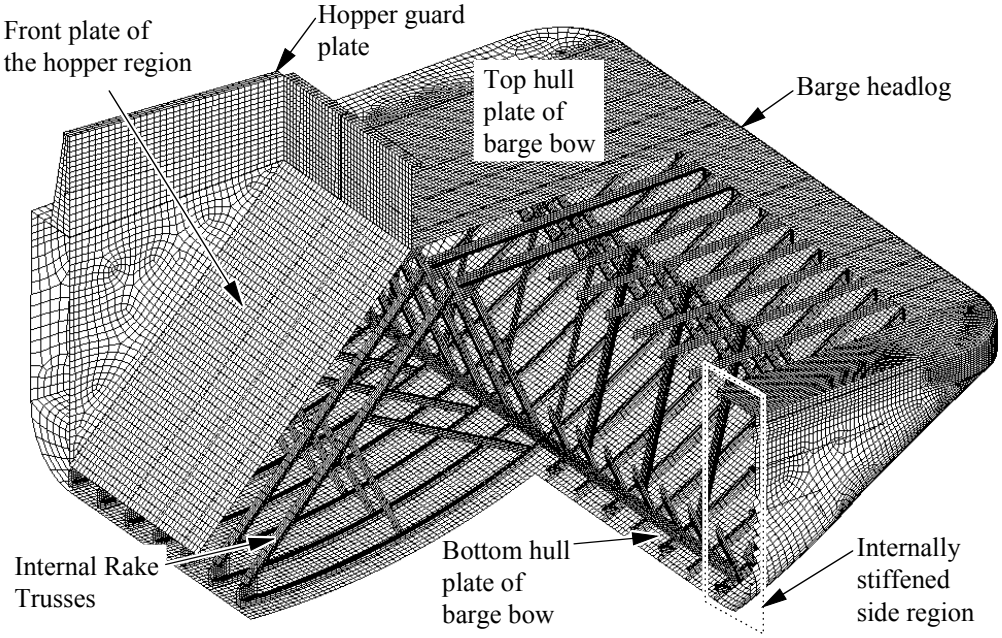

Figure 4.7 Hopper barge bow model with cut-section showing internal structure

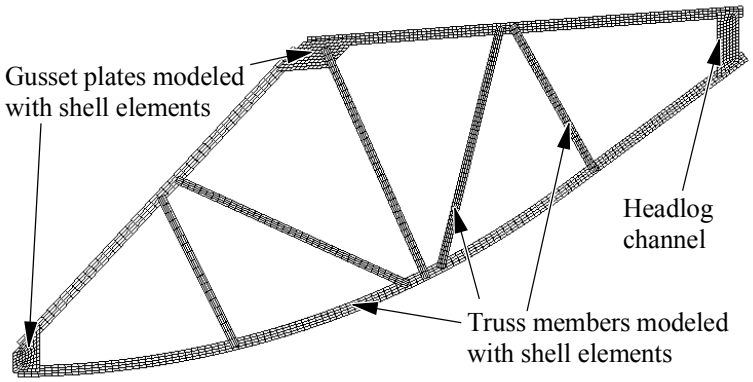

Figure 4.8 Internal rake truss model

Individual steel components in the physical barge are inter-connected through a collection of continuous and intermittent welds. Since the finite element model was intended to mimic the physical barge with reasonable accuracy, approximation in the model of the weld conditions was necessary (Figure 4.9). In the LS-DYNA model, this was accomplished using `CONSTRAINED_SPOTWELD` constraints (LSTC 2003) which allow the user to define a massless spotweld between two nodes. The spotweld is effectively treated as a rigid beam connecting the two nodes. Although an option is available in LS-DYNA to define a spotweld failure criteria, the welds within this model are not permitted to fail. Instead, failure is represented only by way of element deletions when element strains reach the defined

material failure criteria. Hence, by using a sufficient density and distribution of spotwelds, a reasonable approximation of the behavior of the continuous and intermittent welds present in the physical barge was achieved.

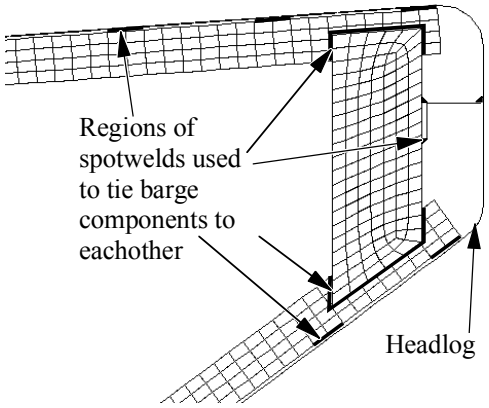

Figure 4.9 Use of spot weld constraints to connect structural components

Since severe structural deformations (up to 16 ft) were to be analyzed using this model, it was important to incorporate a material model capable of exhibiting nonlinearity and failure. Therefore, the `MAT_PIECEWISE_LINEAR_PLASTICITY` material model available in LS-DYNA was used to model all barge components. This is an elastic-plastic behavior model that allows the user to define an arbitrary effective-true-stress vs. effective-plastic-strain relationship. This material model also permits specification of an effective plastic failure strain at which element failure (and subsequent element deletion from the model) occur. Additionally, this model allows the user to define arbitrary strain-rate dependency using the Cowper-Symonds model. However, for the purposes of this study, strain-rate effects were not included in the barge bow model.

With regard to steel material properties, an A36 structural steel was selected to model the barge components because most barges fabricated in the United States are constructed from this material. Thus, material properties (Table 4.1) and a truss-stress vs. effective-plastic-strain relationship for A36 steel (Figure 4.10) were specified for all barge components.

Table 4.1 Barge material properties

Parameter	Value
Elastic modulus	29000 ksi
Poisson's ratio	0.33
Unit weight	490 pcf
Failure strain	0.2
Yield stress	36 ksi
Ultimate stress	58 ksi (eng. stress) 69.8 ksi (true stress)

Finite element based determination of barge crush curves involves calculating the force generated by an impactor (e.g. pier column) deforming the bow of the barge. Such analyses are achieved by fixing the rear section of the barge bow model and then pushing a

rigid impactor (having the shape of a pier column) into the bow model at a constant prescribed velocity (Figure 4.11). Finite element models of several different sizes and shapes of pier columns were developed to capture the effects that pier shape and size have on barge-bow force-deformation relationships. Each pier was modeled using eight-node solid brick elements.

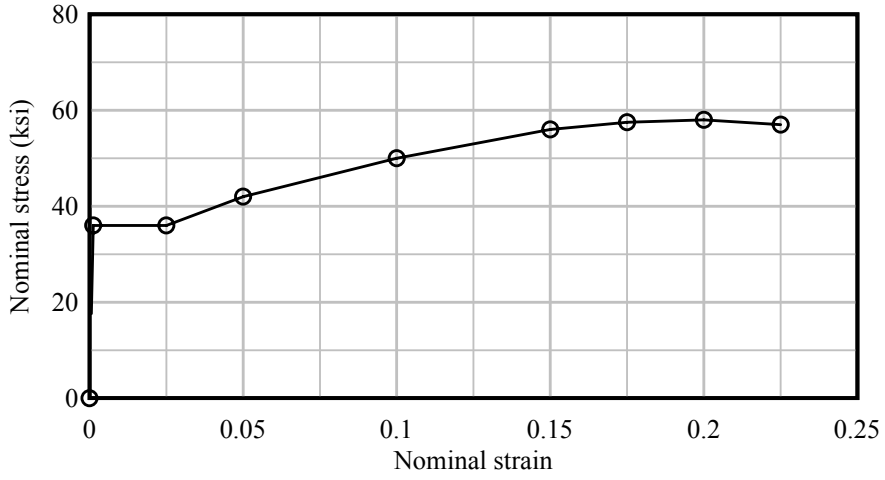

(a)

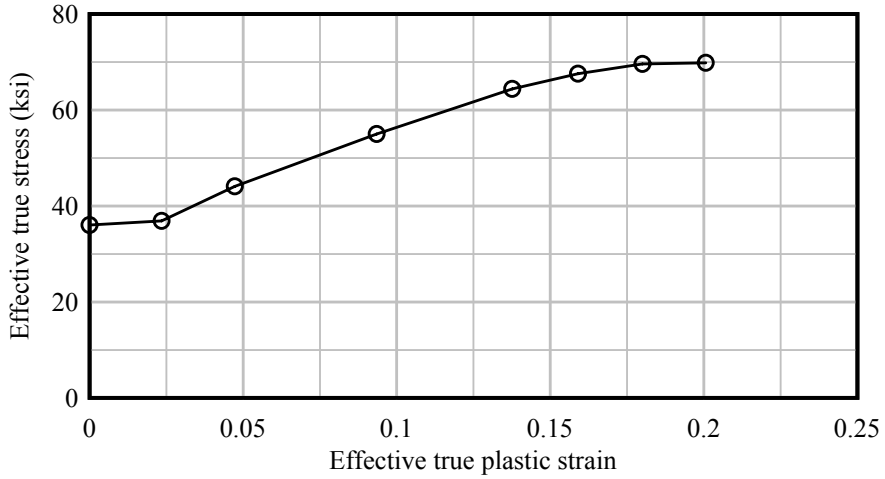

(b)

Figure 4.10 Stress-strain curve for A36 structural steel: a) Nominal stress vs. nominal strain, and b) Effective true stress vs. effective true plastic strain

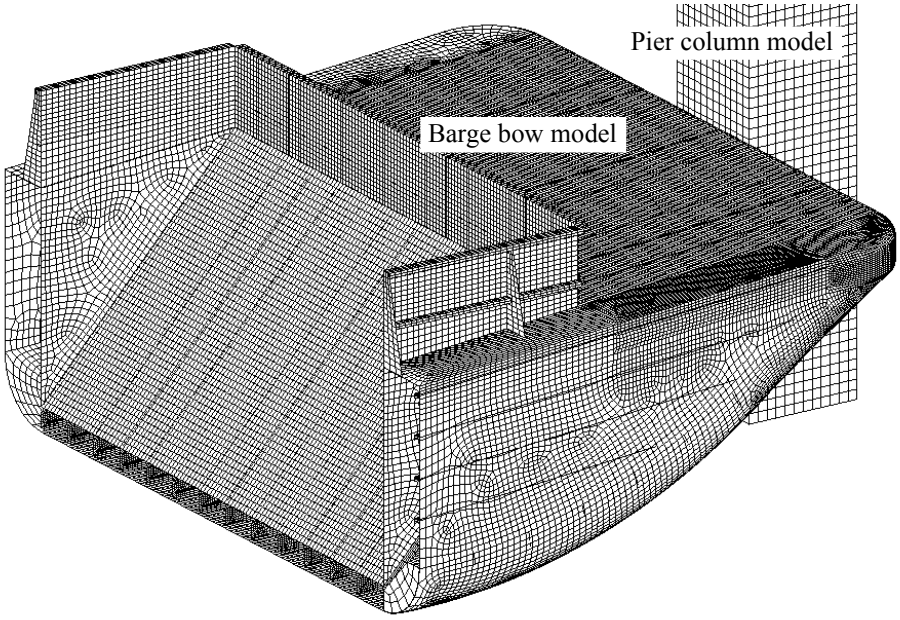

Figure 4.11 Barge bow model with a six-foot square impactor

To simulate contact interaction between the barge bow and the impactor, a contact definition was defined using the LS-DYNA `CONTACT_AUTOMATIC_NODES_TO_SURFACE` option. Static and dynamic coefficients of friction, 0.5 and 0.3 respectively, and a soft-constraint formulation were specified in this contact definition. A soft-constraint option was also used because this method is typically more effective when the contact entities have dissimilar stiffness or mesh density (LS-DYNA 2003).

In addition to the barge-pier contact interface, a contact definition capable of detecting self-contact between all components within the barge bow was also defined. This contact definition differs from the barge-pier contact definition in that there are not two distinct surfaces between which contact can be defined. Rather, it is not known in advance which surfaces of the barge will come into contact with each other during crushing deformation. Therefore, in LS-DYNA, the `CONTACT_AUTOMATIC_SINGLE_SURFACE` definition was specified. By including all barge bow elements in this contact definition, it was possible to detect internal self-contacts within the barge bow.

4.3.2 Tanker Barge Finite Element Model

In addition to the jumbo hopper barge model, a finite element model of a tanker barge was also developed (primarily by Mr. Cory Salzano and Mr. Michael Davidson) as part of the larger funded research program. Similar to hopper barges, tanker barges are constructed from steel plates and trusses, where the trusses are each composed of welded structural steel sections. In contrast to the hopper barge, the tanker barge bow has twenty-three internal rake trusses instead of fourteen, and is 49’-6” wide instead of 35’-0”.

The first 35’-0” was considered in the tanker bow model (Figure 4.12). This distance corresponds to 5 internal rake truss bays, where each bay spans approximately 7’-0”. All elements associated with the first four bays (a distance of approximately 28’-0”) were discretely modeled in the same way as described above for all elements of the hopper model.

However, the tanker barge internal rake truss members of the fifth bay were deemed to be significantly far from the maximum crush depth of 16'-0" to warrant the use of non-discrete elements. Hence, for computational efficiency, the internal rake truss members of the fifth bay were modeled using integrated cross-section beam elements.

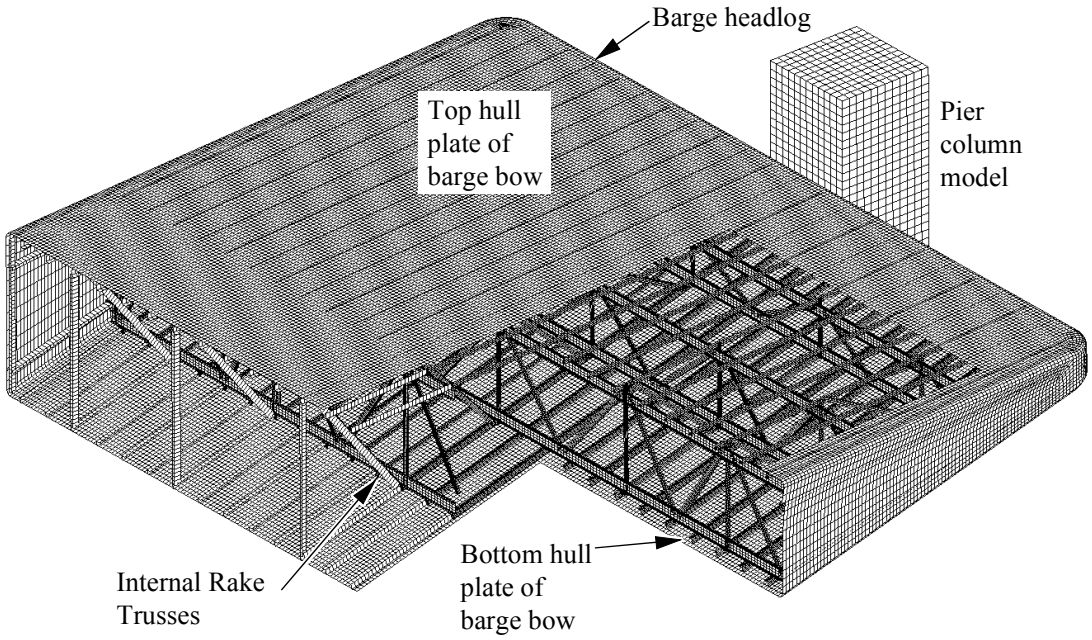

Figure 4.12 Tanker barge bow model

4.4 High-Fidelity Finite Element Barge Crush Analyses

Using finite element models of the jumbo hopper and tanker barges, quasi-static barge bow crush simulations were conducted to determine force-deformation relationships for the barge bow models. Such analyses provide a means of characterizing barge force-deformation relationships in a manner that is independent of AASHTO and Meier-Dörnberg.

4.4.1 Finite Element Barge Bow Crush Simulations

Contact force data and barge bow deformation data were extracted and combined for each crush simulation to produce load-deformation relationships. Both the hopper and tanker barges were crushed using both flat and round pier-impactors of varying widths. Most crush simulations involved centerline crushing of the barge model; however, several crush analyses were conducted involving corner-zone crushing of the barge model. Corner-zone crush analyses were conducted to investigate the effect pier position has on the contact force generated (Figure 4.13).

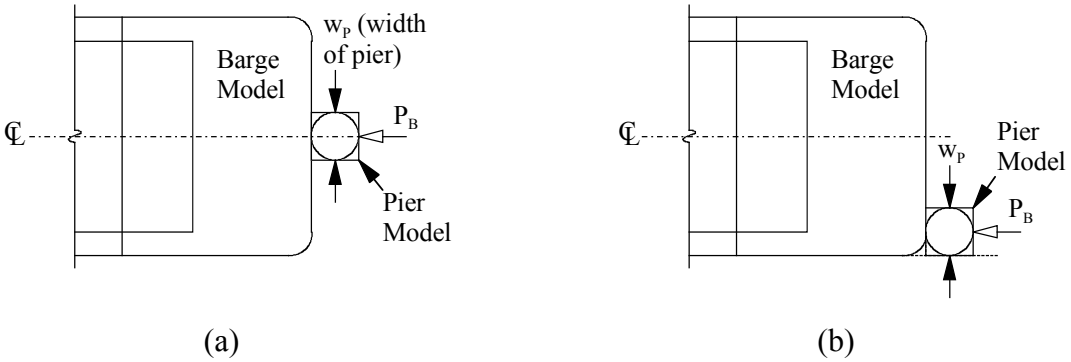

Figure 4.13 Crush analysis models: a) Centerline crushing of barge bow model, and b) Corner-zone crushing of barge bow model

Each crush case is designated by a specific identification tag composed of two letters and a number. The first letter represents the barge type; the second letter designates the pier shape; and the two digit number indicates the size (cross-sectional width or diameter) of the pier in units of feet. For example, a simulation involving a hopper barge crushed by a 6 ft wide flat faced pier (e.g., square or rectangular in cross-section) is designated HF06. Hopper and tanker barges are denoted by H and T respectively, and the flat and round pier impact face geometries are denoted F and R respectively.

Force-deformation data for the hopper and tanker barges crushed by a flat-faced square pier are presented in Figures 4.14, 4.15, 4.16, and 4.17. The most notable observation regarding the flat faced pier data is that the peak force values achieved are dependent upon the widths of the piers. Both the hopper and tanker force-deformation results indicate that as the width of the pier increases, so does the peak contact force. This trend is attributable to the internal configuration of stiffening trusses inside the barge. The number of internal rake trusses directly engaged during impact and deformation increases as pier width increases (Figure 4.18). Hence, the stiffness of the barge effectively increases as the number of trusses that are directly engaged during crushing increases. In the current AASHTO provisions, the effect of pier width on vessel impact forces is not taken into account.

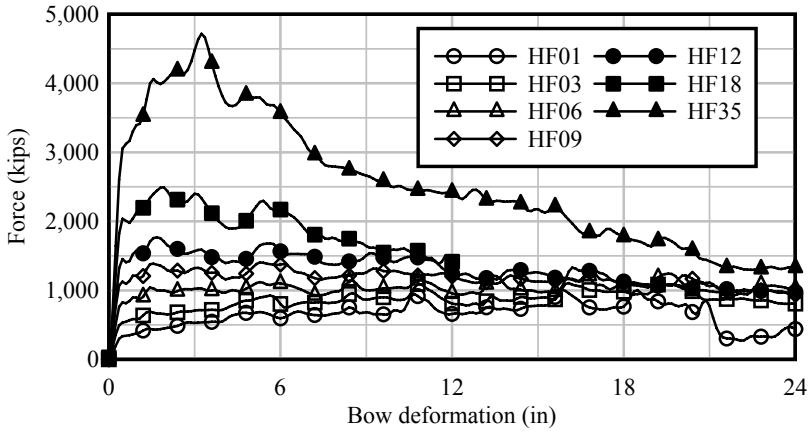

(a)

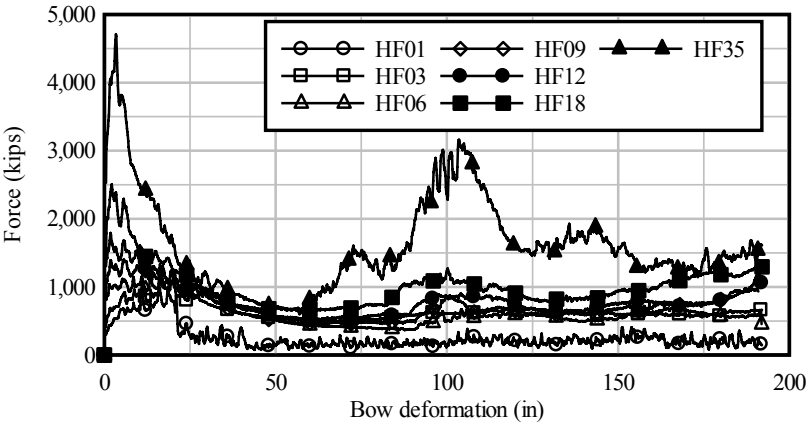

(b)

Figure 4.14 Hopper barge bow force-deformation for flat piers subjected to centerline crushing: a) Low deformation, and b) High deformation

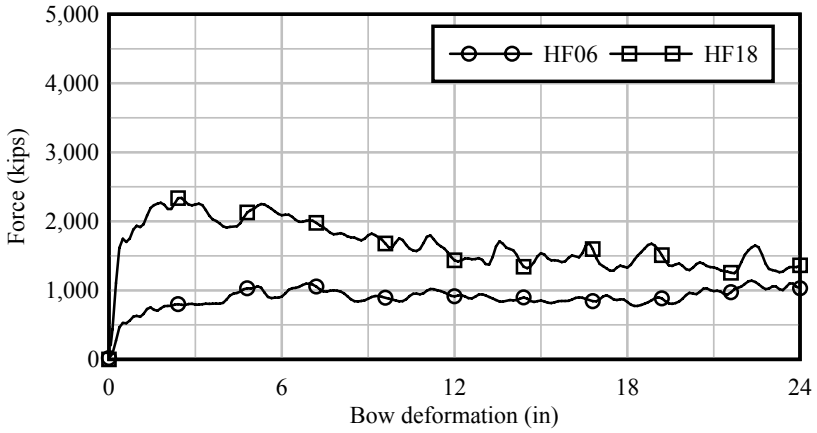

(a)

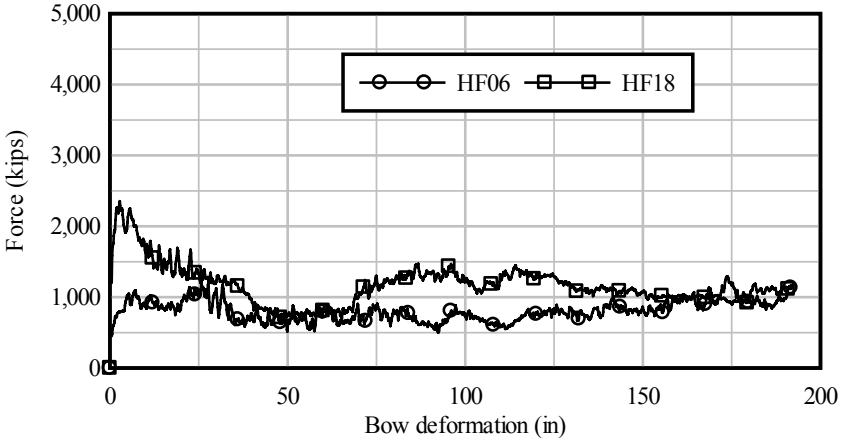

(b)

Figure 4.15 Hopper barge bow force-deformation for flat piers subjected to corner-zone crushing: a) Low deformation, and b) High deformation

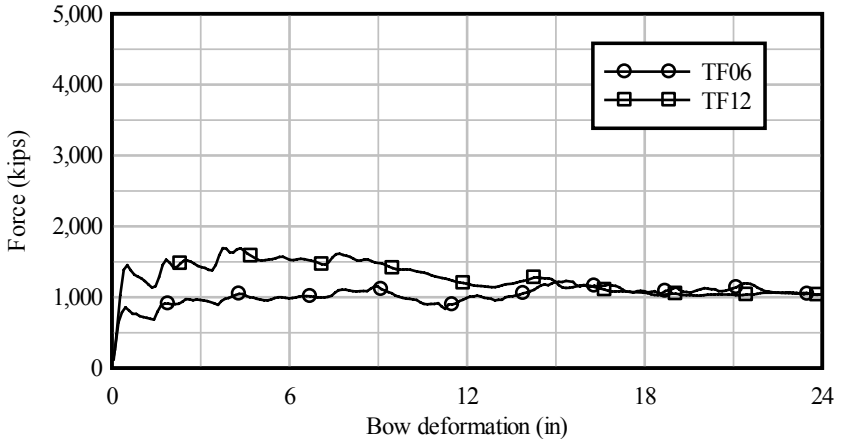

(a)

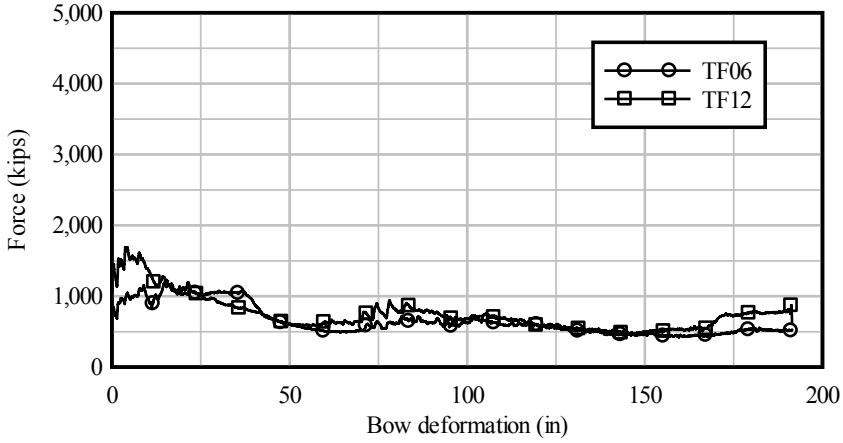

(b)

Figure 4.16 Tanker barge bow force-deformation data for flat piers subjected to centerline crushing: a) Low deformation, and b) High deformation

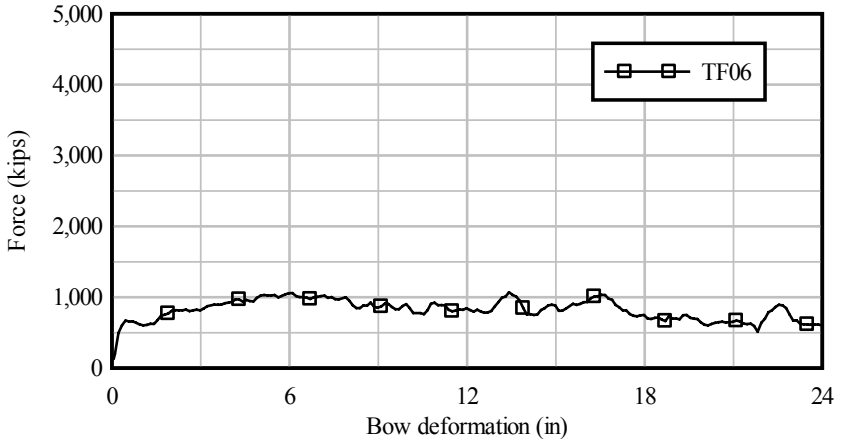

(a)

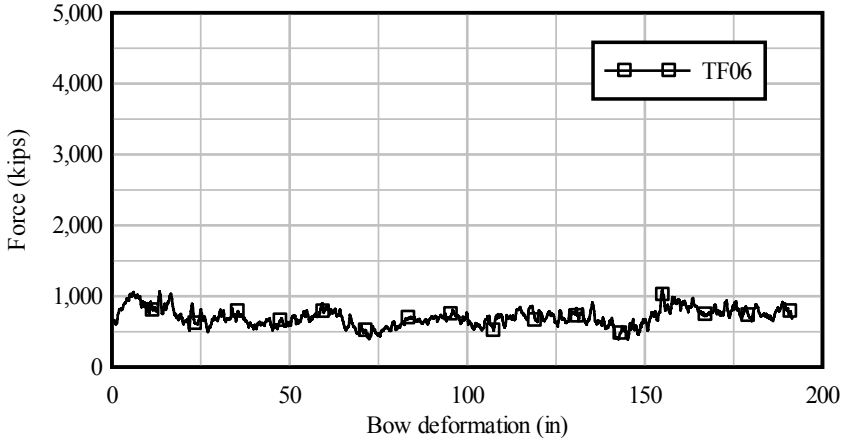

(b)

Figure 4.17 Tanker barge bow force-deformation data for flat piers subjected to corner-zone crushing: a) Low deformation, and b) High deformation

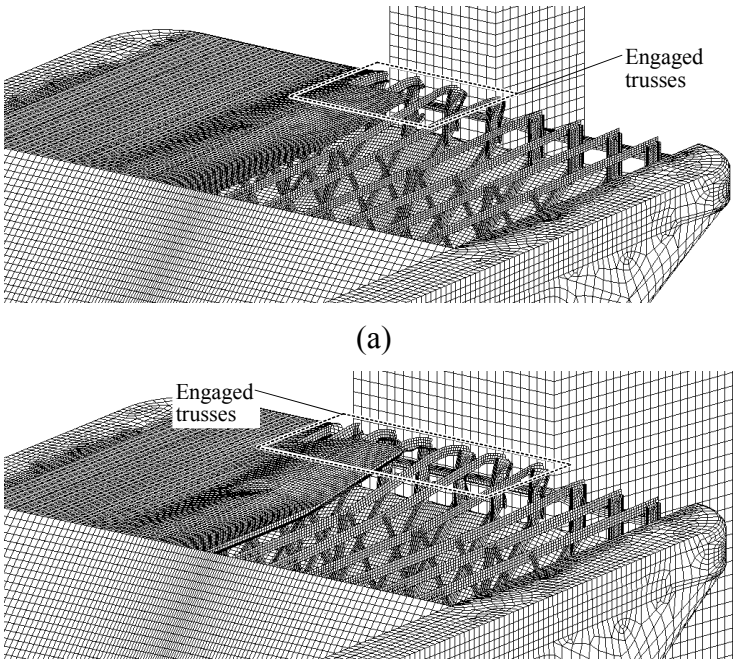

Figure 4.18 Relationship of pier width to engaged trusses:
a) A 6 ft wide flat pier (HF06), and b) A 12 ft wide flat pier (HF12)

Force-deformation data for the hopper barge, when crushed by a round pier, are presented in Figures 4.19, 4.20, 4.21, and 4.22. Unlike the flat faced pier results, the peak contact forces generated in round pier simulations are not strongly influenced by the width of the pier. During impact by a round pier, internal stiffening trusses inside the barge are engaged gradually and sequentially (Figure 4.23) as the deformation level increases. This is in contrast to the behavior for impact by a flat faced pier where all of the trusses within the impact zone width are immediately engaged at the same point in time.

In the AASHTO and Meier-Dörnberg equations, the peak impact force is computed based on the maximum expected barge bow deformation (which is itself computed based on initial kinetic impact energy). However, the simulation results presented above indicate that the peak force often does not occur at the maximum sustained level of barge bow deformation. Additionally, the AASHTO and Meier-Dörnberg equations exhibit a work-hardening phenomenon in which the impact force levels continue to rise with increasing deformation depth (recall Figure 4.2). However, data from finite element simulations indicate that generally no such hardening occurs, and in many cases a softening of the barge bow occurs after the peak impact force has been reached. At significant deformation levels, widespread buckling of the internal stiffening trusses, combined with fracturing of the outer hull plates, produces this structural softening, particularly in impacts that involve flat faced piers. Based on these observations, it is apparent that an elastic, perfectly-plastic force-deformation curve is adequate to conservatively describe bow crushing behavior (Figure 4.24).

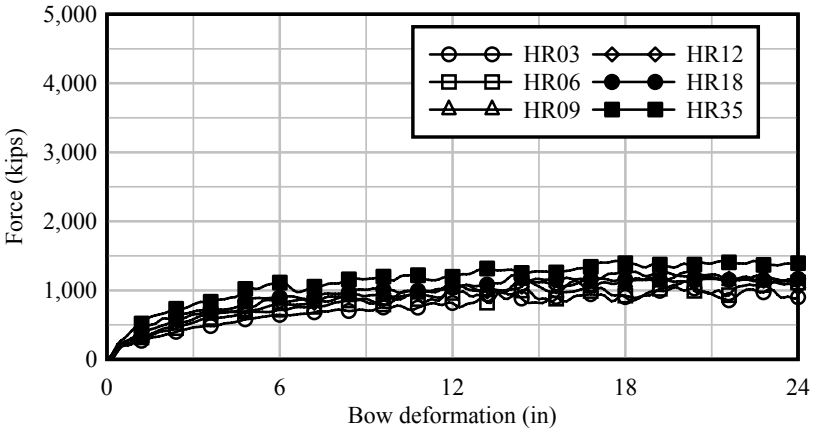

(a)

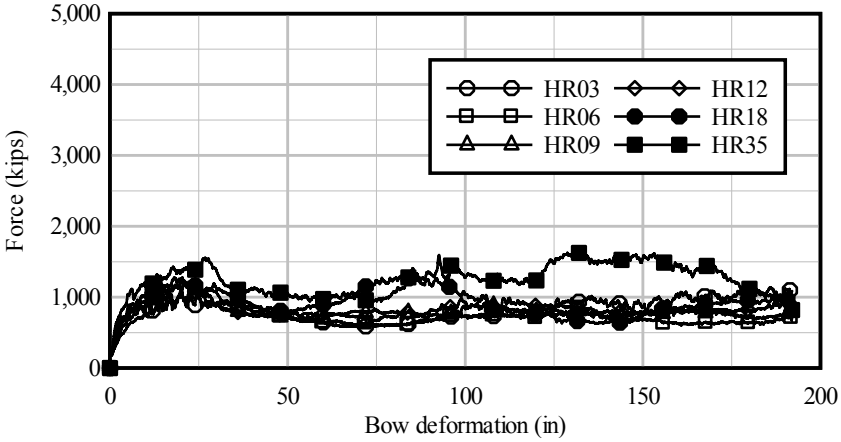

(b)

Figure 4.19 Hopper barge bow force-deformation for round piers subjected to centerline crushing: a) Low deformation, and b) High deformation

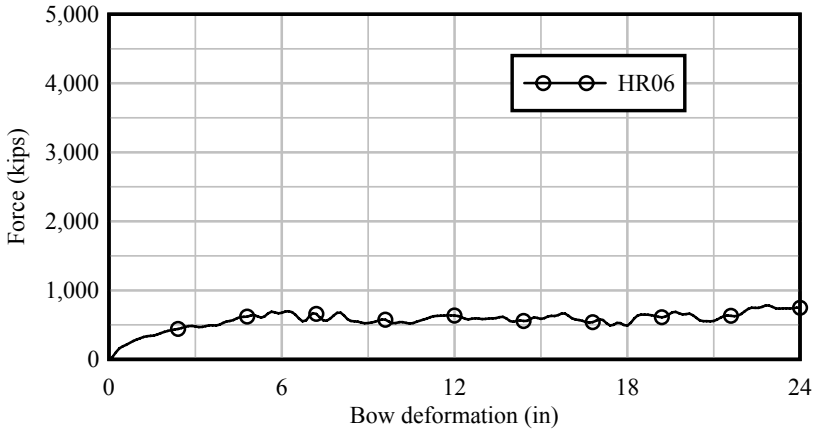

(a)

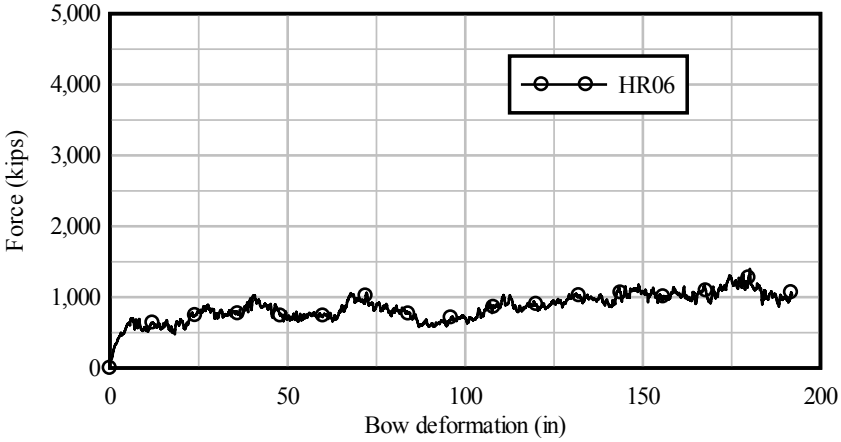

(b)

Figure 4.20 Hopper barge bow force-deformation for round piers subjected to corner-zone crushing: a) Low deformation, and b) High deformation

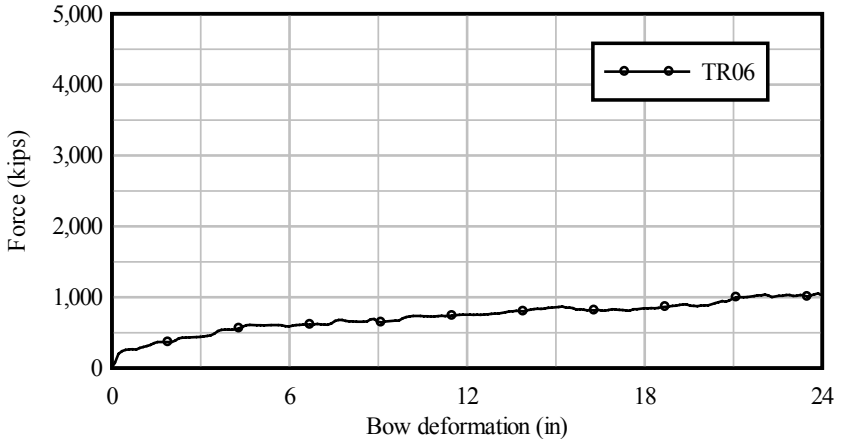

(a)

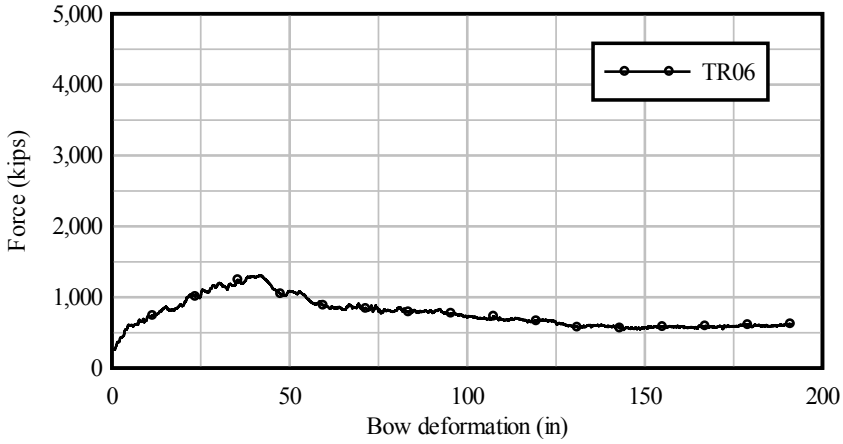

(b)

Figure 4.21 Tanker barge bow force-deformation for round piers subjected to centerline crushing: a) Low deformation, and b) High deformation

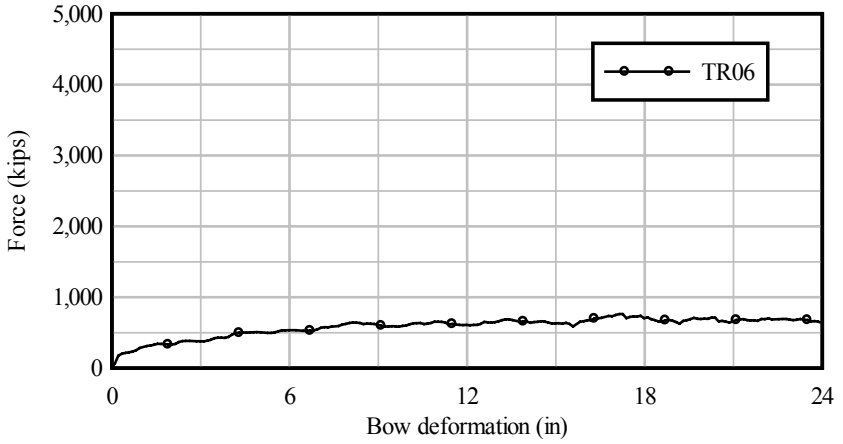

(a)

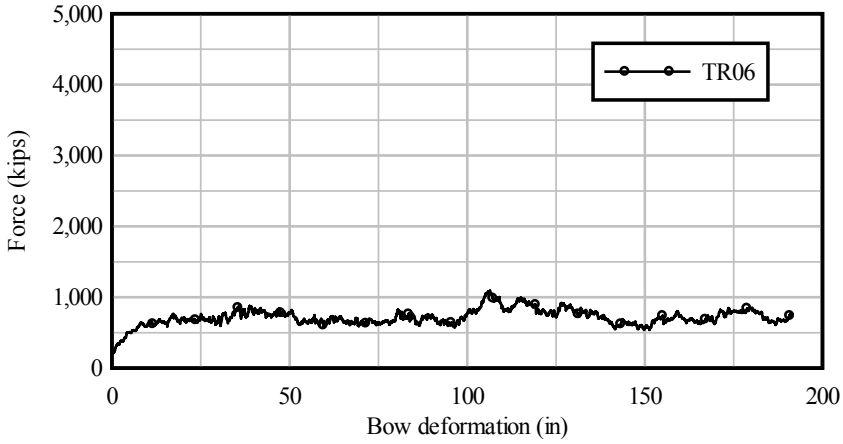

(b)

Figure 4.22 Tanker barge bow force-deformation for round piers subjected to corner-zone crushing: a) Low deformation, and b) High deformation

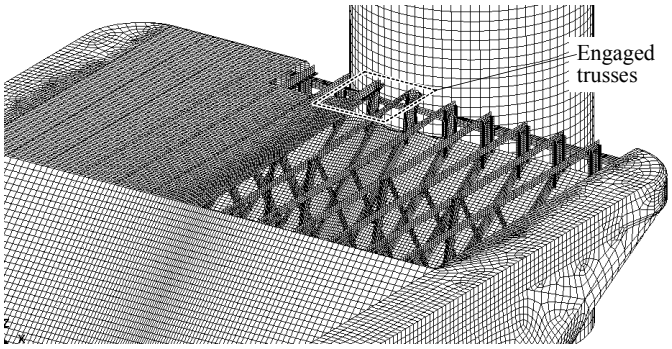

(a)

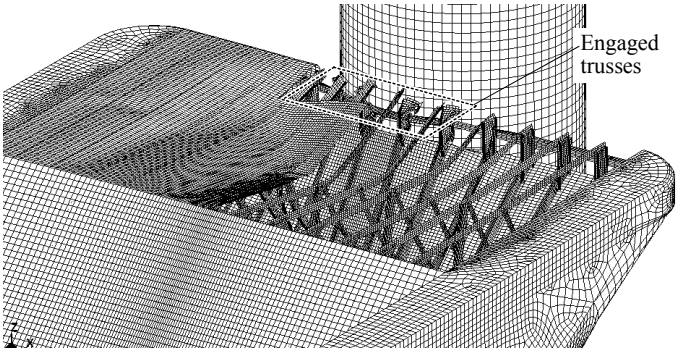

(b)

Figure 4.23 Gradual increase in trusses engaged with deformation in round pier simulations: a) A 6 ft diameter round pier at 10 in of deformation, and b) A 6 ft diameter round pier at 20 in of deformation

Figure 4.24 Elastic-perfectly plastic barge bow force-deformation curve

4.4.2 Development of Barge Bow Force-Deformation Relationships

Barge crush analyses of the type described above produce highly detailed force-deformation relationships that are specific to vessel type, pier shape and size, and impact location. In this section, the detailed data obtained from these finite element crush simulations are used to develop simplified barge crush models suitable for use in bridge design.

Examination of Figures 4.14 through 4.17; 4.19 through 4.22 indicates that, generally, barge bow contact force either remains constant or decreases after the peak contact force has been reached. Therefore, in order to envelope both of these situations, it is assumed that the barge bow will exhibit an elastic-perfectly plastic load-deformation behavior (recall Figure 4.24). Despite the fact that current AASHTO provisions utilize a barge width correction factor (R_B) to account for the relationship between impact force magnitude and barge width, it is important to note that crush data obtained in this study indicate that no strong relationship of this type exists. Because the hopper and tanker barges have different widths (35 ft and 50 ft, respectively), based upon the current AASHTO specifications, it would be expected that the impact forces for a given pier size would be quite different if impacted by a hopper versus a tanker barge. However, the impact force magnitudes obtained for both barge types are in close agreement, indicating that a correction factor for barge width is not appropriate.

A key element in developing a simplified barge bow behavior model is the formulation of a relationship between peak impact force and pier width. Formation of this relationship is accomplished by filtering the barge bow force history data—obtained from the crush simulations described in the previous section—using a low-pass filter. For each crush simulation, the time history of contact force was transformed from the time domain to the frequency domain using a fast Fourier transform (FFT). A previous study (Consolazio et. al 2006) indicated that barge impact forces can be adequately represented using frequencies of less than approximately 50 Hz. In the present study, this limit was conservatively doubled and simulation data above 100 Hz were filtered out. An inverse transformation was then performed to obtain a final filtered force time history. For each crush simulation, the filtered force data were scanned and the maximum (peak) impact force for each simulation quantified. In Figure 4.25, peak impact forces obtained from this procedure are plotted as a function of pier column width for both flat and round column cross-sectional shapes.

Inspection of the crush data for flat-faced piers indicates that one of two distinct mechanisms determines the magnitude of peak force that can be achieved. In Figure 4.26, it is evident that for flat-faced piers with widths of less than approximately 9 ft, the contact force reaches a temporary (local) peak magnitude within the first 2 to 4 in. of barge bow deformation. With continued bow deformation, the contact force gradually increases up to a global peak magnitude at deformation levels of 16 to 20 in. Detailed inspection of finite element results for the moderate-width flat-faced piers reveals that the initial local maxima are associated with initial yielding of the internal rake trusses. As the barge bow deforms beyond crush depths associated with this condition, the internal trusses begin to buckle, and combined membrane action in the outer hull plates begin to contribute the bulk of the crush force. When the hull plates exhibit significant yielding, the global peak force has been reached. Thus, for moderate-width flat-faced piers, the membrane yield capacity of the barge hull plates governs the global contact force maxima.

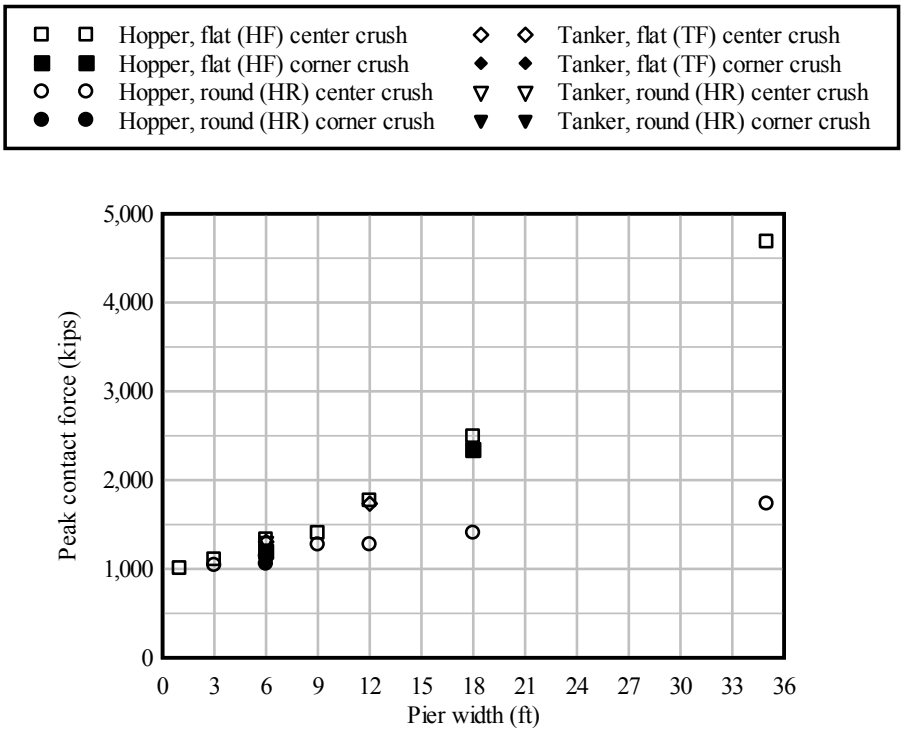

Figure 4.25 Peak barge contact force versus pier width

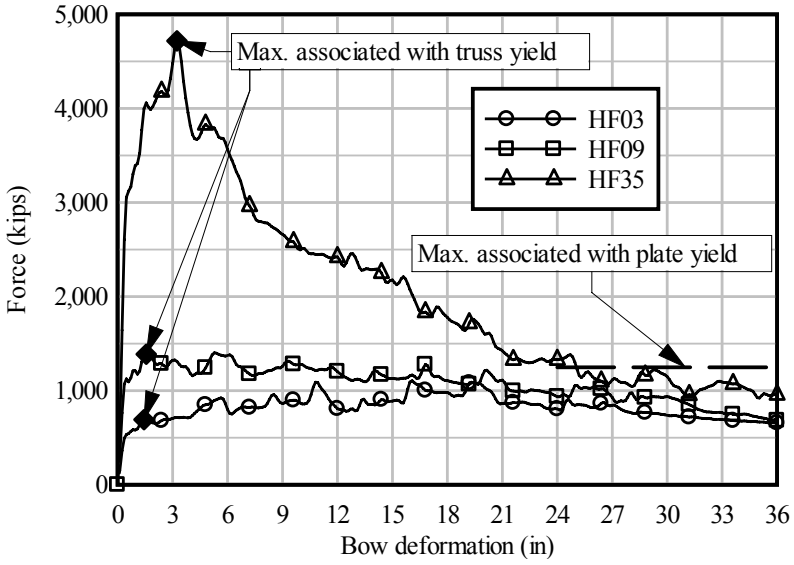

Figure 4.26 Peak barge contact force versus pier width

For flat-faced pier with widths of greater than approximately 9 ft, a maximum force magnitude—associated with yielding of the internal trusses—also occurs within the first 2 to 4 in of barge bow deformation. However, in contrast to moderate-width flat-faced piers, the force maximum at the 2 to 4 in. deformation level in large-width piers represents the global force maximum for all crush depths. Instead of a continuous force level increase with additional deformation, the contact force decreases as the barge bow deforms further and the internal trusses buckle. At large deformations (greater than 20 in), the trusses have buckled, and membrane action of the outer hull plates determines the magnitude of load generated. Thus, for large-width flat-faced piers, the yield capacity of the internal trusses in the barge governs the global maximum of contact force (and therefore impact load).

Force-deformation data for a 9 ft wide flat-faced pier indicate that the force maximums associated with truss yielding and outer hull plate yielding are approximately equal in magnitude (Figure 4.26). This fact suggests that a pier width of 9 ft represents the approximate transition point between force maximums that are controlled by truss-yielding and those that are controlled by yielding of the outer hull plates of the barge.

In Figure 4.27, force maxima associated with both barge truss yielding and outer hull plate yielding are plotted for flat-faced piers as a function of pier width. Distinct linear trends associated with each of these behavioral modes are clearly identified. For each mode of barge deformation behavior, a linear regression trend line was fit through the data (Figure 4.27). For data points associated with truss yielding, a least-squares linear curve fit through the origin yields the following relationship between maximum force and pier width:

$$P_{BY} = 134.41 w_P \tag{4.4}$$

where P_{BY} is the barge yield force in kips, and w_P is the width of the flat-faced pier in ft. A general least-squares line was also fit through the data points associated with outer hull plate yielding produced the relationship:

$$P_{BY} = 953.48 + 48.43 w_P \tag{4.5}$$

Equating Eqns. 4.4 and 4.5 and solving for the pier width at which the two trend lines intersect, the transition point between force maxima controlled by truss-yield and plate-yield was determined to be 11.15 ft.

Eqns. 4.4 and 4.5 are based on analyses of hopper and tanker models that are representative of typical vessel fabrication practices employed in the United States (in terms of steel strength, structural configuration, and steel plate thicknesses). Outer hull plate thicknesses of barges very commonly range between 0.25 in and 0.625 in, and 91-percent of barges have plate thicknesses of 0.3125 in (Nguyen 1993) and a steel strength of 36 ksi is often used. As noted earlier, the models analyzed in this study employed a 3/8 in. (0.375 in.) hull plate thickness and 36 ksi steel. However, some variability in barge fabrication practices is possible. Additionally, the data points, used to develop the trend lines of Eqns. 4.4 and 4.5, include some variability and are not perfectly linear in form. Therefore, in order to develop conservative equations that can be recommended for general purpose use in bridge design, some modifications to Eqns. 4.4 and 4.5 were made.

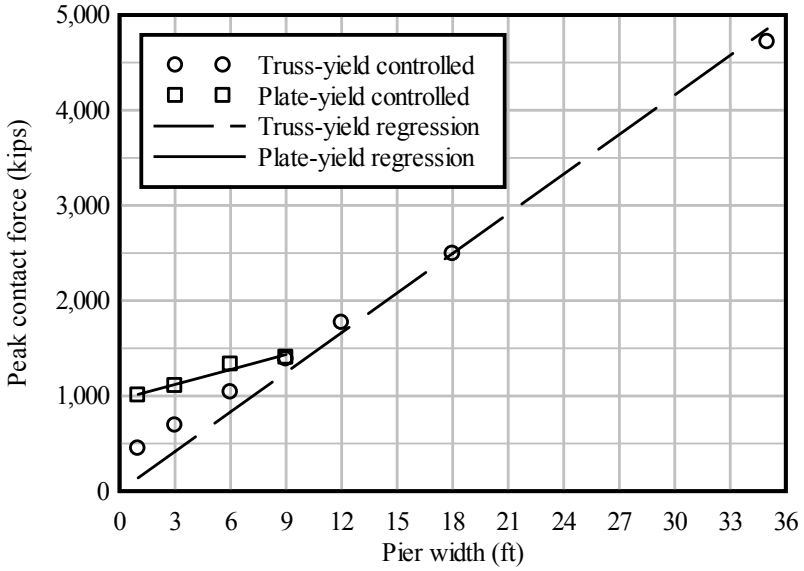

Figure 4.27 Comparison of truss-yield controlled peak force versus plate-yield controlled peak force

First, the regression lines were scaled to account for the possibility of either higher steel strengths or thicker hull plates. Increases in either of these parameters would lead to an increase in impact force levels. Steel having a yield strength of 50 ksi rather than 36 ksi corresponds to a yield strength ratio of (50 / 36) = 1.39. A hull plate thickness of 1/2 in. (0.5 in.) instead of 3/8 in. leads to a plate thickness ratio of (0.5 / 0.375) = 1.33. Some variability of vessel characteristics is implicitly incorporated in the AASHTO provisions through the probability of collapse (PC) term, which was derived from vessel-to-vessel collision data. Hence, accounting for both increased material strength and increased hull plate thickness was deemed unnecessarily conservative. Instead, Eqns. 4.4 and 4.5 were each scaled simply by a factor of 1.33. Then, the resulting coefficients in the equations were rounded off, resulting in simplified design equations for the peak impact force as a function of pier width for flat-face pier columns:

$$P_{BY}=1500 + 60w_P \quad \text{if } w_P<10 \text{ ft} \tag{4.6}$$

$$P_{BY} = 300 + 180w_P \quad \text{if } w_P \geq 10 \text{ ft} \tag{4.7}$$

where P_{BY} is the peak impact force in kips. Eqns. 4.6 and 4.7 are graphically illustrated in Figure 4.28. By equating Eqns. 4.6 and 4.7 and solving for the pier width at which the equations intersect, the transition point between the truss-yield and plate-yield dominated modes of barge behavior was determined to be 10 ft.

Unlike flat-faced pier columns, pier columns having round (circular) cross-sectional shapes may be represented by a single linear regression line in terms of predicting maximum magnitude force levels (Figure 4.29). Even so, development of a relationship between maximum impact force and pier column diameter was carried out in a manner analogous to that used for flat-faced piers.

Linear regression was used to fit a trend line through the complete round pier crush dataset (Figure 4.29). The least-squares trend line was found to be:

$$P_{BY} = 1130.14 + 13.89w_P \quad (4.8)$$

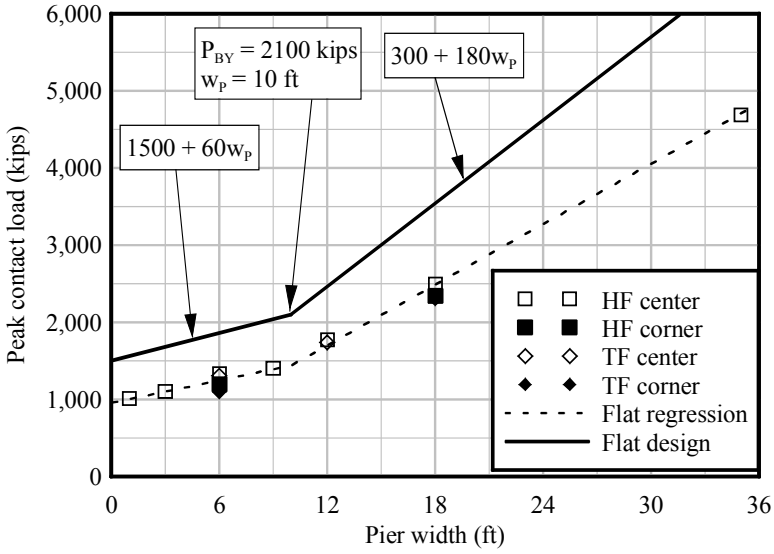

Figure 4.28 Design curve for peak impact force versus flat pier width

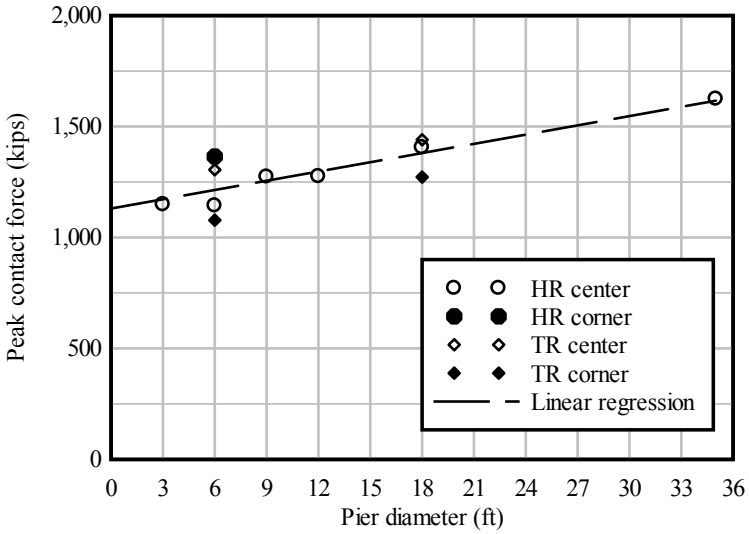

Figure 4.29 Comparison of low diameter peak force versus large diameter peak force

As with the flat-faced pier data, the round pier regression line was scaled by a factor of 1.33. After rounding off the coefficients, the resulting equation for barge yield force as a function of circular pier diameter was:

$$P_{BY}=1500 + 20w_P \quad (4.9)$$

The equation is graphically illustrated in Figure 4.30.

Construction of a complete design barge crush curve (recall Figure 4.24) requires not only determination of the barge crush force (P_{BY}) but also the barge yield deformation (a_{BY}). The first step in calculating the barge bow deformation at yield is to extract the initial barge bow stiffness from the force-deformation data. The initial stiffness for each case was calculated by taking the slope of the line connecting the first two data points of each curve in Figures 4.14 through 4.17; 4.19 through 4.22. In Figure 4.31, the initial stiffnesses computed in this manner are plotted as a function of pier width for all crush analysis cases.

Dividing the peak force values from Figure 4.25 by the respective stiffnesses from Figure 4.31 yields barge bow deformations that—in conjunction with the peak force value—envelope the force-deformation data. In Figure 4.32, barge bow deformations at yield are plotted as a function of pier width. In most design situations, pier columns will be larger than 4 ft in width. Consequently, based on the data shown in Figure 4.32, barge bow yield deformations of 0.5 in. and 2 in. were selected for flat-faced and round piers respectively.

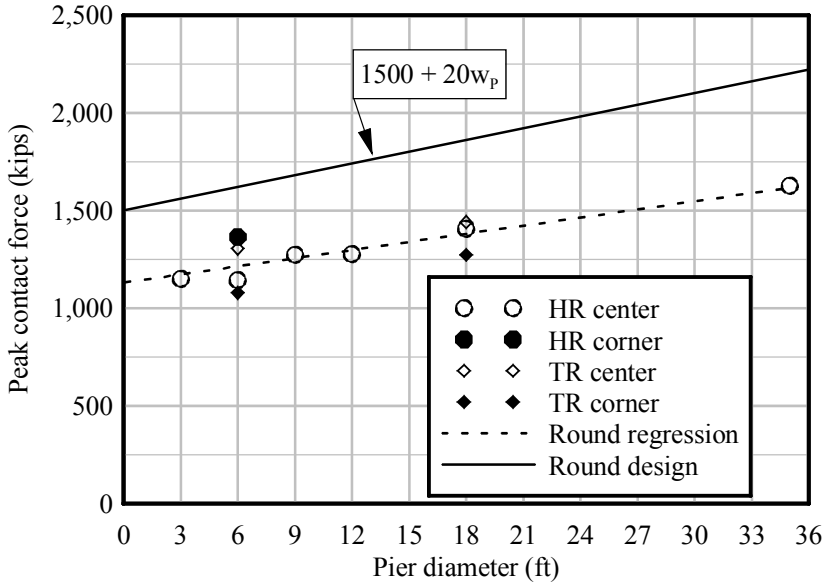

Figure 4.30 Design curve for peak impact force versus round pier diameter

4.4.3 Summary of Barge Bow Force-Deformation Relationships

Figure 4.33 presents a flowchart for calculating the force-deformation relationship for the barge bow. Based upon the geometry and size of the pier column on the impact pier, the design barge yield force is calculated. Additionally, based upon pier column geometry, the barge bow deformation at yield is selected, and the barge bow force-deformation relationship is defined. The resulting force-deformation relationship of Figure 4.33 is a necessary component of all of the analysis methods presented in later chapters. This elastic, perfectly-plastic relationship ultimately determines the magnitude and duration of the force imparted to a bridge structure during an impact.

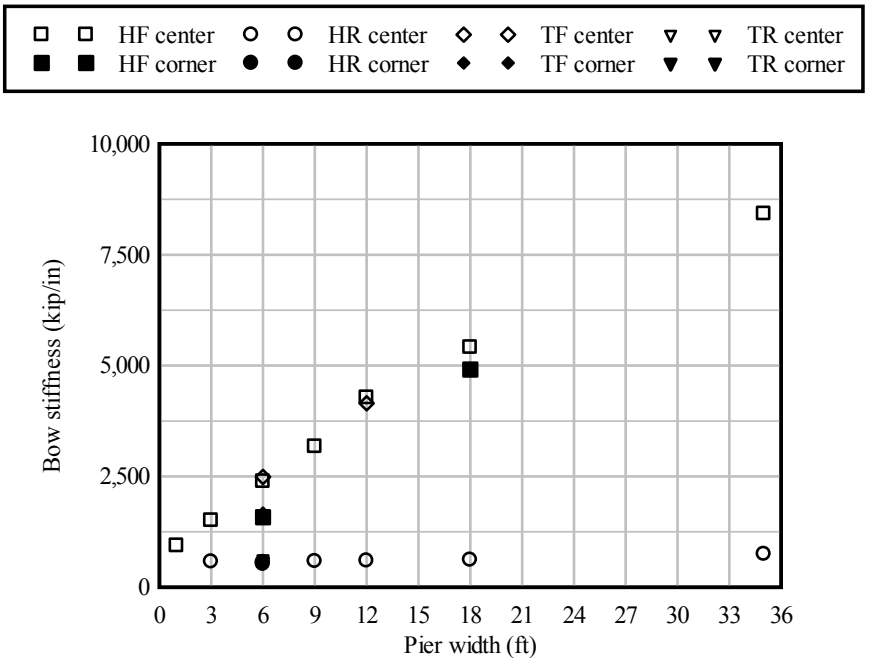

Figure 4.31 Initial barge bow stiffness as a function of pier width

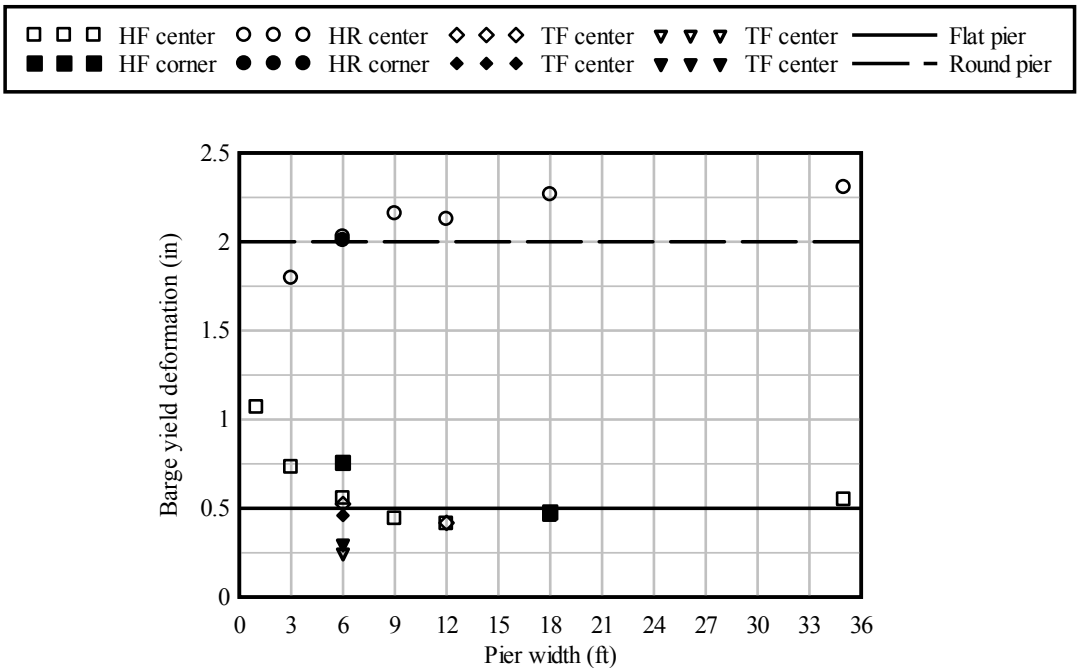

Figure 4.32 Barge bow deformation at yield versus pier width

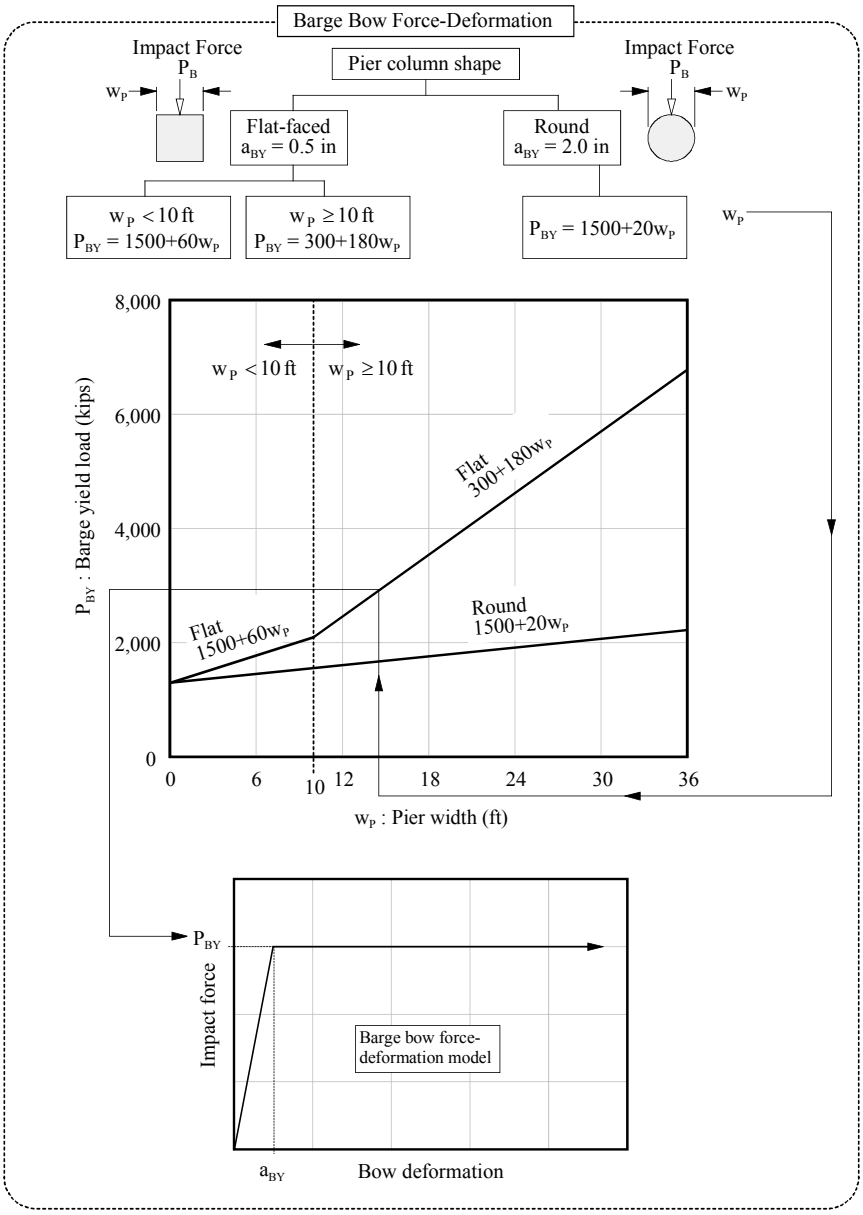

Figure 4.33 Barge bow force-deformation flowchart

CHAPTER 5
COUPLED VESSEL IMPACT ANALYSIS (CVIA)

5.1 Introduction

A numerically efficient computational procedure is proposed and validated in this chapter for dynamically analyzing pier response under varying barge impact loading conditions. Factors such as barge type, barge mass, impact speed, impact angle, pier stiffness, pier mass, pier geometry, and soil conditions may all be taken into consideration. Results predicted by this procedure include time-histories of collision load, pier displacements, plastic barge deformations, and structural design (member) forces.

5.2 Conceptual Overview

Coupled vessel impact analysis (CVIA) involves coupling (linking) a single degree of freedom (SDOF) nonlinear dynamic barge model to a multi-degree of freedom (MDOF) nonlinear dynamic pier analysis code. In the current context, the term "coupled" refers to the use of a shared contact force between the barge and impacted bridge structure (Figure 5.1). The impacting barge is assigned a mass, initial velocity, and bow force-deformation (crush) relationship. Traveling at a prescribed initial velocity, the barge impacts a specified location on the bridge structure and generates a time-varying impact force in accordance with the crush curve of the barge and the relative displacements of the barge and bridge model at the impact location. The MDOF pier-soil model, subjected to the time-varying impact force, displaces, develops internal forces, and interacts with the SDOF barge model through the shared impact force. Hence, coupled analysis automatically generates a time-history of barge impact force that is specific to the bridge structural configuration and impact condition (barge type, mass, speed) being analyzed.

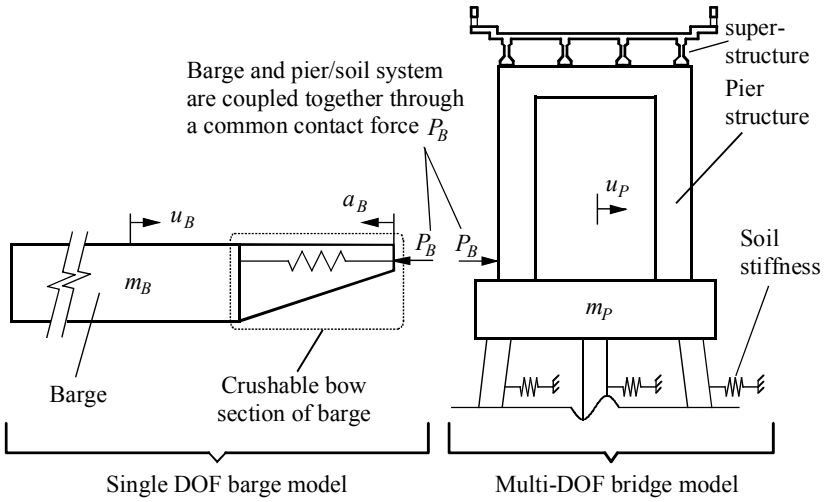

Figure 5.1 Coupling between barge and bridge

5.3 Barge Model

Conducting a barge collision analysis requires that consideration be given to both inertial forces and nonlinear structural behavior. Properly modeling structural behavior (the inelastic force-deformation response of the barge) is particularly important as it affects both force development and energy dissipation during impact. The approach taken here is to approximate behavior of the barge by independently representing dynamic behavior (mass related barge inertia) and nonlinear structural behavior (barge crushing). The total mass of the barge (or multi-barge flotilla) is represented as a single degree of freedom (SDOF) point mass while inelastic stiffness of the barge bow is modeled using a nonlinear crush relationship (a P_B vs. a_B curve, where P_B is the barge impact force and a_B is the crush deformation of the barge bow).

For general purpose bridge design, it is recommended that the simplified bilinear elastic, perfectly-plastic crush curves proposed in Chapter 4 be used to model barge deformation behavior. However, in special situations where more detailed vessel crush data are available, e.g. from high-resolution finite element analysis or experimental testing, the detailed data points can be assembled together to form a fully-generalized vessel crush curve. Since the proposed analysis algorithm is capable of utilizing either generalized crush curves or simplified crush curves, the method will be presented and illustrated below using fully generalized crush curves.

5.3.1 Barge Loading and Unloading Behavior

During barge collisions with bridge piers, the bow section of the barge will typically undergo permanent plastic deformation. However, depending on the impact speed, barge type, and pier flexibility, dynamic fluctuations may occur (Hendrix 2003, Consolazio et al. 2004, Consolazio et al. 2005) that produce loading with plastic deformation, unloading, and subsequent reloading of the bow. In the barge model proposed here, representation of this behavior is achieved by tracking the deformation state of the barge throughout the dynamic collision event. In Figure 5.2, the various stages of barge bow loading, unloading, and reloading are illustrated. Whenever the barge is in contact with the pier, the crush is computed as $a_B=(u_B-u_P)$, where u_B and u_P are the barge and pier displacements, respectively.

Upon contact with a bridge pier, the barge bow loads elastically until the crush depth (deformation level) a_B exceeds the yield value a_{BY}. For crush depths $a_B>a_{BY}$, plastic deformation of the bow is assumed to occur (Figure 5.2a). Continued loading generates additional plastic deformation as the crush curve is followed. At some stage in the collision event, the contact force (P_B) between the barge and the pier may diminish (e.g., due to barge deceleration, or pier acceleration in response to the impact loading). As this occurs, the crush depth a_B will drop rapidly (Figure 5.2b) from the maximum sustained level a_{Bmax} to the residual plastic deformation level a_{Bp} as the barge bow unloads. Once the condition $P_B=0$ is reached, all elastic deformation ($a_{Bmax}-a_{Bp}$) will have been recovered. When $a_B<a_{Bp}$ (Figure 5.2c), the barge is not physically in contact with the pier and therefore $P_B=0$. If reloading subsequently occurs (e.g., due to rebound of the pier once soil resistance has been

mobilized), the unloading/reloading path will be followed back up to the loading curve (Figure 5.2d) and plastic deformation will once again initiate when a_B exceeds the previously achieved a_{Bmax}. Algorithmically, the barge behavior illustrated in Figure 5.2 is modeled as a nonlinear compression-only (zero tension) spring.

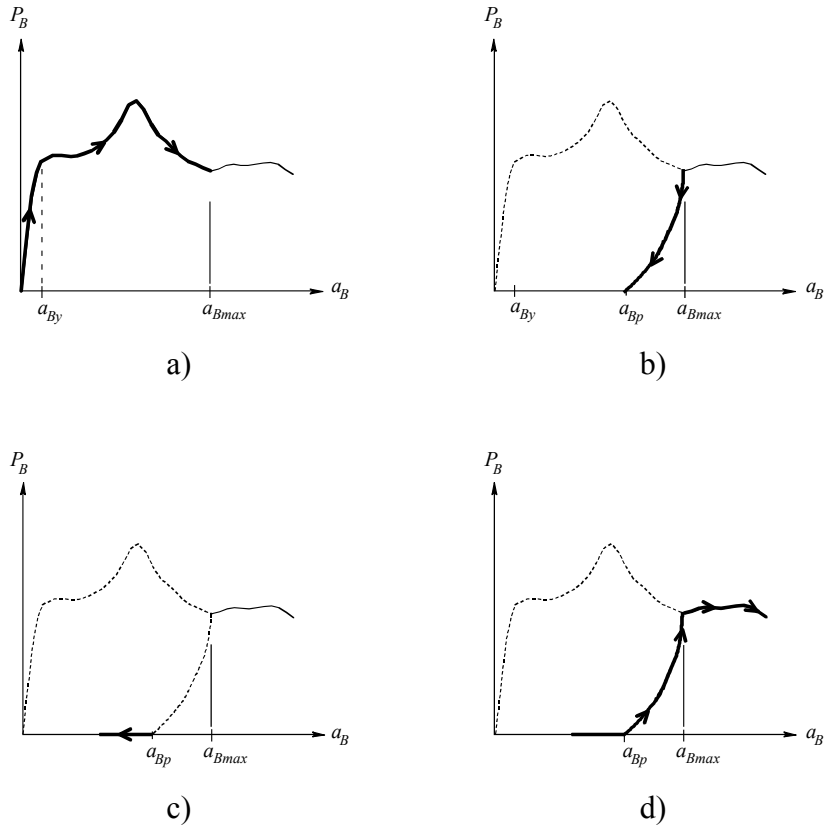

Figure 5.2 Stages of barge crush
a) Loading; b) Unloading; c) Barge not in contact with pier;
d) Reloading and continued plastic deformation

Barge unloading curves may consist of simple linear lines equal in slope to the initial part of the barge crush curve (Figure 5.3a), or fully-general nonlinear, deformation-dependent curves (Figure 5.3b). In the latter case, each unloading curve specified must be associated with a particular maximum barge crushing deformation a_{Bmax}. When such curves are used to model barge unloading behavior in a collision analysis, the deformation level a_{Bmax} at which unloading begins will normally not correspond to one of the specified a_{Bmax} values. In this situation, the two unloading curves that bracket the initial unloading point, $a_{Bmax(i)} \le a_{Bmax} \le a_{Bmax(i+1)}$, are identified. An intermediate unloading curve is then generated for deformation level a_{Bmax} by linearly interpolating between the two bounding curves (Figure 5.4).

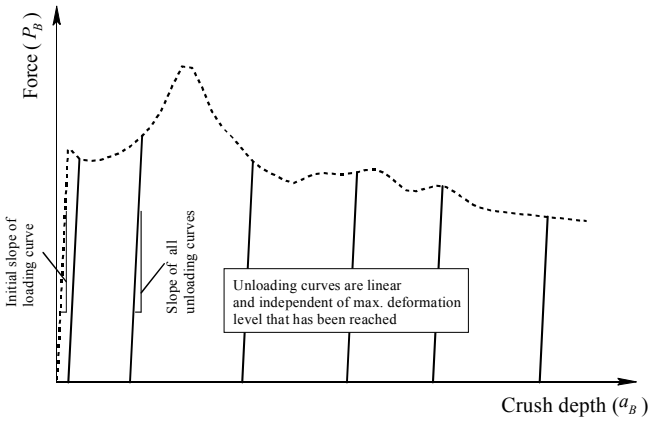

a)

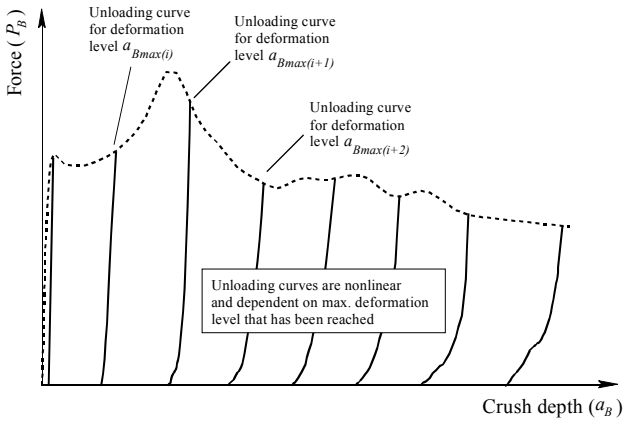

b)

Figure 5.3 Unloading curves generated by cyclic high resolution crush a) linear unloading curves parallel to initial slope b) fully-general nonlinear unloading curves

5.3.2 Time Integration of Barge Equation of Motion

Given the nonlinearities inherent in barge crushing, time-integration of the barge equation of motion must be performed using numerical methods. Energy dissipation produced by plastic crushing of the barge bow is included in the method, but viscous damping forces associated with water surrounding the barge are neglected. Recalling Figure 5.1, the equation of motion for the barge (SDOF) is written as :

$$m_B \ddot{u}_B = P_B \tag{5.1}$$

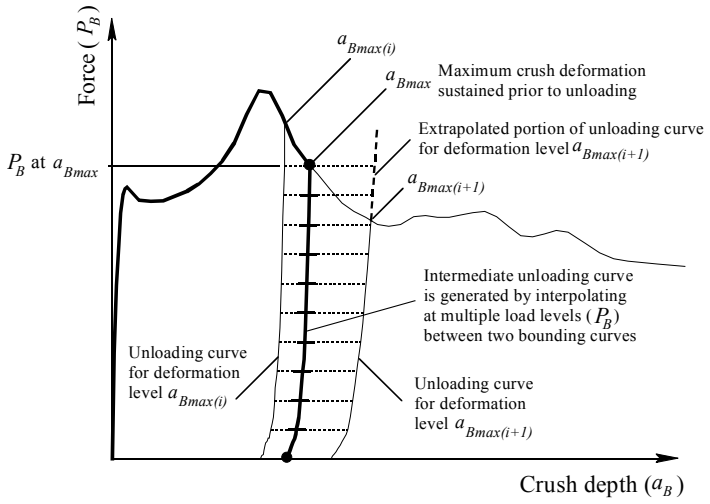

Figure 5.4 Generation of intermediate unloading curves by interpolation

where m_B is the barge mass, $\ddot{u}_B$ is the barge acceleration (or deceleration), and P_B is the contact force acting between the barge and pier. Assuming that the mass of the barge remains constant, then evaluating Eqn. (5.1 at time t, we have

$$m_B \, {}^t\ddot{u}_B = {}^tP_B \tag{5.2}$$

where ${}^t\ddot{u}_B$ and ${}^tP_B$ are the barge acceleration and force at time t. The acceleration of the barge at time t can be estimated using the central difference equation :

$${}^t\ddot{u}_B = \frac{1}{h^2}({}^{t+h}u_B - 2\,{}^tu_B + {}^{t-h}u_B) \tag{5.3}$$

where h is the time step size; and ${}^{t+h}u_B$, ${}^tu_B$, and ${}^{t-h}u_B$ are the barge displacements at times $t+h$, t, and $t-h$ respectively. Substituting Eqn. (5.2 into Eqn. (5.3 yields the explicit integration central difference method (CDM) dynamic update equation :

$${}^{t+h}u_B = -({}^tP_B\, h^2/m_B) + 2\,{}^tu_B - {}^{t-h}u_B \tag{5.4}$$

which uses data at times t and $t-h$ to predict the displacement ${}^{t+h}u_B$ of the barge at time $t+h$. Since the barge crush behavior is nonlinear, the force ${}^tP_B$ is computed using the loading and unloading crush model described earlier.

5.4 Pier Analysis Software Selection and Overview

The coupled impact analysis algorithm was originally implemented in the pier analysis software, FB-Pier (2003), and was shown to produce force and displacement time-histories in agreement with those obtained from high-resolution contact-impact finite element pier-soil model simulations (Consolazio and Cowan 2005). Subsequent to

implementation of the coupled analysis procedure in FB-Pier, an enhanced program called FB-MultiPier (2007) became available. FB-MultiPier possesses the same analysis capabilities as FB-Pier (including coupled analysis) but also has the ability to account for bridge superstructure elements. FB-MultiPier was therefore selected for all model development and analysis conducted in this chapter.

FB-MultiPier employs fiber-based frame elements for piles, pier columns, and pier caps; flat shell elements for pile caps; beam elements, based on gross section properties, for superstructure spans; and, distributed nonlinear springs to represent soil stiffness. Rayleigh damping, which was applied to all structural elements in the models was specified such that approximately 5% of critical damping was achieved over the first five natural modes of vibration. (A natural damping level of 5% is routinely employed in dynamic analysis for seismic design of structures). FB-MultiPier allows either linear elastic or material-nonlinear analysis of structural elements. Linear elastic analysis was selected for all structural (non-soil) element components of models discussed in this chapter.

5.5 Coupling Between Barge and Pier

Coupling between the SDOF barge model and the FB-MultiPier bridge-soil model is accomplished through the use of a shared impact force P_B that acts on both the barge and the pier at the point of contact between the two. Since the pier columns in the bridge-soil module are modeled using resultant line elements (nonlinear frame elements), the barge impact force P_B is applied to the pier in a consistent manner using a time varying nodal force rather than a distributed contact surface pressure. Contact-surface effects related to the geometry of the pier-column cross-section and the barge crush zone are approximated by selecting an appropriately generated barge crush model for use in the analysis (see Chapter 4).

Conceptually, the overall coupled barge-bridge-soil system can be thought of as two separate components: a bridge-soil control component (Figure 5.5), and a barge dynamics component (Figure 5.6). Dynamic time integration is primarily controlled by the bridge-soil component with the barge component determining the magnitude of the impact force P_B based on the dynamic barge and pier motions, and based on the barge crush model. Coupling is achieved through three links in the bridge-soil component (Figure 5.5). Each link instructs the barge module to perform a particular task : mode=INIT initializes the barge component; mode=CALC calculates an initial estimate of barge force at the start of a time step; mode=CONV determines if convergence of the overall coupled system has occurred.

Implicit direct time step integration in the bridge-soil system (FB-MultiPier) is accomplished using Newmark's method (Fernandez 1999). As Figure 5.5 indicates, the overall flow of the process involves an outer loop that controls time stepping, and an inner loop that controls iteration to convergence, i.e. satisfaction of dynamic equilibrium at each time step. For complete details the reader is referred to Fernandez (1999).

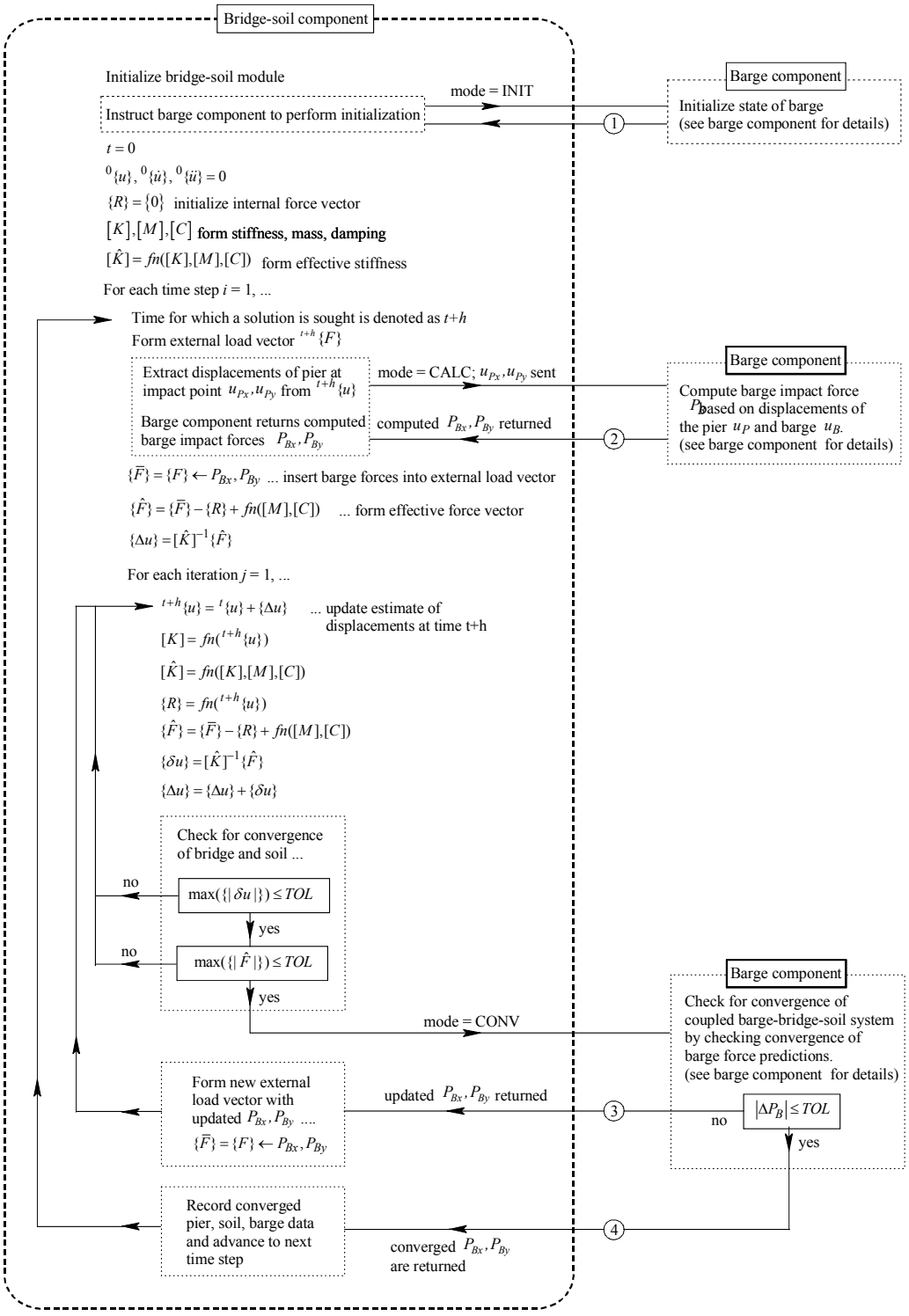

Figure 5.5 Flow-chart for nonlinear dynamic bridge-soil control component

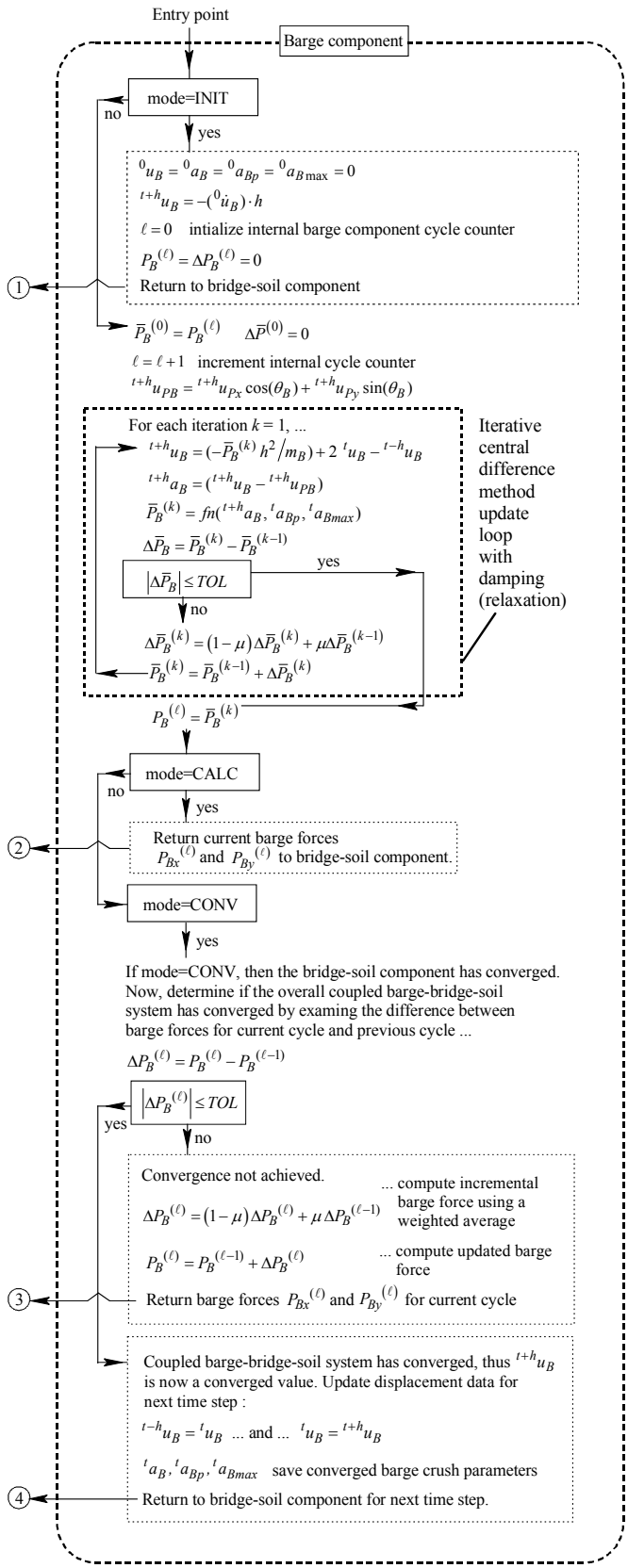

Figure 5.6 Flow-chart for nonlinear dynamic barge component

At the beginning of each time step, the barge component is invoked (mode=CALC) to calculate an estimate of impact force P_B for that time step. Determination of the force P_B first requires that the barge crush depth be computed as $a_B = \max\left((u_B - u_{PB}), a_{Bp}\right)$ where u_{PB} is the component of pier motion in the direction of barge motion (Figure 5.7a), computed as $u_{PB} = u_{Px}\cos(\theta_B) + u_{Py}\sin(\theta_B)$. In performing this computation, the bridge-soil component has supplied the most up-to-date estimates of pier displacements u_{Px} and u_{Py}.

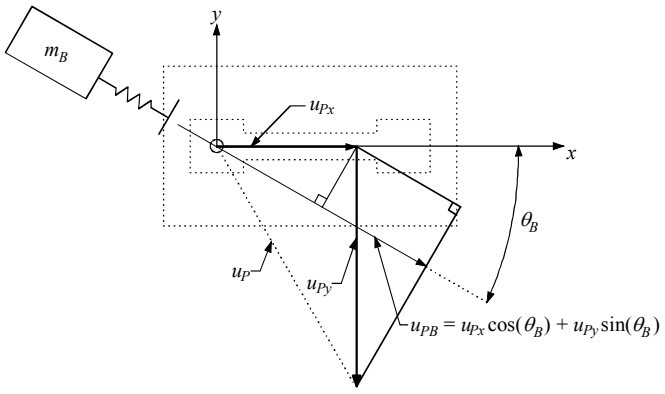

a)

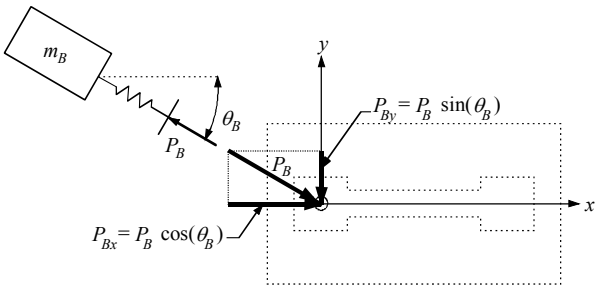

b)

Figure 5.7 Treatment of oblique collision conditions
a) Displacement transformation; b) Force transformation

An iterative variation of the CDM is then used (Figure 5.6) to satisfy the dynamic equation of motion for the barge. At each pass through this iteration loop, the estimated barge impact force is refined until convergence is achieved. To accelerate convergence of the iteration process, numerical damping (relaxation) is used to adjust the changes made to the estimates of impact force. In Figure 5.6, an exponentially decaying historical averaging process is used to compute damped increments of barge impact force for each iteration k:

$$\underbrace{\Delta\bar{P}_B^{(k)}}_{a} = (1-\mu)\underbrace{\Delta\bar{P}_B^{(k)}}_{b} + \mu\underbrace{\Delta\bar{P}_B^{(k-1)}}_{c} \tag{5.5}$$

In this expression, part-a is the damped force increment; part-b is the "raw" force increment computed for the current iteration; part-c is the damped force increment from the previous iteration; and μ is a factor that determines the relative weighting of current versus previous data in determining the damped incremental change (μ=0 indicates that previous data should be disregarded altogether). Note that by the recursive nature of this process, part-c contains not only data for the previous iteration k but also data for all previous iterations. The influence of older cycles diminishes in an exponentially decaying fashion that is controlled by the choice of μ.

An investigation involving test values of μ=0.25, μ=0.50, and μ=0.75 revealed that moderate damping (μ=0.25) was sufficient to ensure reliable convergence in otherwise oscillatory solution cases, whereas heavier damping levels ($\mu \geq 0.5$) resulted in stable but slower convergence. Hence, all analyses discussed here were conducted using a value of μ=0.25.

With the damped increment of force $\Delta\overline{P}_B^{(k)}$ determined using Eqn. (5.5, the actual barge force is computed by the barge component as:

$$\overline{P}_B^{(k)}=\overline{P}_B^{(k-1)}+\Delta\overline{P}_B^{(k)} \tag{5.6}$$

Once a converged value of $\overline{P}_B$ is computed, $P_B^{(\ell)}$ is set to $\overline{P}_B$ (Figure 5.6). The parameter $P_B^{(\ell)}$ is the barge force estimate for cycle ℓ, where a "cycle" is defined as one invocation of the barge component by the pier component. Denoting $P_B^{(\ell)}$ simply as P_B, the components of force acting on the pier in the x and y directions (Figure 5.7b) are then computed as $P_{Bx}=P_B\cos(\theta_B)$ and $P_{By}=P_B\sin(\theta_B)$. Both head-on and oblique-angle impacts (Figure 5.7) occurring along the centerline of the barge may be analyzed using this algorithm.

After assembling P_{Bx} and P_{By} into the appropriate locations in the bridge-soil external load vector (which generally will also contain additional loads such as gravity), the bridge-soil component iterates until it has reached dynamic equilibrium (i.e., convergence). During this process the values of P_{Bx} and P_{By}, that have been merged into the load vector, are not altered (attempting to update the barge force components within each bridge-soil equilibrium iteration results in unreliable convergence behavior). Once the bridge-soil component has converged, the resultant displacement of the pier at the impact point (u_P) is extracted from the bridge-soil displacement vector $\{u\}$. While the bridge-soil system has converged at this stage, the overall coupled barge-pier-soil system may still not have converged.

Determination of overall convergence is accomplished by once again invoking the barge component (now as mode=CONV). Using the newly updated u_P value provided by the bridge-soil component, the barge component once again carries out iterative CDM integration on the SDOF barge. It is very important to note that each time the barge component is invoked, time integration is performed using displacement data ($^{t}u_B$ and $^{t-h}u_B$) and barge crush data ($^{t}a_{Bp}$ and $^{t-h}a_{Bmax}$) that correspond to previous points in time

at which the *entire* coupled barge-pier-soil system has achieved convergence. Once a new estimate of the barge force has been computed, the difference in value between the current invocation ("cycle ℓ") and the previous invocation ("cycle $\ell-1$") is computed (see the calculation $\Delta P_B^{(\ell)} = P_B^{(\ell)} - P_B^{(\ell-1)}$ in Figure 5.6). If $\Delta P_B^{(\ell)}$ is sufficiently small, then not only has the bridge-soil system converged, but the prediction of barge force for this time step has also converged, and therefore the entire barge-bridge-soil coupled system is in dynamic equilibrium. Thus, if $\left|\Delta P_B^{(\ell)}\right| \le \text{TOL}$ is satisfied, the barge component instructs the bridge-soil component to advance to the next time step.

If instead, $\left|\Delta P_B^{(\ell)}\right| > \text{TOL}$, then an updated estimate of barge force P_B must be computed and returned to the bridge-soil component. While the simplest choice would be to return the value of $P_B^{(\ell)}$ just used in the $\Delta P_B^{(\ell)} = P_B^{(\ell)} - P_B^{(\ell-1)}$ calculation, this is in fact a poor choice. Because the bridge-soil component and the barge component each iterate to convergence independently in an alternating "back-and-forth" fashion, the barge forces $P_B^{(\ell)}$ predicted during sequential barge component invocations (i.e., cycles ℓ = 0, 1, 2, etc.) tend to oscillate as the two systems seek to achieve coupled dynamic equilibrium. This oscillation in $P_B^{(\ell)}$ values can result in slow coupled convergence and typically involves sequentially computed values of $\Delta P_B^{(\ell)}$ that alternate in sign.

To reduce these oscillations and accelerate convergence, the same damping (relaxation) technique described above is once again used. Rather than returning the raw computed $P_B^{(\ell)}$ value to the bridge-soil component, an exponentially decaying historical averaging process is used to compute a damped increment of barge impact force :

$$\underbrace{\Delta P_B^{(\ell)}}_{a} = (1-\mu)\underbrace{\Delta P_B^{(\ell)}}_{b} + \mu\underbrace{\Delta P_B^{(\ell-1)}}_{c} \tag{5.7}$$

As stated earlier, a damping level of μ=0.25 was used in all of the impact analyses described in this paper.

With the damped increment of force $\Delta P_B^{(\ell)}$ determined using Eqn. (5.7, the barge force is computed by the barge component (Figure 5.6) as :

$$P_B^{(\ell)} = P_B^{(\ell-1)} + \Delta P_B^{(\ell)} \tag{5.8}$$

Next, $P_B^{(\ell)}$ is broken into components P_{Bx} and P_{By}, which are returned to the pier component (the superscript ℓ is omitted in Figure 5.5 since the cycle number concept is local to the barge component). After assembling the new P_{Bx} and P_{By} values into a clean copy of the external load vector $\{F\}$ to form $\{\bar{F}\}$, the bridge-soil component resumes the process of iterating toward convergence using the newly formed load vector. Advancement to a new time step only occurs when the overall coupled barge-pier-soil system has converged.

5.6 Validation of the Coupled Vessel Impact Analysis Procedure

Analytical validation of the coupled vessel impact analysis (CVIA) algorithm was previously carried out (Consolazio and Cowan 2005) by using high-resolution contact-impact finite element simulation. Data obtained from the CVIA algorithm were compared to corresponding data obtained by analyzing highly detailed MDOF barge and pier models using LS-DYNA. Good agreement was found between the CVIA and LS-DYNA analysis results.

Presently, however, the CVIA algorithm can be further validated against experimental data collected during the St. George Island full-scale barge impact experiments (Consolazio et al. 2006). Using the experimental test data, validation of the coupled analysis procedure may be carried out in four stages: 1) select structures from the experimental dataset; 2) develop corresponding numerical models; 3) analyze the models using coupled vessel impact analysis (implemented in FB-MultiPier); and, 4) compare time-history results obtained from coupled analysis to data obtained experimentally at St. George Island.

5.6.1 Barge Impact Validation Cases

During the St. George Island full-scale barge impact test program, data were extensively collected for tests conducted on Pier 1-S in isolation (i.e., with the superstructure removed). Furthermore, an isolated pier configuration is representative of the type of structure often used in static design procedures for barge collision analysis (Knott and Prucz 2000). Hence, Pier 1-S of the old St. George Island Bridge (Figure 5.8a) was selected for coupled analysis validation using experimental data. Of the eight experimental tests conducted on Pier 1-S, the fourth test (termed P1T4) consisted of a head-on impact at an undamaged portion of the barge bow, as would be assumed in bridge design. Therefore, test P1T4, with velocity and impact weight as specified in Table 5.1, was selected for use in validation.

In addition to validating the coupled analysis procedure for a single-pier, data from the partial bridge (B3 series) tests were also employed for validation purposes. The fourth test (termed B3T4) generated the largest pier response among the B3 test series. Hence, test B3T4 (Figure 5.8b), with velocity and impact weight as specified in Table 5.1, was used for validation.

Table 5.1 Validation Case Descriptions

			Barge impact parameters		
Case	**No. Piers**	**Spans**	**Weight**	**Velocity**	**Energy**
P1T4	1	0	604 tons	2.59 knots (4.37 ft/sec)	357 kip-ft
B3T4	4	3	344 tons	1.53 knots (2.58 ft/sec)	71.3 kip-ft

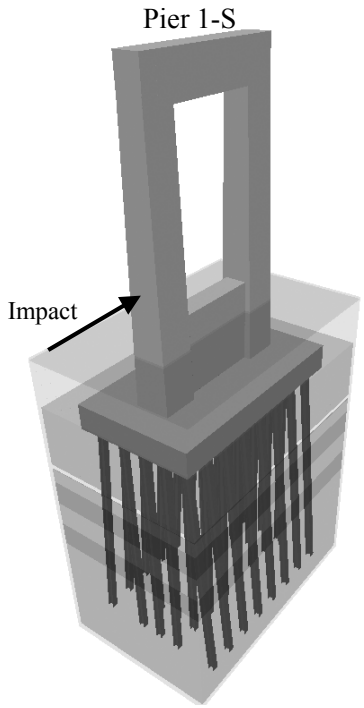

a)

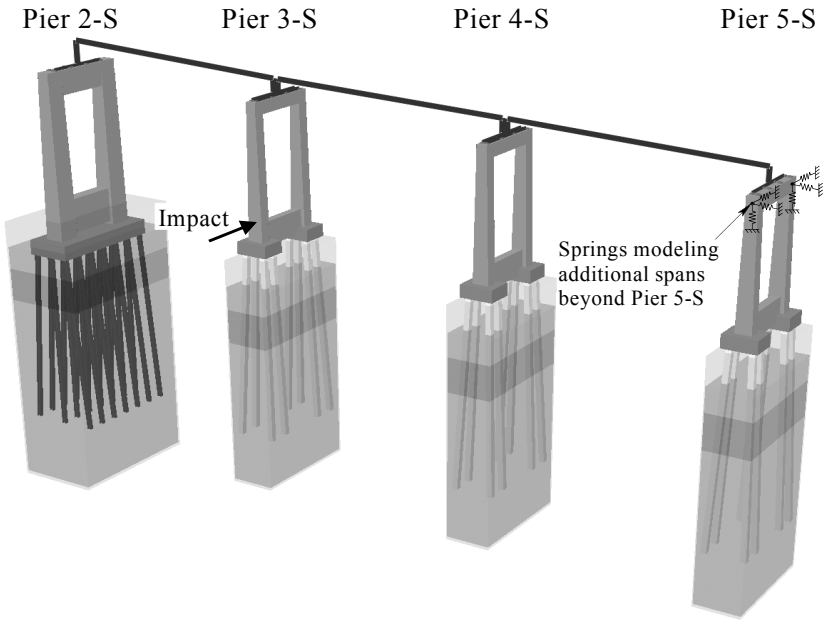

b)

Figure 5.8 Structural configurations analyzed (not to relative scale)
a) Case P1T4: Single pier; b) Case B3T4: Four piers with superstructure

5.6.2 Model Development

Structural models (Figure 5.8) for cases P1T4 and B3T4 were developed from original construction drawings and direct site measurements. The case B3T4 structural model was limited to four piers, with springs representing the stiffness contributions of piers beyond Pier 5-S (Figure 5.8b). The soil model for case P1T4 was developed based on boring logs and dynamic soil properties obtained from a geotechnical investigation conducted in parallel with the full-scale barge impact testing (McVay et al. 2005). For the development of the case B3T4 soil model, boring logs formed the sole data source available.

For each structure (P1 and B3), soil and structural model calibration steps were conducted in a previous research project (Consolazio et al. 2006). However, SDOF barge models and barge-bridge-soil coupling were not used in these earlier validation efforts. Instead, in each case, an experimentally measured time-history of impact loading was *directly applied* to the impact point in the corresponding structural model. The calculated displacement time-history of the structure was then compared to the experimentally measured displacement data. Soil and structural parameters in the models were calibrated until good agreement was obtained between model and experiment. Based on the earlier calibration efforts, the structural and soil models for cases P1T4 and B3T4 were known to respond in reasonable agreement with the experimental tests. In the present validation effort, SDOF barge models and the barge-bridge-soil coupling algorithm are added to the overall analysis process.

5.6.3 Modeling Barge Bow Force-Deformation Behavior

In the coupled analysis procedure, the barge is modeled by a SDOF point mass and nonlinear compression-only spring. Barge impact conditions for the validation cases (P1T4 and B3T4) were directly measured during the experimental tests. Thus, the experimental impact weights and velocities were directly input into analytical case P1T4 as 604 tons traveling at 2.59 knots and case B3T4 as 344 tons traveling at 1.53 knots, respectively.

The loading portion of the barge crush curve used in cases P1T4 and B3T4 (Figure 5.9) was developed from impact-point force and displacement time-history data measured during the P1T4 test. Test P1T4 was selected for this purpose, specifically, due to the undamaged bow impact location and head-on nature of this collision test. The portion of the barge force-crush relationship up to the peak force was obtained by performing coupled analysis using P1T4 impact conditions, and an initially arbitrary force-crush relationship. After analysis completion, the coupled analysis prediction of impact force was compared to that experimentally measured during the P1T4 test. The analytical barge crush relationship was then adjusted to more closely match that measured experimentally. After several iterations of this calibration process, a force-deformation loading relationship was obtained that produced force time-history data in agreement with the experimental measurements.

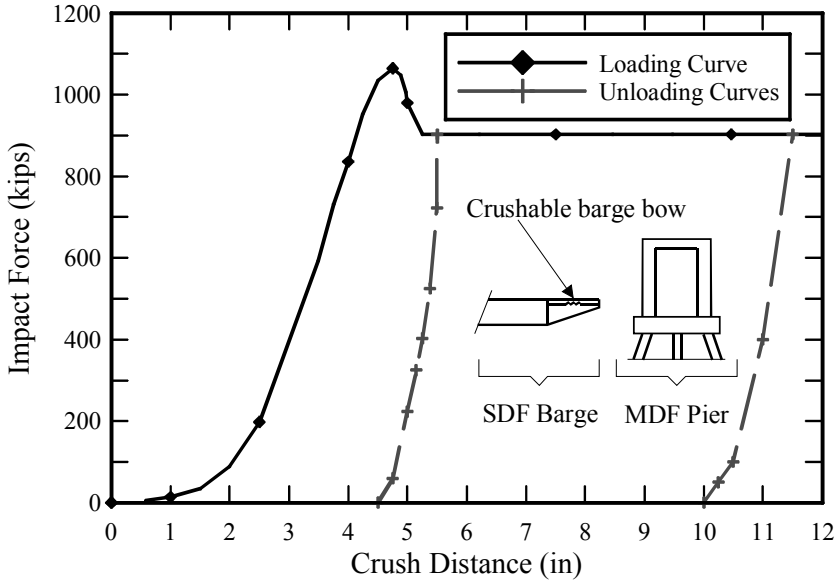

Figure 5.9 Barge force-deformation relationship derived from experimental and analytical data

The experimentally derived loading portion of the force-crush curve (Figure 5.9) has a peak impact force value of 1065 kips at a crush depth of 4.75 in. Beyond the peak force point on the crush curve, experimental data were not available for force-crush relationship development. Hence, analytical data, generated by subjecting high-resolution contact-impact finite element barge models to quasi-static crushing (see Chapter 4), were used to develop the remainder of the crush curve. The unloading curves (Figure 5.9) constructed for case P1T4 and B3T4 were chosen to be consistent with curves employed in a prior study (Consolazio and Cowan 2005) involving a barge subjected to quasi-static crushing by flat-faced piers.

5.6.4 Modeling Payload Sliding During Impact Testing

During the Pier 1-S test series, payload in the form of 55 ft reinforced concrete bridge superstructure span segments was placed on the barge to simulate a loaded-barge condition. However, during the collision events, the payload was observed to slide implying the development of frictional forces and dissipation of energy (Consolazio et al. 2006). In general bridge design, it would be assumed that the barge payload would not slide. However, for purposes of validating the coupled vessel impact analysis procedure as accurately as possible against the available experimental data, modifications were made to the coupled analysis algorithm to numerically simulate payload sliding (Figure 5.10). At each time-step and iteration, the ratio of barge acceleration (which, before sliding occurs, is equal to the payload acceleration) to gravitational acceleration was computed and compared to the static coefficient of friction (μ) between the payload and the barge. When the acceleration ratio exceeded the static coefficient of friction, sliding was initiated (Figure 5.10b) and the barge payload was assigned an initial velocity (u_0) equal to the velocity of the barge-payload system at that instant in time. The payload was then assumed to continue sliding until the

initial payload kinetic energy was completely dissipated through friction. At all points in time during which sliding was occurring, a constant frictional force, equal to the product of the static coefficient of friction and the weight of the payload, was applied to the barge. When the sliding kinetic energy of the payload barge was fully dissipated, the payload mass (m_p) and barge mass (m_B) were assumed to rejoin as a single loaded barge-payload system. For the P1T4 test, a sliding distance of 14.8 in. was predicted from the CVIA analysis, which agreed very well with the observed payload slide of approximately 15 in.

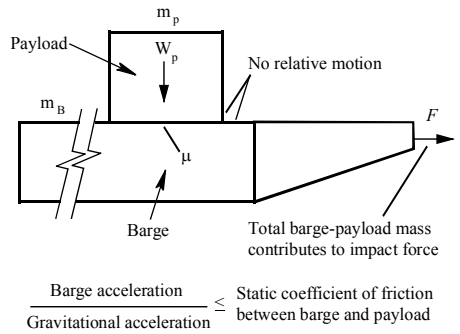

a)

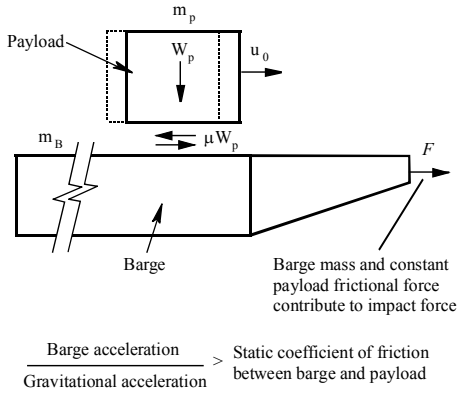

b)

Figure 5.10 Sliding criterion between payload and barge
a) No sliding; b) Sliding

5.6.5 Comparison of Analytical and Experimental Data

Case P1T4

The computed case P1T4 impact load time-history (Figure 5.11a) is nearly identical to the experimentally measured load curve up to the peak load, and expectedly so, since the portion of the barge force-crush relationship (Figure 5.9), up to the peak impact load, was

derived from the impact force and displacement data acquired from test P1T4. Agreement of the analytical and experimental portions of the case P1T4 force time-history curve beyond the initial peak justifies the assumptions that were made during development of the load softening, load plateau, and unloading components of the barge crush curve (Figure 5.9). One notable exception is the presence of a second peak in the experimental data that occurred due to a tug boat striking the rear of the test barge after the primary collision event.

In terms of pier response to the imparted impact loading, the analytically computed peak displacement exceeded the experimental value by 16% (Figure 5.11b). Supplementary coupled analyses were also conducted on the Pier 1-S model using impact velocities corresponding to additional series-P1 impact tests. Comparisons of computed and experimental displacement data for these cases (Davidson 2007) showed agreement as good as, or better, than that observed for case P1T4.

Case B3T4

Validation case B3T4, in contrast to P1T4, consists of a low-energy barge collision on a flexible pier with superstructure effects included. The barge bow crush curve used in analyzing case B3T4 was the same as that used in the P1T4 validation analysis. Experimentally measured and analytically computed impact force time-histories for case B3T4 (Figure 5.12a) are generally in good agreement, with the analytically computed force being moderately conservative in comparison to the measured experimental data. Comparisons of bridge displacement in response to the applied impact loads are in even better agreement (Figure 5.12a) with the analytically computed data again being conservative in comparison to the experimental data. Agreement of pier response is the most important outcome of the coupled analysis procedure, since the accompanying internal forces generated throughout the bridge-soil model ultimately govern structural member design.

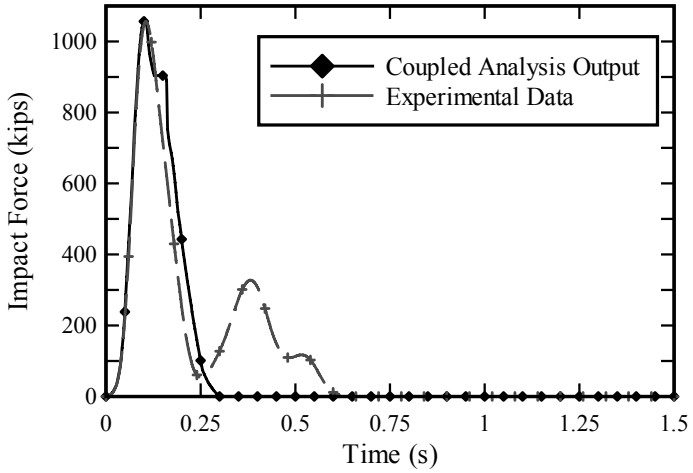

a)

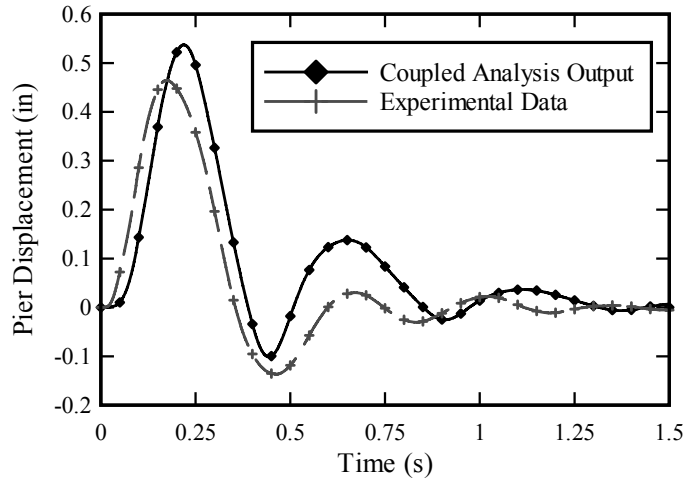

b)

Figure 5.11 Comparison of case P1T4 coupled analysis output and P1T4 experimental data
a) Impact force; b) Pier displacement

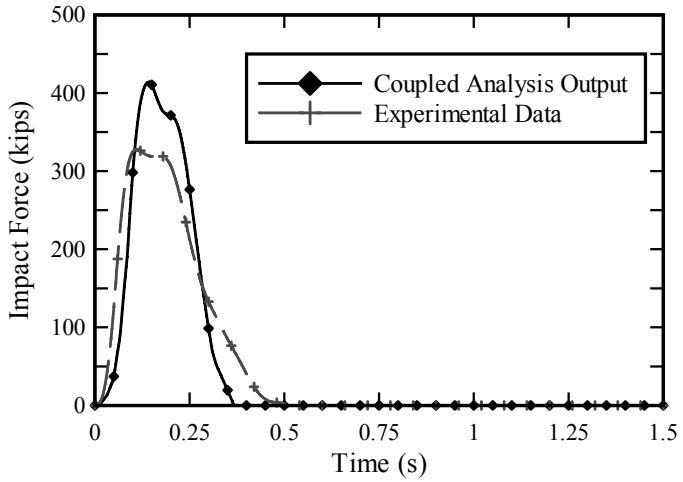

a)

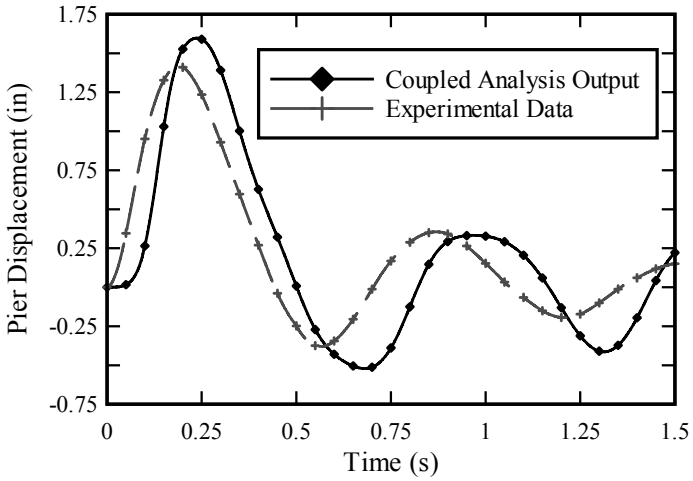

b)

Figure 5.12 Comparison of case B3T4 coupled analysis output and B3T4 experimental data
a) Impact force; b) Pier displacement

CHAPTER 6
SIMPLIFIED BRIDGE ANALYSIS USING THE ONE-PIER TWO-SPAN (OPTS) MODELING METHOD

6.1 Overview

At typical personal-computer processing speeds, coupled vessel impact analysis of multiple-pier, multiple-span bridge models can require from tens of minutes to several hours of processing time. However, such structures can also be analyzed in a numerically efficient manner using an equivalent one-pier two-span (OPTS) bridge model. In this chapter, it will be demonstrated that OPTS models are capable of matching full-resolution (multiple-pier, multiple-span) models to within a satisfactory degree of accuracy while requiring substantially less analysis time.

6.2 Reduction (Simplification) of the Bridge Model

Barges impart predominantly horizontal forces to impacted bridge piers during collision events. Displacement and acceleration based superstructure restraint (due to superstructure stiffness and mass, respectively) can attract a significant portion of the horizontal forces and cause the impact load to "shed" to the superstructure (Consolazio et al. 2006). The horizontal force that is shed to the superstructure then propagates away from the impacted pier. Consequently, lateral translational and plan-view rotational stiffnesses influence structural response as the force propagates through the superstructure spans from the impacted pier to the adjacent piers. The distributed mass of the superstructure may generate inertial resistance and/or inertial loading, depending on the configuration of the bridge and nature of the impact condition (barge mass and speed). Simplification of the multiple-pier, multiple-span structural model must therefore adequately retain the influences of the superstructure elements (spans) and the adjacent non-impacted piers.

6.2.1 Uncoupled Condensed Stiffness Matrix

Degrees-of-freedom (DOF) in a bridge model, beyond the superstructure spans that are connected to the impacted pier (Figure 6.1), may be approximated by equivalent lateral translational springs and plan-view rotational springs. These springs are linear elastic and represent the predominant DOF of the structural elements in the full-resolution model at piers adjacent to the impacted pier. Soil nonlinearities at piers other than the impacted pier are ignored during formation of the translational and rotational springs.

Replacement of numerous DOF from the flanking portions of a full bridge model (Figure 6.1) by two uncoupled springs at each end of a simplified one-pier, two-span model may be described in terms of a condensed stiffness matrix:

$$[K_{condensed}] = \begin{bmatrix} K_{\Delta} & K_{coupling} \\ K_{coupling} & K_{\theta} \end{bmatrix} \tag{6.1}$$

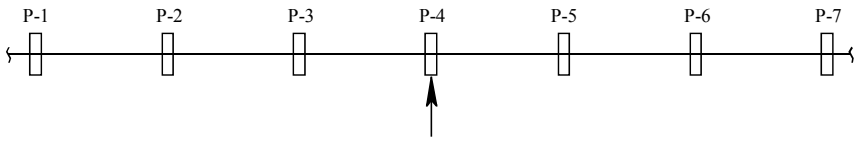

Impact location on full bridge model

Form left-flanking and right-flanking structures, excluding impacted pier P-4 and the two connecting spans

Left-flanking structure

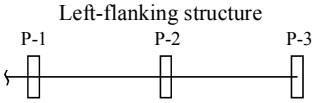

Right-flanking structure

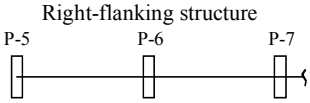

Apply unit shear force at center of P-3 pier cap and center of P-5 pier cap

Record shear-induced translations and rotations at center of P-3 pier cap and center of P-5 pier cap

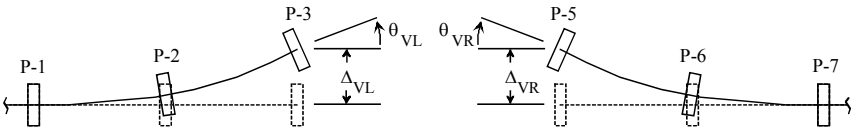

Apply unit moment at center of P-3 pier cap and center of P-5 pier cap

Record moment-induced rotations and translations at center of P-3 pier cap and center of P-5 pier cap

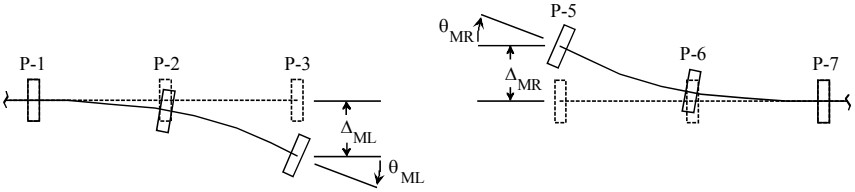

Form 2x2 left-flanking and right-flanking flexibility matrices using displacements and invert to form condensed stiffness

$$\left[F^{L}\right]^{-1}=\begin{bmatrix}\Delta_{VL} & \Delta_{ML}\\ \theta_{VL} & \theta_{ML}\end{bmatrix}^{-1}=\left[K^{L}_{condensed}\right]=\begin{bmatrix}K^{L}_{\Delta} & K^{L}_{coupling}\\ K^{L}_{coupling} & K^{L}_{\theta}\end{bmatrix}$$

$$\left[F^{R}\right]^{-1}=\begin{bmatrix}\Delta_{VR} & \Delta_{MR}\\ \theta_{VR} & \theta_{MR}\end{bmatrix}^{-1}=\left[K^{R}_{condensed}\right]=\begin{bmatrix}K^{R}_{\Delta} & K^{R}_{coupling}\\ K^{R}_{coupling} & K^{R}_{\theta}\end{bmatrix}$$

Neglect off-diagonal stiffness and replace flanking-structures in full bridge model with diagonal stiffness as uncoupled springs

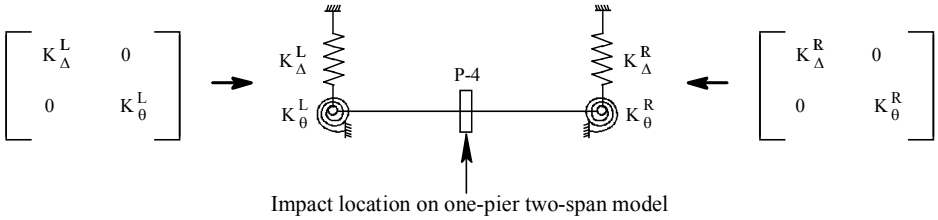

Impact location on one-pier two-span model

Figure 6.1 Plan view of multiple-pier numerical model and location of equivalent springs in a one-pier two-span (OPTS) model

where $[K_{condensed}]$ is the condensed stiffness matrix of the flanking bridge portion eliminated at each side of the impacted pier; K_{Δ} is the condensed lateral translational stiffness term; $K_{coupling}$ is an off-diagonal stiffness term that couples the translational DOF to the rotational DOF; and K_{θ} is the condensed stiffness plan-view rotational stiffness term. In the simplified OPTS model, the diagonal terms K_{Δ} and K_{θ} are represented by translational and rotational springs, respectively, and the $K_{coupling}$ terms are neglected. The exclusion of $K_{coupling}$ in the simplified model is justified by examining the forces generated by the condensed stiffness terms on one side of an example five-pier model.

A channel pier was added to the previously discussed four-pier case B3T4 model (Chapter 5), using bridge plans of the old St. George Island Causeway Bridge. This new five-pier model (Figure 6.2) is referred to as demonstration case D1, as defined in Table 6.1. Through flexibility inversion (Figure 6.1), the left-flanking bridge structure in case D1 (consisting of Pier 1-S to Pier 2-S), is reduced to the 2-DOF linear elastic condensed stiffness matrix in Equation 6.1, where K_{Δ}= 548 kip/in; K_{θ}= 1.88E+08 kip-in/rad; and, $K_{coupling}$= 6.29E+03 kip/rad. In row one of $[K_{condensed}]$, the $K_{coupling}$ term may be interpreted as a horizontal shear force generated when a unit rotation (1 rad) is induced at the Pier 2-S end of the left-flanking structure. However, static application of an impact load of 275 kips (the AASHTO load obtained using the case D1 impact conditions) at Pier 3-S in the *full* five-pier case D1 model produces a plan-view rotation of only θ = 3.20E-04 rad at Pier 2-S. The same loading produces a lateral deflection of Δ = 0.0821 in at Pier 2-S. The horizontal shear produced as a result of this rotation is:

$$V_{\theta}^{coupling} = (K_{coupling})(\theta) \tag{6.2}$$

where $V_{\theta}^{coupling}$ is the shear produced from the coupling of rotational and translational DOF. In this instance, $V_{\theta}^{coupling}$ = 2.02 kips. In comparison, the horizontal shear force V_{Δ} resulting from lateral stiffness K_{Δ} and lateral deflection Δ is:

$$V_{\Delta} = (K_{\Delta})(\Delta) \tag{6.3}$$

where V_{Δ} is the shear produced directly from lateral translation. For this loading, V_{Δ} = 45.0 kips.

Table 6.1 Descriptions of Demonstration Cases

				Barge impact parameters			
Case	**Use [a]**	**No. Piers**	**Spans**	**Weight**	**Velocity**		**Energy**
D1	U/D	5	4	200 T	1.0 knot	1.69 ft/sec	17.7 kip-ft
D2	D	5	4	2020 T	3.0 knots	5.06 ft/sec	1610 kip-ft
D3	D	5	4	7720 T	7.0 knots	11.82 ft/sec	33500 kip-ft

[a] U = Uncoupled Condensed Stiffness Calculation; D = Demonstration

The horizontal shear generated at Pier 2-S, due to the coupling stiffness term, is small relative to the amount of horizontal shear generated due to the diagonal stiffness term ($V_{\theta}^{coupling}$ is only 4.5% of V_{Δ}). A similar examination of the K_{θ} and $K_{coupling}$ terms yields ratios of comparable values (Davidson 2007). The large difference in magnitude between the two shear forces demonstrates that the off-diagonal stiffness terms of $[K_{condensed}]$ generate negligible forces relative to those generated by the diagonal, stiffness terms. Uncoupling the condensed stiffness terms by applying two independent springs is therefore warranted for design applications, as the uncoupled springs form a reasonable static approximation of the stiffness of the excluded portions of the model.

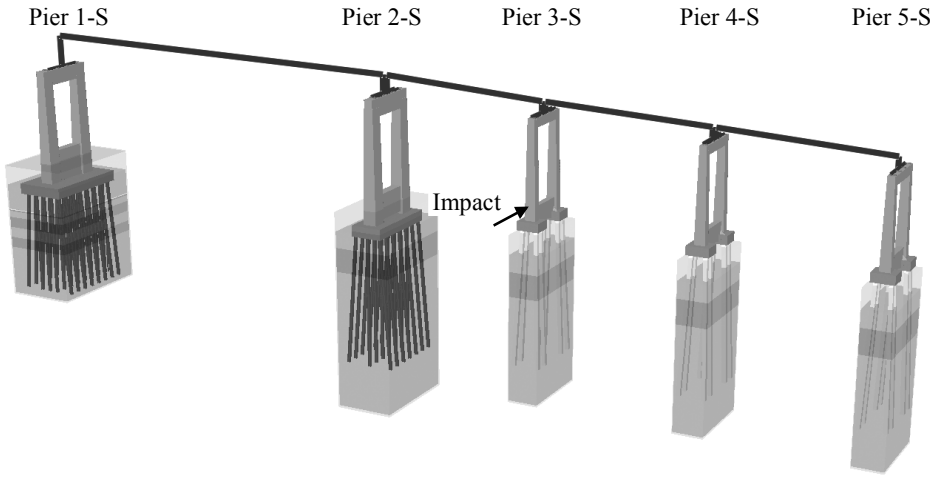

Figure 6.2 Structural configuration analyzed in case D1

As a further simplification to the full-bridge model, the diagonal stiffness terms K_{Δ} and K_{θ} may be approximated by direct inversion of the individual diagonal flexibility coefficients. Specifically, this entails directly inverting the translational Δ_V and rotational θ_M displacements, respectively, induced by the application of a unit shear force V^{unit} and unit force-couple M^{unit} on the applicable flanking structure (Figure 6.1). This approximation produces only nominally different magnitudes of stiffness with respect to that obtained by a flexibility matrix inversion (Davidson 2007) and is simpler to carry out.

6.2.2 Additional Stiffness Considerations

The stiffness formulation described above is intended for barge impact analysis on simplified OPTS models of bridges employing common superstructure types (e.g. slab-and-girder and segmental box girder superstructures) with clearly discernable bearing conditions at each pier top. Other bridge types may warrant additional consideration and analysis. Regardless of superstructure type, however, bridge analysis requires model stability under all pertinent loading conditions and may require supplemental spring application at the outer boundaries of the OPTS model when subjected to certain loading conditions.

For instance, the routine inclusion of self-weight in bridge analysis necessitates the inclusion of vertical translational stiffness (or constraints) at the boundaries of OPTS bridge models. Inclusion of such stiffness results in comparable distribution of self-weight between full-resolution and simplified bridge models. Alternatively, due to the large vertical translational stiffness of the piers, the boundaries of the OPTS model may simply be constrained with respect to the vertical-translation DOF. Therefore, a typical OPTS bridge model may be configured as shown in Figure 6.3, with lateral-translational springs, plan view-rotational springs, and vertical-translation constraints.

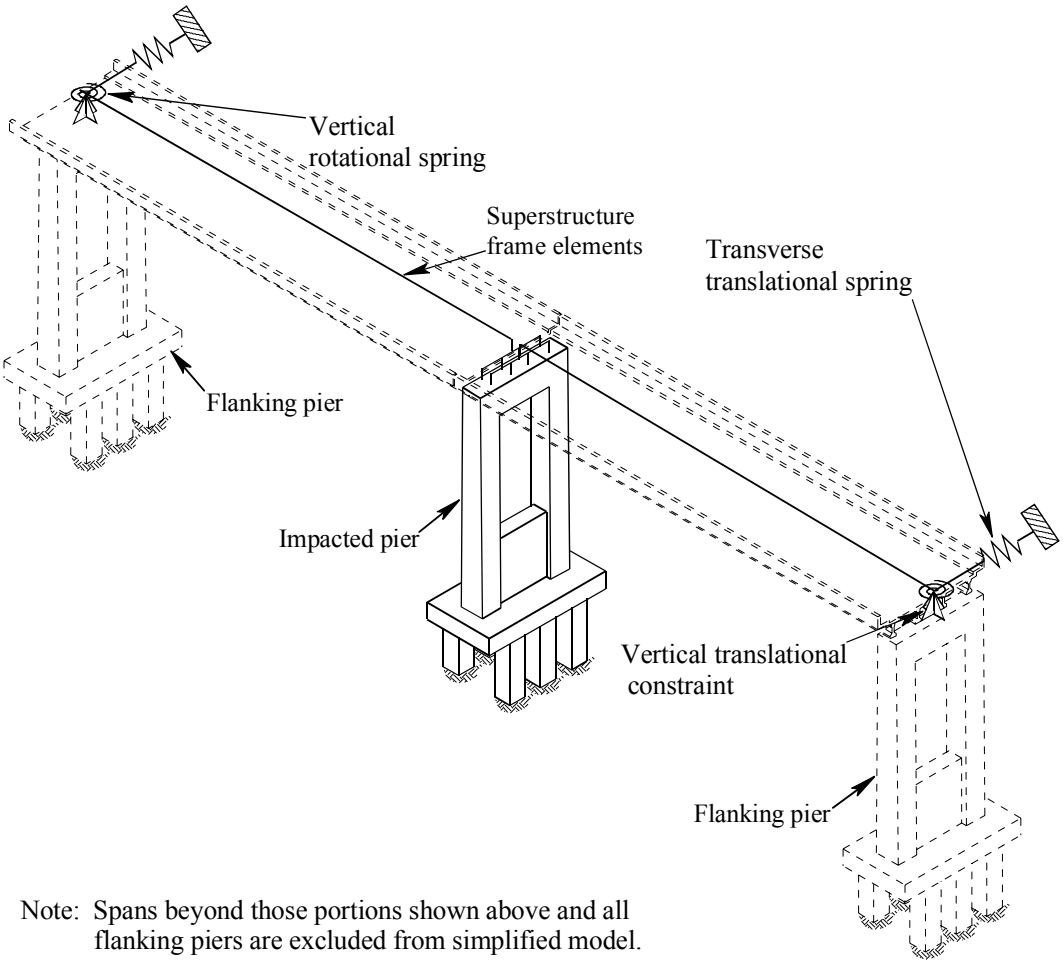

Figure 6.3 Simplified bridge model with typical stiffness assignments

Additionally, certain bridge configurations may warrant additional types of springs at boundaries of the OPTS model (see Figure 6.4). For instance, OPTS models of bridges containing skewed superstructure spans require application of span-longitudinal translation springs, in addition to the aforementioned stiffness formulation. Similarly, bridges containing continuous segmental box girders may require application of span-transverse rotational springs (representing the torsional stiffness of the eliminated spans). Furthermore, specialized analysis techniques may require additional stiffness inclusion at specific DOF of OPTS model boundaries. The impact response spectrum analysis (IRSA) method, discussed in Chapter 8 of

this report, constitutes one such method. In the IRSA method, span-longitudinal springs are required to prevent non-pertinent vibration modes from being included in the modal (eigen) analysis calculations. The effectiveness of the reduced stiffness may be quantified by comparing full and simplified model displacements under static loading, and infrequently, may warrant inclusion of the full-condensed stiffness at simplified model boundaries. In all instances, however, the additional stiffness terms may be formulated in a manner analogous to those illustrated in Figure 6.1.

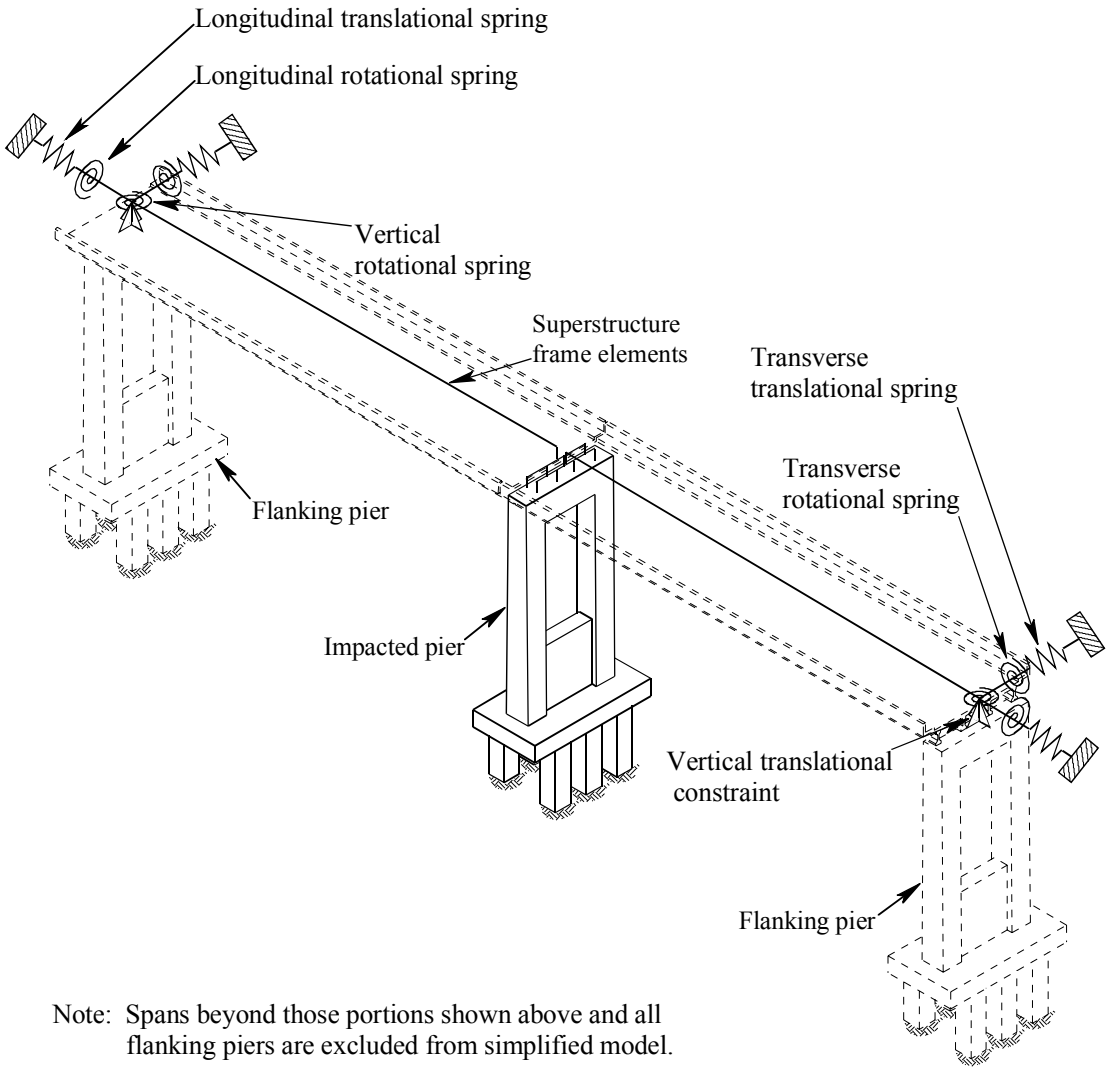

Figure 6.4 Simplified bridge model with typical and supplemental stiffness assignments

Finally, if significant nonlinear behavior is expected at adjacent non-impacted piers, then loads representative of the forces that will be shed to the superstructure, and subsequently transmitted into these piers, should be used to compute the corresponding flexibility coefficients (displacements). Inversion of flexibility coefficients formed in this manner yields a condensed secant stiffness for the nonlinear structure that can then be employed in the OPTS model as described previously.

6.2.3 Lumped Mass Approximation

To properly model the distribution of mass within a bridge structure, every node in the model should be allocated an appropriate quantity of mass. However, since large portions of the bridge are eliminated in an OPTS model, mass associated with the excluded structural components must be approximately taken into account. The mass of all superstructure components falling within the tributary area show in Figure 6.5 is lumped and placed at respective ends of the OPTS model.

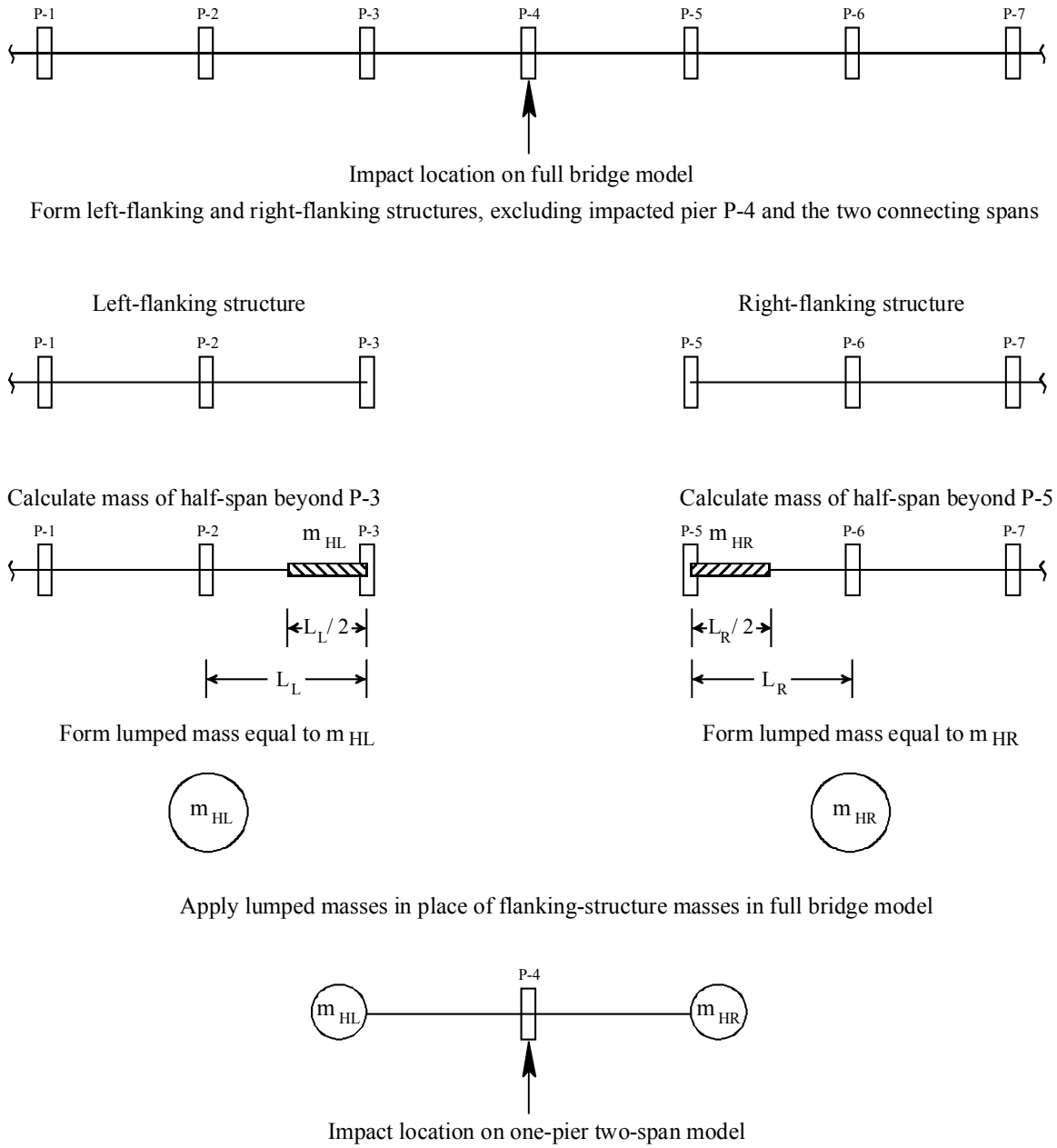

Figure 6.5 Plan view of multiple pier numerical model and location of lumped masses in the OPTS model

6.3 Coupled Vessel Impact Analysis (CVIA) Using a One-Pier Two-Span (OPTS) Model

Simplified coupled analysis occurs in two stages. First, the OPTS model is assembled by replacing extraneous portions of the multiple-pier model with uncoupled linear elastic springs and half-span lumped tributary masses. Coupled vessel impact analysis is then performed as discussed previously in Chapter 5. The model simplification algorithm automatically retains the ability to capture dynamic effects, such as internal member force amplification, that are not accounted for in static procedures. Furthermore, hundreds to thousands of DOF are eliminated because the non-impacted piers and respective superstructure spans from the full-resolution model are omitted from the OPTS model.

6.4 Demonstration of Simplified Coupled Analysis

To illustrate the efficacy of the simplification algorithm, three demonstration cases (FB-MultiPier bridge models) are presented. Each model was developed using methods representative of those employed by bridge designers. Impact conditions prescribed for the models are such that typical scenarios encountered in practical bridge design for barge impact loading are represented. The cases employ the elastic, perfectly-plastic barge deformation-force relationships recommended in Chapter 4. Also, the demonstration cases consist of OPTS models of increasing impact resistance that are subjected to impacts with corresponding increases in impact energy. Time-histories of internal pier structural member forces obtained from both full-resolution and OPTS models are compared for each case.

Each full-resolution model contains five piers: a centrally located impact pier and additional structural components (soil, non-impacted piers, and superstructure spans) for a length of two spans to either side of the central pier. A five-pier model contains a sufficient number of piers and spans such that inclusion of additional piers would increase analytical computation costs without appreciably improving the computed structural response. The appropriateness of the decision to limit the full-resolution models to five piers is substantiated by the consistently negligible acceleration response exhibited by the outer-most piers included in the five-pier models. That is, the added restraint provided by including additional piers is not necessary, as the outer-most piers of the five-pier models are only nominally active throughout respective barge impact analyses.

A single time-step increment, 0.0025 sec, was employed for all demonstration analyses. Each model also utilized Rayleigh damping, which was configured such that the first 5 free-vibration modes underwent damping at approximately 5% of critical damping.

6.4.1 Descriptions of Bridges, Impact Conditions, and Barge

Case D1

The first demonstration case consists of analysis of the previously described case D1 model (Figure 6.2). This model was based on the old St. George Island Causeway Bridge from the Apalachicola Bay area, linking St. George Island to mainland Florida, in the southeastern United States. Apalachicola Bay is located approximately 50 miles southwest of Tallahassee, Florida in the “panhandle” portion of the state.

The structure of the old St. George Island Causeway Bridge, constructed in the 1960s, was detailed in a prior report (Consolazio et al. 2006). Pertinent to demonstration case D1,

the superstructure spanning from Pier 2-S to Pier 5-S (Figure 6.2) consisted of 75.5 ft concrete girder-and-slab segments overlying concrete piers with waterline footings. Spanning the navigation channel and one additional pier to either side, a 619.5 ft continuous three-span steel girder and concrete slab segment rested on Pier 1-S and Pier 2-S, each containing a mudline footing and steel H-piles. The central pier in case D1, Pier 3-S, contained two tapered rectangular pier columns, with a 5 ft wide impact face at approximately the same elevation as the top of a small shear strut that spanned between the two 4 ft thick waterline pile-cap segments. The pier rested on eight battered 20 in square prestressed concrete piles, each containing a free length of approximately 12 ft.

The case D1 finite element model includes the southern channel pier and extends southward from the centerline of barge traffic. The impacted pier, Pier 3-S, was constructed before the AASHTO provisions were written (1991), and was flexible as it was not a channel pier. The pier was located 380 ft from the channel centerline, which was significantly closer to a distance of three times the impacting vessel length, 450 ft, than the distance to the edge of the navigation channel, 124 ft. Per the AASHTO specifications pertaining to design vessel impact velocities, the pier would be subject to a reduced impact velocity, approaching that of the yearly mean current velocity. The kinetic energy (Table 6.1) associated with an empty jumbo-hopper barge drifting at a rate comparable to the yearly mean current velocity for the Apalachicola Bay is representative of a low-energy impact condition.

Case D2

Escambia Bay abuts Pensacola, Florida, in the southeastern United States. Case D2 (Figure 6.6) consists of impact analysis of a model based on the Escambia Bay Bridge. Structural components of this bridge model were derived from bridge plans developed in the 1960s. The superstructure spanning from Pier 2-W to Pier 2-E consists of a 410 ft continuous three-span steel girder and concrete slab. A 92 ft concrete girder-and-slab segment spans the underlying concrete piers beyond Pier 2-E. All piers, except for the channel piers denoted as Pier 1-E and Pier 1-W, contain two pier columns, a shear wall, pile cap, and waterline footing foundation. The channel piers in case D2 each contain two tapered rectangular pier columns, with a 8.5 ft wide head-on impact face at approximately the mid-height elevation of a 17.5 ft shear wall. The pier columns and shear wall overlie a 5 ft thick mudline footing and 6 ft tremie seal. The channel pier foundations consist of eighteen battered and nine plumb 24 in square prestressed concrete piles.

The case D2 finite element model includes both of the channel piers and three auxiliary piers. The impacted pier, Pier 1-E, was constructed before the AASHTO provisions were written (1991), but contains large impact resistance relative to the impacted pier from case D1, as Pier 1-E is a channel pier. Impact on a channel pier with a relatively high impact resistance was chosen to demonstrate the accuracy of the simplification algorithm for the medium-energy impact of a fully-loaded jumbo hopper barge and towboat, traveling at a higher speed than the mean waterway velocity (Table 6.1).

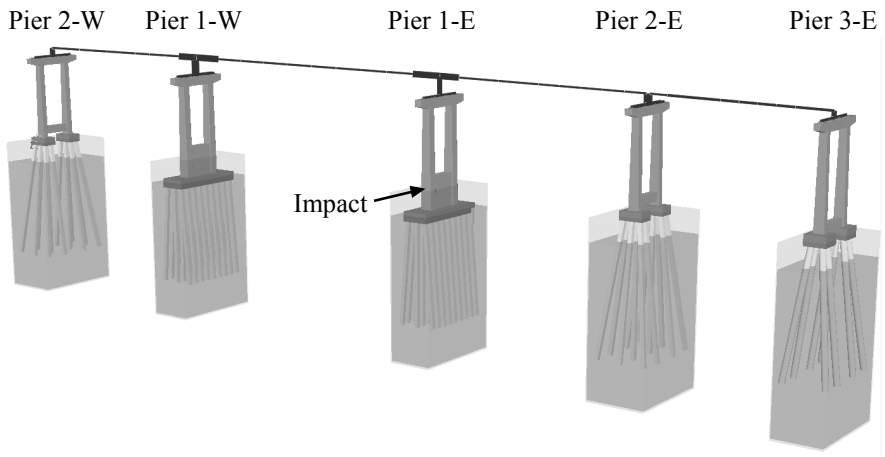

Figure 6.6 Structural configuration analyzed in case D2

Case D3

Case D3 (Figure 6.7) consists of impact analysis of piers from the new St. George Island Causeway Bridge, which replaced the old St. George Island Causeway Bridge in 2004. The structural model of the new St. George Island Causeway Bridge was derived from construction drawings. Per these drawings, Pier 46 through Pier 49 support five cantilever-constructed Florida Bulb-T girder-and-slab segments at span lengths of 250 ft for the channel and 257.5 ft for the flanking spans. Due to haunching, the depth of the post-tensioned girders vary from 6.5 ft at drop-in locations to 12 ft at respective pier cap beam bearing locations. Simply supported Florida Bulb-T beams with a depth equal to that of the haunched beams at the drop-in locations span either side of Pier 50. All piers included in this model contain two pier columns, a shear strut centered near a respective pier column mid-height, a pile cap, and a waterline footing system. The central pier in case D3, Pier 48, contains two round 6 ft pier columns, a 6.5 ft thick pile cap, and fourteen battered and one plumb 4.5 ft diameter prestressed cylinder piles with a 10 ft concrete plug extending earthward from the pile cap.

The new St. George Island Causeway Bridge was designed in accordance with current AASHTO barge collision design standards and provided a means of validating the simplification algorithm for barge impact energies similar to those used in present day design. The case D3 finite element model includes both of the channel piers and three auxiliary piers. The impacted pier, Pier 48 was designed for a static impact load of 3255 kips. With respect to the static AASHTO design impact load, an energy equivalent impact condition (Davidson 2007) is employed in case D3. The prescribed vessel mass and velocity yields an impact kinetic energy equivalent to four fully-loaded jumbo hopper barges and a towboat traveling slightly above typical waterway vessel speeds for the Apalachicola Bay waterway (Table 6.1).

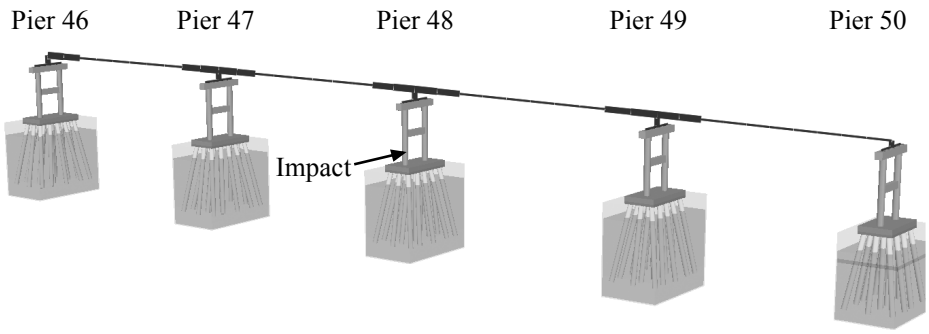

Figure 6.7 Structural configuration analyzed in case D3

Barge force-deformation (crush) relationship

Per Chapter 4, the barge yield force for flat-faced pier columns with a width of less than 10 ft is given by:

$$P_{BY} = 1500 + 60w_P \tag{6.4}$$

where P_{BY} is the peak impact force in kips, and w_P is the width of the pier column in feet. Eqn. 6.4 yields an elastic, perfectly-plastic crush curve (Figure 6.8) peak impact force of 1800 kips for the case D1, Pier 3-S impact face of 5 ft. Similarly, for the case D2, Pier 1-E impact width of 6 ft, Eqn. 6.4 yields a peak barge force-crush impact force of 1860 kips as shown in Figure 6.8. As discussed in Chapter 4, the barge bow crush depth corresponding to yield for flat-faced impactors is 0.5 in.

In contrast to cases D1 and D2, the impacted pier in case D3 contains round columns. Per Chapter 4, the barge yield force for round pier columns is given by:

$$P_{BY} = 1500 + 20w_P \tag{6.5}$$

where P_{BY} is the peak impact force in kips, and w_P is the diameter of the round pier column in feet. Eqn. 6.5, yields an elastic, perfectly-plastic crush curve (Figure 6.8) peak impact force of 1620 kips for the case D3, Pier 48 impact face of 6 ft. As discussed in Chapter 4, the barge bow crush depth corresponding to yield for round impactors is 2.0 in.

6.4.2 Comparison of Full-Resolution and Simplified (OPTS) Results

In bridge design applications related to waterway vessel collision, the analytically quantified internal forces in a given pier structure govern subsequent structural component sizing. Hence, accurate determination of internal forces is a necessary outcome of any proposed bridge structural analysis method. To highlight the ability of simplified analysis to accurately quantify design forces over the full range of impacted pier structures, time-histories of internal shear force induced by the impact loading are shown for the top of the impacted pier column and an underlying pile-head node for case D1 through case D3 shown in Figure 6.9 through Figure 6.11, respectively (additional comparisons of impact force, displacements, and internal moments are documented in Davidson 2007).

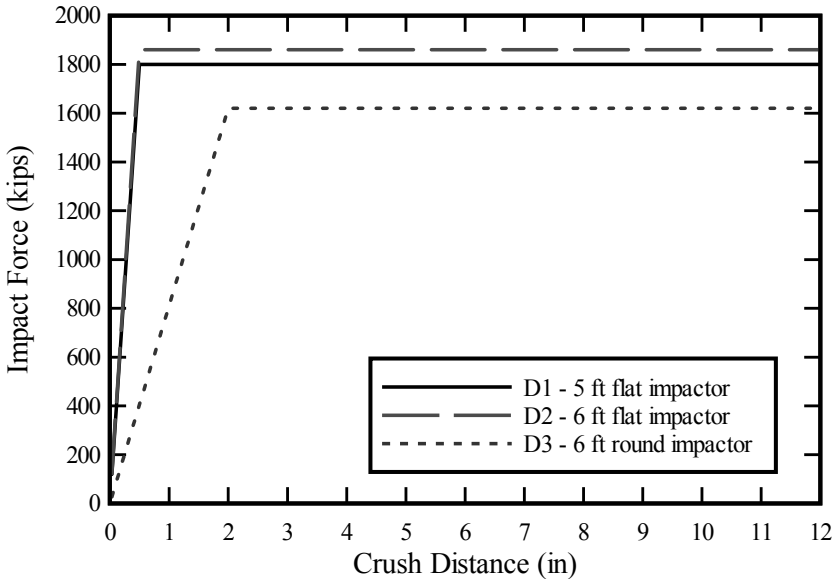

Figure 6.8 Barge force-deformation (crush) relationships employed in demonstration cases

The predictions of load duration (the time during which the barge and pier are in contact), common to both simplified and full-resolution analyses, are 0.14 sec, 0.59 sec, and 4.1 sec, respectively, for case D1, case D2, and case D3. At points in time greater than the respective load durations, each bridge is in an unloaded condition and undergoes damped free-vibration. Accordingly, pier response to time-history barge collision analysis may be divided into two phases: first a load-phase then a free-vibration phase. In all three demonstration cases, peak internal pier forces occur during the load-phase (0.085 sec, 0.14 sec, and 0.52 sec for case D1, case D2, and case D3, respectively). Therefore, agreement between the OPTS and full-resolution models is most critical during the load-phase, as forces obtained during this phase ultimately govern bridge pier member design. Simplified analysis retains the ability to accurately capture forces during the load-phase of response (Figure 6.9 through Figure 6.11 for each case, respectively). Peak shear forces generated by full-resolution and simplified analysis during the load-phase for each case differ by less than 3%. Reduced, yet still reasonable, agreement with respect to period of response and subsequent peak values of shear force occur during the free-phase of response for each case, however, such agreement is less critical and typically irrelevant for design purposes.

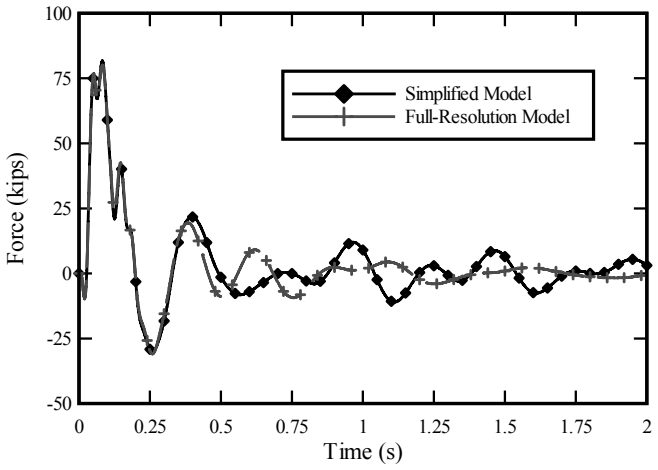

(a)

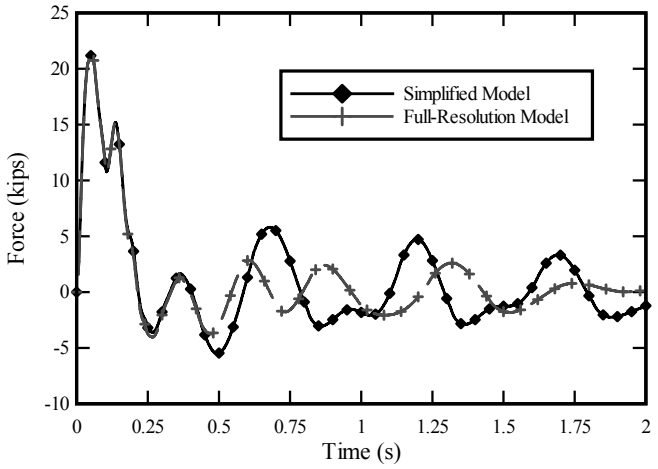

(b)

Figure 6.9 Comparison of case D1 simplified and full-resolution coupled analyses a) Pier column top node horizontal shear; b) Pile head node horizontal shear

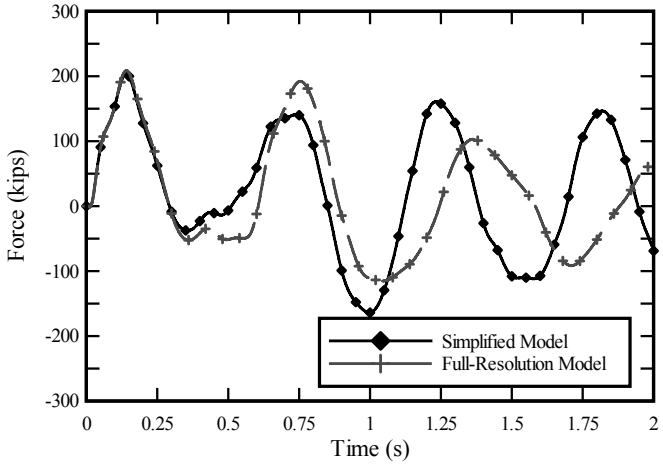

(a)

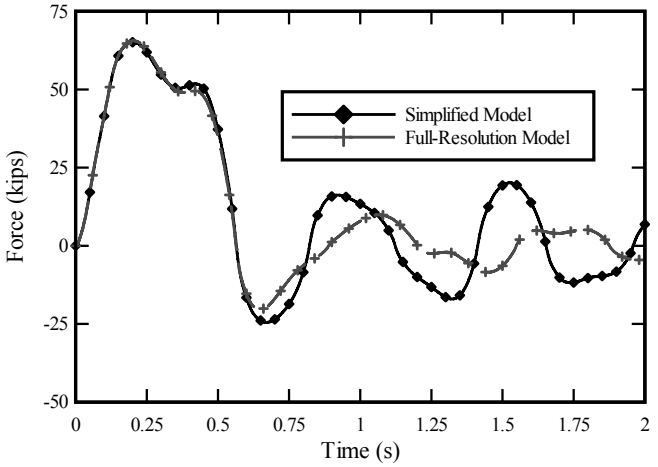

(b)

Figure 6.10 Comparison of case D2 simplified and full-resolution coupled analyses
a) Pier column top node horizontal shear; b) Pile head node horizontal shear

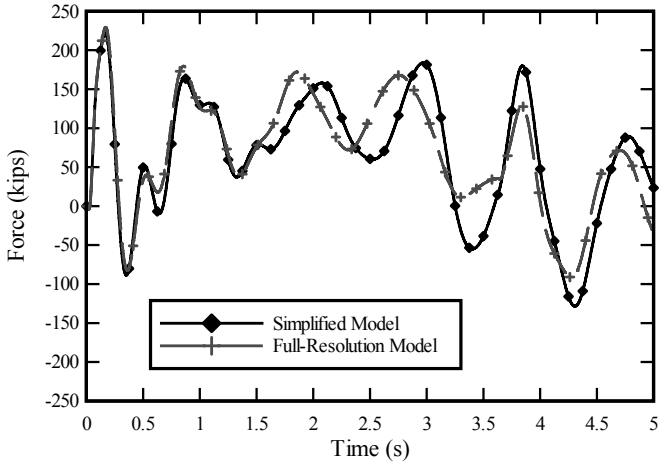

(a)

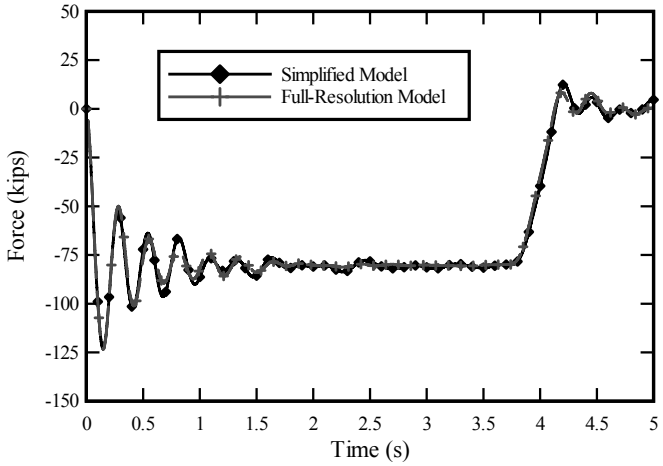

(b)

Figure 6.11 Comparison of case D3 simplified and full-resolution coupled analyses
a) Pier column top node horizontal shear; b) Pile head node horizontal shear

6.4.3 Analysis Time Requirements

Cases D1 through D3 were analyzed on a Dell Latitude D610 notebook computer using a single 2.13 GHz Intel PentiumM CPU and FB-MultiPier. The computation times necessary for analysis completion of the OPTS models were only 3%, 15%, and 6% of those required for the full-resolution models of cases D1 through D3, respectively (Figure 6.12). Hence, significant computational efficiency resulted from using the simplified analysis technique. Engineering judgment is required to determine the appropriate duration of analysis for a given bridge and impact condition; however, such analyses generally need not be conducted beyond the end of load-phase, as evidenced by the data shown in Figures 6.9

through 6.11. Conducting simplified coupled analyses for cases D1 through D3 only through the end of the load phases would require less than approximately 15 min of wall-clock time; well within reasonable limits required for use in practical bridge design.

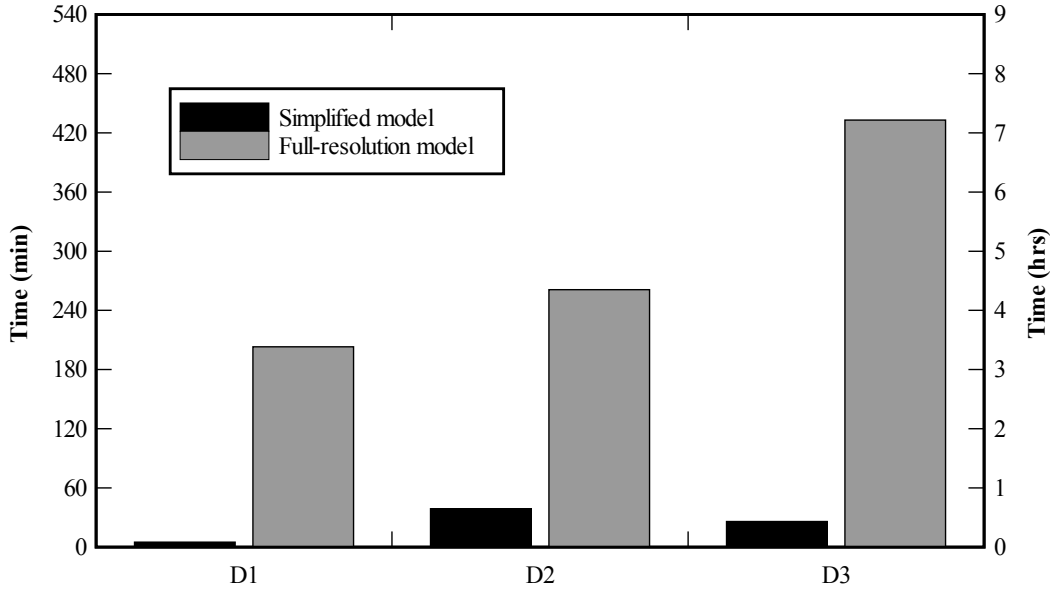

Figure 6.12 Time computation comparison of coupled analyses

6.4.4 Dynamic Amplification of Impacted Pier Column Forces

Application of the simplification algorithm to each of the demonstration cases inherently incorporates mass and acceleration based inertial forces that emerge from integration of the dynamic system equations of motion. The simplification algorithm accurately captures dynamic amplification of forces generated in the pier columns that would be absent from static analysis results. Dynamic amplification in each case may be quantified by considering the maximum pier column shears developed in models subjected to static application of the peak impact load predicted through the coupled analysis. The peak shear and moments developed in the pier due to static loading are then compared to those from the simplified and full-resolution dynamic analyses (Figure 6.13)

With respect to peak pier column structural demand, the dynamic analyses are in excellent agreement with each other for all cases. However, the peak magnitudes of the statically generated shears and moments, respectively, correspond to 54% and 69%, of the magnitude of the dynamically obtained counterparts for case D1; 27% and 31%, respectively, for case D2; and, 92% and 84% for case D3 (Figure 6.13). In each of these cases, a static analysis employing a dynamically obtained peak impact load leads to un-conservative predictions of peak pier column demand, as static analysis only encompasses stiffness considerations. In contrast, dynamic analyses incorporate both stiffness and inertial effects associated with the superstructure and therefore capture dynamic amplification of pier column forces due to the mass of the superstructure. Furthermore, the simplified procedure retains the ability to capture pier column force amplification as evidenced by the agreement between the simplified and full-resolution output pertaining to peak pier column demand.

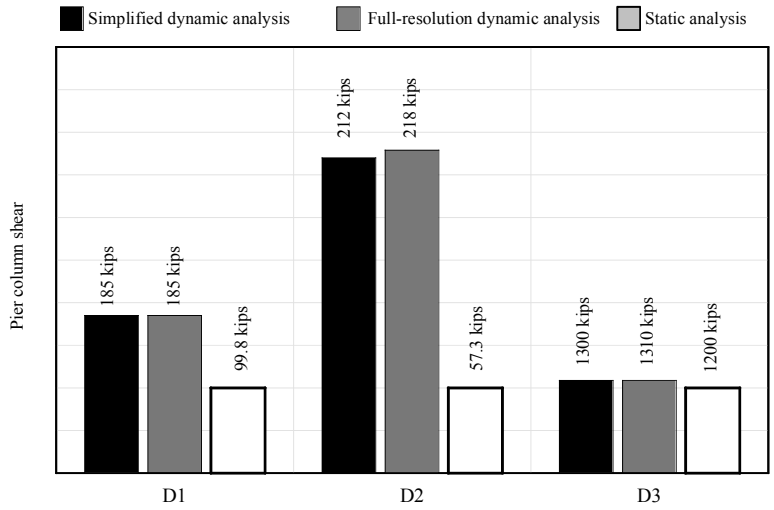

(a)

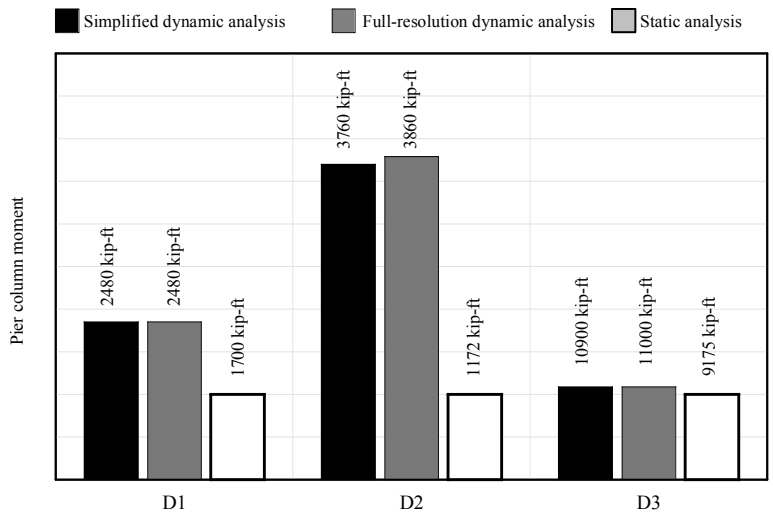

(b)

Figure 6.13 Comparison of demonstration case simplified, full-resolution, and static analyses a) Peak pier column shear; b) Peak pier column moment

CHAPTER 7
APPLIED VESSEL IMPACT LOAD HISTORY METHOD

7.1 Introduction

In previous chapters, a coupled vessel impact analysis (CVIA) procedure, which was implemented in FB-MultiPier, was validated against experimental data, and demonstrated for several different bridges. In a coupled analysis, the dynamic impact load is computed as part of the analysis procedure. In this chapter, an alternative analysis approach is presented in which an approximate time history of impact force is generated using characteristics of the vessel (barge mass, initial velocity, and bow force-deformation relationship). The approximate time history of impact load is then externally applied to the bridge structure, and a traditional (non-coupled) dynamic analysis is performed to determine member design forces. As in previous chapters, all models analyzed herein contain linear structural elements with nonlinear soil stiffness springs.

7.2 Development of Load Prediction Equations

The equations from which the load history is calculated are based upon the principles of conservation of energy and conservation of linear momentum. Development of the applied vessel impact load (AVIL) equations is based primarily on characteristics of the barge, although basic bridge structure characteristics are also incorporated.

7.2.1 Prediction of Peak Impact Load from Conservation of Energy

The first step in calculating the impact load time history is to determine the peak dynamic load to which the structure is subjected using the principle of conservation of energy. Assuming that the system is not sensitive to changes in temperature, conservation of energy for the system can be expressed as follows:

$$\Delta KE_{if} + \Delta DE_{if} = 0 \tag{7.1}$$

where ΔKE_{if} is the change in kinetic energy of the barge, and ΔDE_{if} is the change in total deformation energy (i.e. the sum of the elastic and plastic deformation energies), associated with the deformation of the barge bow, from the initial state (i) to the final state (f). Conservation of energy is used to define a relationship between the peak impact load, and the barge parameters.

Assuming that the change in mass of the barge is negligible, the change in barge kinetic energy can be expressed by the following relation:

$$\Delta KE_{if} = 1/2\, m_B \left(v_{Bf}^2 - v_{Bi}^2 \right) \tag{7.2}$$

where m_B is the constant (unchanging) mass of the barge and v_{Bf} and v_{Bi} are the magnitudes of the barge velocities at the initial and final states respectively.

In general, the deformation energy for the barge can be described using the following relation:

$$\Delta DE_{if} = \int_{a_{Bi}}^{a_{Bf}} P_B(a_B)da_B \tag{7.3}$$

where $P_B(a_B)$ is the impact force as a function of barge crush depth (a_B), and a_{Bi} and a_{Bf} are the barge crush depths at the initial and final states respectively.

To calculate the peak impact load on the pier, the following assumptions are made: 1.) the pier is assumed to be rigid and fixed in space, 2.) the initial barge crush depth (a_{Bi}) is assumed to be zero, and 3.) the barge bow force-deformation relationship is assumed to be elastic perfectly-plastic (Figure 7.1).

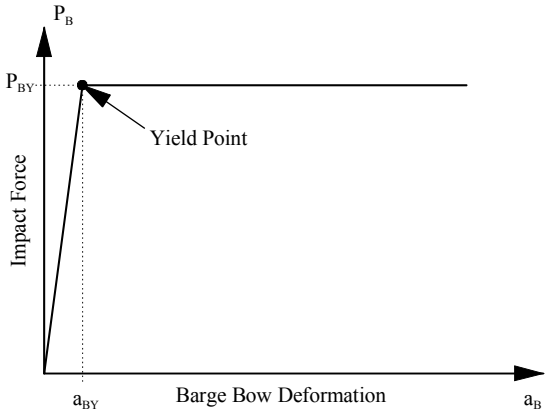

Figure 7.1 Barge bow force-deformation relationship

The first assumption implies that the initial kinetic energy of the barge is fully converted into deformation energy of the barge bow during loading of the barge (Figure 7.2a). Thus, once all of the barge initial kinetic energy has been converted into deformation of the barge bow (i.e. the barge velocity becomes zero) the barge bow crush depth has reached its maximum value. Additionally, when the barge bow recovers the elastic portion of its deformation energy through unloading, this energy is then converted back into rebound motion of the barge (Figure 7.2b). Final barge kinetic energy can then be determined from the recovered deformation energy.

If the barge bow remains linear and elastic, the conservation of energy up to the point of maximum barge bow deformation can be represented by the following equation:

$$\Delta KE_{im} + \Delta DE_{im} = -1/2 \cdot m_B \cdot v_{Bi}^2 + 1/2 \cdot P_{Bm} \cdot a_{Bm} = 0 \tag{7.4}$$

where P_{Bm} is the maximum impact force observed during the impact, and a_{Bm} is the maximum barge bow deformation. The maximum impact force and barge bow deformation however, remain undetermined up this point, and thus, an additional equation is required.

If the barge bow remains elastic, the maximum bow deformation can be defined as follows:

$$a_{Bm} = \frac{P_{Bm}}{k_B} = \frac{P_{Bm}}{(P_{BY}/a_{BY})} \tag{7.5}$$

where a_{BY} and P_{BY} are the barge bow deformation and force at yield, respectively, and k_B is the initial elastic stiffness of the barge bow. Combining Equations 7.4 and 7.5, and then solving for the peak load produces the following equation:

$$P_{Bm} = v_{Bi}\sqrt{\frac{P_{BY}}{a_{BY}}m_B} = v_{Bi}\sqrt{k_B m_B} \le P_{BY} \tag{7.6}$$

Due to the elastic perfectly-plastic assumption for the barge bow force-deformation relationship, the peak barge impact force is limited to the yield load of the barge bow.

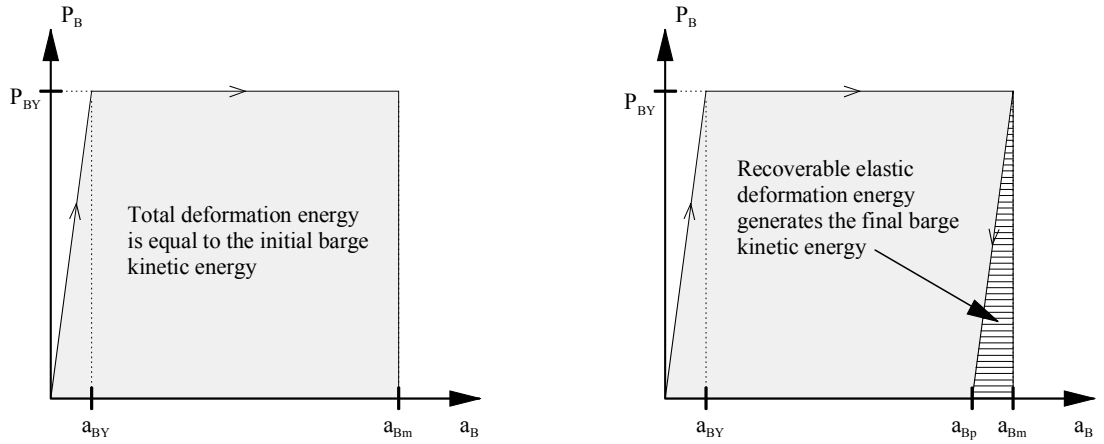

(a) (b)

Figure 7.2 Inelastic barge bow deformation energy: a) Loading, and b) Unloading

To validate Equation 7.6, the central difference method was used to analyze a two degree-of-freedom barge-pier-soil system (Figure 7.3) subjected to various impact conditions. For these analyses, barge bow contact was modeled as a nonlinear spring using an elastic perfectly plastic force-deformation relationship (Figure 7.1), and the pier-soil resistance was approximated using a linear-elastic spring. For each analysis, the barge weight was varied from 250 tons to 8000 tons, and the initial velocity was varied from 0.5 knots to 10 knots. From the analysis results, the maximum impact force generated between the barge and the pier was extracted for each case. Additionally, Equation 7.6 was used to predict peak barge impact forces for each case.

As shown in Figure 7.4, although conservative, the estimate of peak forces as predicted by Equation 7.6 are not in very good agreement with coupled analysis results. Referring to Equation 7.6, it is noted that the ratio of the barge yield load to the barge bow yield deformation represents the initial elastic stiffness of the system, assuming that the pier is rigid. However, recalling Figure 7.3, the barge bow spring is in series with the pier-soil spring. Thus, if a linear pier-soil spring is introduced and combined with the barge bow spring in series, an effective barge-pier-soil spring stiffness can be defined as follows:

$$k_S = \left(\frac{1}{k_B} + \frac{1}{k_P}\right)^{-1} = \left(\frac{a_{BY}}{P_{BY}} + \frac{1}{k_P}\right)^{-1} \tag{7.7}$$

where k_P is the linear pier-soil spring stiffness.

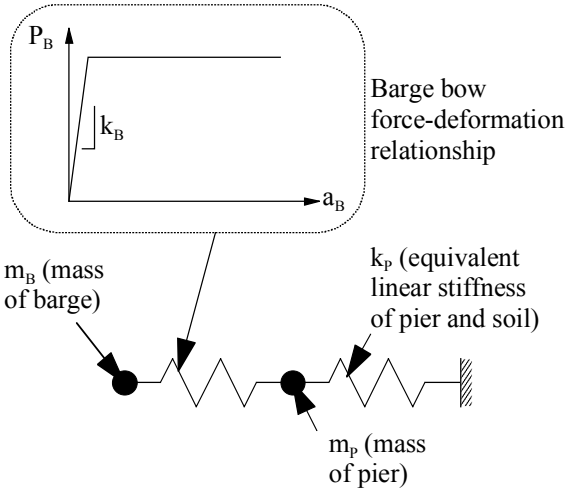

Figure 7.3 Two degree-of-freedom barge-pier-soil model

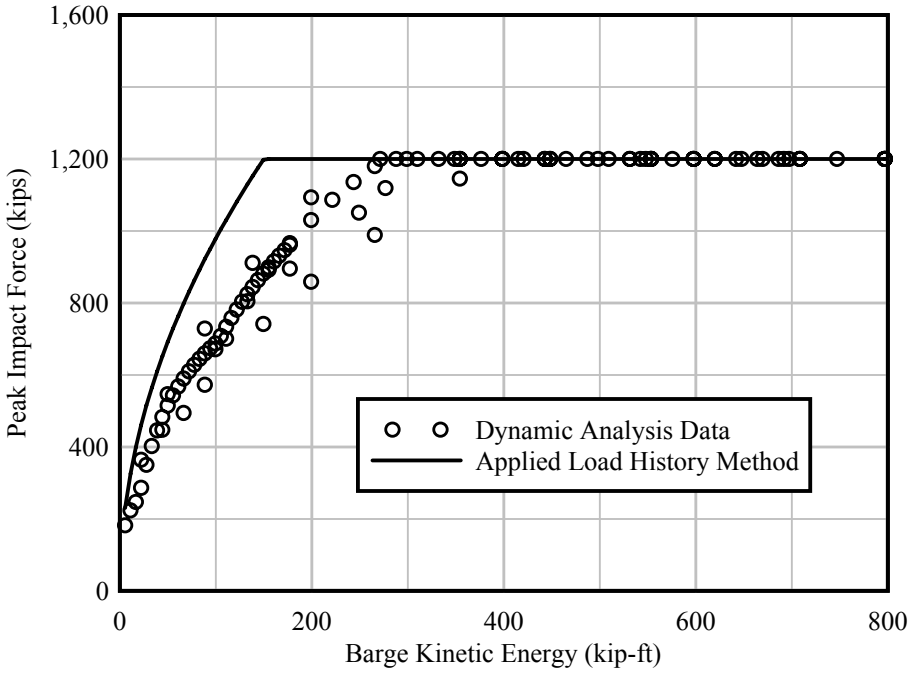

Figure 7.4 Peak impact force vs. initial barge kinetic energy using a rigid pier assumption

Replacing the initial elastic barge stiffness (k_B) in Equation 7.6 with the effective barge-pier-soil series spring stiffness (k_S) (Equation 7.7) produces the following equation:

$$P_{Bm} = v_{Bi}\sqrt{k_S m_B} = v_{Bi} \cdot c_{BP} \le P_{BY} \tag{7.8}$$

where c_{BP} is the barge-pier pseudo-damping coefficient, defined as follows:

$$c_{BP} = \sqrt{k_S m_B} \tag{7.9}$$

Using Eqn. 7.8 in place of Eqn. 7.6 to predict the peak impact load imparted to the pier, and comparing the results to two-DOF coupled time-integrated dynamic analysis results, good agreement between the two methods (Figure 7.5) is observed.

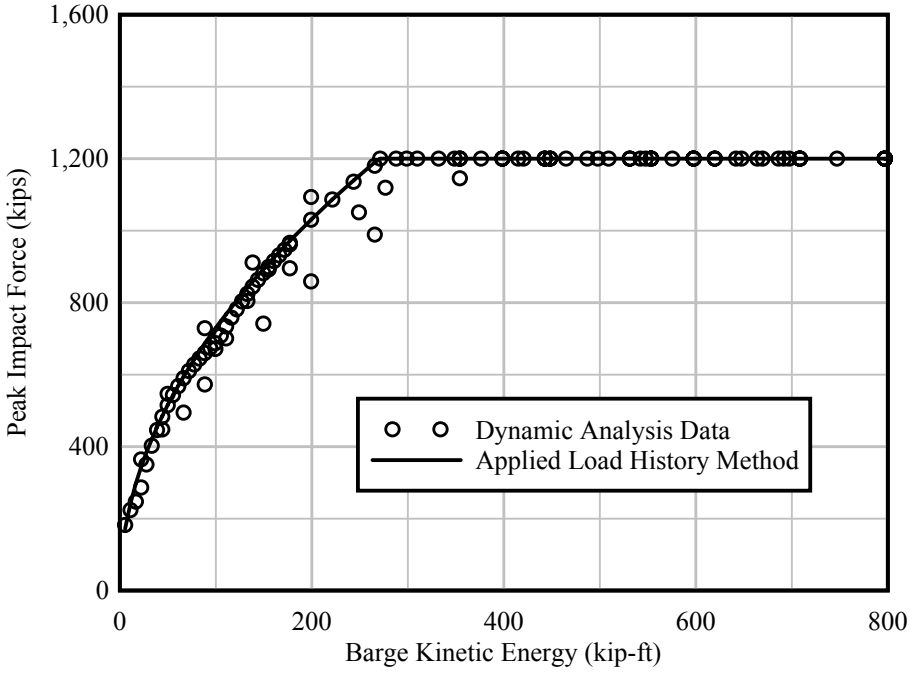

Figure 7.5 Peak impact force vs. initial barge kinetic energy using an effective barge-pier-soil stiffness

With the peak impact load calculated, the final barge velocity after impact can now be calculated using the unloading characteristics of the barge bow. It is assumed that unloading of the barge bow occurs along a path that has a slope equal to the initial elastic barge stiffness (Figure 7.2b). Using this assumption, the conservation of energy equation from the point of maximum barge bow deformation to the point at which the barge and pier are out of contact can be written as follows:

$$\Delta KE_{mf} + \Delta DE_{mf} = 1/2 \cdot m_B \cdot v_{Bf}^2 + 1/2 \cdot P_{Bm} \cdot (a_{BP} - a_{Bm}) = 0 \tag{7.10}$$

where v_{Bf} is the final barge velocity and a_{BP} is the plastic barge bow crush depth (Figure 7.2b). Note that in Equation 7.10, the final barge velocity and the plastic crush are unknown. However, it is not necessary to actually calculate the plastic crush depth. It is only necessary to know that the difference between the plastic and maximum barge bow deformations, which is the same as the initial elastic portion of the barge-bow crush, and thus:

$$(a_{Bm} - a_{BP}) = \frac{P_{Bm}}{k_B} \tag{7.11}$$

Then, combining Equations 7.10 and 7.11, and solving for the final barge velocity produces the following:

$$v_{Bf} = P_{Bm}\sqrt{\frac{1}{k_B m_B}} \tag{7.12}$$

Replacing the initial elastic barge stiffness (k_B) with the effective barge-pier-soil stiffness (k_S) and introducing the barge-pier-soil pseudo-damping coefficient ($c_{BP}=\sqrt{k_S m_B}$), the final barge velocity can be approximated as follows:

$$v_{Bf} = P_{Bm}\sqrt{\frac{1}{k_S m_B}} = \frac{P_{Bm}}{c_{BP}} \tag{7.13}$$

For the situation in which the barge bow yields, the velocity at initial yield must be calculated. Conservation of energy from initial state to yield can be expressed as:

$$\Delta KE_{iy} + \Delta DE_{iy} = 1/2 \cdot m_B\left(v_{BY}^2 - v_{Bi}^2\right) + 1/2 \cdot P_{BY} \cdot a_{BY} = 0 \tag{7.14}$$

where v_{BY} is the barge velocity at yield. Solving for this velocity using Equation 7.14 the velocity at yield can be expressed as:

$$v_{BY} = \sqrt{v_{Bi}^2 - \frac{P_{BY} a_{BY}}{m_B}} \tag{7.15}$$

Next, multiplying the numerator and denominator of the second term within the square-root, and simplifying the equation results in the following:

$$v_{BY} = \sqrt{v_{Bi}^2 - \frac{P_{BY} a_{BY}}{m_B} \cdot \frac{P_{BY}}{P_{BY}}} = \sqrt{v_{Bi}^2 - \frac{P_{BY}^2}{k_B m_B}} \tag{7.16}$$

Again, replacing the initial elastic barge stiffness (k_B) with the effective barge-pier-soil stiffness (k_S) and introducing the barge-pier-soil pseudo-damping coefficient (c_{BP}), the barge velocity at yield can be approximated as follows:

$$v_{BY} = \sqrt{v_{Bi}^2 - \frac{P_{BY}^2}{k_S m_B}} = \sqrt{v_{Bi}^2 - \left(\frac{P_{BY}}{c_{BP}}\right)^2} \tag{7.17}$$

7.2.2 Prediction of Load Duration from Conservation of Linear Momentum

The next step in calculating the impact load history is to determine the duration of time that the load will act on the structure. This is accomplished by using the principle of conservation of linear momentum:

$$\{\Delta L_{if}\} = \{I\} \tag{7.18}$$

where $\{\Delta L_{if}\}$ is the vector change of barge linear momentum from the initial state to the final state, and $\{I\}$ is the load impulse. Assuming that the mass of the barge does not change, the change in barge linear momentum can be expressed as:

$$\{\Delta L_{if}\} = m_B(\{v_{Bf}\} - \{v_{Bi}\}) \tag{7.19}$$

where $\{v_{Bf}\}$ and $\{v_{Bi}\}$ are the barge velocity vectors at the final and initial states respectively. In general, the load impulse for the barge can be defined as:

$$\{I\} = \int_{t_i}^{t_f} \{P_B(t)\}dt \tag{7.20}$$

where $\{P_B(t)\}$ is the vector impact force as a function of time (t), t_i is the initial time at which impact occurs, and t_f is the final time at which the impact ends and the impact force becomes zero.

Although momentum and impulse are vector quantities, the analysis method used here is one-dimensional. Therefore, the vector notation can be dropped by taking into consideration that final barge velocity will have a negative sign when the barge moves away from the pier following impact. Additionally, the impact force on the barge will have a negative sign since it acts opposite to the direction of the initial barge motion. Taking these facts into account, the conservation of linear momentum can be rewritten as:

$$m_B(v_{Bf} + v_{Bi}) = \int_{t_i}^{t_f} P_B(t)dt \tag{7.21}$$

If the barge bow remains elastic for the duration of the analysis, it is assumed that the elastic load history pulse takes the shape of a half-sine wave (Figure 7.6a). Assuming that the analysis starts at 0 secs (t_i = 0 secs), the impulse of the impact force between the barge and the pier can be calculated as:

$$\int_0^{t_E} P_{Bm} \sin\left(\pi \frac{t}{t_E}\right)dt = \frac{2}{\pi} t_E \cdot P_{Bm} \tag{7.22}$$

where t_E is the duration of loading for an elastic pulse. Combining Equations 7.21 and 7.22, and solving for the elastic load duration:

$$t_E = \frac{\pi m_B}{2P_{Bm}}(v_{Bf} + v_{Bi}) \tag{7.23}$$

Comparing Eqn. 7.8 and 7.13, the final velocity of the barge is equal to the initial barge velocity when the barge bow remains elastic, and thus Eqn. 7.23 becomes:

$$t_E = \frac{\pi m_B}{P_{Bm}} v_{Bi} \tag{7.24}$$

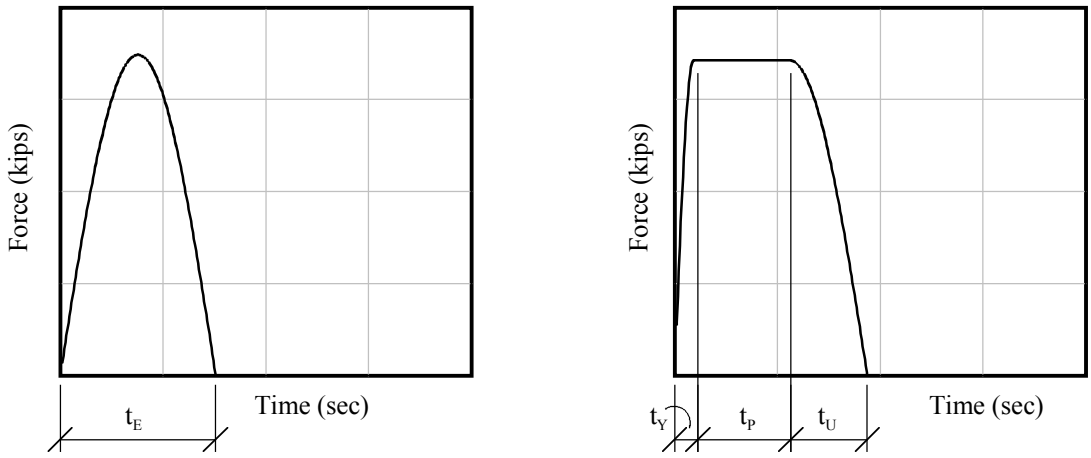

(a) (b)

Figure 7.6 Impact load histories: a) Elastic loading, and b) Inelastic loading

For situations in which the barge bow yields, the load history is subdivided into three distinct stages: 1.) elastic loading to yield, 2.) plastic loading, and 3.) elastic unloading (Figure 7.6b). The time history of elastic loading to yield is assumed to take the shape of a quarter-sine wave (Figure 7.7). For the purpose of calculating the time required to yield the barge bow, it is assumed that the analysis starts at 0 secs (t_i = 0 secs). The elastic loading portion of the load impulse can be calculated as:

$$\int_0^{t_Y} P_{BY} \sin\left(\pi \frac{t}{2t_Y}\right) dt = \frac{2}{\pi} t_Y \cdot P_{BY} \tag{7.25}$$

where t_Y is the time required to yield the barge bow.

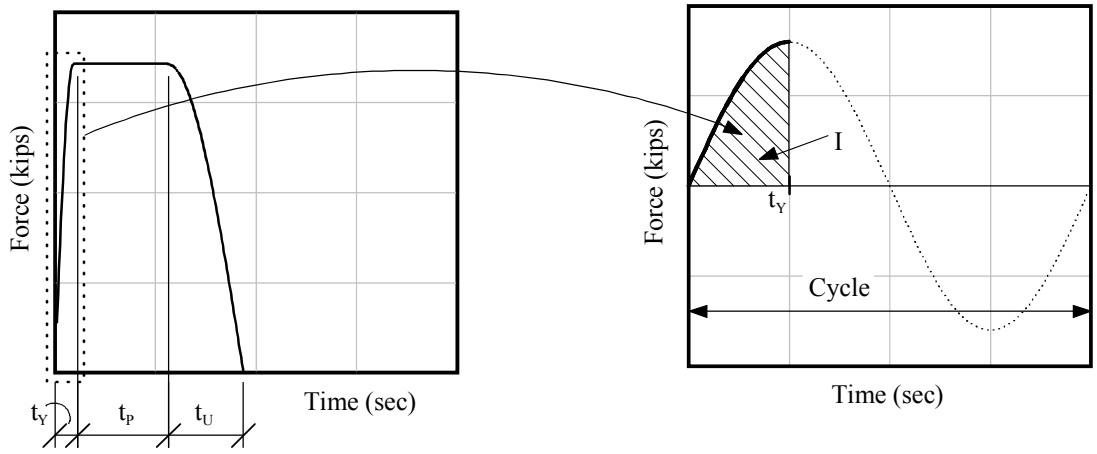

Figure 7.7 Construction of loading portion of impact force

Using Equation 7.25 and the conservation of linear momentum the following relationship can be defined:

$$m_B\left(v_{Bi} - v_{BY}\right) = \frac{2}{\pi} t_Y \cdot P_{BY} \tag{7.26}$$

This equation accounts for the fact that the impact force acts in the opposite direction of the initial motion of the barge, and that the barge velocity at yield acts in the same direction as the initial barge velocity. Solving Equation 7.26 for the time to yield gives:

$$t_Y = \frac{\pi m_B}{2P_{BY}}\left(v_{Bi} - v_{BY}\right) = \frac{\pi m_B}{2P_{BY}}\left(v_{Bi} - \sqrt{v_{Bi}^2 - \left(\frac{P_{BY}}{c_{BP}}\right)^2}\right) \tag{7.27}$$

Following the initial elastic loading stage, an inelastic stage occurs. During this latter stage, the plastic load is assumed to remain constant from the time at which the barge bow yields to the time at which unloading of the barge bow begins. The load impulse for this stage is given by:

$$\int_{t_Y}^{t_Y + t_P} P_{BY} dt = P_{BY} \cdot t_P \tag{7.28}$$

where t_P is the duration of plastic loading.

Taking into account the direction of the impact force, and assuming that the velocity of the barge immediately before the barge bow unloads is zero, the conservation of linear momentum can be defined as follows:

$$m_B \cdot v_{BY} = P_{BY} \cdot t_P \tag{7.29}$$

The assumption that the velocity of the barge immediately before the barge bow unloads is zero is valid because, the deformation of the pier-soil system is much lower than the inelastic barge bow deformation. Solving Equation 7.29 for the plastic load duration:

$$t_P = \frac{m_B \cdot v_{BY}}{P_{BY}} = \frac{m_B}{P_{BY}}\sqrt{v_{Bi}^2 - \left(\frac{P_{BY}}{c_{BP}}\right)^2} \tag{7.30}$$

Following the plastic loading stage, the time history of elastic unloading is assumed to take the shape of the second quarter of a single sine wave cycle (Figure 7.8):

$$\int_0^{t_U} P_{BY} \sin\left(\pi \frac{t}{2t_U}\right) dt = \frac{2}{\pi} t_U \cdot P_{BY} \tag{7.31}$$

where t_U is the duration of unloading.

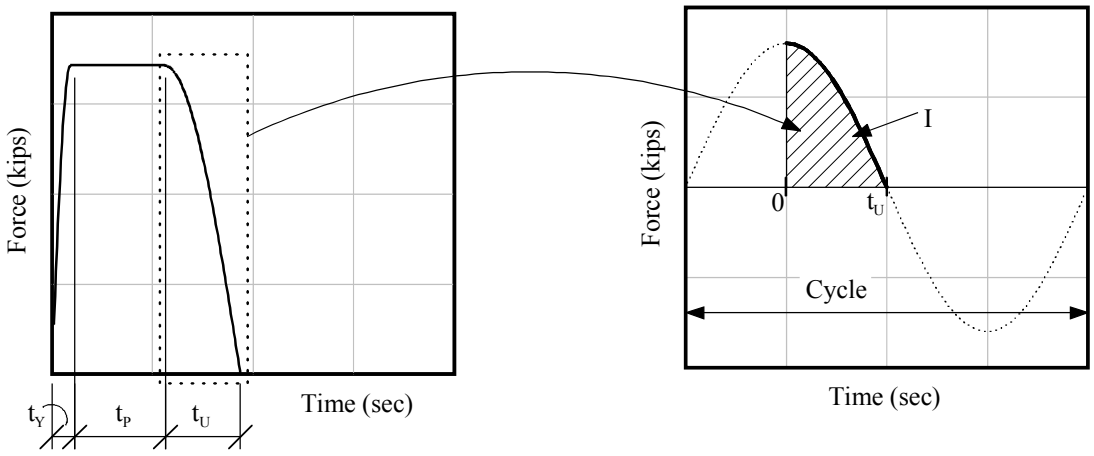

Figure 7.8 Construction of unloading portion of impact force

Assuming that the barge velocity at the beginning of the unloading stage is zero, and that the impact load acts in the same direction as the final barge velocity, conservation of linear momentum can be expressed as:

$$m_B \cdot v_{Bf} = \frac{2}{\pi} t_U \cdot P_{BY} \tag{7.32}$$

Rearranging Equation 7.32, the duration of unloading is given by:

$$t_U = \frac{\pi m_B}{2P_{BY}} v_{Bf} = \frac{\pi m_B}{2P_{BY}} \frac{P_{BY}}{c_{BP}} \tag{7.33}$$

Additionally, summing Eqns. 7.27, 7.30, and 7.33, the total duration for inelastic loading is defined as:

$$t_T = \frac{\pi m_B}{2P_{Bm}} \left(v_{Bi} + \frac{P_{BY}}{c_{BP}} + \left(\frac{2}{\pi} - 1 \right) \sqrt{v_{Bi}^2 - \left(\frac{P_{BY}}{c_{BP}} \right)^2} \right) \tag{7.34}$$

7.2.3 Summary of Procedure for Constructing an Impact Load History

Using key equations from the detailed derivations given in the sections above, a summary of the complete procedure for constructing an impact load time-history function is presented (Figure 7.9). The curves presented in Figure 7.9 are time-varying impact forces that may be applied to a bridge structure in a dynamic sense. Although the AVIL method is not exact, it is expected that it will approximate the CVIA well.

7.3 Validation of the Applied Vessel Impact Load History Method

To assess the accuracy of the AVIL method, three coupled dynamic analyses were conducted on a one-pier two-span (OPTS) model of a new St. George Island Causeway

Bridge channel pier and the connecting two superstructure spans (Davidson 2007). The three cases selected represent low, moderate, and high energy impacts respectively (Table 7.1). Comparing each case to the current AASHTO provisions (Figure 7.10) indicates that the low-energy analysis represents a situation in which the barge bow remains elastic throughout the duration of impact; the moderate-energy case represents a situation in which the barge bow deformation is slightly larger than the yield deformation (according to AASHTO); and the high-energy case exhibits significant barge bow yielding.

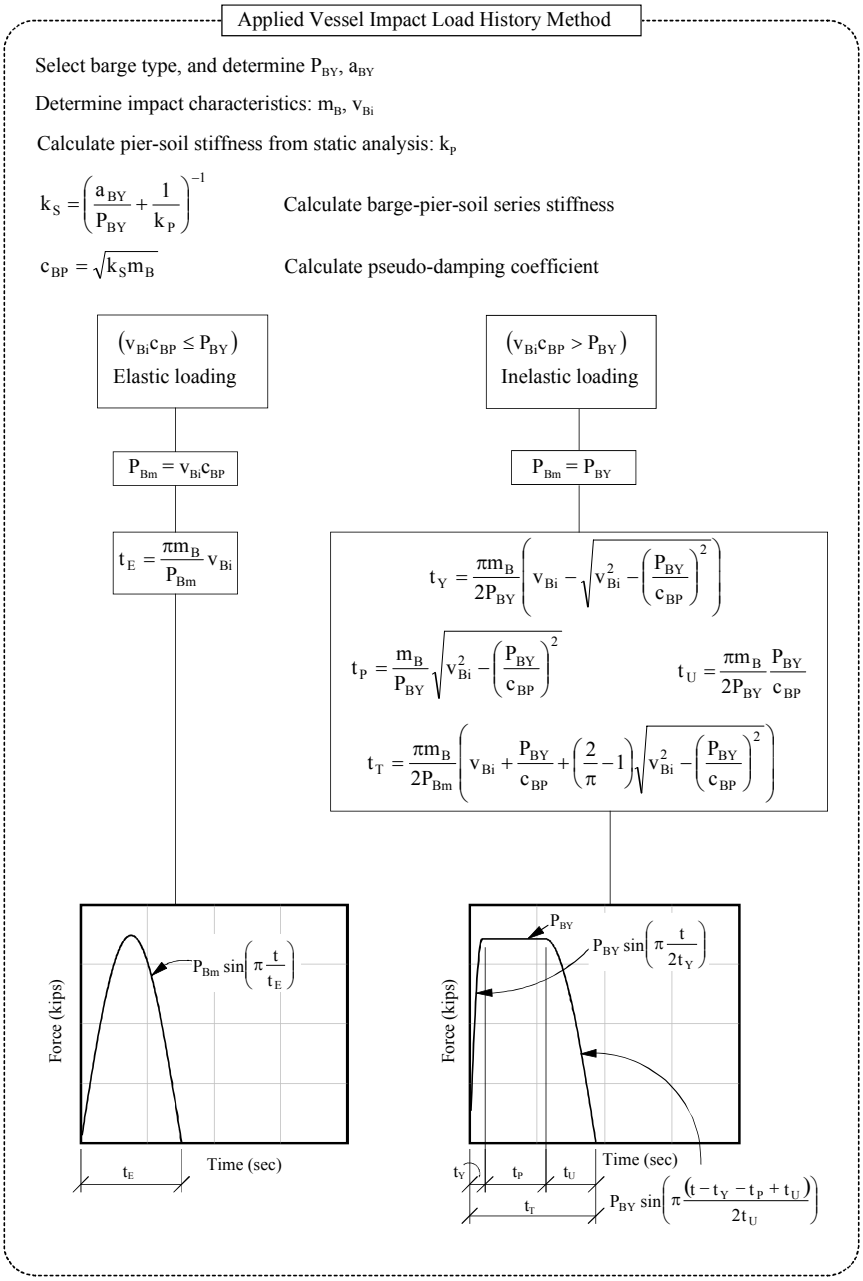

Figure 7.9 AVIL procedure

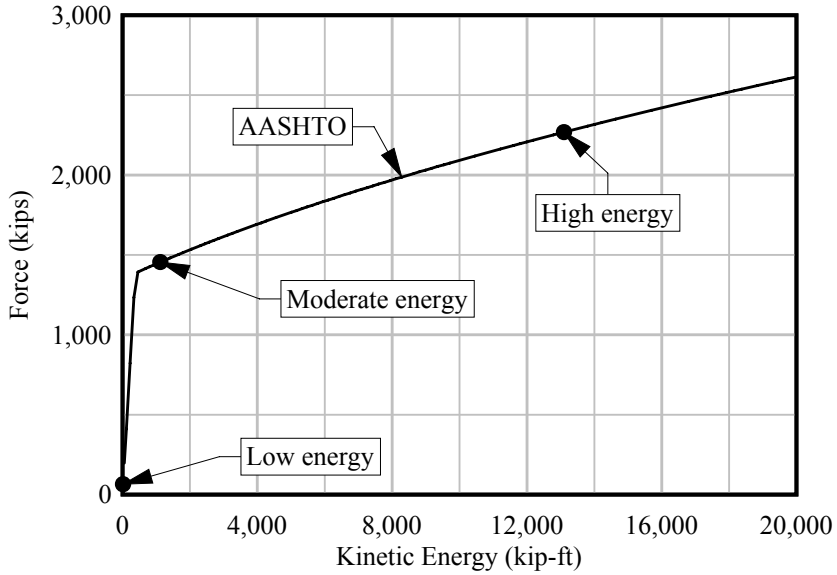

Figure 7.10 AASHTO load curve indicating barge masses and velocities used in validating the applied load history method

Table 7.1 Impact energies for AVIL validation

Energy	Barge weight (tons)	Barge velocity (knot)	Impact-energy (kip-ft)
Low	200	1	17.71
Moderate	2030	2.5	1123
High	5920	5	13100

The force-deformation relationship for the barge is dependent upon the size and shape of the impacted pier column. Pier columns for channel piers of the new St. George Island Causeway Bridge are round with a 6-foot diameter. Thus, using Equation 4.8, the yield load and bow deformation at yield for the barge are 1620 kips and 2 in respectively (Figure 7.11).

For each collision analysis, the impact load history computed using coupled analysis was compared to the load history predicted by the AVIL method. Comparisons between the CVIA force history results and the AVIL results are presented in Figure 7.12. For the low-energy case (Figure 7.12a), the AVIL method predicts a slightly higher peak load and a slightly longer load duration than is predicted by coupled analysis. Comparing the load impulses for each analysis—44 kip-sec and 37 kip-sec for the AVIL and coupled analysis methods respectively—reveals that the two differ by about fifteen percent.

The moderate-energy force history comparison (Figure 7.12b) shows good agreement between the coupled analysis and the AVIL method. Comparing the load impulses for this case—771 kip-sec and 721 kip-sec for the AVIL and CVIA respectively—indicates that the AVIL method over-predicts the load impulse by about seven percent.

Inspecting the results for the high-energy impact (Figure 7.12c), there is a negligible discrepancy in the load histories predicted by the AVIL and CVIA methods. Load impulses for the two methods—3628 kip-sec versus 3431 kip-sec for the AVIL and CVIA methods respectively—reveals that the two methods differ by about six percent.

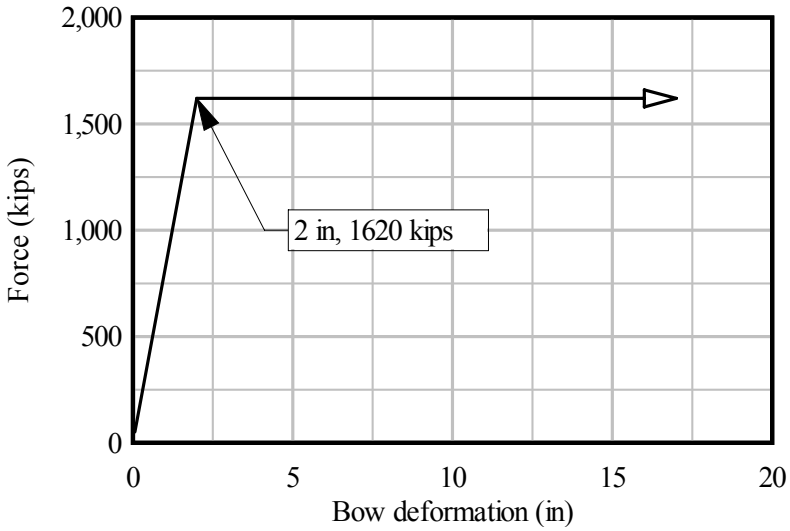

Figure 7.11 Barge bow force-deformation relationship for an impact on a six-foot round column

Comparisons of the maximum bending moments from dynamic analyses performed using the two methods are presented in Table 7.2 and Figure 7.13. Moments in Figure 7.13 represent the maximum absolute bending moment throughout the duration of the analysis at a given elevation across all pier columns or all piles, whereas values in Table 7.2 are the maximum absolute bending moments for all piles or columns in the model, regardless of elevation. However, it must be noted that numerical analysis results for elevations within the pile cap thickness are not meaningful due to the manner in which FB-MultiPier models both the pile cap and the connections of the pier columns to the pile cap. For this reason, Figure 7.13 is formatted such that straight-lines connect the individual response profiles immediately above and below elevations that lie within the pile cap thickness.

Inspection of Table 7.2 and Figure 7.13 reveals that pile and column moments from the AVIL analysis agree well with the CVIA results. Additionally, for the low and high impact energy conditions, the AVIL method produces moments that are slightly conservative in comparison to the coupled analysis moment results.

Table 7.2 Maximum moments in all pier columns and piles

Impact energy	Location	Moment (kip-ft)		
		CVIA	AVIL	Percent difference
Low	Column	1541	1609	4.4%
	Pile	453.4	480.9	6.1%
Moderate	Column	5288	5028	-4.9%
	Pile	1488	1428	-4.0%
High	Column	5307	5309	0.0%
	Pile	1515	1518	0.2%

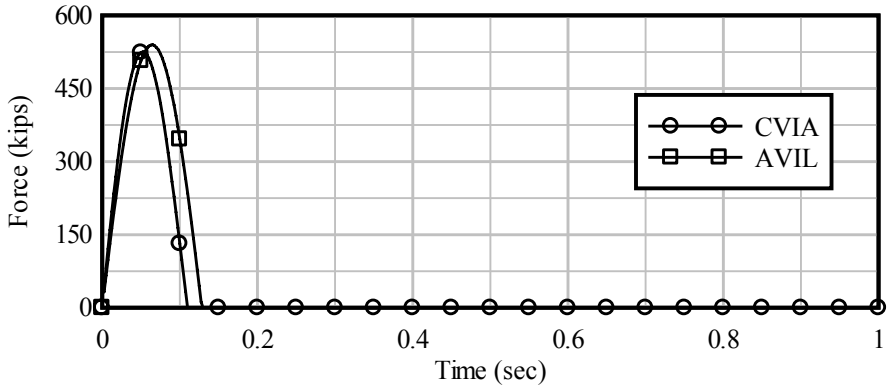

(a)

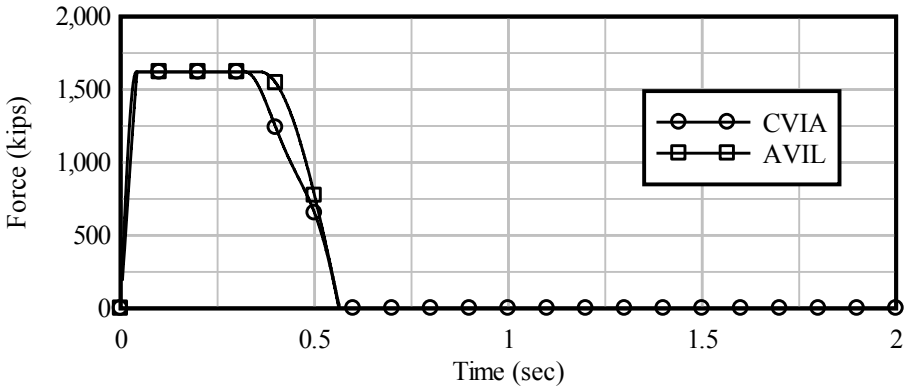

(b)

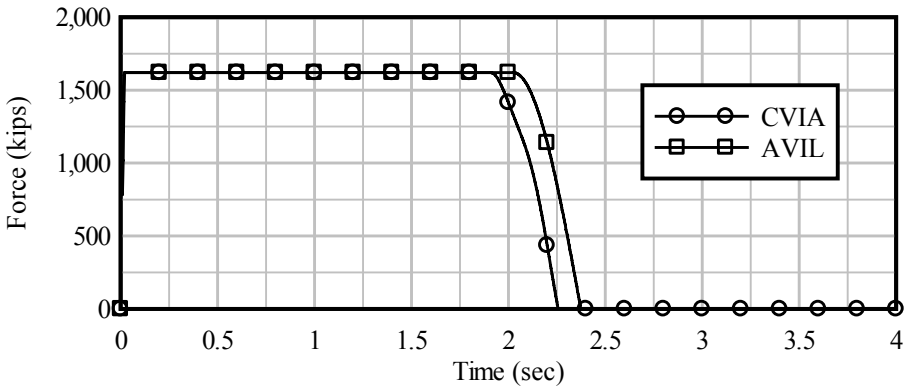

(c)

Figure 7.12 Impact load history comparisons: a) Low-energy impact, b) Moderate-energy impact, and c) High-energy impact

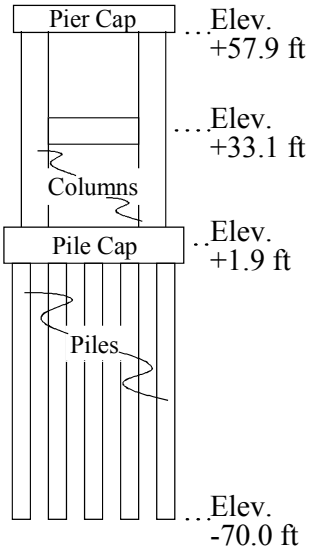

(a)

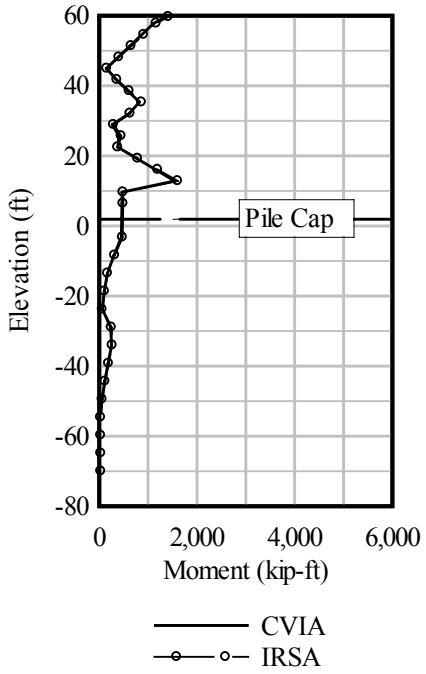

(b)

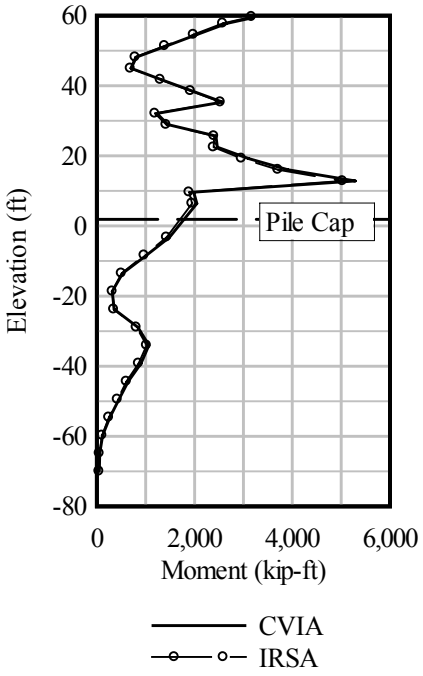

(c)

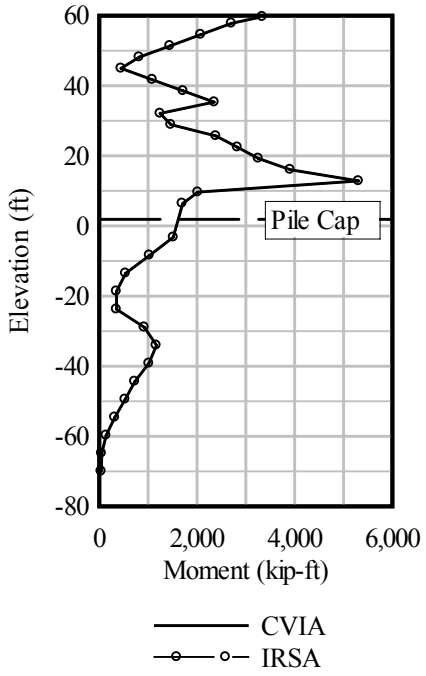

(d)

Figure 7.13 Moment results profile for the new St. George Island Causeway Bridge channel pier: a) Channel pier schematic, b) Low-energy impact, c) Moderate-energy impact, and d) High-energy impact

CHAPTER 8
IMPACT RESPONSE SPECTRUM ANALYSIS (IRSA) METHOD

8.1 Introduction

In previous chapters, the dynamic response of the bridge structure (Figure 8.1) was computed using time history impact analysis techniques. These techniques used numerical time-step integration to obtain a solution to the equation of motion:

$$[M]\{\ddot{u}(t)\}+[C]\{\dot{u}(t)\}+[K]\{u(t)\}=\{F(t)\} \tag{8.1}$$

In this equation, [M], [C], and [K] are the mass, damping, and stiffness matrices, respectively, of the structure; {F(t)} is the time varying external force vector; and {u(t)}, $\{\dot{u}(t)\}$, and $\{\ddot{u}(t)\}$ are the time varying displacement, velocity, and acceleration vectors, respectively. An alternative dynamic analysis technique that does not require time-integration is the response spectrum analysis technique. Response spectrum analysis is carried out using structural vibration characteristics such as mode shapes and frequencies and involves estimating the maximum dynamic structural response rather than computing the response at each point in time. In this chapter, a response spectrum analysis technique that is suitable for analyzing dynamic barge impact conditions is presented, validated, and demonstrated.

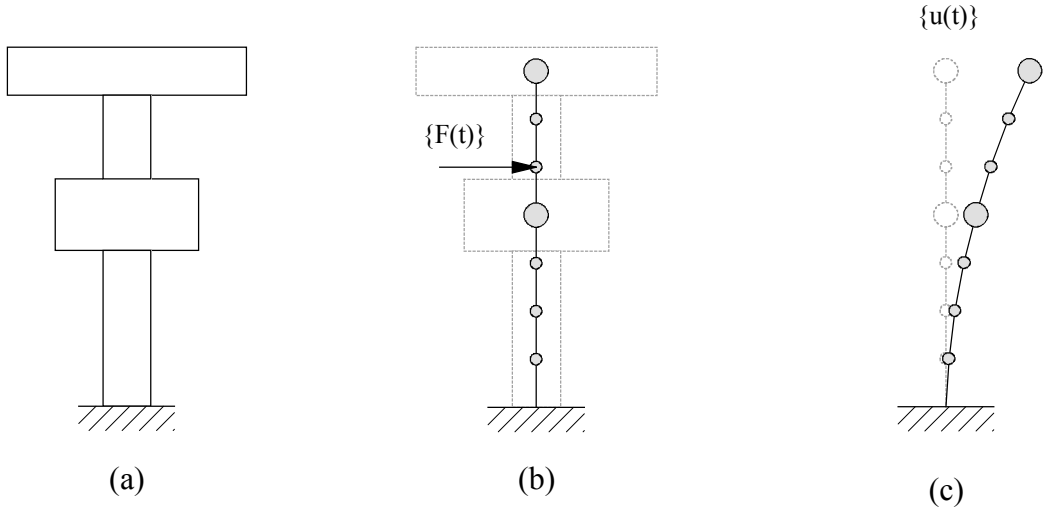

Figure 8.1 Time history analysis of a structure: a) Structure, b) Finite element model of structure, and c) Displaced shape of structural model

8.2 Response Spectrum Analysis

In order to conduct a response spectrum analysis, the numerical model must be transformed from the structural system to the modal system. This process is generally achieved through the use of an eigenanalysis, from which structural vibration characteristics are obtained. Using the eigenanalysis results, the multiple degree-of-freedom (MDOF) structural system matrices, forces, and displacements can be transformed into single degree-of-freedom (SDOF) modal properties, forces (P_i), and displacements (q_i) for each mode

(Figure 8.2). Once the model has been transformed into modal coordinates, an analysis on the modal equations of motion can be conducted.

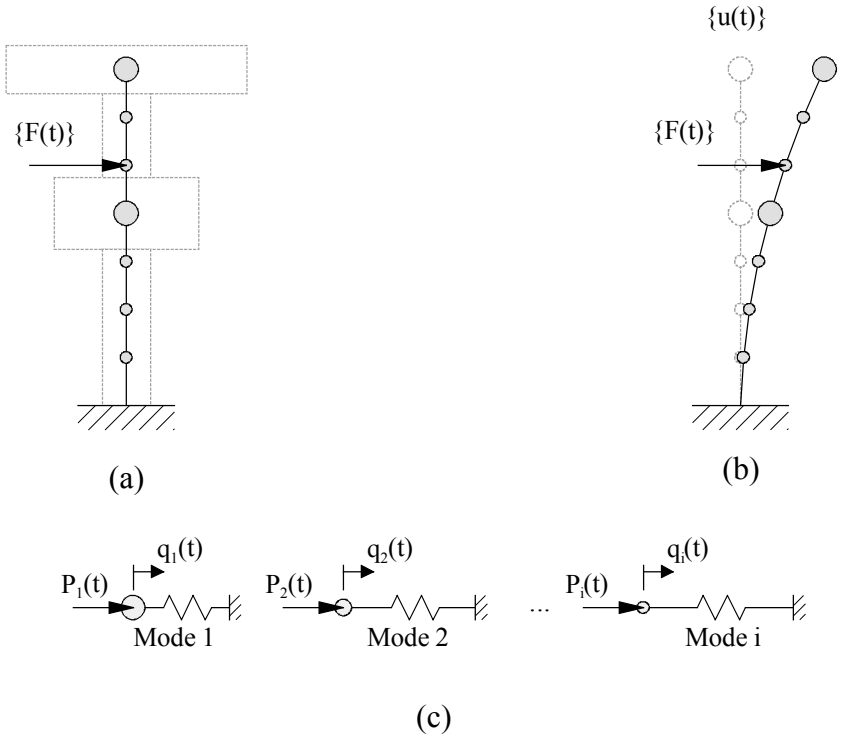

Figure 8.2 Time-history versus modal analysis a) Finite element model of structure, b) MDOF time-history analysis of structural system, and c) SDOF systems representing each mode of vibration

8.2.1 Modal Analysis

The generalized eigenproblem can be expressed by the following equation:

$$[K][\Phi] = \lambda[M][\Phi] \tag{8.2}$$

where [K] and [M] are respectively, the stiffness and mass matrices of the system, λ are the eigenvalues of the system, and [Φ] is a matrix whose columns are the eigenvectors (i.e. modal shapes of vibration) of the structure. Both the stiffness and mass matrices are square matrices with dimensions equal to the number of degrees-of-freedom in the structural system model. In general, the matrix of eigenvectors is also square with dimensions equal to the number of degrees-of-freedom in the system. Each eigenvalue (λ_i) corresponds to a natural circular frequency of the structure squared (ω_i^2, where ω_i has units of rad/sec) which in turn can be related to the period of vibration of the structure:

$$T_i = \frac{2\pi}{\omega_i} \tag{8.3}$$

Likewise, each eigenvector $\{\Phi_i\}$ represents a shape (referred to as a mode shape) that the structure assumes when it is excited (loaded) at its respective natural frequency (Figure 8.3).

The eigenvalue problem, Eqn. 8.2, can also be rewritten as follows:

$$\left(\left[D\right] - \omega^2\left[I\right]\right)\left[\Phi\right] = \left[0\right] \tag{8.4}$$

where [D] is the dynamic system matrix (defined as $[D] = [M]^{-1}[K]$), and [I] is the identity matrix. To ensure a nontrivial solution to the above equation, the characteristic matrix—the parenthetical quantity in Eqn. 8.4—must necessarily be singular. For a matrix to be singular, its determinant must be zero. Imposing this condition leads to an n^{th} degree polynomial, commonly referred to as the characteristic polynomial:

$$p\left(\omega^2\right) = \det\left|\left[D\right] - \omega^2\left[I\right]\right| = 0 \tag{8.5}$$

where $p(\omega^2)$ is the characteristic polynomial. Solutions for the eigenvalues of the system are generally obtained by solving for the n-roots of the characteristic polynomial. Once the eigenvalues are known, the corresponding eigenvectors can be solved for by rewriting Eqn. 8.4 for a specific mode i:

$$\left(\left[D\right] - \omega_i^2\left[I\right]\right)\left\{\Phi_i\right\} = \left\{0\right\} \tag{8.6}$$

Further examination of Eqn. 8.6 shows that this equality holds true even if the eigenvector $\{\Phi_i\}$ is scaled by an arbitrary constant (c_i). Although the relative magnitude of each element with respect to the other elements in an eigenvector is unique, the absolute magnitude of each eigenvector is not.

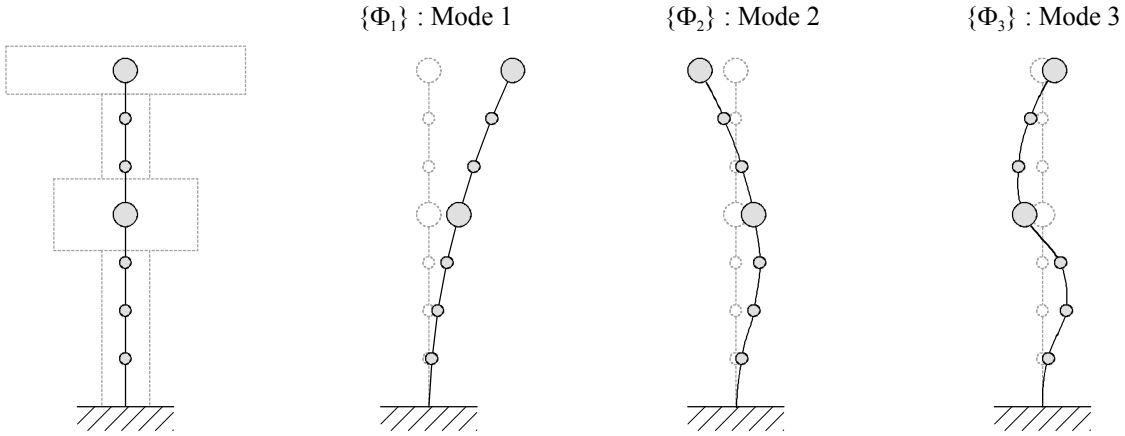

Figure 8.3 Modal analysis: a) Structural model, b) First mode shape, c) Second mode shape, and d) Third mode shape

The process of scaling the eigenvectors such that they each have a specific magnitude is called normalization. A normalization method often used in structural analysis software is called mass-normalization and involves scaling each eigenvector such that the following condition is satisfied:

$$\left\{\hat{\Phi}_i\right\}^T [M]\left\{\hat{\Phi}_i\right\} = 1 \quad \text{or} \quad \left[\hat{\Phi}\right]^T [M]\left[\hat{\Phi}\right] = [I] \tag{8.7}$$

where $\left\{\hat{\Phi}_i\right\}$ is a mass-normalized eigenvector. A mass-normalized eigenvector can be computed from an arbitrarily normalized eigenvector as follows:

$$\left\{\hat{\Phi}_i\right\} = \frac{\{\Phi_i\}}{\{\Phi_i\}^T [M]\{\Phi_i\}} \tag{8.8}$$

If the eigenvectors of a system have been computed, the model can be transformed into the generalized modal system (recall Figure 8.2). Structural displacements of the system model may be related to modal displacements through the eigenvectors as follows:

$$\{u(t)\} = [\Phi]\{q(t)\} \tag{8.9}$$

where $\{u(t)\}$ and $\{q(t)\}$ are the time varying structural and modal displacements, respectively. Because the eigenvectors are not dependent upon time, taking the first and second derivatives of $\{u(t)\}$ with respect to time yields:

$$\{\dot{u}(t)\} = [\Phi]\{\dot{q}(t)\} \tag{8.10}$$

$$\{\ddot{u}(t)\} = [\Phi]\{\ddot{q}(t)\} \tag{8.11}$$

where $\{\dot{u}(t)\}$ and $\{\ddot{u}(t)\}$ are the structural velocity and acceleration vectors, and $\{\dot{q}(t)\}$ and $\{\ddot{q}(t)\}$ are the modal velocity and acceleration vectors.

Eqn. 8.9 provides a means of transforming modal displacements into structural displacements. An inverse process that transforms structural displacements into modal displacements is achieved using the inverse of the eigenvector matrix:

$$\{q(t)\} = [\Phi]^{-1} \{u(t)\} \tag{8.12}$$

However, inversion of the eigenvector matrix $[\Phi]$ in Eqn. 8.12 may be computationally expensive. A more computationally efficient procedure for achieving the same transformation as that described by Eqn. 8.12 is available and involves the use of both the eigenvector matrix and the structural mass matrix. Assuming that the eigenvectors of the system have been mass-normalized, and premultiplying each term in Eqn. 8.9 by $\left[\hat{\Phi}\right]^T [M]$ yields:

$$\left(\left[\hat{\Phi}\right]^T [M]\right)\{u(t)\} = \left(\left[\hat{\Phi}\right]^T [M]\right)\left[\hat{\Phi}\right]\{q(t)\} = \left[\hat{\Phi}\right]^T [M]\left[\hat{\Phi}\right]\{q(t)\} = [I]\{q(t)\} \tag{8.13}$$

Making use of Eqn. 8.7, Eqn. 8.13 is reduced to provide the transformation of modal displacements into structural displacements:

$$\{q(t)\} = \left[\hat{\Phi}\right]^T \ [M] \ \{u(t)\} \tag{8.14}$$

Although Eqn. 8.14 is more computationally efficient than Eqn. 8.12, use of Eqn. 8.14 is dependent upon the mass-normalization of the eigenvectors, and thus requires greater caution in its use. Throughout the remainder of this chapter, it is assumed that the eigenvectors are mass-normalized.

Typically, the equation of motion for the structural system is expressed as in Eqn. 8.1. Introducing the displacement, velocity, and acceleration relationships (Eqns. 8.9, 8.10, and 8.11), into Eqn. 8.1 produces:

$$[M][\Phi]\{\ddot{q}(t)\} + [C][\Phi]\{\dot{q}(t)\} + [K][\Phi]\{q(t)\} = \{F(t)\} \tag{8.15}$$

Premultiplying each term in this equation by the transpose of the eigenvector matrix (i.e. $[\Phi]^T$) yields:

$$[\Phi]^T \ [M][\Phi]\{\ddot{q}(t)\} + [\Phi]^T \ [C][\Phi]\{\dot{q}(t)\} + [\Phi]^T \ [K][\Phi]\{q(t)\} = [\Phi]^T \ \{F(t)\} \tag{8.16}$$

The above equation can be simplified by defining the following relationships:

$$[m] = [\Phi]^T \ [M] \ [\Phi] \tag{8.17}$$

$$[c] = [\Phi]^T \ [C] \ [\Phi] \tag{8.18}$$

$$[k] = [\Phi]^T \ [K] \ [\Phi] \tag{8.19}$$

$$\{f(t)\} = [\Phi]^T \ \{F(t)\} \tag{8.20}$$

where [m], [c], and [k] are the modal mass, modal damping, and modal stiffness matrices, and {f(t)} is the modal force vector.

The fact that eigenvectors are orthogonal with respect to the stiffness and mass matrices results in the modal stiffness and modal mass matrices being diagonal (Chopra 2007). If an orthogonal formulation is used to construct the structural damping matrix [C], then the modal damping matrix [c] will also be diagonal. In this case, each diagonal term in [c] can be expressed as a ratio of the critical damping for each mode:

$$c_i = 2\omega_i \xi_i m_i \tag{8.21}$$

where ξ_i is the ratio of critical damping for the i^{th} mode. When [m], [c], and [k] are diagonal, the coupled structural equation of motion (Eqn. 8.15) reduce to a series of uncoupled single DOF modal equations of motion. (Note that the use of the term "coupled" here is different from that discussed in Chapter 5. In Chapter 5, the coupling discussed was between the impacting vessel and the bridge structure. The coupling being referred to in the present context, however, refers to the linking of various DOF within the structural model to each

other. Such linking occurs when off-diagonal terms are present in the system matrices). For a given mode i, the SDOF modal equation of motion is:

$$m_i \ddot{q}_i(t) + 2\omega_i \xi_i m_i \dot{q}_i(t) + k_i q_i(t) = f_i(t) \tag{8.22}$$

Normalizing each term by the modal mass yields:

$$\ddot{q}_i(t) + 2\omega_i \xi_i \dot{q}_i(t) + \omega_i^2 q_i(t) = \frac{f_i(t)}{m_i} \tag{8.23}$$

Solving each SDOF modal equation of motion yields modal displacements, modal velocities, and modal accelerations. With the time-varying modal quantities known, the individual modal contributions to overall structural displacements, velocities, and accelerations can be computed for each mode using Eqns. 8.9, 8.10, and 8.11. Structural response quantities are thus determined through modal superposition in which the contributions from all modes are added together.

8.2.2 General Response Spectrum Analysis

Time-step integration of the equations of motion, either structural (Eqn. 8.15) or modal (Eqn. 8.22), generally requires hundreds or thousands of time steps to be analyzed in order to evaluate the response of a structure. Subsequently, the results must be scanned to identify the maximum absolute force values needed for design. In contrast, response spectrum analysis can be used to estimate these maximums without the need for conducting time-history analysis. In a response spectrum analysis, Eqns 8.22 and 8.23 are not directly time-integrated. Instead, the maximum response contributed by each mode is determined using relationships that correlate loading to peak response as a function of modal frequency (or period).

8.2.2.1 Modal Combination

To determine the maximum overall structural response, the individual modal contributions must be combined. The simplest possible combination technique consists of direct superposition of the maximum absolute response from each mode. This approach assumes that the peak responses for each mode occur at the same point in time, which leads to overly-conservative design forces. An alternative, and more reasonable, approach is to use a square-root-of-the-sum-of-the-squares (SRSS) method. The SRSS method is based upon probabilistic theory and is expressed as follows:

$$R_{comb} = \sqrt{\sum_{i=1}^{n} r_i^2} \tag{8.24}$$

where R_{comb} is the combined result of the response parameter under consideration (e.g. displacement, force, etc.), and r_i is the response parameter value for the i^{th} mode. Use of the SRSS combination method tends to provide accurate approximations of structural response for two-dimensional models in which the natural frequencies are well-spaced (Tedesco et al. 1999). However, for three-dimensional models in which closely spaced natural frequencies may be present, the complete-quadratic-combination (CQC) method yields more accurate results:

$$R_{comb} = \sqrt{\sum_{i=1}^{n}\sum_{j=1}^{n}\rho_{ij}|r_i|\cdot|r_j|} \tag{8.25}$$

where ρ_{ij} is defined as follows:

$$\rho_{ij} = \frac{8\sqrt{\xi_i\xi_j}\left(\xi_i + \alpha\xi_j\right)\alpha^{3/2}}{\left(1-\alpha^2\right)^2 + 4\xi_i\xi_j\alpha\left(1+\alpha^2\right) + 4\left(\xi_i^2 + \xi_j^2\right)\alpha^2} \tag{8.26}$$

where ξ_i and ξ_j are the modal damping ratios for modes i and j respectively, and α is the frequency ratio (ω_i/ω_j).

8.2.2.2 Mass Participation Factors

Although the total number of modes for a multiple degree-of-freedom structural model is equal to the number of degrees-of-freedom, typically, only a relatively small number of these modes are required in order to adequately describe the behavior of the system. Consequently, eigenanalyses are typically conducted on a reduced system (or subspace), instead of the full system. Subspace methods are advantageous in that significantly fewer computations are required to obtain modal properties (shapes and frequencies) when only a small number of modes are needed. However, a key step in using subspace methods is determining the number of modes that are required to adequately capture the response of the system. Typically, this number of modes is determined through the use of mass participation factors which represent the amount of structural mass present in each mode of vibration.

To calculate the mass participation factor for a specific mode-i, the mass excitation factor must be calculated as:

$$L_i = \{\Phi_i\}^T \left[M\right] \{1_F\} \tag{8.27}$$

where L_i is the direction specific mass excitation factor for the i^{th} mode, and $\{1_F\}$ is a unit vector where the subscript (F) indicates that the unit values are associated with degrees-of-freedom in the direction of impact loading, and zero values are associated with degrees-of-freedom not associated the direction of impact loading. The effective modal mass in each mode is calculated as:

$$m_{eff_i} = \frac{L_i^2}{m_{i,i}} \tag{8.28}$$

where $m_{i,i}$ is the diagonal term of modal mass matrix [m] associated with mode-i, and [m] is defined in Eqn. 8.17:

$$\left[m\right] = \left[\Phi\right]^T \left[M\right] \left[\Phi\right] \tag{8.29}$$

The mass participation factor for each mode is defined as:

$$\Gamma_i = \frac{m_{eff_i}}{M_{total}} = \frac{L_i^2}{(m_{i,i})(M_{total})} \tag{8.30}$$

where M_{total} is the total mass of the structure being analyzed.

In seismic (earthquake) response spectrum analysis, design codes (ASCE-7 2005, FEMA 2003, etc.) require that sufficient modes be used such that the total mass participation of the modes included adds up to at least ninety-percent (90%) of the total mass of the structure in two orthogonal directions. For use in vessel impact response spectrum analysis (described in this chapter) it is recommended that 99% mass participation in the direction of applied impact loading be required.

8.3 Dynamic Magnification Factor (DMF)

For a single degree-of-freedom (SDOF) system, the maximum response of the system to a time-varying dynamic loading condition can be determined through the combined use of static response calculation and a dynamic magnification factor (DMF). The maximum dynamic response is computed as the product of the static response and the DMF. When DMFs are calculated for many different SDOF systems having different natural periods (and corresponding natural frequencies), a DMF spectrum is produced. In this section, a DMF design spectrum appropriate for use in barge impact analysis is developed.

Calculation of a single point on the DMF spectrum involves selecting an impact condition (barge mass and speed), determining a time-history of impact loading, and analyzing an equivalent SDOF bridge-pier-soil structural model subjected to the loading condition using both dynamic and static analysis procedures. For a given impact condition, the applied vessel impact loading (AVIL) method, described earlier in this report, may be used to form a time-history of impact loading. Using this loading, the SDOF structural system is dynamically analyzed and the maximum dynamic displacement of the system (u_D) is recorded. Subsequently, the peak magnitude of the dynamically applied load is determined (Figure 8.4) and is applied to the SDOF structural system as a static load. A static analysis is then performed to determine the maximum static displacement of the system (u_S). The DMF is then given computed as the ratio of maximum-dynamic and static displacements computed for the SDOF system (i.e., $DMF = u_D / u_S$). Repeating this process for different SDOF structural models (having varying natural periods and frequencies), but using the same time-history of impact loading, produces a collection of points that constitute the DMF spectrum (Figure 8.5) for the specific loading condition that has been used in the calculations.

If this process is repeated not only for different SDOF structural models but also for different impact load histories, the result is a family of event-specific DMF spectra (Figure 8.6a). The data in Figure 8.6a was generated by first varying the mass of the barge from 250 ton-mass to 8000 ton-mass, and the initial velocity from 0.25 knots to 8 knots to generate various impact load histories. A 250 ton-mass barge corresponds to a single jumbo hopper barge with 50 tons of cargo, and the 8000 ton-mass is slightly larger than four fully-loaded jumbo hopper barges. The upper bound on initial barge velocity, 8.0 knots, was selected based upon maximum barge tow velocities reported at past-point data along Florida's intracoastal waterway system. Overall, 1024 individual impact scenarios were investigated to generate the data in Figure 8.6a.

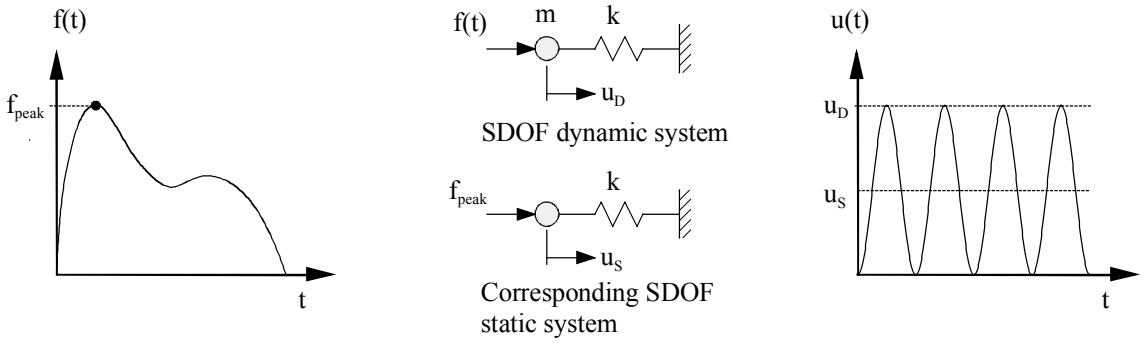

(a) (b) (c)

Figure 8.4 Dynamic magnification of single degree-of-freedom system:
a) Impact force history, b) Dynamic and static SDOF systems, and
c) Dynamic and static displacements

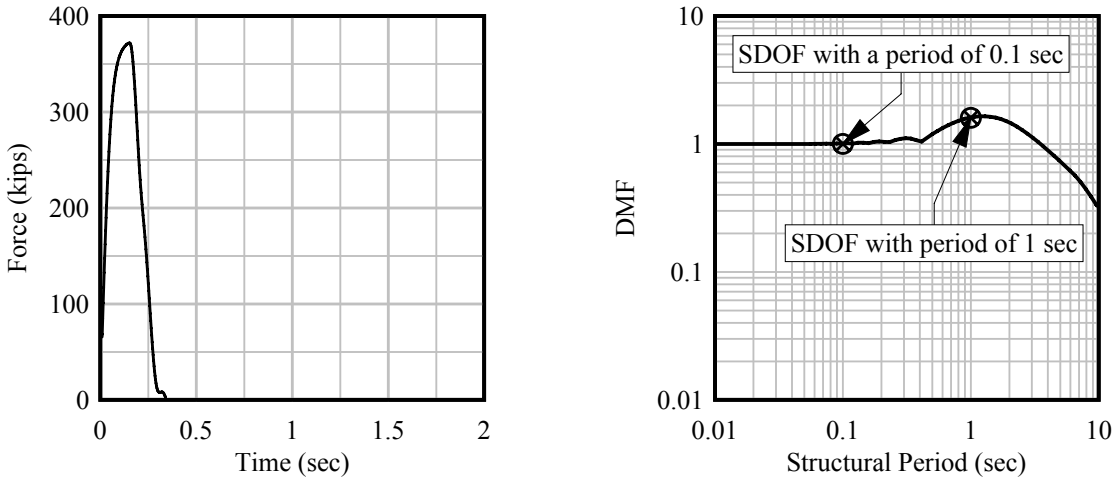

(a) (b)

Figure 8.5 Dynamic magnification factor for a specific impact load history:
a) Impact load history, and b) Corresponding dynamic magnification factor

It is worth noting that the DMF data shown in Figure 8.6 never exceed a value of 2.0. A DMF of 2.0 indicates that the magnitude of dynamic response is twice that of the corresponding static response. Stated in other terms, for a DMF of 2.0, the dynamic response is 100% greater than the corresponding static response.

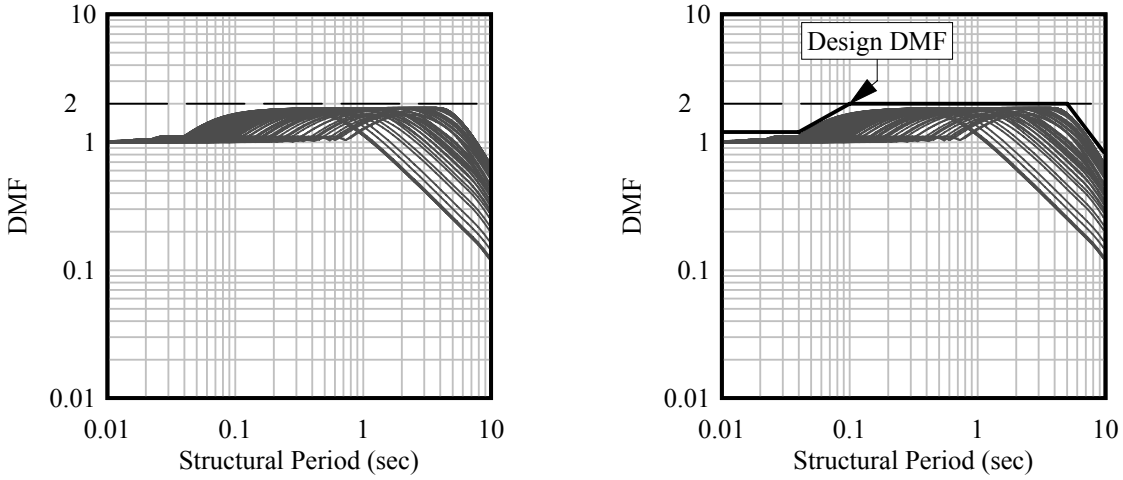

Figure 8.6 Dynamic magnification factor: a) For a range of load histories, and b) With a broad-banded design spectrum

In regard to the development of a design DMF spectrum, one of the simplest options is a broad-banded design spectrum that envelopes all of the data generated (Figure 8.6b). While this approach is simple and provides conservative estimates of dynamic response, in some cases, a broad-banded design spectrum will yield results that are excessively conservative. For low-energy impacts, a broad-banded design spectrum will grossly over-predict amplification effects for long-period modes (modes with a natural structural period greater than one-second). In Figure 8.7, the event-specific DMF spectrum for a low energy impact (200 ton barge drifting at 1.0 knots) is compared to a broad-banded design spectrum. For a mode with a structural period of 5 sec, the broad-banded design envelope predicts a dynamic magnification factor of 2.0, whereas the event-specific spectrum predicts a DMF of approximately 0.7 (a DMF less than 1.0 indicates that the dynamic response is less severe than the static response). Thus, in this instance, a broad-banded design spectrum would over-predict the DMF by more than a factor of 2.0.

An alternative to the broad-banded design spectrum is a DMF spectrum that evolves based upon impact condition characteristics. This approach yields a design spectrum that is closer to the event-specific spectrum. Inspection of Figure 8.8 shows that as the impact energy increases, the width of the event-specific DMF spectrum increases by expansion in the short and long-period ranges.

One of the key components of an evolving design DMF spectrum is to find a relationship between the impact characteristics and the short and long-period transition points (Figure 8.9a), which shift along the structural period axis, producing an expansion as the impact energy increases. This is accomplished by defining the points that mark a transition from a constant DMF of 2.0 to a sloping DMF. Based on a qualitative investigation of the event-specific DMF data, the transition points are set at a dynamic magnification factor of 1.6 (Figure 8.9b).

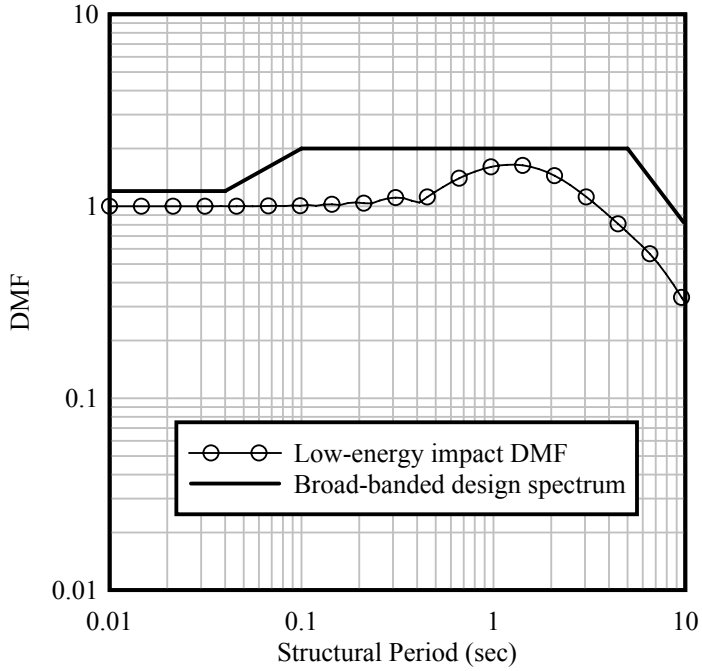

Figure 8.7 Specific dynamic magnification factor for a low-energy impact vs. a broad-banded design spectrum

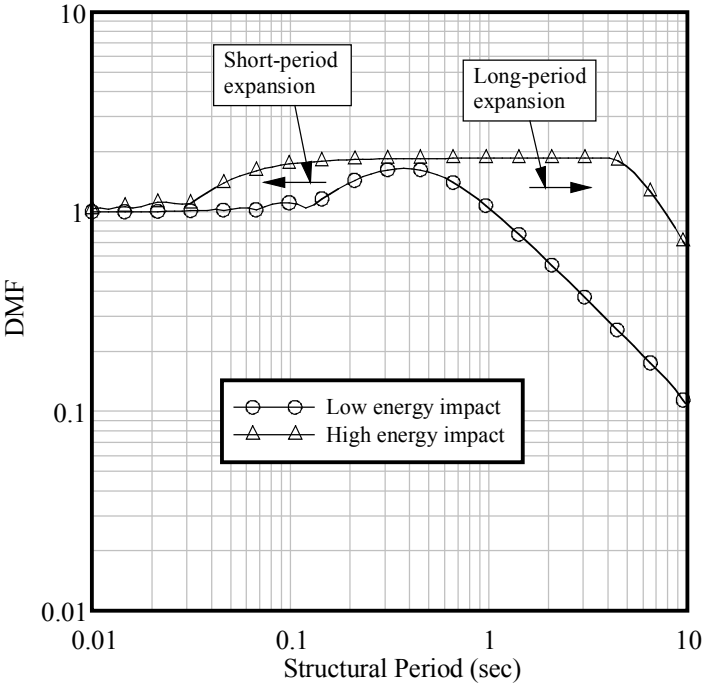

Figure 8.8 Evolution of the dynamic magnification spectrum from short to long duration loading

For each event-specific DMF spectrum in Figure 8.6, the short and long-period transition points are defined in this manner, and an empirical expression for the structural period at each transition point is defined based on the data shown in Figure 8.6. The expression for the short-period transition point is defined as the minimum of the following two expressions:

$$T_S = T_I\left(\frac{1300}{m_B v_{Bi}^2}\right)^{0.9} \tag{8.31}$$

$$T_S = \frac{T_I}{2.2} \tag{8.32}$$

where T_S is the period for the short-period transition point in seconds, T_I is the period of impact loading (Figure 8.10)—calculated as twice the duration of loading predicted by the equations from Chapter 6—and m_B and v_{Bi} are the barge mass (kip-sec^2/in) and initial velocity (in/sec) respectively.

Figure 8.11 shows the short-period transition point as a function of barge kinetic energy. Event-specific DMF data were calculated using the process described earlier, and short-period expression data were calculated using Eqns 8.31 and 8.32. The data in Figure 8.11 are merely a subset of all the data used to generate the expressions, reduced for visual clarity. Additionally, each line indicates a change in barge mass with the initial barge velocity held constant. In general, Eqns 8.31 and 8.32 predict short-periods that are lower than the data obtained from event-specific DMF spectra generation. Referring to Figure 8.9, this indicates that the short-period transition point for the design DMF spectrum is slightly left of the corresponding point in the event-specific DMF spectrum.

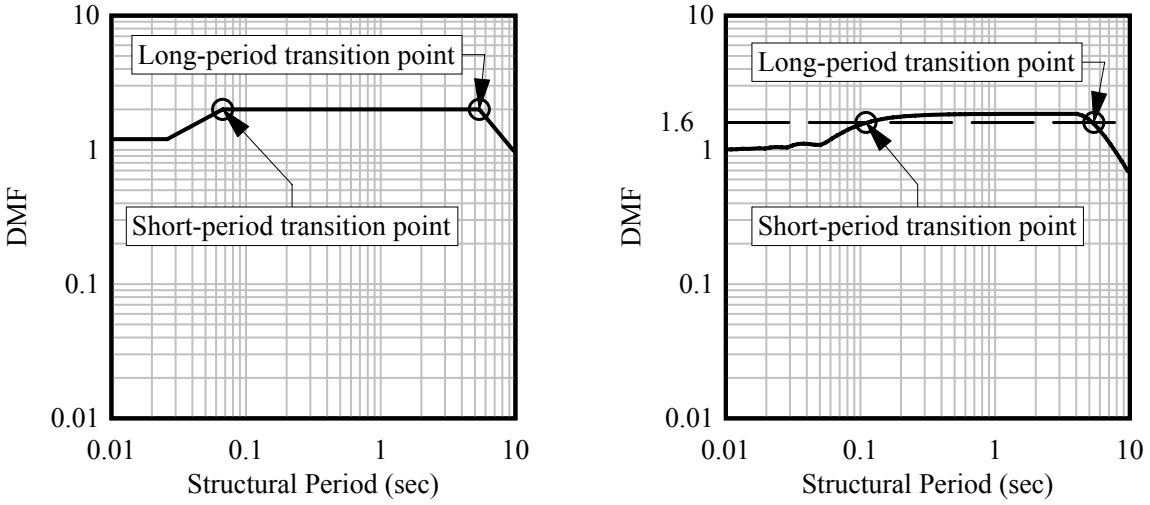

Figure 8.9 Definition of the short and long-period transition points:
a) Design DMF spectrum, and b) Event-specific DMF spectrum

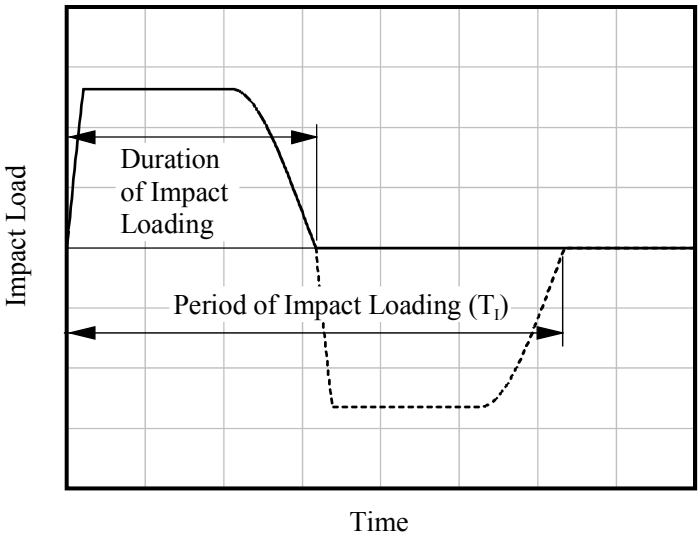

Figure 8.10 Period of impact loading

Based on the data shown in Figure 8.6, an empirical expression for the long-period transition point is defined as the minimum of the following two expressions:

$$T_L = T_I\left(\frac{m_B v_{Bi}^2}{100}\right)^{0.1} \tag{8.33}$$

$$T_L = \frac{T_I}{0.7} \tag{8.34}$$

where T_L is the period for the long-period transition point in seconds, and T_I, m_B, and v_{Bi} are in seconds, kip-sec^2/in, and in/sec respectively.

Long-period transition point data as a function of barge kinetic energy is shown in Figure 8.12. As with the short-period transition point data, event-specific DMF data were calculated using the process illustrated in Figure 8.9b, and the long-period expression data were calculated using Eqns 8.33 and 8.34. Generally, the long-period expression predicts a period that is higher than the data generated from the event-specific DMF spectra; thus, indicating that the long-period transition point for the design DMF spectrum is slightly right of the corresponding point in the event-specific DMF spectrum (Figure 8.9).

With the transition points of the evolving design DMF spectrum quantified, expressions for the design DMF spectrum as a function of structural period are defined. For impact response spectrum analysis, the design DMF spectrum is assumed to be a piecewise linear function in log-log space:

$$DMF = 2.0\left(\frac{T}{T_S}\right)^{0.6} \geq 1.2 \qquad \text{if } T < T_S \tag{8.35}$$

$$\text{DMF} = 2.0 \quad \text{if } T_S \le T \le T_L \tag{8.36}$$

$$\text{DMF} = 2.0\left(\frac{T}{T_L}\right)^{-0.95} \ge 0.1 \quad \text{if } T > T_L \tag{8.37}$$

where, recalling Eqns. 8.31 through 8.34, T_S is the short period transition point, the lesser of:

$$T_S = T_I\left(\frac{1300}{m_B v_{Bi}^2}\right)^{0.9} \text{ and } T_S = \frac{T_I}{2.2} \tag{8.38}$$

T_L is the long-period transition point, defined as the lesser of:

$$T_L = T_I\left(\frac{m_B v_{Bi}^2}{100}\right)^{0.1} \text{ and } T_L = \frac{T_I}{0.7} \tag{8.39}$$

Eqns 8.35 and 8.37 are applicable to structural periods outside of the transition points. For periods between the transition points, the DMF is set to a value of 2.0 (Figure 8.13).

In Figure 8.14, event-specific DMF spectra are compared to design DMF spectra for four different impact conditions that span a broad range of impact energies. The plots demonstrate that the evolving design DMF spectrum equations adequately envelope the corresponding event-specific DMF data over a broad range of impact energies. Furthermore, none of the design spectra are excessively conservative as was the case for the broad-banded design spectrum discussed earlier.

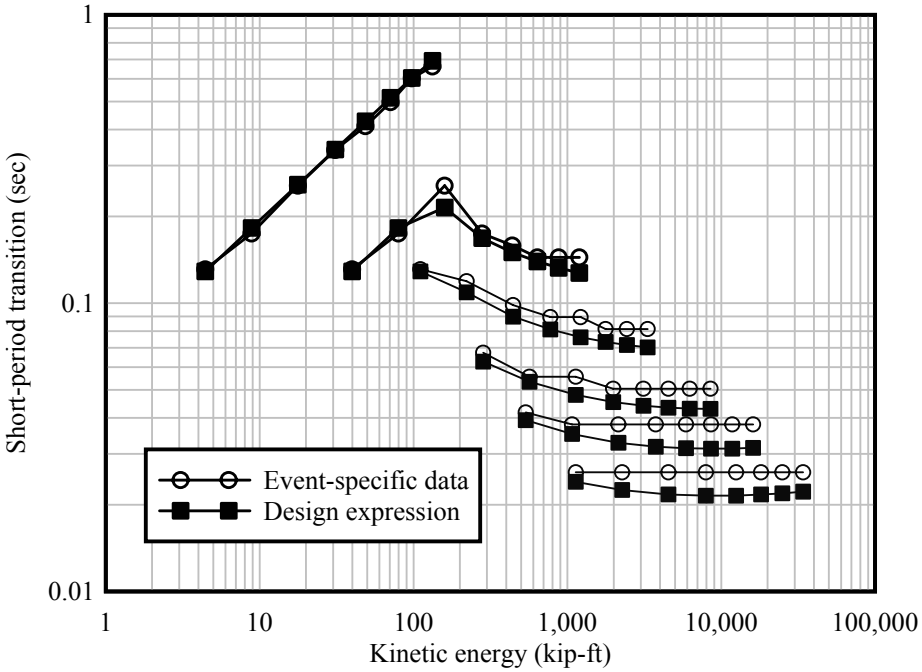

Figure 8.11 Short-period transition point data

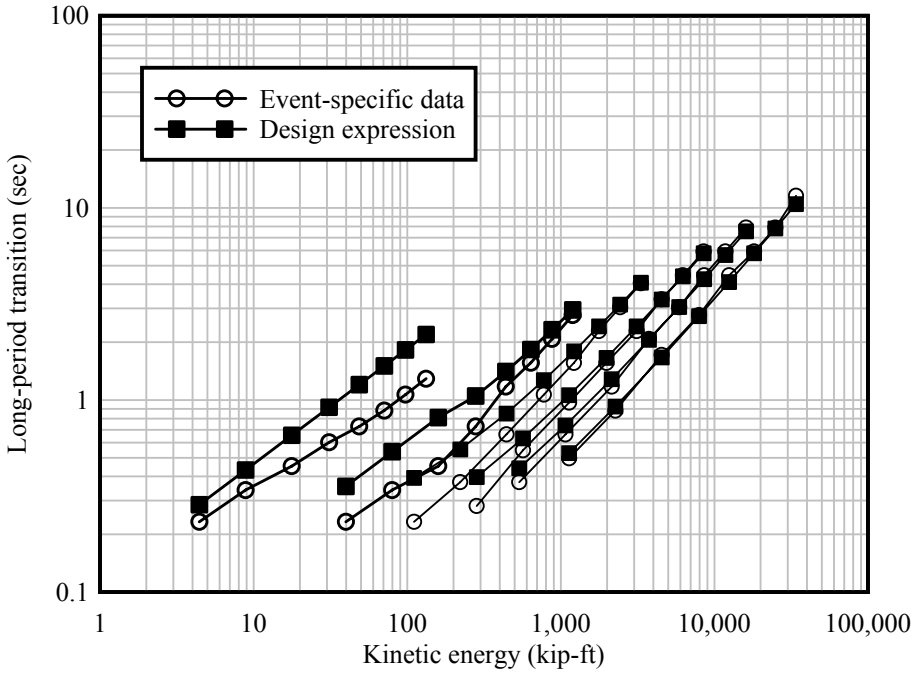

Figure 8.12 Long-period transition point data

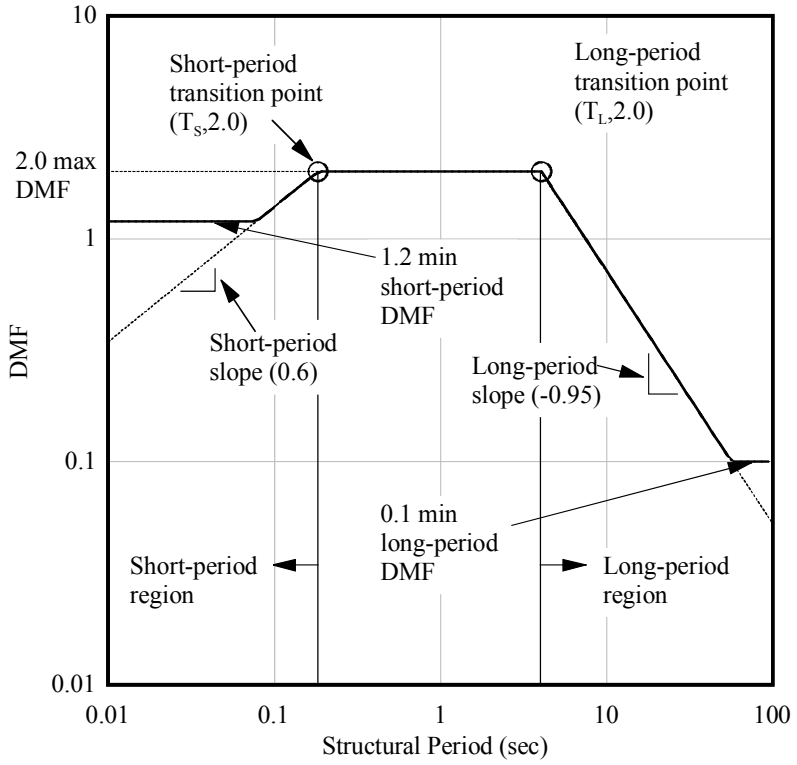

Figure 8.13 Evolving design DMF spectrum

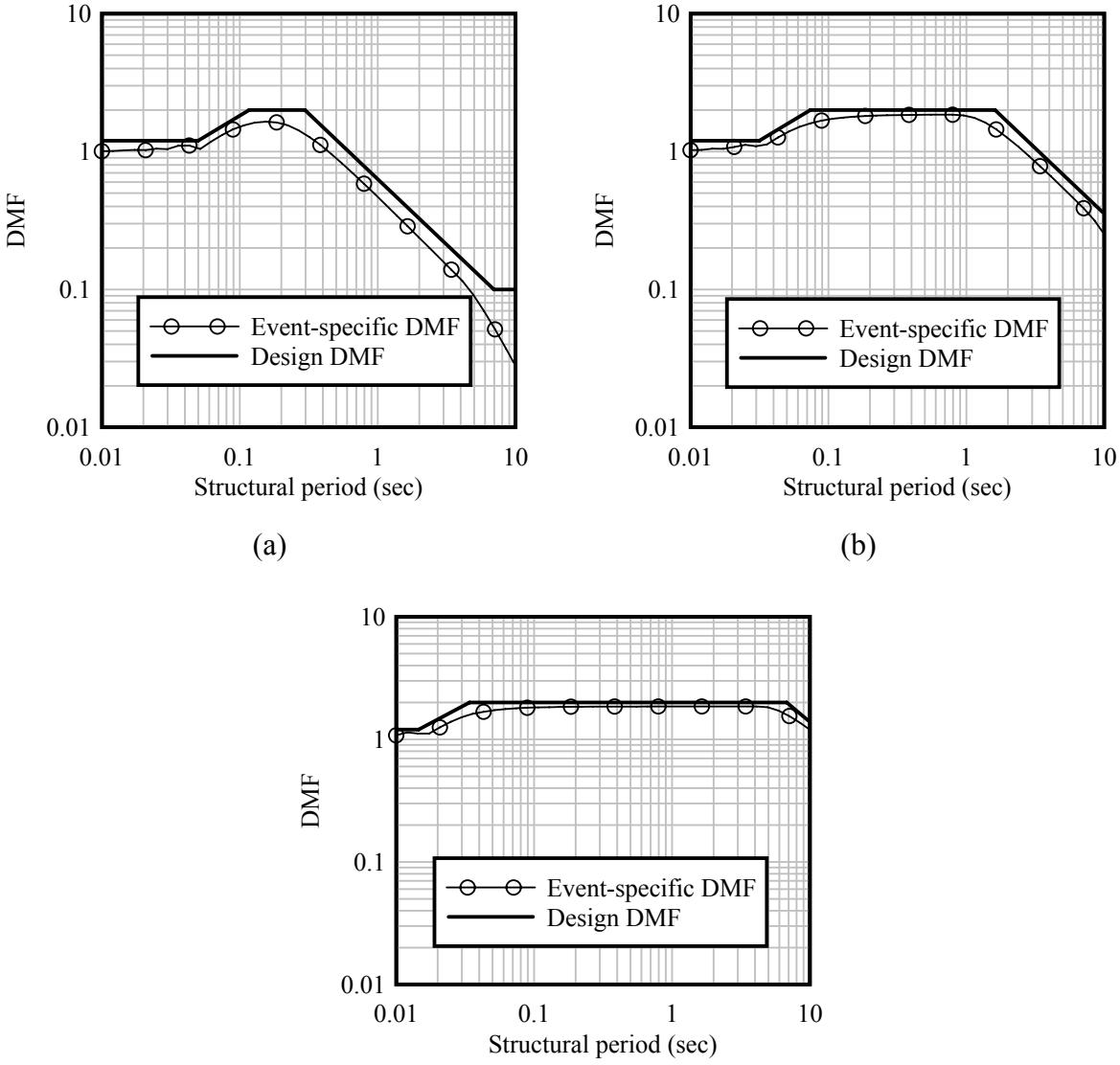

Figure 8.14 Event-specific and design DMF spectra for varying impact energies:
a) 200 ton barge at 1.0 knots, b) 2030 ton barge at 2.5 knots, and
c) 5920 ton barge at 5.0 knots

8.4 Impact Response Spectrum Analysis

Using the concept of a dynamic magnification factor (DMF), it is possible to approximate the maximum dynamic response (displacement, internal member forces, etc.) of a SDOF system using results from a static analysis of the same system. To achieve such an outcome, the DMF-magnitude for the structural system and the applied load must be based upon vibration characteristics of the system. As noted earlier, a modal analysis (e.g., eigen analysis) may be used to obtain modal vibration characteristics and uncouple the MDOF dynamic equations of motion—essentially transforming the MDOF system into many

uncoupled SDOF modal equations. The impact response spectrum analysis (IRSA) procedure proposed here uses modal (eigen) analysis, in conjunction with a DMF spectrum, to simulate dynamic barge impacts on MDOF bridge models. Key steps in the IRSA calculation process are

- Calculating the peak magnitude of impact load
- Applying the peak impact load to the structure in a static sense, and computing the resulting static displacements
- Transforming the static structural displacements into static modal displacements
- Magnifying the static modal displacements—using a DMF spectrum—into dynamic modal displacements
- Transforming the dynamic modal displacements into dynamic structural displacements for each mode
- Recovering the internal member forces for each mode using the corresponding dynamic structural displacements
- Combining the internal member forces and dynamic structural displacements from the modal contributions using SRSS or CQC modal combination

A detailed flowchart for this process is illustrated in Figure 8.15. To calculate the static displacements $\{u_S\}$ of the structure, the peak value of the dynamic load (P_{Bm}) is calculated using the applied vessel impact load (AVIL) equations developed in the previous chapter. Using impact characteristics, a barge bow force-deformation relationship, and the stiffness of the pier, the peak dynamic load can be calculated. Using AVIL equations, the period of loading—an important component of DMF spectrum calculation—is calculated as twice the load duration (recall Figure 8.10). For elastic loading:

$$T_I = \frac{2\pi m_B}{P_{Bm}} v_{Bi} \tag{8.40}$$

and for inelastic loading:

$$T_I = \frac{\pi m_B}{P_{Bm}} \left(v_{Bi} + \frac{P_{BY}}{c_{BP}} + \left(\frac{2}{\pi} - 1 \right) \sqrt{v_{Bi}^2 - \left(\frac{P_{BY}}{c_{BP}} \right)^2} \right) \tag{8.41}$$

Characteristics of the DMF spectrum are calculated from the impact vessel characteristics and the loading period using Eqns. 8.31 through 8.37.

The peak dynamic load is applied to the structure at the impact point in a static sense, and a static analysis is conducted to compute the resulting structural displacements $\{u_S\}$ (Figure 8.16). These static displacements can subsequently be amplified, in a modal sense, to obtain the dynamic response of the system.

Impact Response Spectrum Analysis Procedure

Select barge type, and determine P_{BY}, a_{BY}

Determine impact characteristics: m_B, v_{Bi}

Calculate pier-soil stiffness from static analysis: k_P

$$k_S = \left(\frac{a_{BY}}{P_{BY}} + \frac{1}{k_P}\right)^{-1}$$ Calculate barge-pier-soil series stiffness

$$P_{Bm} = v_{Bi} c_{BP} \le P_{BY} \qquad c_{BP} = \sqrt{k_S m_B}$$ Calculate peak dynamic load

Calculate period of impact loading

$$T_I = \frac{2\pi m_B}{P_{Bm}} v_{Bi}$$ Elastic loading $\left(v_{Bi} c_{BP} \le P_{BY}\right)$

$$T_I = \frac{\pi m_B}{P_{Bm}}\left(v_{Bi} + \frac{P_{BY}}{c_{BP}} + \left(\frac{2}{\pi} - 1\right)\sqrt{v_{Bi}^2 - \left(\frac{P_{BY}}{c_{BP}}\right)^2}\right)$$ Inelastic loading $\left(v_{Bi} c_{BP} > P_{BY}\right)$

Calculate DMF characteristics

$$T_S = T_I\left(\frac{1300}{m_B v_{Bi}^2}\right)^{0.9} \le \frac{T_I}{2.2}$$ Short-period transition point

m_B in kip-sec2/in, v_{Bi} in in/sec, and T_I in sec

$$T_L = T_I\left(\frac{m_B v_{Bi}^2}{100}\right)^{0.1} \le \frac{T_I}{0.7}$$ Long-period transition point

Apply static load (P_{Bm}) and conduct a static analysis to determine static displacements $\{u_S\}$

Recover static member forces $\{F_S^{int}\}$

Conduct eigenanalysis and recover mode shapes $\{\Phi_i\}$ and natural circular frequencies (ω_i)

$$\{q_S\} = [\Phi]^T [M] \{u_S\}$$ Transform structural static displacements into modal coordinates

For each mode (i)

$$T_i = \frac{2\pi}{\omega_i}$$ Calculate structural period

Calculate DMF

$$DMF_i = 2.0\left(\frac{T_i}{T_S}\right)^{0.6} \ge 1.2$$ Short-period region $\left(T_i < T_S\right)$

$$DMF_i = 2.0$$ Intermediate periods $\left(T_S \le T_i \le T_L\right)$

$$DMF_i = 2.0\left(\frac{T_i}{T_L}\right)^{-0.95} \ge 0.1$$ Long-period region $\left(T_i > T_L\right)$

$$q_{Di} = DMF_i q_{Si}$$ Magnify static modal displacement

$$\{u_{Di}\} = q_{Di}\{\Phi_i\}$$ Dynamic displaced mode shape

Recover internal member forces (F_{Di}) for each mode from the displaced mode shapes

Combine modal and static quantities using SRSS or CQC combination:

$\{u_D\} = SRSS(\{u_{D1}\},\{u_{D2}\},...,\{u_{Dn}\},\{u_S\})$ or $\{u_D\} = CQC(\{u_{D1}\},\{u_{D2}\},...,\{u_{Dn}\},\{u_S\})$

$\{F_D\} = SRSS(\{F_{D1}\},\{F_{D2}\},...,\{F_{Dn}\},\{F_S^{int}\})$ or $\{F_D\} = CQC(\{F_{D1}\},\{F_{D2}\},...,\{F_{Dn}\},\{F_S^{int}\})$

Figure 8.15 Impact response spectrum analysis procedure

(a) (b)

Figure 8.16 Static analysis stage of IRSA: a) Structural model with peak dynamic load applied statically, and b) Resulting statically displaced shape

To transform the structural analysis into modal coordinates, an eigenanalysis is conducted on the structure to determine the natural frequencies (and periods) and eigenvectors of the system (recall Figure 8.3). Using the eigenvectors, the static displacements are transformed from structural coordinates into modal coordinates using a variation of Eqn. 8.14 (Figure 8.17):

$$\{q_S\} = [\Phi]^T \, [M] \, \{u_S\} \tag{8.42}$$

where $\{q_S\}$ and $\{u_S\}$ are vectors of static displacements in the modal and structural coordinate systems respectively. Each entry in the static modal displacement vector corresponds to a specific mode shape and natural frequency (and period). Using the natural period for each mode, and the design DMF spectrum (Eqns 8.35 and 8.37), a DMF value is computed for each mode (Figure 8.18). The modal static displacement q_{Si} for mode-i is then magnified by the DMF to produce a dynamic modal displacement q_{Di} (Figure 8.19). Using a modified version of Eqn. 8.9, the contribution from mode-i to the overall dynamic structural displacements is then calculated as:

$$\{u_{Di}\} = q_{Di} \{\Phi_i\} \tag{8.43}$$

Internal dynamic member forces $\{F_{Di}\}$ for each mode are determined by performing force recovery on the structure using the dynamic displacements $\{u_{Di}\}$. Maximum dynamic structural displacements $\{u_D\}$ of the system are obtained by combining the modal contributions to displacement $\{u_{Di}\}$ and the static displacements $\{u_S\}$ using either SRSS or CQC combination techniques (where the static displacements are included to account for localized internal member force effects at the impact location, due to the nodal application of impact load):

$$\{u_D\} = \text{SRSS}\left(\{u_{D1}\},\{u_{D2}\},\ldots,\{u_{Dn}\},\{u_S\}\right) \tag{8.44}$$

$$\{u_D\} = CQC\left(\{u_{D1}\},\{u_{D2}\},\ldots,\{u_{Dn}\},\{u_S\}\right) \tag{8.45}$$

The same process is then applied to the modal internal force vectors $\{F_{Di}\}$ and the internal force vector $\{F_S^{int}\}$ (which corresponds to the static displacement vector):

$$\{F_D\} = SRSS\left(\{F_{D1}\},\{F_{D2}\},\ldots,\{F_{Dn}\},\{F_S^{int}\}\right) \tag{8.46}$$

$$\{F_D\} = CQC\left(\{F_{D1}\},\{F_{D2}\},\ldots,\{F_{Dn}\},\{F_S^{int}\}\right) \tag{8.47}$$

to obtain the maximum dynamic internal member design forces $\{F_D\}$ for the structural system.

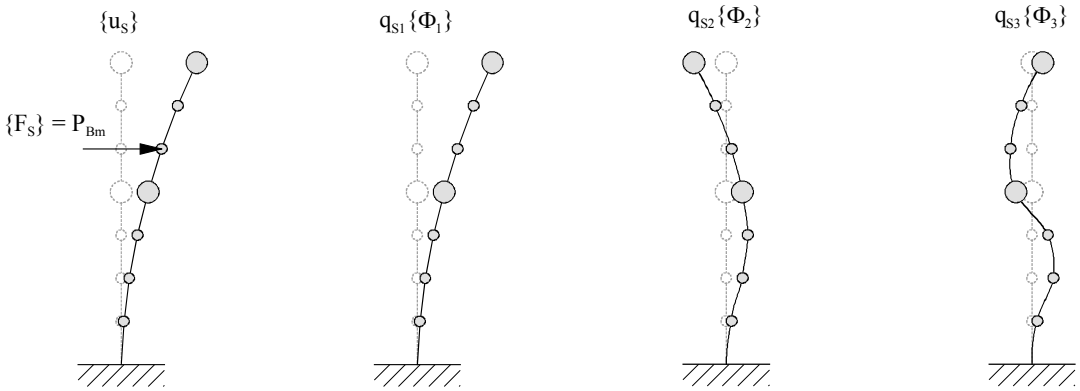

Figure 8.17 Transformation of static displacements into modal coordinates:
a) Statically displaced shape, b) Component of first mode in static displacement,
c) Component of second mode in static displacement, and
d) Component of third mode in static displacement

8.5 Impact Response Spectrum Analysis for Nonlinear Systems

In the IRSA procedure presented above, it is assumed—for purposes of performing the eigenanalysis—that the system matrices (stiffness and mass) correspond to a linear elastic structure. Hence the procedure can only be used for the specific case in which the system is approximated as being linear. Considering the fact that severe vessel-bridge collision events generally exhibit nonlinear behavior, the linear IRSA procedure must be altered to account for system nonlinearity—specifically the nonlinear stiffness matrix. Two iteration stages are required to account for such nonlinearity: 1.) load determination iterations, and 2.) stiffness linearization iterations for eigenanalysis.

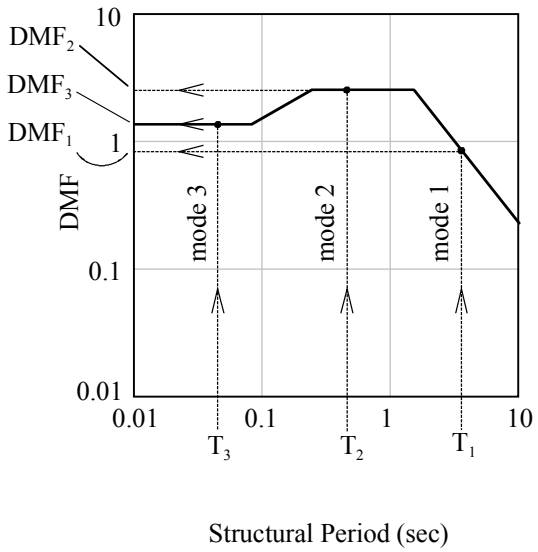

Figure 8.18 Dynamic magnification factor as a function of structural period

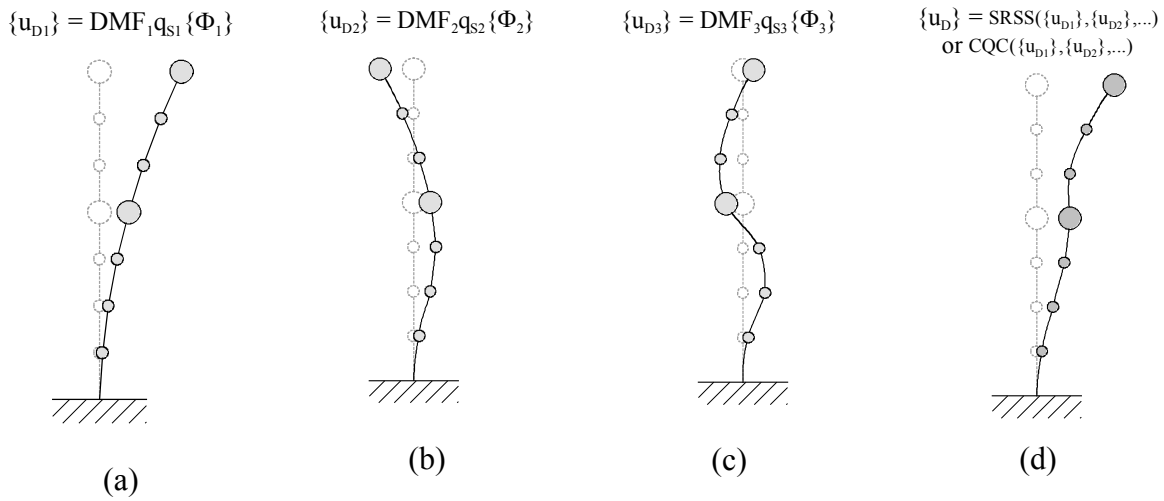

Figure 8.19 Combination of dynamic modal into dynamic structural displacements:
a) Dynamic displaced shape of mode 1, b) Dynamic displaced shape of mode 2,
c) Dynamic displaced shape of mode 3, and d) Modally combined dynamic displaced shape

8.5.1 Load Determination and DMF Spectrum Construction

For a nonlinear system, the effective (secant or tangent) pier-soil stiffness (k_P) is dependent upon the ultimate displacement level that is reached by the system, and is therefore unknown at the beginning of the analysis. An iterative process (Figure 8.20) is therefore required to calculate k_P and the peak dynamic load (P_{Bm}). In order to start the process, the pier is initially assumed to be rigid ($k_P=\infty$), which causes the barge-pier-soil series stiffness to reduce to the following:

$$ {}^{(0)}k_S = \left(\frac{a_{BY}}{P_{BY}} + \frac{1}{k_P} \right)^{-1} = \left(\frac{a_{BY}}{P_{BY}} + \frac{1}{\infty} \right)^{-1} = \frac{P_{BY}}{a_{BY}} \tag{8.48} $$

where ${}^{(0)}k_S$ is the initial estimate for the effective barge-pier series spring stiffness. The peak dynamic load for the first iteration (${}^{(0)}P_{Bm}$) can then be calculated as:

$$ {}^{(0)}c_{BP} = \sqrt{{}^{(0)}k_S \cdot m_B} \tag{8.49} $$

$$ {}^{(0)}P_{Bm} = v_{Bi} \cdot {}^{(0)}c_{BP} \le P_{BY} \tag{8.50} $$

The initial load estimate (${}^{(0)}P_{Bm}$) is then applied to the structure in a static sense, and the structural displacement at the load application point is computed. With both the load and the displacement at the impact point known, the pier-soil secant stiffness for the next iteration (n) can be calculated as:

$$ {}^{(n)}k_P = \frac{{}^{(n-1)}P_{Bm}}{{}^{(n-1)}u_P} \tag{8.51} $$

where ${}^{(n)}k_P$ is the pier-soil secant stiffness for the current iteration (n) and ${}^{(n-1)}P_{Bm}$ and ${}^{(n-1)}u_P$ are, respectively, estimates of the peak dynamic load and structural static displacement of the impact point for the previous iteration (n-1). Furthermore, the effective barge-pier-soil series spring stiffness (${}^{(n)}k_S$) for the current iteration (n) can be updated as:

$$ {}^{(n)}k_S = \left(\frac{a_{BY}}{P_{BY}} + \frac{1}{{}^{(n)}k_P} \right)^{-1} \tag{8.52} $$

With the effective barge-pier-soil series spring stiffness (${}^{(n)}k_S$) known, the load (${}^{(n)}P_{Bm}$) for the current iteration (n) can be updated accordingly:

$$ {}^{(n)}c_{BP} = \sqrt{{}^{(n)}k_S \cdot m_B} \tag{8.53} $$

$$ {}^{(n)}P_{Bm} = v_{Bi} \cdot {}^{(n)}c_{BP} \le P_{BY} \tag{8.54} $$

The incremental change in computed impact load from iteration (n-1) to iteration (n) is then calculated as follows:

$$ \Delta P_{Bm} = {}^{(n)}P_{Bm} - {}^{(n-1)}P_{Bm} \tag{8.55} $$

If the incremental change in computed load (ΔP_{Bm}) is smaller than a chosen convergence tolerance, then calculation of the peak load has converged to a solution. With the load (P_{Bm}) determined, the design DMF may be constructed using Eqns. 8.31 through 8.37.

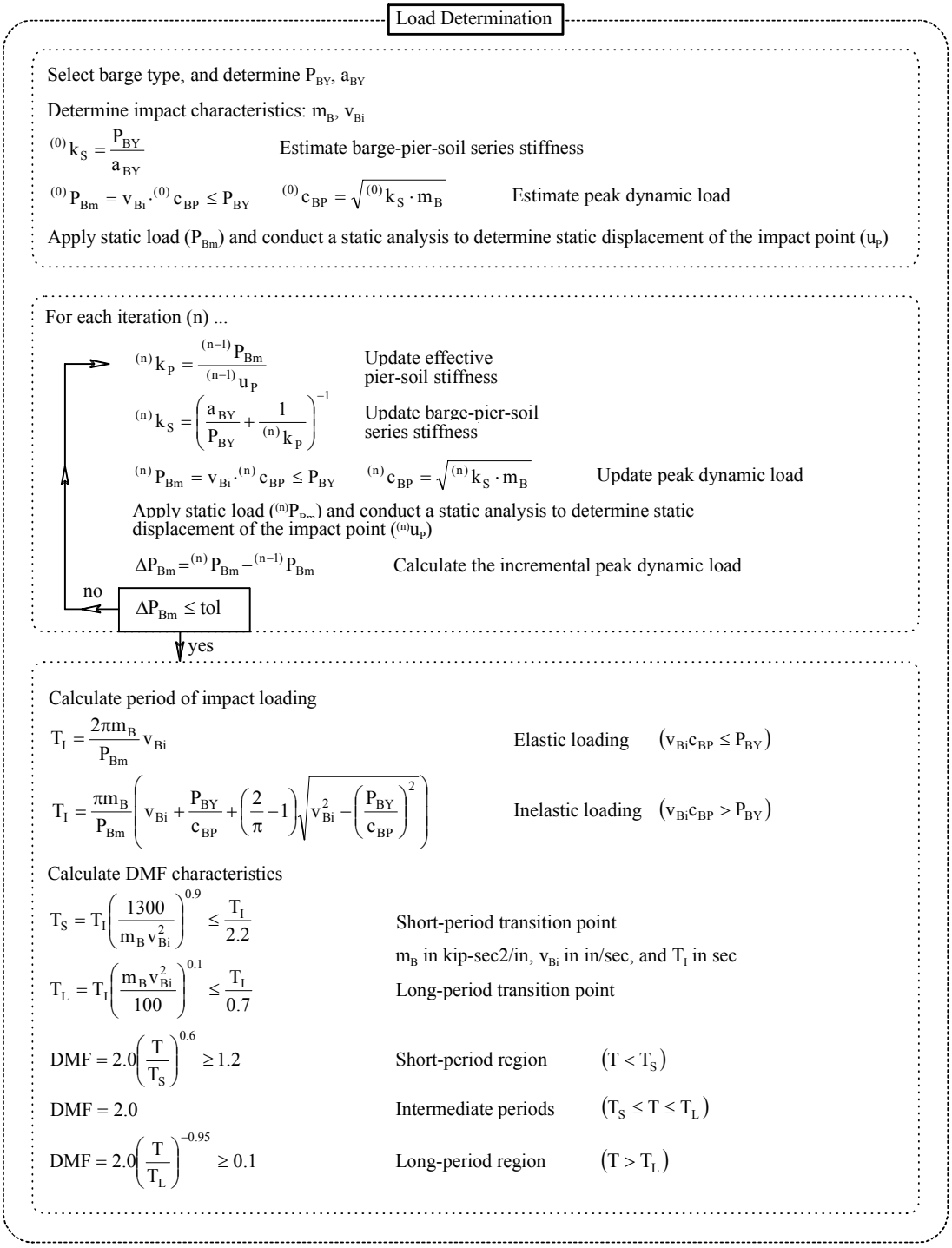

Figure 8.20 Nonlinear impact response spectrum analysis procedure

8.5.2 Structural Linearization Procedure

For a linear system, eigenanalysis can be carried out directly using the system stiffness and mass matrices. However, for a nonlinear system, the stiffness matrix itself is dependent upon the displacements of the system. In such a case, an iterative process

(Figure 8.21) must be used in which the system secant stiffness matrix is updated using the dynamically magnified structural displacements computed within each iteration. However, during the initial iteration, static displacements are used to approximate the dynamically amplified displacements that will be used in later iterations. Thus, to initialize the linearization process, the static external force vector ($\{F_S\}$)—which contains the peak impact load (P_{Bm}), as well as all other static loads on the structure (e.g. gravity loads)—is used to compute the external force vector for the first iteration:

$$^{(0)}\{F_E\} = \{F_S\} \tag{8.56}$$

Additionally, the structural static displacements are used to estimate the dynamic displacements for the initial iterations:

$$^{(0)}\{u_D\} = \{u_S\} \tag{8.57}$$

These dynamic displacements are in turn used to compute the secant stiffness matrix for the first iteration.

An eigenanalysis is then conducted using the mass matrix and the current secant stiffness matrix. Eigenvectors and natural frequencies are extracted from the eigenanalysis results for use in the IRSA. Static structural displacements $\{u_S\}$ are transformed into static modal coordinates $\{q_S\}$ using the current estimate of the eigenvectors for nonlinear iteration-n:

$$^{(n)}\{q_S\} = ^{(n)}[\Phi]^T\ [M]\ \{u_S\} \tag{8.58}$$

Using the estimate of structural period for mode-i obtained from the eigenanalysis at the n-th nonlinear iteration:

$$^{(n)}T_i = \frac{2\pi}{^{(n)}\omega_i} \tag{8.59}$$

the DMF is calculated as:

$$^{(n)}DMF_i = 2.0\left(\frac{^{(n)}T_i}{T_S}\right)^{0.6} \le 1.2 \qquad \text{if } ^{(n)}T_i < T_S \tag{8.60}$$

$$^{(n)}DMF_i = 2.0 \qquad \text{if } T_S \le ^{(n)}T_i \le T_L \tag{8.61}$$

$$^{(n)}DMF_i = 2.0\left(\frac{^{(n)}T_i}{T_L}\right)^{-0.95} \ge 0.1 \qquad \text{if } ^{(n)}T_i > T_L \tag{8.62}$$

Static modal displacements for mode-i are then magnified using the current estimate of the DMF to obtain dynamic modal displacements:

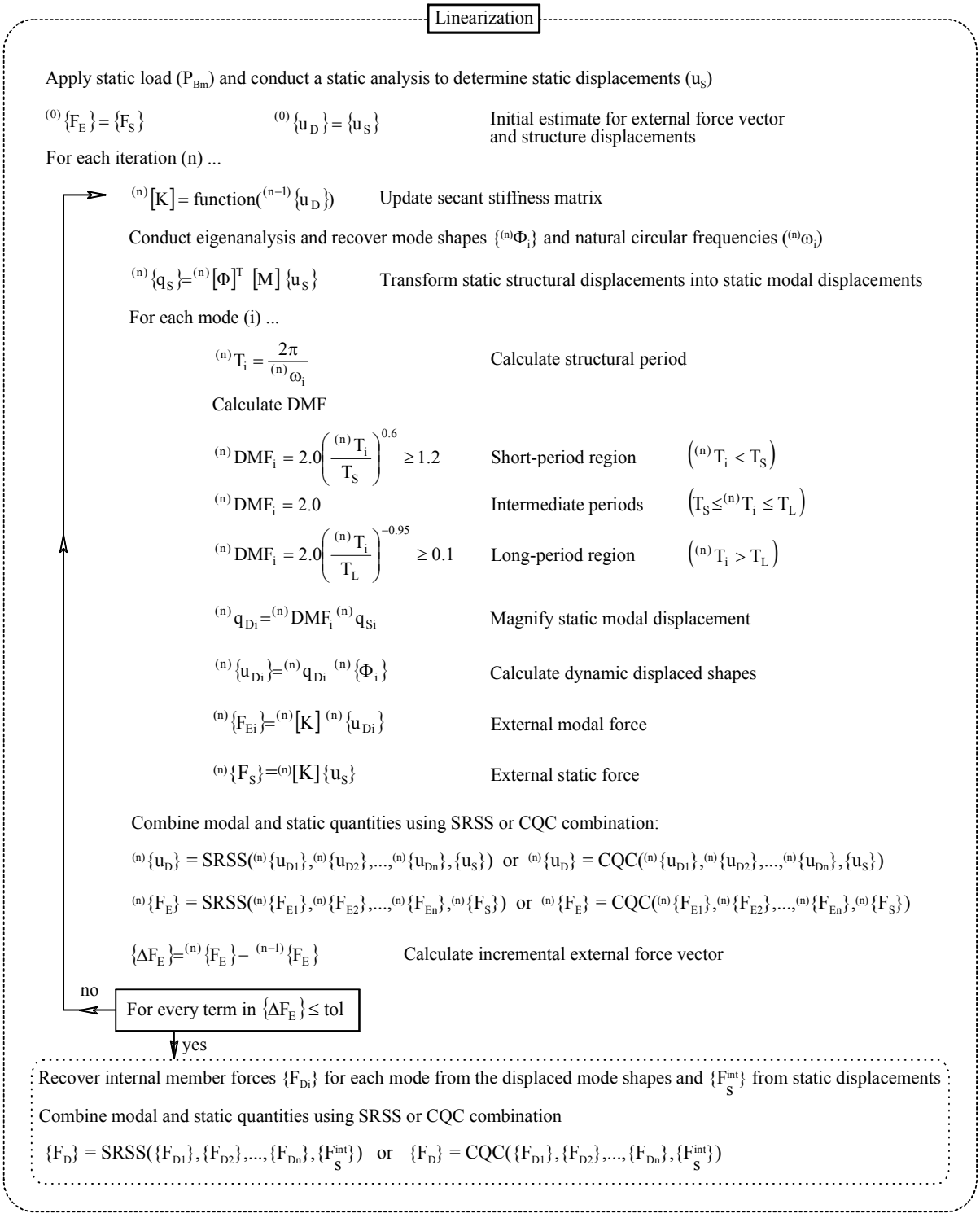

Figure 8.21 Nonlinear impact response spectrum analysis procedure

$$^{(n)}q_{Di} = {}^{(n)}DMF_i \, {}^{(n)}q_{Si} \tag{8.63}$$

and the dynamic displaced shape for each mode is obtained as:

$$^{(n)}\{u_{Di}\} = {}^{(n)}q_{Di} \; {}^{(n)}\{\Phi_i\} \tag{8.64}$$

The overall structural displacement response of the system is updated by combining the displaced mode shapes and the static displacements using the SRSS or CQC combination techniques (where static displacements are also included to account for localized internal member force effects at the impact location, due to the nodal application of impact load):

$$^{(n)}\{u_D\} = SRSS\left({}^{(n)}\{u_{D1}\}, {}^{(n)}\{u_{D2}\}, \ldots, {}^{(n)}\{u_{Dn}\}, \{u_S\} \right) \tag{8.65}$$

$$^{(n)}\{u_D\} = CQC\left({}^{(n)}\{u_{D1}\}, {}^{(n)}\{u_{D2}\}, \ldots, {}^{(n)}\{u_{Dn}\}, \{u_S\} \right) \tag{8.66}$$

The external force vector for each mode-i is updated by premultiplying the updated displaced shape for each mode by the most recent estimate for the stiffness matrix:

$$^{(n)}\{F_{Ei}\} = {}^{(n)}[K] \; {}^{(n)}\{u_{Di}\} \tag{8.67}$$

The external force vector associated with the static displacements is updated analogously:

$$^{(n)}\{F_S\} = {}^{(n)}[K]\{u_S\} \tag{8.68}$$

Combining the external force vectors for each mode and the external force vector associated with the static displacements, and using either SRSS or CQC combination, the updated estimate of external force is calculated:

$$^{(n)}\{F_E\} = SRSS\left({}^{(n)}\{F_{E1}\}, {}^{(n)}\{F_{E2}\}, \ldots, {}^{(n)}\{F_{En}\}, {}^{(n)}\{F_S\} \right) \tag{8.69}$$

$$^{(n)}\{F_E\} = CQC\left({}^{(n)}\{F_{E1}\}, {}^{(n)}\{F_{E2}\}, \ldots, {}^{(n)}\{F_{En}\}, {}^{(n)}\{F_S\} \right) \tag{8.70}$$

Using the modally combined external force vector, the incremental change in force vector from the previous nonlinear iteration (n-1) to the current iteration (n) is calculated:

$$\{\Delta F_E\} = {}^{(n)}\{F_E\} - {}^{(n-1)}\{F_E\} \tag{8.71}$$

If any term in the incremental external force vector $\{\Delta F_E\}$ is greater than the chosen tolerance, then the process begins anew with recalculation of the secant stiffness matrix using the updated displaced shape. Alternatively, if every term in $\{\Delta F_E\}$ is less than or equal to the chosen tolerance, then the linearization process has converged. In this case, internal dynamic member forces $^{(n)}\{F_{Di}\}$ for each mode and the static internal forces $^{(n)}\left\{F_S^{int}\right\}$ are determined by performing force recovery on the structure using the dynamic displacements $^{(n)}\{u_{Di}\}$ and the

static displacements $\{u_S\}$ respectively. Modal and static internal member forces are then combined using SRSS or CQC modal combination:

$$\{F_D\} = \text{SRSS}\left(\{F_{D1}\},\{F_{D2}\},\ldots,\{F_{Dn}\},\{F_S^{int}\}\right) \tag{8.72}$$

$$\{F_D\} = \text{CQC}\left(\{F_{D1}\},\{F_{D2}\},\ldots,\{F_{Dn}\},\{F_S^{int}\}\right) \tag{8.73}$$

to obtain the maximum overall dynamic structural internal member design forces $\{F_D\}$.

8.6 Validation and Demonstration of Impact Response Spectrum Analysis

Validation of the IRSA method is carried out by analyzing a series of jumbo hopper barge impacts on bridge structures using both IRSA and coupled vessel impact analysis (described earlier in Chapter 5) and subsequently comparing results. Since both methods are implemented in the same software analysis package, FB-MultiPier, any difference in analysis results are solely due to differences in the analysis procedures themselves. Since the coupled vessel impact analysis (CVIA) method was previously validated against both high-resolution finite element models and experimental data (see Chapter 5), results obtained from this method are considered the benchmark (or reference datum) against which the accuracy of the IRSA method is judged.

8.6.1 Event-Specific Impact Response Spectrum Analysis (IRSA)Validation

To validate the IRSA method, coupled dynamic time-history analyses were conducted on a one-pier two-span (OPTS) model of the new St. George Island Causeway Bridge channel pier and the two connected superstructure spans (Davidson 2007). Three impact cases (Table 8.1) were analyzed: a low energy impact; a moderate energy impact; and a high energy impact. The low-energy case represents a situation in which the barge bow remains elastic throughout the duration of impact; the moderate-energy case represents a situation in which barge bow deformation is slightly greater than the barge yield deformation; and the high-energy case corresponds to a situation in which significant barge bow yielding is expected. (Note that these are the same three cases previously used in the validation of the applied vessel impact load (AVIL) method in Chapter 6).

Both the size and shape of the pier column that will be impacted affect the barge force-deformation relationship that needs to be used. Pier columns for channel piers of the new St. George Island Causeway Bridge are circular in cross-section and 6-ft in diameter. Using equations presented earlier in Chapter 4, the yield load and yield deformation for a jumbo hopper barge are determined to be 1620 kips and 2 in. respectively (Figure 8.22).

Table 8.1 Impact energies for IRSA validation

Energy	Barge weight (tons)	Barge velocity (knot)	Impact energy (kip-ft)
Low	200	1	17.71
Moderate	2030	2.5	1123
High	5920	5	13100

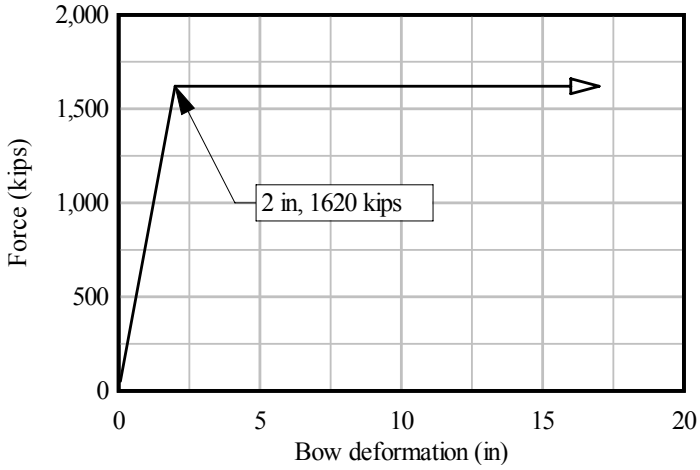

Figure 8.22 Barge bow force-deformation relationship for an impact on a six-foot round column

Each IRSA validation case used an event-specific DMF spectrum that corresponded to the impact energy of the collision being analyzed. Therefore, before each IRSA validation was performed, a corresponding CVIA was conducted to establish a time-history of impact load corresponding to the impact energy of interest. Each such impact load history was applied dynamically to a large number of SDOF structural systems (having varying natural periods) and the maximum dynamic displacement of each system (u_D) recovered. Additionally, for each case, the peak magnitude of impact load was determined (recall Figure 8.4) and applied to the SDOF structural system in a static sense so that the maximum static displacement of the system (u_S) was recovered. For each structural period (i.e. each SDOF system) the DMF was then calculated as the ratio of maximum dynamic to static displacement (i.e., DMF = u_D / u_S). For the given impact load history, the collection of all such DMF data points constitutes an event-specific DMF spectrum (recall Figure 8.5).

For each case in Table 8.1, an event-specific spectrum was generated (Figure 8.23) and an event-specific IRSA was conducted using the corresponding DMF spectrum. In each case, a total of 12 eigen modes were used and combined together using the SRSS and CQC techniques. The use of 12 eigen modes was necessary to ensure that the internal member force results from the IRSA using a design DMF spectrum were conservative with respect to CVIA results for all impact energy conditions.

Comparisons of the maximum absolute bending moments for all piles and columns in the model from dynamic analyses performed using the IRSA and CVIA methods are presented in Tables 8.2 and 8.3. The IRSA values presented in Table 8.2 were modally combined using the SRSS technique, whereas corresponding values in Table 8.3 were combined using the CQC technique. Additionally, Tables 8.2 and 8.3 present the total modal mass participation that was achieved by using 12 modes for each IRSA.

Figure 8.24 shows a profile of bending moments, which represents the maximum absolute bending moment throughout the duration of the analysis at a given elevation across all pier columns or piles, for both the CVIA and the event-specific IRSA using the CQC modal combination technique. Comparing values from Tables 8.2 and 8.3, the results from CQC modal combination are slightly more conservative than the results obtained from SRSS

combination. It should be noted that numerical analysis results for elevations within the pile cap thickness are not meaningful due to the manner in which FB-MultiPier models both the pile cap and the connections of the pier columns to the pile cap. For this reason, figures containing moment profiles (Figure 8.24 and, later, Figure 8.26) are formatted such that straight-lines connect the individual response profiles immediately above and below elevations that lie within the pile cap thickness.

Table 8.2 Maximum moments for all columns and piles for event-specific IRSA validation with SRSS combination

Impact energy	Bridge component	Bending moment (kip-ft)			IRSA total mass participation (12 modes)
		CVIA	Event-specific IRSA	Percent difference	
Low	Column	1541	1479	-4.0%	99.8%
	Pile	453.4	717.9	58%	
Moderate	Column	5288	5216	1.4%	99.9%
	Pile	1488	2642	78%	
High	Column	5307	5340	0.6%	99.9%
	Pile	1515	2665	76%	

Table 8.3 Maximum moments for all columns and piles for event-specific IRSA validation with CQC combination

Impact energy	Bridge component	Bending moment (kip-ft)			IRSA total mass participation (12 modes)
		CVIA	Event-specific IRSA	Percent difference	
Low	Column	1541	1496	-2.9%	99.8%
	Pile	453.4	762.1	68%	
Moderate	Column	5288	5613	6.1%	99.9%
	Pile	1488	2758	85%	
High	Column	5307	5745	8.2%	99.9%
	Pile	1515	2782	84%	

Inspection of Tables 8.2 and 8.3, and Figure 8.24 reveals that the pile and column moments from the event-specific IRSA cases (SRSS and CQC) generally agree well with the CVIA results, with the pile moments being relatively more conservative. In a few cases, the bending moments from the event-specific IRSA method are slightly unconservative in comparison to the coupled analysis results. This is due to the approximate nature of modal combination techniques such as SRSS and CQC. Such methods attempt to quantify maximal dynamic responses by combining individual modal responses that may maximize at different points in time during the vessel collision. Since response spectrum techniques do not account for such timing issues, the results obtained are approximate in nature. However, in practical design situations, a design DMF spectrum will be used instead of an event specific DMF spectrum. Since a design DMF spectrum is inherently more conservative than an event-specific spectrum, the use of IRSA in design situations will generally lead to conservative results, although this is not absolutely guaranteed. Additionally, using a CQC modal

combination rather than an SRSS combination can further increase the likelihood of obtaining conservative design data.

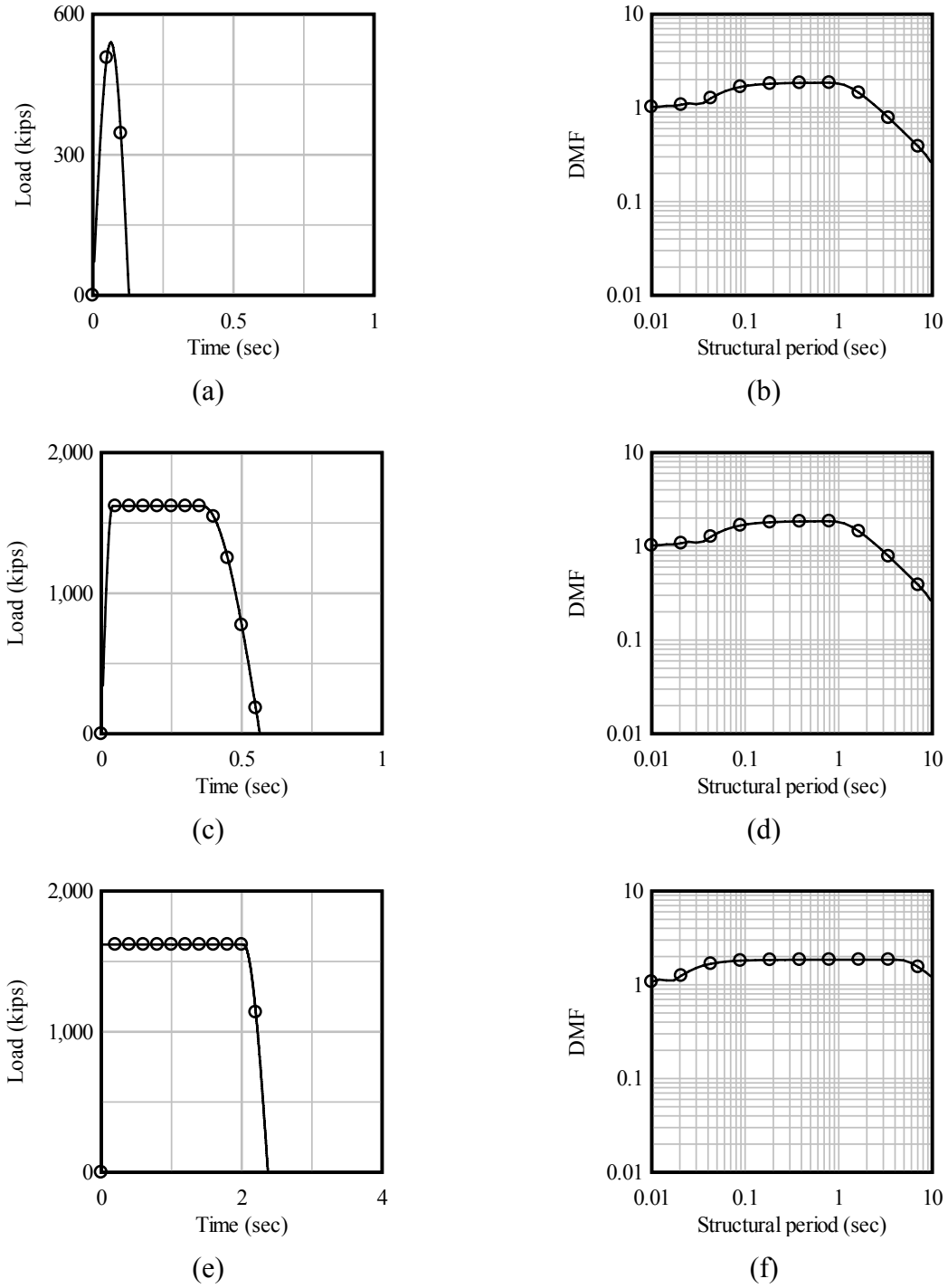

Figure 8.23 Event-specific IRSA validation: a) Low-energy impact load, b) Low-energy event-specific DMF, c) Moderate-energy impact load, d) Moderate-energy event-specific DMF, e) High-energy impact load, f) High-energy event-specific DMF

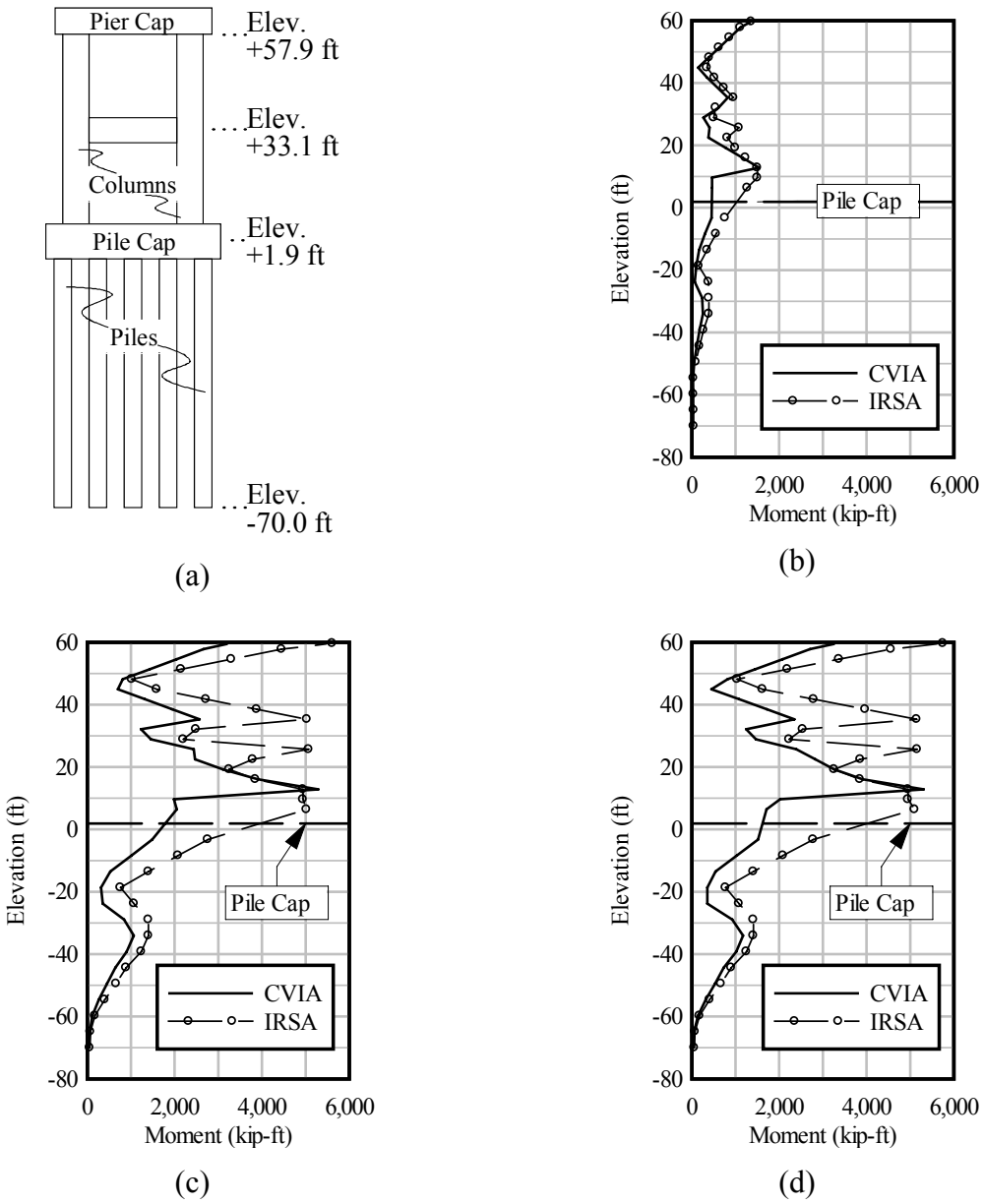

Figure 8.24 Moment results profile for the new St. George Island Causeway Bridge channel pier:a) Channel pier schematic, b) Low-energy impact, c) Moderate-energy impact, and d) High-energy impact

8.6.2 Design-Oriented Impact Response Spectrum Analysis Demonstration

To demonstrate the IRSA method as it would be used in design, the three impact scenarios considered above for validation purposes are re-analyzed. With the exception of the DMF spectra used, all parameters and procedures in the demonstration analyses are the same as those used during validation. In the demonstration cases, design DMF spectra (constructed using Eqns. 8.31 through 8.37) are used in place of the event-specific spectra that were used in the validation process.

For each case in Table 8.1, an IRSA was conducted using the non-linear procedure outlined in Figures 8.20 and 8.21. In each case, a total of 12 eigen modes were combined together using the SRSS and CQC techniques. Comparisons of the maximum absolute bending moments for all piles or columns in the model from dynamic analyses performed using the IRSA and CVIA methods are presented in Tables 8.4 and 8.5. The IRSA values presented in Table 8.4 were modally combined using the SRSS technique, whereas corresponding values in Table 8.5 were obtained by modal combination using the CQC technique. Tables 8.4 and 8.5, also present the total modal mass participation that was achieved by using 12 modes for each IRSA.

Table 8.4 Maximum moments for all columns and piles for design IRSA demonstration with SRSS combination

Impact energy	Bridge component	Moment (kip-ft)			IRSA total mass participation (12 modes)
		CVIA	Design IRSA	Percent difference	
Low	Column	1541	1542	0.1%	99.8%
	Pile	453.4	777.5	71%	
Moderate	Column	5288	5731	8.4%	99.9%
	Pile	1488	2786	87%	
High	Column	5307	5731	8.0%	99.9%
	Pile	1515	2786	84%	

Table 8.5 Maximum moments for all columns and piles for design IRSA demonstration with CQC combination

Impact energy	Bridge component	Moment (kip-ft)			IRSA total mass participation (12 modes)
		CVIA	Design IRSA	Percent difference	
Low	Column	1541	1694	9.9%	99.8%
	Pile	453.4	835.2	84%	
Moderate	Column	5288	6164	17%	99.9%
	Pile	1488	2903	95%	
High	Column	5307	6164	16%	99.9%
	Pile	1515	2903	92%	

As stated above, inclusion of 12 eigen modes was necessary to ensure that the design IRSA results were conservative with respect to CVIA results for all impact energy conditions. Table 8.6 shows the modal mass participation for each of the 12 eigen modes used and the cumulative mass participation.

Table 8.6 Mass participation by mode for design IRSA

Modes	Low energy		Moderate energy		High energy	
	Mass Participation	Cumulative Participation	Mass Participation	Cumulative Participation	Mass Participation	Cumulative Participation
1	0.00%	0.00%	0.00%	0.00%	0.00%	0.00%
2	3.95%	3.95%	5.86%	5.86%	5.86%	5.86%
3	56.60%	60.55%	55.04%	60.90%	55.04%	60.90%
4	16.59%	77.14%	16.58%	77.48%	16.58%	77.48%
5	0.01%	77.15%	0.00%	77.48%	0.00%	77.48%
6	14.94%	92.09%	15.56%	93.04%	15.56%	93.04%
7	0.01%	92.10%	0.02%	93.06%	0.02%	93.06%
8	0.00%	92.10%	0.00%	93.06%	0.00%	93.06%
9	0.00%	92.10%	0.00%	93.06%	0.00%	93.06%
10	0.00%	92.10%	0.00%	93.06%	0.00%	93.06%
11	2.87%	94.97%	5.24%	98.30%	5.24%	98.30%
12	4.84%	99.81%	1.63%	99.92%	1.63%	99.92%

Including 6 modes in the IRSA analyses yields 90% mass participation—as is required in earthquake analysis. However, it was found that the use of 90% mass participation yielded IRSA results that were unconservative with respect to CVIA results. Therefore, inclusion of mode 11 (the next major modal contribution) was investigated—bringing the cumulative mass participation to between 95% and 98.3%. Inclusion of mode 11 for the low impact energy condition, however, still yielded column force results that were slightly unconservative with respect to CVIA pile force results. Inclusion of mode 12—which corresponded to greater than 99% cumulative mass contribution for all impact energy conditions—yielded IRSA results that were conservative with respect to CVIA results. Therefore, it is recommended that 99% modal mass participation be achieved to ensure conservative IRSA results.

Figure 8.26 shows profiles of bending moments, which represents the maximum absolute bending moment throughout the duration of the analysis at a given elevation across all pier columns or piles, for both the CVIA and the design IRSA using a CQC modal combination technique. As with the validation cases discussed above, comparing values from Tables 8.4 and 8.5, results from CQC modal combination are slightly more conservative than results obtained from SRSS combination.

The data presented in Tables 8.4 and 8.5, and Figure 8.26 reveal that pile and column moments from the design-oriented IRSA agree well with the CVIA results, with the pile results being relatively more conservative. Additionally, as expected, use of a design DMF spectrum added an extra level of conservatism, making the IRSA results conservative with respect to CVIA results.

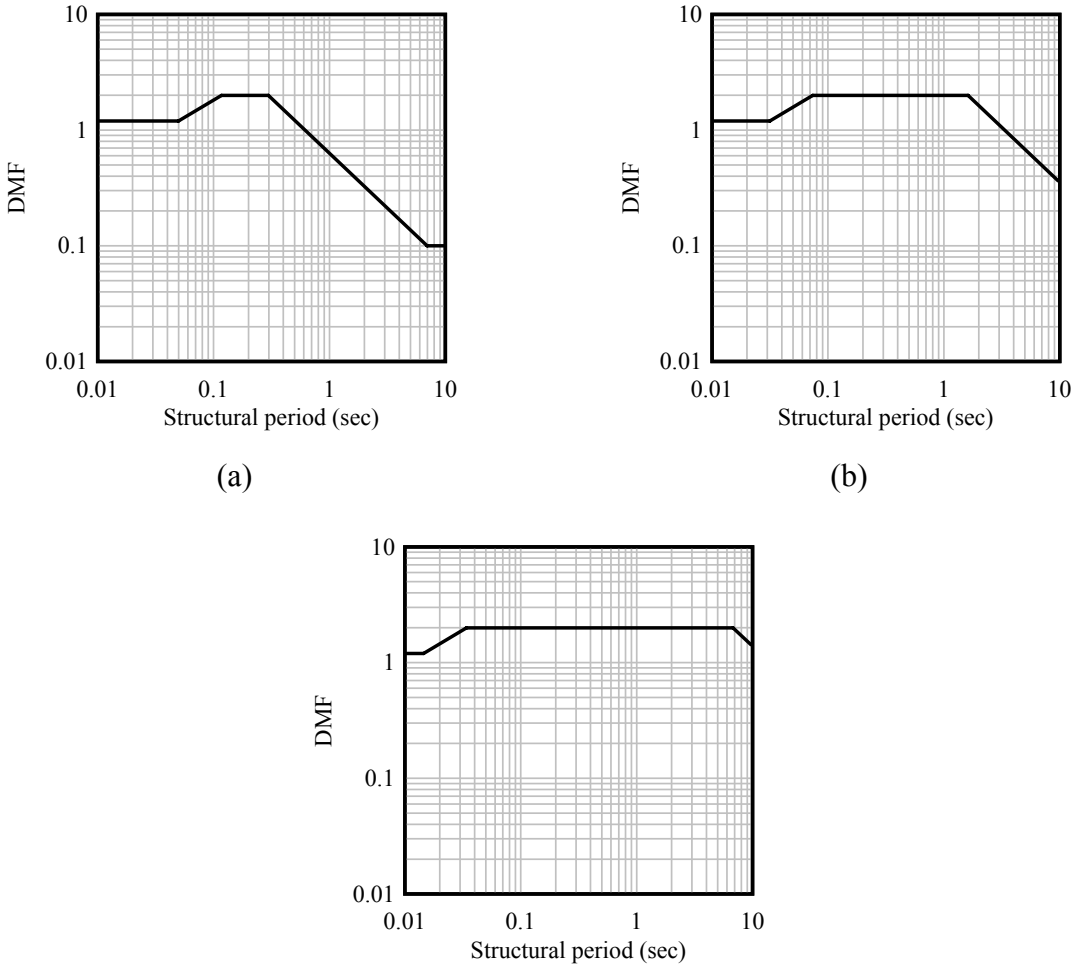

Figure 8.25 Design-oriented IRSA demonstration: a) Low-energy design DMF, b) Moderate-energy design DMF, and c) High-energy design DMF

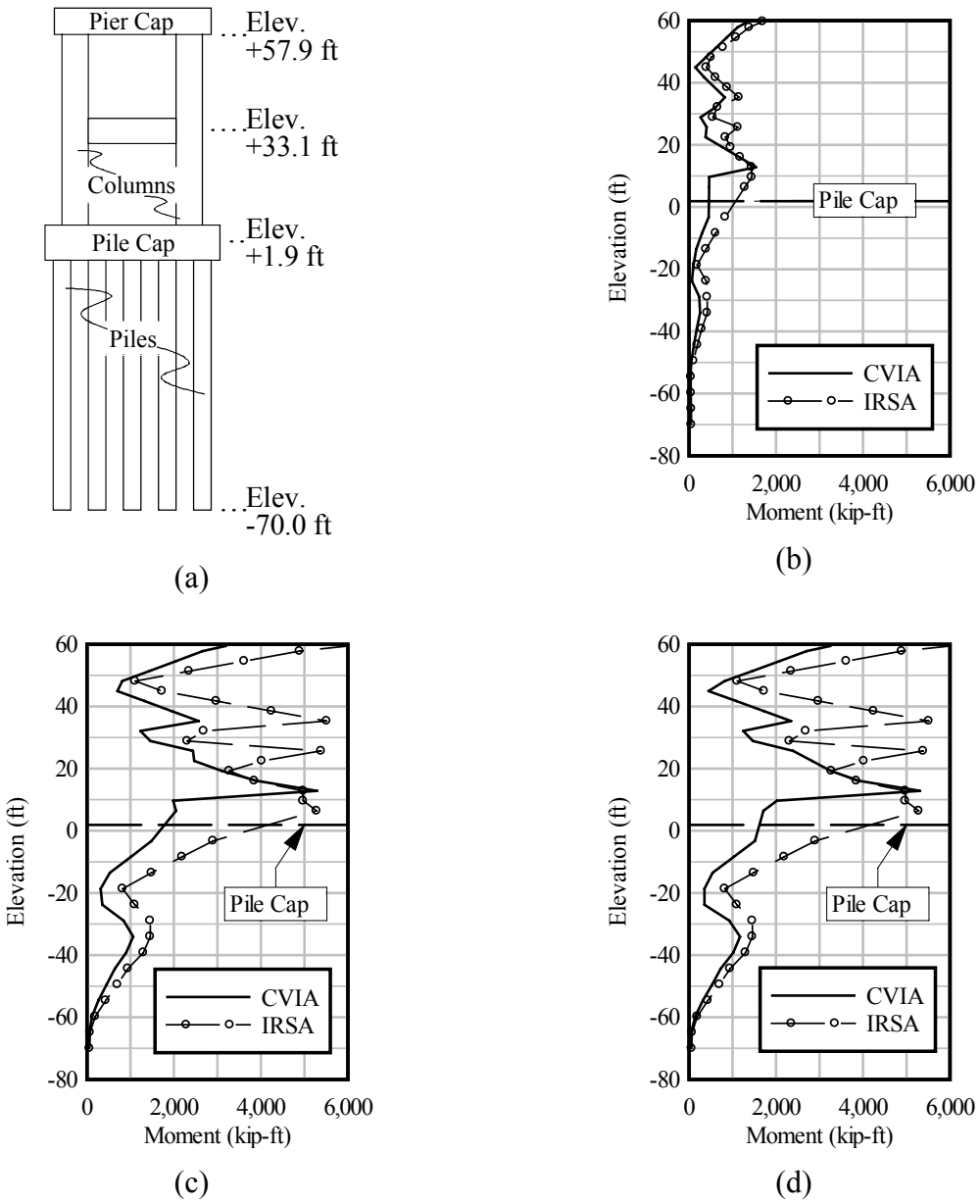

Figure 8.26 Moment results profile for the new St. George Island Causeway Bridge channel pier: a) Channel pier schematic, b) Low-energy impact, c) Moderate-energy impact, and d) High-energy impact

CHAPTER 9
PARAMETRIC STUDY

9.1 Introduction

Two dynamic analysis techniques have been proposed in this report: coupled vessel impact analysis (CVIA) and impact response spectrum analysis (IRSA). The CVIA technique has been validated against both experimental data and high-resolution finite element analysis, and has been demonstrated for selected impact conditions (Chapter 5 of this report; Hendrix 2003; Consolazio 2005). The IRSA method has also been validated and demonstrated (Chapter 8). Additionally, the one-pier-two-span (OPTS) modeling technique has been successfully demonstrated in conjunction with CVIA and IRSA in Chapters 6 and 8, respectively.

Previously presented validation cases for each method have focused on three bridges: old St. George Island Causeway Bridge; new St. George Island Causeway Bridge; and the I-10 bridge spanning Escambia Bay. While these are representative bridges, they do not encompass the full range of bridge structures currently in service in Florida and throughout the nation. Therefore, FB-MultiPier models of additional bridge structures of varying age, size, and structural configuration were developed to form a bridge model database.

Once developed, models from the database were employed in a parametric study, the primary goals of which were to :

- Evaluate the level of agreement between full-bridge and simplified OPTS models for a broad range of bridge and pier configurations;
- Ensure that reasonable levels of conservatism were obtained from IRSA as compared to corresponding CVIA results; and
- Evaluate the extent to which dynamic effects generated increased design forces as compared to those produced by the current AASHTO static procedure.

Consequently, a series of bridge-pier models were analyzed in FB-MultiPier using three analysis methods: CVIA, IRSA, and the current AASHTO equivalent static load method.

9.2 Parametric Study Description

9.2.1 Bridge Model Parameters

For purposes of demonstrating the proposed dynamic methods, and comparing them to the current AASHTO method, a total of seventeen models were developed for various piers of thirteen different bridges currently located in Florida (Table 9.1). For conciseness and to simplify discussion, each bridge structure has been given a three letter identification code. For use in generating the models, structure and soil data for each bridge were obtained from construction drawings. The bridges listed in Table 9.1 were specifically selected from a larger catalog of almost two-hundred bridge structures to represent a diverse cross-section of bridge types currently in service. The thirteen bridges that were selected vary widely in age, with construction dates spanning from the 1960s up to 2004.

Considering that the *AASHTO Guide Specification and Commentary for Vessel Collision Design of Highway Bridges* was first published in 1991, only bridges constructed

after that date would have been designed for impact scenarios according to current design specifications. Thus, several bridges from the catalog are characteristic of bridges designed for vessel impact using the AASHTO provisions, whereas others were not designed according to current specifications. In Table 9.2, impact design forces for each bridge pier are reported, per the AASHTO design specifications. Bridge piers for which no impact force is specified were not designed in accordance with the AASHTO specifications.

Table 9.1 Bridge inventory

Bridge	Identifier
Acosta Bridge	ACS
SR-20 at Blountstown	BLT
Eau Gallie Bridge	EGB
I-10 over Escambia Bay	ESB
Gandy Bridge	GND
Howard Frankland	HFK
Melbourne Cswy	MBC
New St George Island	NSG
Old St George Island	OSG
Pineda Cswy	PNC
Ringling	RNG
Seabreeze	SBZ
Santa Rosa Bay	SRB

Table 9.2 Bridge pier impact design force

Bridge		Design static impact force (kips)
ID	Span	
ACS	Channel	3500
BLT	Channel	2550
	Off-channel	-
EGB	Channel	-
ESB	Channel	2067
GND	Channel	2400
HFK	Channel	-
MBC	Channel	-
NSG	Channel	3255
	Off-channel	2300
OSG	Channel	-
	Off-channel	-
PNC	Channel	-
RNG	Channel	2100
	Off-channel	100
SBZ	Channel	2200
SRB	Channel	2000

Earlier, in Chapter 4, results from high-resolution finite element barge bow crush simulations demonstrated that the geometry (shape and size) of the impacted portion of the

bridge pier affects the magnitude of impact loads generated during a collision. Hence, in the parametric study, bridges were selected that varied both in pier column shape (planar vs. non-planar) and pier column size (from 4 ft to 18 ft in width). Table 9.3 summarizes pier shape and size data. While the current AASHTO equivalent static load method does not account for pier column geometry and width, the load generated for each of the proposed methods is pier-width dependent. Thus, it is necessary to account for the varying size and shape of the pier columns.

Table 9.3 Bridge pier column geometry

Bridge		Column		
Identifier	Location	Num. columns in impacted pier	Width	Shape
ACS	Channel	1	20 ft	Planar
BLT	Channel	2	5 ft – 6 in.	Non-planar
	Off-channel	2	5 ft – 6 in.	Non-planar
EGB	Channel	4	4 ft	Planar
ESB	Channel	2	6 ft	Planar
GND	Channel	1	4 ft – 6 in.	Planar
HFK	Channel	2	4 ft – 6 in.	Planar
MBC	Channel	2	4 ft – 6 in.	Non-planar
NSG	Channel	2	6 ft	Non-planar
	Off-channel	2	5 ft – 6 in.	Non-planar
OSG	Channel	2	5 ft – 6 in.	Planar
	Off-channel	2	3 ft – 6 in.	Planar
PNC	Channel	2	4 ft – 6 in.	Non-planar
RNG	Channel	1	13 ft	Non-planar
	Off-channel	1	13 ft	Non-planar
SBZ	Channel	1	8 ft	Planar
SRB	Channel	1	8 ft	Planar

Bridge structures were also chosen for their varying foundation types (pile-and-cap or drilled shaft) and sizes. Table 9.4 summarizes foundation types and sizes for bridges included in the parametric study. Additionally, the general elevation where the pier structure transitions to the foundation is given. A waterline footing indicates that the foundation begins near mean sea level, whereas a mudline footing indicates the foundation begins near the elevation of the top of the soil.

The extent to which impact load on a pier is distributed to adjacent piers through the superstructure is dependent upon the type of superstructure that connects the piers together. In the parametric study, three common superstructure types (Table 9.5) were included : slab on concrete girders; slab on steel girders; and segmental concrete box girder.

Table 9.4 Bridge pier foundations

Bridge		Foundation			
Identifier	Location	Cap elevation	Shaft / pile type	Shaft / pile width (in)	Total num. of shafts / piles
ACS	Channel	Waterline	Drilled Shaft	60	31
BLT	Channel	Waterline	Drilled Shaft	108	2
	Off-channel	Waterline	Drilled Shaft	72	2
EGB	Channel	Mudline	Steel pile	14	39
ESB	Channel	Waterline	Concrete pile	24	12
GND	Channel	Waterline	Drilled Shaft	84	4
HFK	Channel	Mudline	Concrete pile	30	32
MBC	Channel	Mudline	Concrete pile	18	32
NSG	Channel	Waterline	Concrete pile	54	15
	Off-channel	Waterline	Concrete pile	54	9
OSG	Channel	Mudline	Steel pile	14	36
	Off-channel	Waterline	Concrete pile	20	8
PNC	Channel	Mudline	Concrete pile	20	30
RNG	Channel	Waterline	Drilled Shaft	108	2
	Off-channel	Waterline	Drilled Shaft	108	2
SBZ	Channel	Mudline	Concrete pile	24	32
SRB	Channel	Waterline	Concrete pile	20	24

Table 9.5 Superstructure type

Bridge		Superstructure Type		
Identifier	Location			
ACS	Channel			Concrete box
BLT	Channel	Concrete slab on:	Concrete girders	
	Off-channel	Concrete slab on:	Concrete girders	
EGB	Channel	Concrete slab on:	Concrete girders	
ESB	Channel	Concrete slab on:	Steel girders	
GND	Channel	Concrete slab on:	Concrete girders	
HFK	Channel	Concrete slab on:	Concrete girders	
MBC	Channel	Concrete slab on:	Steel girders	
NSG	Channel	Concrete slab on:	Concrete girders	
	Off-channel	Concrete slab on:	Concrete girders	
OSG	Channel	Concrete slab on:	Steel girders	
	Off-channel	Concrete slab on:	Concrete girders	
PNC	Channel	Concrete slab on:	Concrete girders	
RNG	Channel			Concrete box
	Off-channel			Concrete box
SBZ	Channel			Concrete box
SRB	Channel			Concrete box

In FB-MultiPier, soil-pile interaction is modeled using nonlinear *p-y*, *t-z*, and *q-z* springs to represent lateral, skin friction, and end-bearing resistance, respectively. FB-MultiPier does not, however, require that the user define the force-deformation relationships for these nonlinear springs. Instead, the software generates force-deformation data automatically, based on user-specified soil properties. Specifically, FB-MultiPier can employ correlations between SPT blow counts and soil type to form the needed soil force-deformation relationships. This method was employed for all models developed and analyzed as part of the parametric study.

9.2.2 Impact Conditions

As previously noted, each bridge in the parametric study was analyzed using three analysis methods: CVIA, IRSA, and AASHTO static analysis. Using each of these methods requires the user to supply the impact characteristics of the barge: barge mass and initial velocity (recall that standardized barge-bow force-deformation relationships were developed in Chapter 4; these are employed in the CVIA and IRSA analyses). Thus, a representative set of barge masses and impact velocities were determined for use in the parametric study.

The first step in establishing the parametric study impact conditions consisted of selecting the barge type. As noted earlier in this report, jumbo hopper barges comprise nearly half of the currently active U.S. barge fleet. Therefore, for the parametric study, a jumbo hopper barge was selected as the design vessel. According to AASHTO, the empty displacement of a jumbo hopper barge is 200 tons, and the maximum payload capacity is 1700 tons—bringing the fully loaded displacement to 1900 tons (AASHTO 1991).

Many of the bridges considered in this study were designed for impact loading according to the AASHTO vessel collision design specifications. Based on the AASHTO design static impact forces presented earlier in Table 9.2, the initial kinetic energy of the barge for each impact case can be calculated from the AASHTO design equations. Eqn. 9.1 and 9.2, which permit kinetic energy to be computed from static impact force, were derived for a jumbo hopper barge ($R_B = 1$) from the AASHTO equations presented in Chapter 2.

$$a_B = \begin{cases} \dfrac{P_B}{4112} & \text{if } P_B < 1398 \\ \dfrac{P_B - 1349}{110} & \text{if } P_B \geq 1398 \end{cases} \tag{9.1}$$

$$KE = 5672\left[\left(\frac{a_B}{10.2} + 1\right)^2 - 1\right] \tag{9.2}$$

In these equations, P_B is the AASHTO equivalent static force (kips); a_B is the barge bow crush depth (ft); and, KE is the initial kinetic energy of the barge (kip-ft). In Table 9.6 AASHTO impact design forces are listed together with the corresponding barge bow crush depths and initial barge kinetic energies.

If the total mass of the barge tow is known, the initial velocity of the tow can be calculated from the design kinetic energy. Construction drawings for several of the bridges considered in the parametric study identified the type, number, and loading of design barges

used to generate the AASHTO loads. Based on general consistency among descriptions of design vessels, it was determined that three fully loaded jumbo hopper barges—which corresponds to a total barge tow displacement of 5700 tons—be used to calculate a design velocity.

Because barges are typically not self-propelled, and thus require a tugboat, the displacement of the tugboat must be included in the total displacement of the barge tow used for design. Based on barge displacement, FDOT has categorized typical tug traffic in Florida into three types: small, medium, and large (Table 9.7) (Liu 2001). Table 9.7 indicates that a large tug (displacement of 220 tons) is required for a 5700-ton barge tow—bringing the total barge tow displacement up to 220 + 5700 = 5920 tons.

Table 9.6 Bridge design impact data per AASHTO

Bridge		Design impact force (kips)	Bow crush depth (ft)	Barge kinetic energy (kip-ft)	Barge initial velocity (knot)
ID	Span				
ACS	Channel	3500	19.55	42594	9.01
BLT	Channel	2550	10.92	18642	5.96
	Off-channel	-	-	-	-
EGB	Channel	-	-	-	-
ESB	Channel	2067	6.53	9589	4.28
GND	Channel	2400	9.55	15603	5.46
HFK	Channel	-	-	-	-
MBC	Channel	-	-	-	-
NSG	Channel	3255	17.33	35639	8.25
	Off-channel	2300	8.65	13690	5.11
OSG	Channel	-	-	-	-
	Off-channel	-	-	-	-
PNC	Channel	-	-	-	-
RNG	Channel	2100	6.83	10134	4.40
	Off-channel	100	0.02	27	0.23
SBZ	Channel	2200	7.74	11867	4.76
SRB	Channel	2000	5.92	8491	4.03

Table 9.7 Tug selection table

Tug type	Displacement (tons)	Tow displacement (tons)
Small	65	≤1000
Medium	130	>1000 and ≤2000
Large	220	>2000

Using the barge tow weight and initial kinetic energy, the initial velocity (impact velocity) of the barge tow can be calculated as:

$$v_{Bi} = \left(\frac{2 \cdot KE \cdot g}{w_B \cdot C_H} \right) \tag{9.3}$$

where v_{Bi} is the impact velocity of the barge tow; W_B is the total displacement of the barge tow; g is the gravitational constant (32.2 ft/sec^2); and, C_H is the hydrodynamic mass coefficient. Note that for all cases analyzed as part of the parametric study, the hydrodynamic mass coefficient (C_H) was set to unity (1.0) to simplify comparisons between the AASHTO static analyses and the dynamic analyses (CVIA and IRSA). Computed barge velocities for all bridge models are presented in Table 9.6. Most of the velocities reported in Table 9.6 fall between 4.0 and 6.0 knots, with the exception of a few outliers: 0.23, 8.25, and 9.01 knots. These outlier velocities are difficult velocities for a tug towing three jumbo hopper barges to maintain. Therefore, excluding the outliers, the mean velocity of the remaining velocity data is 4.9 knots. Rounding to the nearest knot, the average design velocity becomes 5.0 knots. Thus, a high-energy design case is defined for the parametric study as a 5920-ton barge tow traveling at 5.0 knots. Additionally, a moderate-energy case is defined as one fully loaded hopper barge (2030-ton displacement with tug) traveling at 2.5 knots (half of the average design speed).

The AASHTO vessel collision specification requires that all bridge components located in navigable water depths be designed for a minimum impact condition (AASHTO 1991). A typical impact condition for most waterways is specified as a single empty hopper barge (200 tons) drifting at a velocity equal to the mean water current for the waterway. Using water-current data for several waterways in Florida, an average current of 0.75 knots was calculated. Rounding this water-current velocity to the nearest knot yields a current of 1.0 knots. Thus, a low-energy design case for this study is defined as a 200-ton barge drifting at 1 knot.

The three design impact-energy cases (low, moderate, and high) encompass all feasible impact scenarios for all but two of the bridges employed in the parametric study. However, as shown in Table 9.2, the NSG and ACS channel piers were designed for loads significantly larger than the other bridge-pier configurations in the dataset. If the initial barge tow velocities for the ACS and NSG channel span models are calculated using a four jumbo hopper barge tow (a total displacement of 7820 tons), then the design velocities become 7.84 and 7.17 knots respectively. These two cases represent a severe-energy design case, defined as a 7820-ton barge tow traveling at 7.5 knots (the average velocity for these two cases).

Parameters for each of impact conditions (low, moderate, high, and severe) are summarized in Table 9.8. Using the AASHTO equations, the barge bow crush depth and static design load can be calculated from the initial barge kinetic energy. The low-energy case represents a situation in which the barge bow remains elastic, whereas in the other cases, the barge bow sustains inelastic (plastic) deformation. The moderate-energy case represents a situation in which the barge bow has just passed the transition from elastic to plastic bow deformation (according to AASHTO). To illustrate the range of impact energies considered, the four standardized impact cases are presented as points along the AASHTO force versus kinetic energy prediction curve (Figure 9.1).

Table 9.8 Barge impact energy conditions

Impact energy	Barge tow weight (tons)	Tow velocity (knots)	KE of barge tow (kip-ft)	Bow crush depth (ft)	Design Load (kips)
Low	200	1	17.71	0.02	65
Moderate	2030	2.5	1123	0.96	1455
High	5920	5	13100	8.36	2268
Severe	7820	7.5	38950	18.41	3374

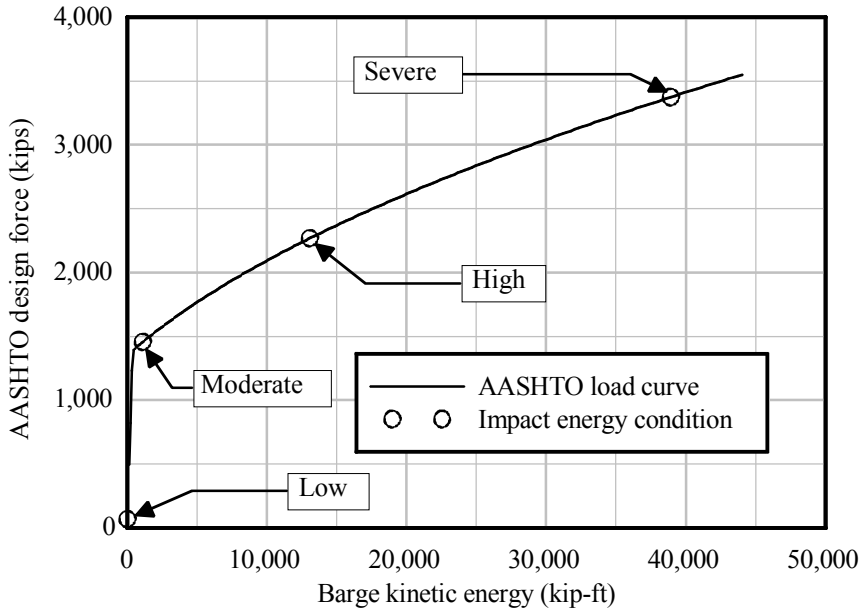

Figure 9.1 Standard impact conditions considered in parametric study

9.2.3 Analyses Performed

As noted earlier, the primary goals in carrying out the parametric study were to 1) evaluate the accuracy simplified OPTS models as compared to full-bridge models; 2) evaluate the level of conservatism of IRSA in comparison to CVIA; and 3) determine the extent to which dynamic amplification effects produce design forces that are larger than those computed using the AASHTO static methodology. These goals were accomplished by conducting the parametric study in two stages:

- Stage I: Conduct coupled vessel impact analyses (CVIA) using full-bridge models and simplified OPTS models for a subset of the overall bridge inventory;
- Stage II: Conduct CVIA, IRSA, and AASHTO analyses using OPTS models for all structures in the bridge inventory.

Stage I of the parametric study consisted exclusively of CVIA analyses for selected full-bridge and OPTS models. The main criterion used for bridge selection during Stage I was structural variability: each bridge was required to possess some feature (e.g. foundation type, superstructure type, age, and/or pier stiffness) not shared by other bridges analyzed in

Stage I. Based on this approach, eight different structural configurations (channel and off-channel structures for four different bridges) were analyzed by conducting CVIA analyses on both OPTS and full-bridge models (Table 9.9).

Structural systems employed in Stage I bridge models were relatively diverse, encompassing: three distinct superstructure types; waterline and mudline footings; and, pile-and-cap and drilled shaft foundations. Collectively, these bridges constitute a range of approximately 40 years in terms of construction date. Impact-energy conditions were assigned to each bridge-pier configuration in accordance with: the pier location within the waterway (channel or off-channel); the completed construction date (bridges designed before the advent of the AASHTO specifications were not subjected to high or severe impact-energy conditions); and, when available, the AASHTO specification design-impact load. Consequently, as shown in Table 9.9, only the NSG channel pier (a modern, stiff pier designed using a relatively large AASHTO static impact load) is subject to the full range of impact-energy conditions (low, moderate, high, severe). This is in contrast to, for example, the OSG off-channel pier (an older, flexible pier designed prior to publication of the current AASHTO design specifications) which is subjected to only the low and moderate impact-energies.

After confirming the accuracy of the OPTS modeling method in Stage I of the parametric study, Stage II was conducted exclusively using OPTS models (i.e., no additional full-bridge models were analyzed). Stage II consisted of CVIA analyses on OPTS models of bridges not analyzed during Stage I, and subsequent IRSA and AASHTO analyses of OPTS models for all 17 bridge-pier configurations in the dataset (Table 9.10). Assignment of impact-energy conditions to individual bridge-pier configurations was conducted in a manner analogous to that employed in Stage I.

Table 9.9 Stage I : OPTS vs. full-bridge analysis matrix

Case identifier	Channel (CHA) or Off-channel (OFF)	Analysis type	Impact energy condition (X = Analyzed)			
			Low	Moderate	High	Severe
BLT	CHA	CVIA		X	X	
	OFF	CVIA	X	X		
NSG	CHA	CVIA	X	X	X	X
	OFF	CVIA	X	X	X	
OSG	CHA	CVIA	X	X		
	OFF	CVIA	X	X		
RNG	CHA	CVIA		X	X	
	OFF	CVIA	X	X		

Table 9.10 Stage II : AASHTO vs. CVIA vs. IRSA analysis matrix

Case identifier	Channel (CHA) or Off-channel (OFF)	Analysis type	Impact energy condition (X = Analyzed)			
			Low	Moderate	High	Severe
ACS	CHA	AASHTO		X	X	X
		CVIA		X	X	X
		IRSA		X	X	X
BLT	CHA	AASHTO		X	X	
		CVIA		X	X	
		IRSA		X	X	
	OFF	AASHTO	X	X		
		CVIA	X	X		
		IRSA	X	X		
EGB	CHA	AASHTO	X	X		
		CVIA	X	X		
		IRSA	X	X		
ESB	CHA	AASHTO		X	X	
		CVIA		X	X	
		IRSA		X	X	
GND	CHA	AASHTO		X	X	
		CVIA		X	X	
		IRSA		X	X	
HFK	CHA	AASHTO	X	X		
		CVIA	X	X		
		IRSA	X	X		
MBC	CHA	AASHTO	X	X		
		CVIA	X	X		
		IRSA	X	X		
NSG	CHA	AASHTO	X	X	X	X
		CVIA	X	X	X	X
		IRSA	X	X	X	X
	OFF	AASHTO	X	X	X	
		CVIA	X	X	X	
		IRSA	X	X	X	
OSG	CHA	AASHTO	X	X		
		CVIA	X	X		
		IRSA	X	X		
	OFF	AASHTO	X	X		
		CVIA	X	X		
		IRSA	X	X		

Table 9.10 Stage II : AASHTO vs. CVIA vs. IRSA analysis matrix (continued)

Case identifier	Channel (CHA) or Off-channel (OFF)	Analysis type	Impact energy condition (X = Analyzed)			
			Low	Moderate	High	Severe
PNC	CHA	AASHTO	X	X		
		CVIA	X	X		
		IRSA	X	X		
RNG	CHA	AASHTO		X	X	
		CVIA		X	X	
		IRSA		X	X	
	OFF	AASHTO	X	X		
		CVIA	X	X		
		IRSA	X	X		
SBZ	CHA	AASHTO		X	X	
		CVIA		X	X	
		IRSA		X	X	
SRB	CHA	AASHTO		X	X	
		CVIA		X	X	
		IRSA		X	X	

9.3 Parametric Study Results

A total of 152 unique barge-bridge impact scenarios were considered in the parametric study. Specifically, 38 AASHTO static analyses; 76 CVIA analyses (including 19 full-bridge models and 57 OPTS models); and, 38 IRSA analyses were conducted. Later in this chapter, detailed graphical summaries of key parametric analysis results will be presented. (Additionally, detailed results for all parametric analysis cases can be found in Appendices A and B). Prior to presenting the result summaries, however, more in-depth discussions of analyses conducted on a single structure, the new St. George Island Causeway Bridge (NSG) channel pier, will be presented. Being recently constructed (the bridge was opened to traffic in 2004), the NSG structure was designed according to current AASHTO standards and is capable of being subjected to the severe impact-energy condition, as defined earlier. Hence, it is representative of current practice in regard to barge impact design of bridge structures.

Both the full-bridge and OPTS models of the NSG bridge (Figure 9.2) were derived from construction drawings. Per these drawings, Pier 46 through Pier 49 support five cantilever-constructed Florida Bulb-T girder-and-slab segments at span lengths of 250 ft for the channel and 257.5 ft for the flanking spans. Due to haunching, the depths of the post-tensioned Bulb-T girders vary from 6.5 ft at drop-in locations to 12 ft at the pier cap beam bearing locations. Simply supported Florida Bulb-T girders with a depth equal to that of the haunched girders at the drop-in locations span either side of Pier 50. All piers included in the full-bridge model contain two pier columns, a shear strut centered near the pier column mid-height, a pile cap, and waterline footing system. The central pier, Pier 48, contains two round 6 ft diameter pier columns; a 6.5 ft thick pile cap; and fourteen battered and one central

plumb 4.5 ft diameter prestressed cylinder piles with 10 ft concrete plugs extending earthward from the pile cap. The NSG full-bridge model includes both of the channel piers and three auxiliary piers. Similar to the full-bridge models discussed in Chapter 6, five consecutive piers were considered to be sufficient to represent the behavior of the full bridge considering impacts at the channel pier. In the OPTS models of the bridge, the impacted pier, Pier 48, was included together with respective adjacent spans, model-end springs, and lumped masses per the methodology established in Chapter 6.

For the severe energy impact condition, the static AASHTO design impact load of 3255 kips was employed in the AASHTO analysis. For the dynamic CVIA and IRSA analyses, the severe impact-energy conditions, obtained using the static impact design load and the AASHTO specification, consisted of a barge-tow of 7820 tons traveling at 7.5 knots.

Impact loads on the NSG structure were applied to one of the pier columns at a point located a nominal distance above the pile cap. At this location, the impact zone width and shape—needed for selection of an appropriate barge crush model per Chapter 4—were 6 ft and circular (non-planar). A barge crush curve corresponding to these parameters was used for both the CVIA and IRSA analyses.

Note that had the impact point been assumed to be at the 28 ft wide pile cap of pier 48, a barge crush-curve corresponding to large-width, planar impact conditions would have been needed for the dynamic analyses. For perfectly head-on impact conditions, very large width planar impact zones produce barge crush curves that exhibit correspondingly large impact forces. However, the probability of achieving a perfectly head-on impact condition decreases as the width of the planar impact zone increases. Addressing this issue is an area of current and ongoing research and is therefore beyond the scope of this report.

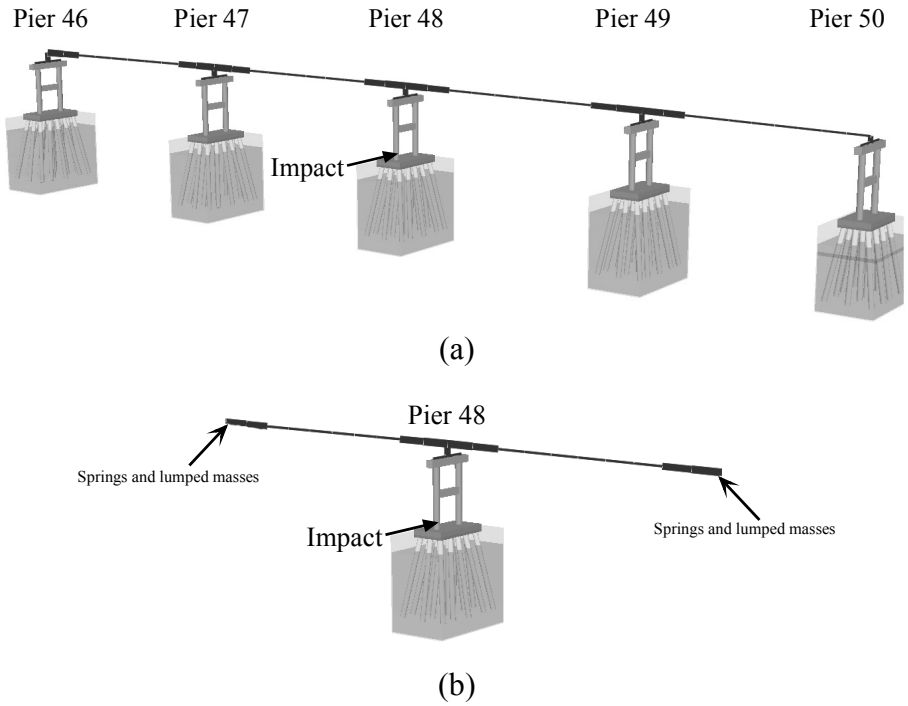

Figure 9.2 NSG channel structural configurations a) full-bridge model; b) OPTS model

9.3.1 Discussion of full-bridge vs. OPTS analyses for a single bridge

Full-bridge versus OPTS summary data for CVIA analyses of the NSG channel pier, subject to the severe impact-energy case, are presented in Figure 9.3. The structural configuration of the pier is also is shown in the figure to provide indicators of the relative elevations of water, soil, and impact point. (Note that although the superstructure is not shown in the figure, it was included in all analyses conducted).

Response time-history plots of displacement, shear force, and moment are presented for points throughout the pier. Data is provided for the left-most pier column top (denoted point Ⓐ), the impact location (denoted point Ⓑ), and the left-corner pile head (denoted point Ⓒ). The response time-history plots show good agreement between the full-bridge and OPTS model analyses at all three locations. Particularly, the impact load-histories and load-displacement plots exhibit excellent agreement regarding magnitude, duration, and barge crush-depth. Most pertinent to the design of structural components, the maximum internal shears and moments for both the piles and pier columns are quantified immediately below the set of response time-history plots. The locations at which these maxima occur are indicated on the structural configuration diagram for both the full-bridge and OPTS model analyses. Note the consistency of predicted maximum force locations between the two model-types (full-bridge and OPTS), and also the internal force magnitudes. Internal forces obtained from OPTS analyses are shown to be slightly to moderately conservative in comparison to corresponding forces obtained from full-bridge analyses.

Data pertaining to all other full-bridge vs. OPTS analyses that were conducted in Stage I of the parametric study are included in Appendix A. For consistency, data shown in Appendix A adhere to the visual layout established in Figure 9.3. Examination of Appendix A reveals agreement between full-bridge and OPTS analyses that are consistent with the data shown in Figure 9.3. In general, OPTS analyses are found to predict design forces that range from nominally to moderately conservative in comparison to corresponding values computed from full-bridge analysis. Given that good agreement between full-bridge and OPTS analyses has been obtained for the entire spectrum of bridge and pier types included in the Stage I parametric study, it is concluded that the OPTS modeling technique can be used as a suitably accurate replacement for full-bridge analysis. Based on this conclusion, Stage II of the parametric study utilized only OPTS models.

9.3.2 Discussion of AASHTO vs. CVIA vs. IRSA comparisons for a single bridge

Results from static AASHTO and dynamic CVIA and IRSA analyses of the NSG channel pier OPTS model, subject to the severe impact-energy condition, are presented in Figure 9.4. Similar to the figures discussed above (Figure 9.3 and Appendix A), the NSG channel pier structural configuration in Figure 9.4 provides indicators of water, soil, and impact elevations, and omits the superstructure (although superstructure elements are included in all three (AASHTO, CVIA, IRSA) analyses).

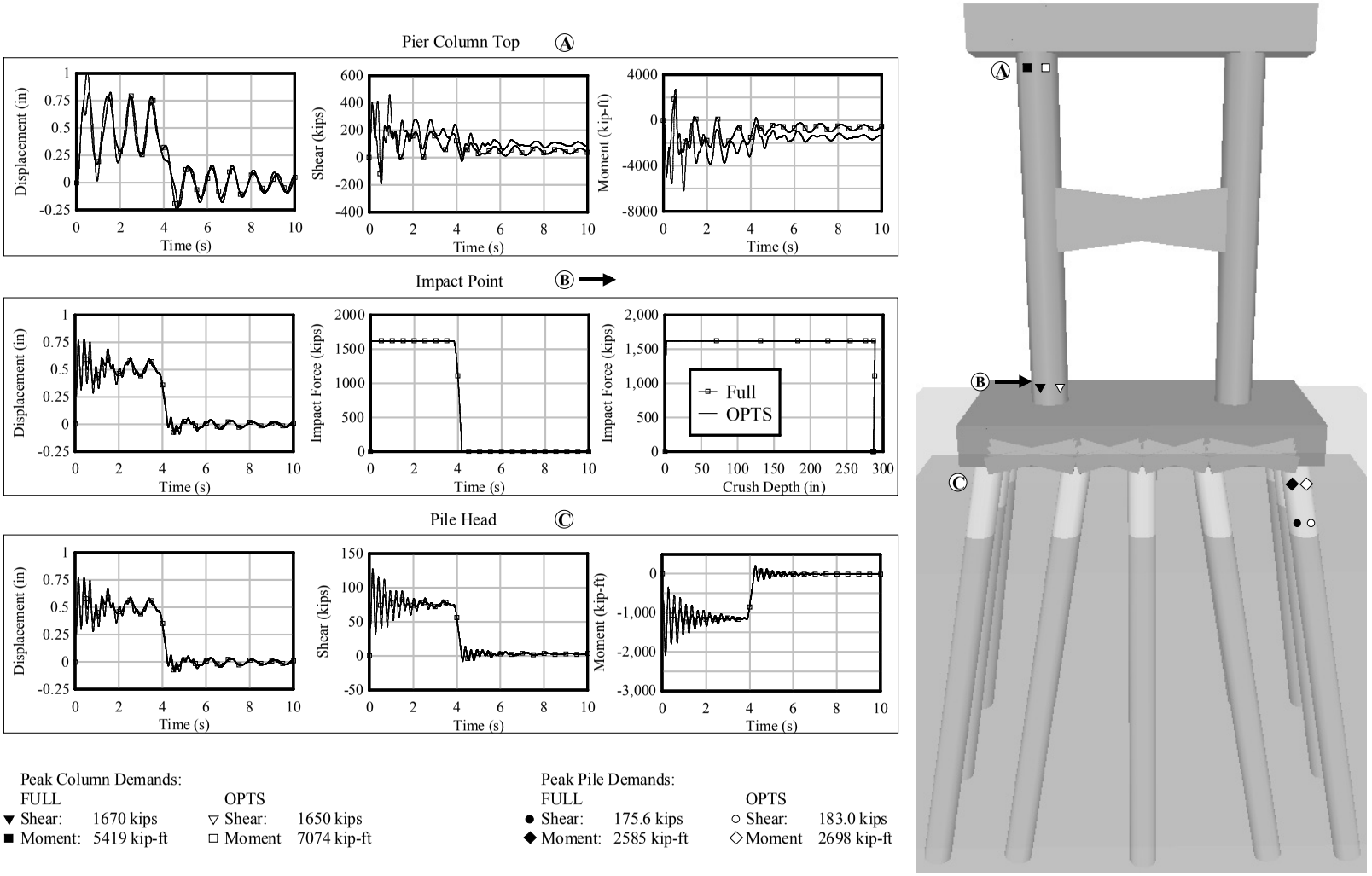

Figure 9.3 OPTS vs. full-bridge CVIA
Bridge: new St. George Island Causeway channel pier; Impact condition: 7820 tons at 7.5 knots

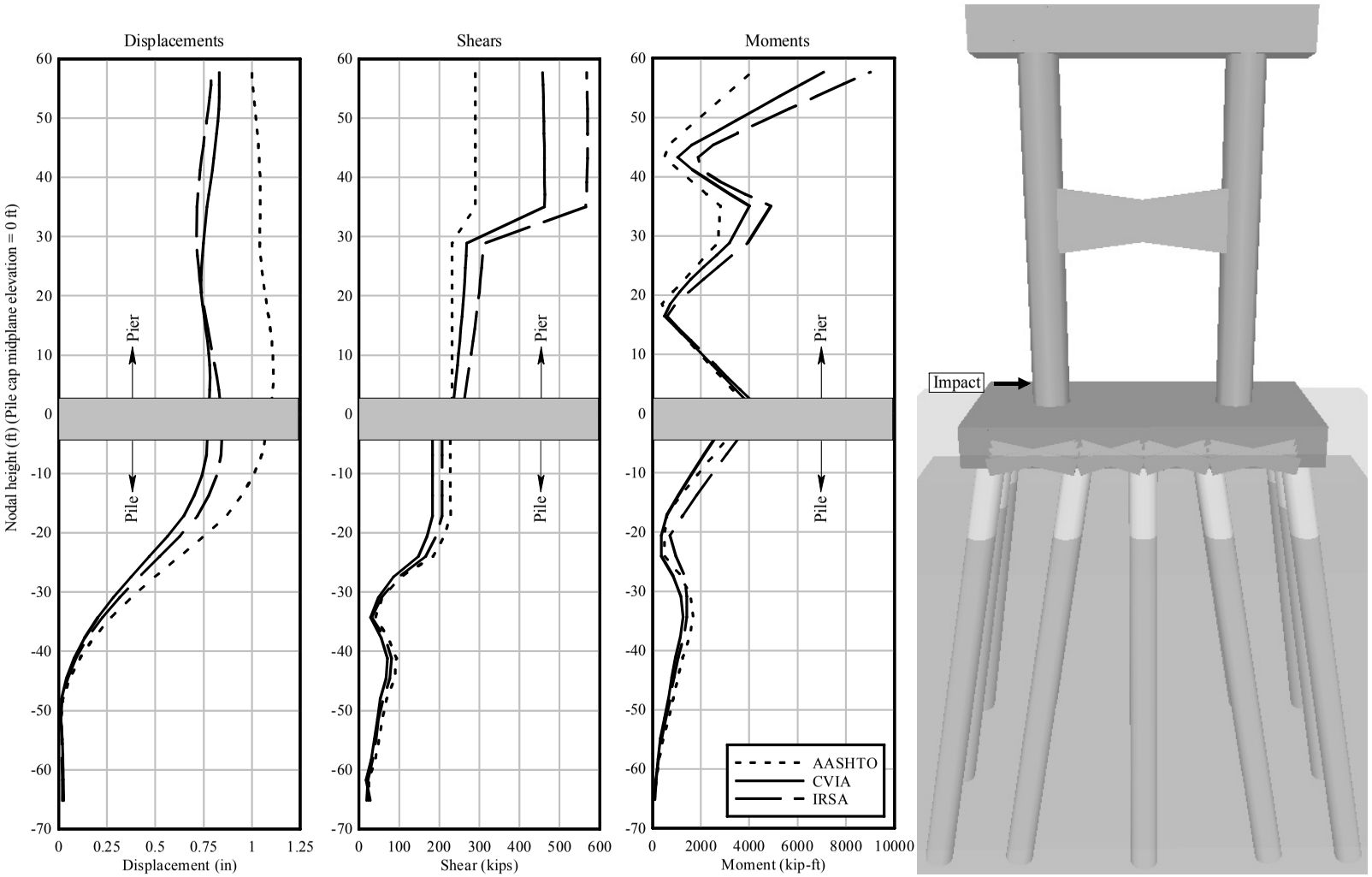

Figure 9.4 AASHTO vs. CVIA vs. IRSA comparison;
Bridge: new St. George Island Causeway channel pier; Impact condition: 7820 tons at 7.5 knots

Profiles of maximum displacement, shear force, and moment are presented for elevations ranging over the full height of the piles and pier columns. To aid in understanding the data, the physical pile cap thickness is also indicated in Figure 9.4. It should be noted that numerical analysis results for elevations within the pile cap thickness are not meaningful due to the manner in which FB-MultiPier models both the pile cap and the connections of the pier columns to the pile cap. Similar issues arise when deep shear walls and struts are modeled with multiple lateral beam elements: internal forces in column elements that lie within the vertical thickness of struts are not meaningful. For these reasons, in Figure 9.4, straight-lines connect the individual response profiles immediately above and below elevations that lie within the pile cap thickness and the shear-strut vertical thickness.

Recall that the two purposes for conducting Stage II of the parametric study were 1) to evaluate the level of conservatism of IRSA in comparison to CVIA; and, 2) to determine the extent to which dynamic amplification effects produce design forces that are larger than those computed using the AASHTO static methodology. For the NSG channel pier (Figure 9.4), IRSA forces (both shear and moment) are shown to be conservative in comparison to CVIA forces for elevations throughout the entire structure. Also highlighted in Figure 9.4 are differences in the results obtained from static and dynamic analysis methods. Regarding internal force profiles associated with pile elevations (those below the pile cap), all three analysis methods (AASHTO, CVIA, IRSA) predict relatively similar magnitudes of shear and moment. However, at elevations near the top of the pier structure, Figure 9.4 indicates that dynamic amplification (discussed in Chapter 6) drives the dynamic predictions of internal shear and moment higher. These differences between static and dynamic predictions of internal force are consistent with prior research findings obtained for different bridges (Consolazio et al. 2006).

In Appendix B, equally detailed figures pertaining to AASHTO vs. CVIA vs. IRSA analyses are included for all bridges and impact-energy conditions included in Stage II of the parametric study. The level of IRSA conservatism relative to CVIA, as observed in Figure 9.4, is representative of that generally found in the data provided in Appendix B. The phenomenon of dynamic amplification is, however, found to be dependent on the specifics of the bridge and pier configuration; soil conditions, and type of barge-bow force-deformation relationship employed (Consolazio and Davidson 2008). In some situations, failure to include dynamic amplification effects can lead to unconservative predictions of member design forces, whereas in other conditions design forces predicted by static and dynamic analyses are essentially equivalent.

9.3.3 Discussion of overall parametric study results

In addition to the detailed data plots presented above and in Appendices A and B, overall graphical summary plots of the Stage I parametric study results are presented in Figure 9.5 and Stage II results are presented in Figure 9.6. In these figures, each bridge analysis is identified using the nomenclature: BBB-PPP-E where, BBB is a three letter bridge identification code (Table 9.1), PPP is a three letter pier identification code (CHA=channel pier, OFF=off-channel pier), and E is an impact energy code (L=low, M=moderate, H=high, and S=severe).

With respect to Stage I of the parametric study (CVIA analyses of full-bridge and respective OPTS models), the resulting predictions of maximum column moments are summarized for each impact energy condition. To enable visual interpretation, these quantities have been normalized for each impact energy condition so that the maximum column moment magnitude associated with a given full-bridge model is always unity (1.0). Data shown in Figure 9.5 indicate a strong level of agreement between OPTS and full model predictions of maximum column moment. Such favorable comparisons demonstrate that the OPTS modeling technique is an adequate predictor of vessel-bridge collision induced structural demand.

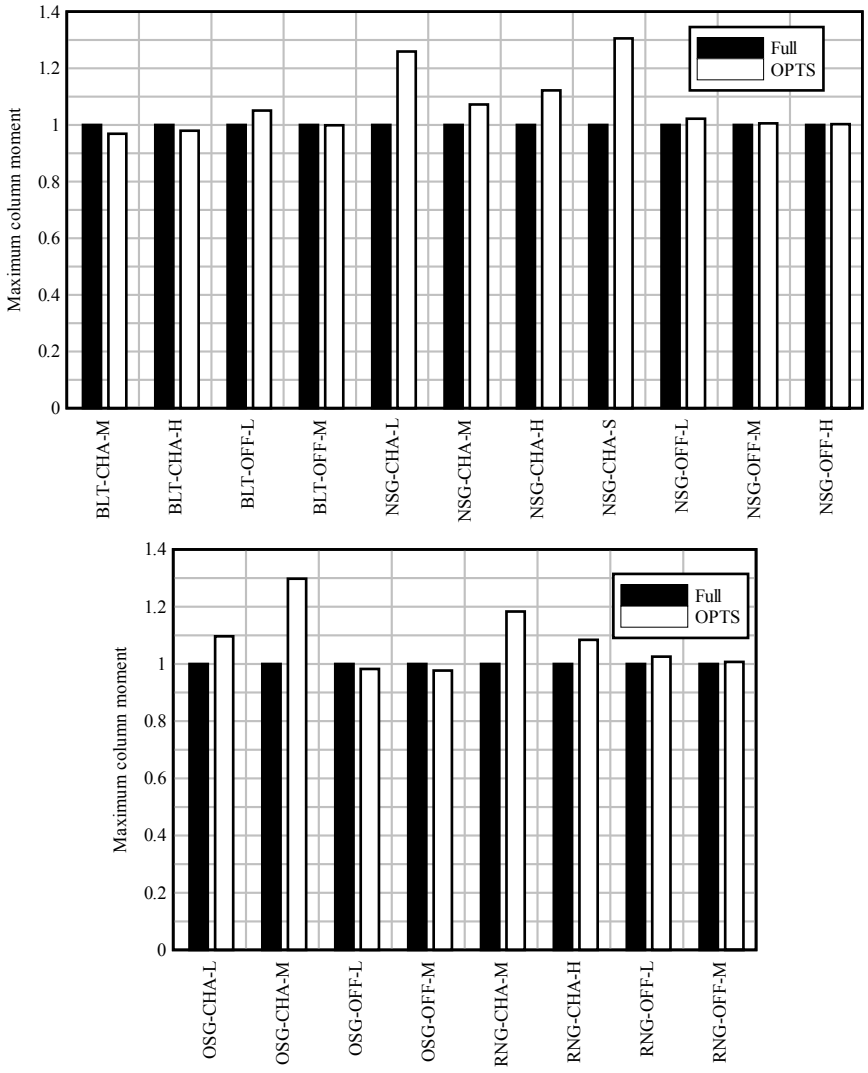

Figure 9.5 Comparison of CVIA results: Full vs OPTS
(Results are normalized to Full = 1)

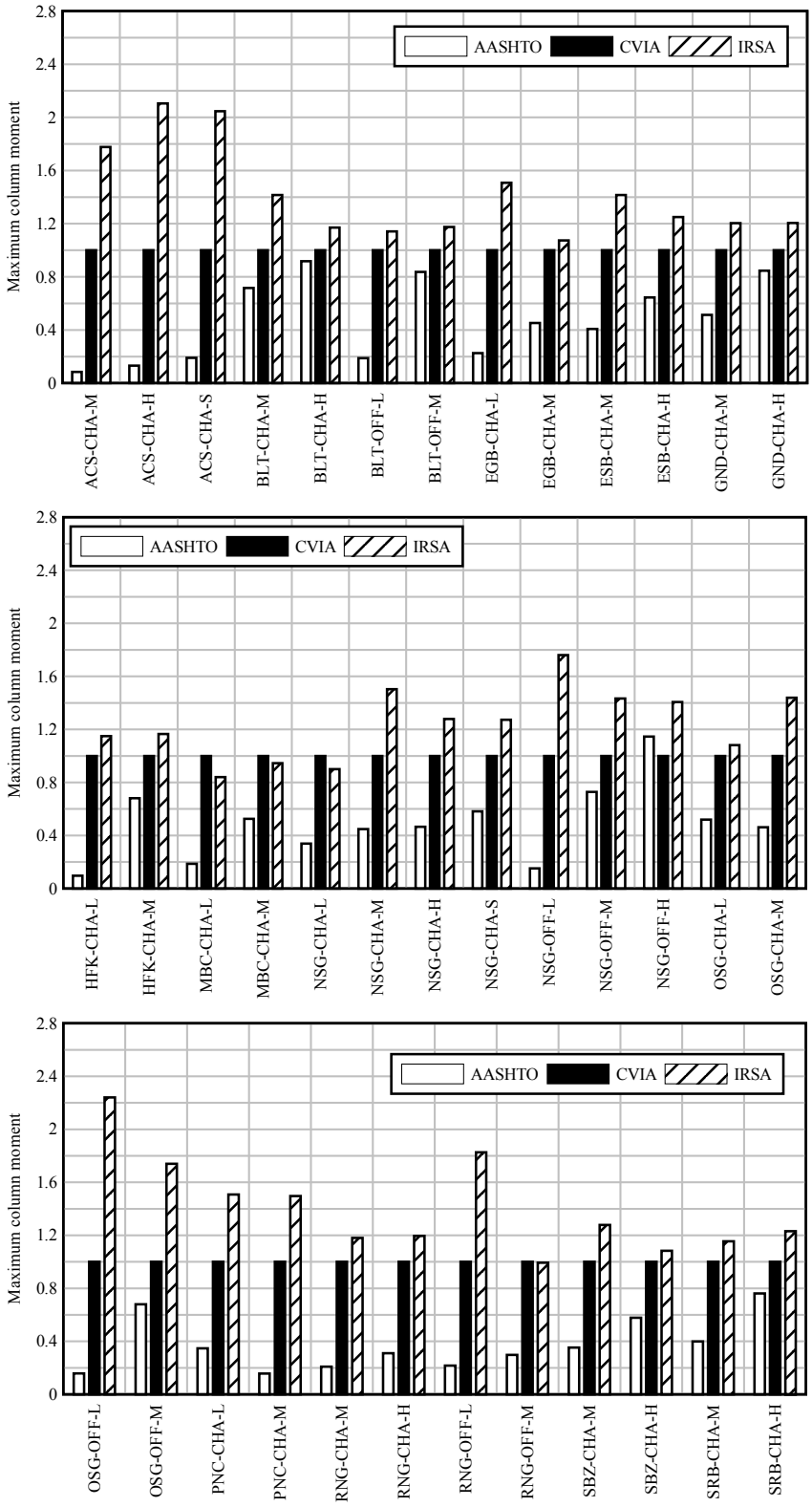

Figure 9.6 Comparison of Results: AASHTO vs. CVIA vs. IRSA summary comparison (Results are normalized to CVIA = 1)

Predictions of maximum column moment are also provided for each impact energy condition associated with Stage II of the parametric study. As noted earlier, this stage consisted of barge impact analyses of OPTS models using the AASHTO static load method and the two dynamic methods (CVIA and IRSA). For barge-impact analysis of bridge piers, the CVIA method proposed in this report is considered to be the most accurate design-based analytical tool currently available. In Figure 9.6, therefore, the maximum column moment magnitudes are normalized for each impact energy condition so that the value associated with a given CVIA analysis is always unity (1.0). Comparing dynamic CVIA results to the corresponding static AASHTO results therefore facilitates a visual indication of the differences between current practice (AASHTO) and proposed practice (dynamic).

Figure 9.6 also provides a means of visually gauging the level of conservatism exhibited by IRSA (relative to CVIA). Relative normalized values of maximum column moment associated with the IRSA analyses generally fall between 1 and 2. This indicates that the IRSA method is generally capable of predicting reasonably conservative peak column-moment values. Because values of maximum demand may be reasonably and conservatively calculated in the IRSA method without conducting a time-history analysis, the IRSA method constitutes an effective means of capturing dynamic amplification effects, when such effects are significant.

9.4 Parametric Study Summary

In this chapter, a parametric study was conducted using numerous bridges subject to an array of barge-impact scenarios. Seventeen bridge-pier models, exhibiting widely varying ages and structural configurations, were developed from thirteen bridges located within the state of Florida, U.S. (Table 9.1). Using known static-impact forces employed in the design of a number of these bridges, barge-impact energy conditions were formulated and applied to models in the bridge database. This resulted in 152 unique impact analyses; some static (AASHTO) and some dynamic (CVIA, IRSA) in nature. Examination of the parametric study results indicated that:

- The OPTS modeling technique predicts accurate measures of pier response and internal force in comparison to those predicted by employing full-bridge models;
- The IRSA analysis technique predicts reasonably conservative measures of pier internal force in comparison to CVIA analysis;
- The dynamic analysis methods (CVIA and IRSA) conservatively predict dynamic amplification effects, when such effects are present, whereas the AASHTO static analysis method does not account for such effects.

Detailed data for the entire parametric study are located in Appendix A (full-bridge versus OPTS analyses) and Appendix B (AASHTO-CVIA-IRSA analyses).

CHAPTER 10
CONCLUSIONS AND RECOMMENDATIONS

10.1 Concluding Remarks

Based on full-scale experimental barge impact test data and numerical simulation data obtained during earlier research studies, it was previously determined that 1) the relationships between barge kinetic energy, barge deformation, and impact force contained in the current AASHTO bridge design specifications needed to be independently examined; and 2) bridge analysis methods capable of accounting for dynamic amplification effects needed to be developed. The research presented in this report has been carried out to address these needs.

An important component of this study has been the development of updated force-deformation relationships for barge bows. High-resolution models of hopper and tanker barges were developed and subjected to crushing by flat-faced and round pier column impactors of various widths. Based on force-deformation results obtained from the high-resolution models, it has been concluded that barge bow crushing behavior may be adequately and conservatively modeled using an elastic, perfectly-plastic representation. This conclusion differs substantially from the current AASHTO relationship in which impact forces increase with additional deformation beyond the transition from elastic to inelastic behavior. Barge bow yield loads have also been found to be strongly dependent on the shape and size of the pier column, and not a function of the barge bow width, as the AASHTO provisions prescribe. Newly proposed barge bow force-deformation relationships have been proposed in this report that are dependent upon pier geometry (impact zone shape and size), but not dependent on barge type.

A new bridge modeling technique—the one-pier two-span (OPTS) technique—has been developed. The OPTS technique consists of the reduction (simplification) of a full-bridge model, which may consist of several piers, to a single pier model with adjacent spans, springs, and lumped masses. The springs and lumped masses are obtained from stiffness and mass characteristics of removed portions of the full-bridge model. Guidance has been provided regarding formation of the springs and masses at the ends of OPTS models for a wide range of bridge-superstructure types and load-conditions. Numerous OPTS models have been analyzed and shown to produce pier-responses in agreement with the predictions of respective full-bridge model analyses. Furthermore, analysis using OPTS models has been shown to consistently produce analytical results in substantially less time than analysis using full-bridge models.

Three distinct procedures for conducting dynamic analyses of barge impacts on bridge piers have also been developed and presented in this report. Two of these methods—coupled vessel impact analysis (CVIA) and applied vessel impact load (AVIL)—use time-step integration to solve the dynamic equations of motion of the bridge structure. The other method—impact response spectrum analysis (IRSA)—is a response spectrum analysis technique that amplifies and combines modal analysis data to predict approximate maximum dynamic design forces.

The CVIA technique, which involves coupling a single degree-of-freedom (SDOF) barge model to a multiple degree-of-freedom (MDOF) bridge model, was validated against both experimental data and high-resolution finite element analysis (FEA) results. Based on good agreement between CVIA results, full-scale experimental data, and high-resolution FEA results, the CVIA method proposed in this report is considered to be the most accurate

analytical tool currently available for conducting barge-bridge collision analysis. CVIA was therefore selected as the baseline analysis to which the two other dynamic analysis methods (AVIL and IRSA) were compared in this study.

The AVIL procedure uses barge impact characteristics and force-deformation behavior of a barge in conjunction with the force-deformation behavior of the bridge to generate an applied load-history. Using conservation of energy and momentum, barge and pier characteristics were correlated to load history characteristics (peak load and load duration), which in turn, were used to develop expressions for time-varying impact loads. These loads were then applied to bridge models dynamically.

The IRSA procedure is a response spectrum analysis procedure specifically tailored to vessel impact loading. The IRSA procedure dynamically magnifies modal components of the static displacement to approximate dynamic modal displacements. Magnification of the static displacements is accomplished through the application of a dynamic magnification factor (DMF), which is obtained from impact DMF spectra. After transforming the dynamic modal response parameters into structural response parameters, internal structural member design forces are recovered and modally combined for use in bridge design. In this study, the generation of a large number of event-specific DMF spectra revealed that barge-impact DMF values do not exceed 2.0 for impacted bridge systems having 5-precent modal damping. Furthermore, comparison of results from the CVIA and IRSA techniques showed good agreement. The IRSA method was found to be capable of adequately modeling barge impact events. Maximum dynamic responses may be approximated using IRSA without requiring a full time-history analysis as is required in the CVIA and AVIL methods.

Although AVIL equations are used as part of the IRSA method, the IRSA method is generally considered more suitable than AVIL for use as a design tool. An important aspect of the AVIL equations is the calculation of the effective pier stiffness at the application of loading. The general nonlinear IRSA method proposed in this report includes force determination iterations in which peak dynamic force and effective pier stiffness are updated to account for pier-soil model nonlinearity. The AVIL method, however, does not incorporate nonlinear force determination iterations, but, instead requires the designer to determine a suitable effective pier stiffness.

10.2 Recommendations

10.2.1 Recommendations for Bridge Design

- Elastic, perfectly-plastic barge bow model: It is recommended that barge bow force-deformation relationships be represented using the elastic, perfectly-plastic model that was presented in Chapter 4. The adequacy of using an elastic, perfectly-plastic relationship is based upon results obtained from high-resolution static finite element crush analyses of the two most common types of barges used in the United States.
- Dependence of barge bow yield force and deformation on pier width and geometry: Based on results obtained from the high-resolution finite element analyses, it has been shown that the barge bow yield load is dependent upon the width of the impacted pier column. Additionally, it has been shown that the barge bow deformation at yield is dependent upon the geometry (flat-faced versus round) of the impacted pier column. It is important to note that although AASHTO prescribes force-deformation

relationships that are dependent on barge width (i.e. inclusion of the R_B factor in the AASHTO provisions), no such correlation was observed in this research. Therefore, it is recommended that the barge force-deformation relationship be formulated as a function of pier width and geometry, as presented in Chapter 4, without dependence on barge bow width.

- Use of the one-pier two-span (OPTS) modeling technique for bridge-pier analysis: OPTS models have been used to carry out dynamic barge-impact analyses and compared to results obtained from analyses of respective full-bridge models. These comparisons demonstrate that analysis using the OPTS modeling technique produces calculated predictions of impact force, and furthermore, pier response in-line with results obtained from employing a full-bridge model. Also, relative to analysis using full-bridge models, the OPTS modeling technique has been shown to drastically reduce the time necessary to complete a given analysis. Consequently, it is recommended that OPTS models, as opposed to full-bridge models, be used for both static and dynamic analyses.
- Use of dynamic analysis techniques in lieu of static techniques: Both experimental data and results from finite element analyses indicate that dynamic inertial-resistances and inertial-forces significantly affect bridge response during a vessel collision. The presence of a superstructure produces large inertial forces, which may in turn generate significant dynamic force amplification effects in pier columns. Thus, it is recommended that dynamic analyses be used to model barge impact events.
    a. If analysis software in which coupled vessel impact analysis (CVIA) is implemented is available, it is recommended that CVIA (with OPTS) techniques be used to dynamically analyze a bridge structure subjected to barge impact.
    b. If software in which CVIA is implemented is not available, it is recommended that the impact response spectrum analysis (IRSA) technique be used (with OPTS) to conduct a barge impact analysis on a bridge model.
- A key aspect of IRSA techniques is the calculation of peak dynamic load and period of loading using the applied vessel impact load AVIL equations. However, for reasons noted earlier, the IRSA technique is more accurate than the AVIL method. Therefore, the AVIL method, as a stand-alone method, is not recommended for use in design.

10.2.2 Recommendations for Future Research

- Equivalent static method employing simplified dynamic amplification: The dynamic analysis techniques developed and recommended in this study, CVIA and IRSA, are capable of accounting for dynamic amplifications when combinations of structural configuration, soil condition, and impact condition give rise to such amplifications. However, for ease of use in bridge design, the development of an equivalent static method employing simple dynamic amplification factors is desirable. The CVIA method and the parametric study data presented in this report should be used to

develop a semi-empirical equivalent static analysis method that incorporates simplified dynamic amplification factors.

- Barge crush-curves corresponding to wide, planar impact surfaces: For bridge piers with wide rectangular water-line footings (common design practice in Florida), the entire width of a barge bow may be engaged during a head-on impact. Such a situation can produce impact forces that are substantially larger than those currently specified by the AASHTO bridge design provisions. However, a potential mitigating factor is that perfectly head-on impacts are very rare events, and most realistic impact conditions will be moderately oblique in nature (i.e., a vessel impacting a pier at a shallow angle, rather than precisely head-on). Research is needed to quantify the reduction of impact force that results when oblique collisions occur on wide, planar impact surfaces.

- Improve probability of collapse: The AASHTO vessel collision specifications use a probabilistic approach to bridge design, which requires designers to determine the return period of collapse for bridge structures spanning navigable waterways. One aspect of this probabilistic approach is calculation of the probability of collapse (PC) term. PC is the probability that a bridge structure will collapse once a bridge component has been struck by a vessel. This probability is a function of many factors: impact vessel size and shape, vessel speed and displacement, ultimate pier strength, etc. However, the AASHTO PC estimation equations were derived from research on damage observed between ship-to-ship collisions at sea. Given that barge-to-bridge collisions are different from ship-to-ship collisions, the accuracy of the AASHTO PC term should be investigated.

- Investigate barge impacts longitudinal to a bridge: In the current research study, analysis of barge impacts on bridge structures has been restricted to impacts transverse to the bridge span direction. However, barge-to-bridge collisions do not always occur transverse to the bridge. Additionally, for design, the AASHTO provisions prescribe that fifty-percent of the design impact load be applied in the direction longitudinal to the bridge. AASHTO, however, prescribes static load cases for impact loading. Therefore, it is recommended that further investigation of the longitudinal impact condition be studied using dynamic techniques.

REFERENCES

American Association of State Highway and Transportation Officials (AASHTO). (1991). *Guide Specification and Commentary for Vessel Collision Design of Highway Bridges*, American Association of State Highway and Transportation Officials, Washington, D.C.

AASHTO. (1994). *LRFD Bridge Design Specifications and Commentary*, American Association of State Highway and Transportation Officials, Washington, D.C.

American Society of Civil Engineers (ASCE). (2005). *Minimum Design Loads for Buildings and Other Structures*, Reston, VA.

Arroyo, J. R., Ebeling, R. M., and Barker, B. C. (2003). *Analysis of Impact Loads from Full-Scale Low-Velocity, Controlled Barge Impact Experiments, December 1998,* ERDC/ITL TR-03-3, US Army Corps of Engineers, New England District, Concord, MA.

Chopra, A. K. (2007). *Dynamics of Structures: Theory and Applications to Earthquake Engineering*, Pearson Prentice Hall, Englewood Cliffs, NJ.

Consolazio, G. R., Lehr, G. B., and McVay, M. C. (2004). "Dynamic Finite Element Analysis of Vessel-Pier-Soil Interaction During Barge Impact Events." *Transportation Research Record: Journal of the Transportation Research Board*, No. 1849, pp. 81-90.

Consolazio, G. R., Hendrix, J. L., McVay, M. C., Williams, M. E., and Bollmann, H. T. (2004). "Prediction of Pier Response to Barge Impacts Using Design-Oriented Dynamic Finite Element Analysis." *Transportation Research Record: Journal of the Transportation Research Board*, No. 1868, pp. 177-189.

Consolazio, G. R., and Cowan, D. R. (2005). "Numerically Efficient Dynamic Analysis of Barge Collisions with Bridge Piers." *ASCE Journal of Structural Engineering*, ASCE, Vol. 131, No. 8, pp. 1256-1266.

Consolazio, G. R., Cowan, D. R., Biggs, A., Cook, R. A., Ansley, M., and Bollmann, H. T. (2005). "Full-Scale Experimental Measurement of Barge Impact Loads on Bridge Piers." *Transportation Research Record: Journal of the Transportation Research Board*, No. 1936, pp. 81-93.

Consolazio, G. R., Cook, R. A., and McVay, M. C. (2006). *Barge Impact Testing of the St. George Island Causeway Bridge - Phase III : Physical Testing and Data Interpretation*, Structures Research Report No. 2006/26868, Engineering and Industrial Experiment Station, University of Florida, Gainesville, Florida.

Consolazio, G. R, and Davidson, M. T. (2008). "Simplified Dynamic Barge Collision Analysis for Bridge Design", *Transportation Research Record: Journal of the Transportation Research Board*, In press.

Davidson, M. T. (2007). "Simplified Dynamic Barge Collision Analysis for Bridge Pier Design." Masters Thesis, Department of Civil and Coastal Engineering, University of Florida, Gainesville, Florida.

FB-PIER. (2003). *User's Manual*, Florida Bridge Software Institute, University of Florida, Gainesville FL.

FB-MULTIPIER. (2007). *User's Manual*, Florida Bridge Software Institute, University of Florida, Gainesville FL.

Fernandez, C., Jr. (1999). "Nonlinear Dynamic Analysis of Bridge Piers." Ph.D. Dissertation, University of Florida, Department of Civil Engineering, University of Florida, Gainesville, Florida.

Federal Emergency Management Agency (FEMA). (2003). *NEHRP Recommended Provisions for Seismic Regulations for New Buildings and Other Structures*, Washington, D.C.

Goble, G., Schulz, J., and Commander, B. (1990). *Lock and Dam #26 Field Test Report for the Army Corps of Engineers*, Bridge Diagnostics Inc., Boulder, CO.

Hendrix, J. L. (2003). "Dynamic Analysis Techniques for Quantifying Bridge Pier Response to Barge Impact Loads." Masters Thesis, Department of Civil and Coastal Engineering, University of Florida, Gainesville, FL.

Knott, M., and Prucz, Z. (2000). "Vessel Collision Design of Bridges." *Bridge Engineering Handbook*, CRC Press LLC, Boca Raton, Florida.

Larsen, O. D. (1993). *Ship Collision with Bridges: The Interaction between Vessel Traffic and Bridge Structures*, IABSE Structural Engineering Document 4, IASBE-AIPC-IVBH, Zurich, Switzerland.

Liu, C., and Wang, T. L. (2001). "Statewide Vessel Collision Design for Bridges." *ASCE Journal of Bridge Engineering*, ASCE, Vol. 6, No. 3, pp. 213-219.

LS-DYNA. (2003). *LS-DYNA Keyword User's Manual: Version 970*, Livermore Software Technology Corporation, Livermore, CA.

Manuel, L., Kallivokas, L. F., Williamson, E. B., Bomba, M., Berlin, K. B., Cryer, A., and Henderson, W. R. (2006). *A Probabilistic Analysis of the Frequency of Bridge Collapses due to Vessel Impact*, University of Texas Center for Transportation Research Report No. 0 4650 1, University of Texas, Austin, TX.

McVay, M. C., Wasman, S. J., and Bullock, P. J. (2005). *St. George Geotechnical Investigation of Vessel Pier Impact*, Engineering and Industrial Experiment Station, University of Florida, Gainesville, Florida.

Meier-Dörnberg, K. E. (1983). *Ship Collisions, Safety Zones, and Loading Assumptions for Structures in Inland Waterways*, Verein Deutscher Ingenieure (Association of German Engineers) Report No. 496, pp. 1-9.

Minorsky, V. U. (1959). "An Analysis of Ship Collisions with Reference to Protection of Nuclear Power Plants." *Journal of Ship Research*, Vol. 3, pp. 1-4.

Nguyen, H. (1993). "Buckling." Marine Safety Center, U.S. Department of Homeland Security, United States Coast Guard, Washington D.C.

National Transportation Safety Board (NTSB). (2004). *U.S. Towboat Robert Y. Love Allision With Interstate 40 Highway Bridge Near Webbers Falls, Oklahoma, May 26, 2002*, National Transportation Safety Board, Washington D.C.

Patev, R. C. (1999). "Full-Scale Barge Impact Experiments." *Transportation Research Board Circular 491*, Transportation Research Board, Washington D.C..

Patev, R. C., and Barker, B. C. (2003). *Prototype Barge Impact Experiments, Allegheny Lock and Dam 2, Pittsburgh, Pennsylvania*, United States Army Corps of Engineers Report ERDC/ITL TR-03-2.

Tedesco, J. W., McDougal, W. G., and Ross, C. A. (1999). *Structural Dynamics: Theory and Applications*, Addison Wesley Longman, Inc., Menlo Park, CA.

Wilson, J. (2003). *Collison Involving the M/V Brownwater V and the Queen Isabella Causeway Bridge*, U.S. Department of Homeland Security, United States Coast Guard, Washington D.C.

Woisin, G. "The Collision Tests of the GKSS." *Jahrbuch der Schiffbautechnischen Gesellschaft*, Vol. 70, pp. 465-487, Berlin.

Yuan, P. (2005a). "Modeling, Simulation and Analysis of Multi-Barge Flotillas Impacting Bridge Piers." Doctoral Dissertation, College of Engineering, University of Kentucky, Lexington, KY.

Yuan, P., Harik, I. E., and Davidson, M. T. (2005b). *Multi-Barge Flotilla Impact Forces on Bridges*, Draft research report, Kentucky Transportation Center, College of Engineering, University of Kentucky, Lexington, KY.

NOMENCLATURE

Matrices

$[C]$	damping matrix
$[D]$	dynamic system matrix
$[F]$	flexibility matrix
$[I]$	identity matrix
$[K_{condensed}]$	condensed stiffness matrix
$[K]$	stiffness matrix
$[\hat{K}]$	effective stiffness matrix
$[M]$	mass matrix
$[c]$	modal damping matrix
$[k]$	modal stiffness matrix
$[m]$	modal mass matrix
$[\hat{\Phi}]$	mass-normalized eigenvector matrix
$[\Phi]$	eigenvector matrix

Vectors

$\{F_S^{int}\}$	static internal member force vector
$\{F_D\}$	internal forces recovered from combining $\{F_{Di}\}$ for all modes and $\{F_S^{int}\}$
$\{F_{Di}\}$	internal forces recovered from dynamic displaced mode shape for mode $_i$
$\{F_E\}$ or $\{F\}$	external force vector
$\{F_S\}$	static external force vector
$\{F(t)\}$	time varying external force
$\{\hat{F}\}$	effective force vector
$\{\bar{F}\}$	external load vector with updated P_{Bx} and P_{By}
$\{I\}$	load impulse
$\{R\}$	internal force vector
$\{f(t)\}$	time varying modal force vector
$\{q_S\}$	modal static displacements of pier-soil system
$\{q(t)\}$	time varying modal displacement
$\{\dot{q}(t)\}$	time varying modal velocity
$\{\ddot{q}(t)\}$	time varying modal acceleration
$\{u_D\}$	dynamic displaced mode shape from combining $\{u_{Di}\}$ for all modes and $\{u_S\}$
$\{u_{Di}\}$	dynamic displaced mode shape for mode $_i$
$\{u_S\}$	structural static displacements of pier-soil system
$\{u\}$	displacement vector of pier-soil system
$\{u(t)\}$	time varying displacement
$\{\dot{u}(t)\}$	time varying velocity
$\{\ddot{u}(t)\}$	time varying acceleration

$\{\Delta L_{ab}\}$	vector change of linear momentum from $_a$ to $_b$
$\{\Phi_i\}$	eigenvector matrix for mode $_i$
$\left\{\hat{\Phi}_i\right\}$	mass normalized eigenvector for mode $_i$

Bridge abbreviations

ACS	Acosta Bridge
BLT	SR-20 Bridge at Blountstown
EGB	Eau Gallie Bridge
ESB	I-10 Bridge over Escambia Bay
GND	Gandy Bridge
HFK	Howard Frankland Bridge
MBC	Melbourne Causeway Bridge
NSG	New St. George Island Bridge
OSG	Old St. George Island Bridge
PNC	Pineda Causeway FB-MultiPier model
RNG	Ringling Bridge
SBZ	Seabreeze Bridge
SRB	Santa Rosa Bay Bridge

Upper-case symbols

AF	annual frequency of collapse
AVIL	applied vessel impact load
B_B	width of barge
B3	pier three with superstructure of the old St. George Island Bridge
B3T4	impact test number 4 on B3 structure
BR	base aberrancy rate of vessel traffic
C_H	hydrodynamic mass coefficient
CDM	central difference method
CPU	central processing unit
CQC	complete quadratic combination
CVIA	coupled vessel impact analysis
DAQ	data acquisition system
DMF	dynamic magnification factor
DOF	degree-of-freedom
E_B	kinetic energy barge
GHz	gigahertz
H	ultimate strength of pier element
HF#	hopper barge model subject to crushing by a flat-faced impactor of width # (feet)
HR#	hopper barge model subject to crushing by a flat-faced impactor of width # (feet)
IRSA	impact response spectrum analysis
$K_{coupling}$	off-diagonal (coupling) stiffness term
K_Δ	translational stiffness term
K_θ	plan-view rotational stiffness term

KE	kinetic energy of barge
L	superstructure span length
L_i	direction specific mass excitation factor for mode $_i$
LOA	length-overall of barge tow
M^{unit}	unit moment
M_{total}	total structural mass
MDOF	multiple degrees-of-freedom
N	annual vessel frequency
OPTS	one-pier two-span bridge model
P	design static vessel impact force
P_i	modal force for mode $_i$
P_B	barge impact force
P_{BY}	barge impact force at yield
P_{Bm}	maximum impact force
P_{Bx}	barge impact force in the x-direction
P_{By}	barge impact force in the y-direction
$\overline{P}_B$	static barge impact force (Chap. 2); numerically damped impact force (Chap. 7)
P1	isolated pier one of the old St. George Island Bridge
P1T4	impact test number 4 on the P1 structure
P3	isolated pier three of the old St. George Island Bridge
PA	probability of vessel aberrancy
PC	probability of bridge collapse due to vessel impact
PG	geometric probability of vessel impact
R_B	bridge width modification factor
R_C	water current correction factor parallel to barge motion
R_D	vessel traffic density factor
R_{XC}	water current correction factor transverse to barge motion
R_{comb}	combined result of the response parameter under consideration
SDOF	single degree-of-freedom
SRSS	square root of the sum of the squares
TF#	tanker barge model subject to crushing by a flat-faced impactor of width # (feet)
TR#	tanker barge model subject to crushing by a flat-faced impactor of width # (feet)
T_I	period of the impact loading
T_L	long-period transition point
T_S	short-period transition point
T_i	natural period for mode $_i$
TOL , tol	convergence tolerance
V^{unit}	unit shear force
V	design velocity of vessel tow
V_C	water current velocity parallel to barge motion
V_T	vessel transit speed
V_{XC}	water current velocity transverse to barge motion
$V_\theta^{coupling}$	shear due to coupled stiffness and plan-view rotation

V_Δ	shear due to translational stiffness and translation
W_p	weight of payload
W	weight of vessel tow

Lower-case symbols

a_B	crush deformation of the barge bow
a_{Bm} , a_{Bmax}	maximum sustained barge crush depth
a_{BP} , a_{Bp}	residual plastic barge crush deformation
a_{BY}	yield crush deformation of the barge bow
c_{BP}	barge-pier pseudo damping coefficient
h	time step size
k_B	initial elastic barge bow stiffness
k_p	linear pier-soil spring stiffness
k_S	barge-pier-soil series spring stiffness
m_H	mass of half-span of superstructure
m_b or m_B	mass of barge
m_p	mass of payload
m_{effi}	effective modal mass for mode $_i$
m_P	mass of pier
$p(\omega^2)$	characteristic polynomial
q_i	modal displacement for mode $_i$
q_{Di}	dynamically magnified modal displacement for mode $_i$
q_{Si}	static modal displacement for mode $_i$
r_i	response parameter for mode $_i$
t	time
t_E	duration of loading for an elastic pulse
t_T	total inelastic load duration
t_U	duration of unloading
t_Y	time required for the barge bow to yield
t_p	duration of plastic loading
u_0	initial sliding velocity of payload
u_B	barge bow displacement
u_D	maximum system dynamic displacement
u_P	pier displacement
u_{PB}	component of pier displacement in direction of barge motion
u_{Px}	pier displacement in the x-direction
u_{Py}	pier displacement in the y-direction
u_S	maximum system static displacement

$\ddot{u}_B$	barge acceleration
v_B	magnitude of barge velocity
v_{BY}	barge velocity at yield
w_P	impactor width
x_C	distance to edge of channel from the channel centerline
x_L	distance of $3 \cdot \text{LOA}$ from the channel centerline

Greek upper-case symbols

Δ	translation
Δ_M	translation due to unit moment
Δ_V	translation due to unit shear
ΔDE_{ab}	change in total deformation energy from a to b
ΔKE_{ab}	change in kinetic energy of the barge from a to b
ΔP_{Bm}	incremental change in computed impact load
$\Delta \bar{P}_B$	numerically damped increment of impact force
Γ_i	mass participation factor for mode $_i$
θ	angle of channel bend (Chap. 2), plan-view rotation angle (Chap. 6)
θ_M	plan-view rotation due to unit moment
θ_V	plan-view rotation due to unit shear
θ_B	the angle between the barge line of motion and x-direction

Greek lower-case symbols

α	frequency ratio
λ	eigenvalue
μ	historical smoothing factor; static friction coefficient between payload and barge
ρ_{ij}	complete quadratic combination weighting factor for mode $_i$ and $_j$
ξ_i	critical damping ratio for mode $_i$
ω_i	circular natural frequency (rad/sec) for mode $_i$

Subscripts

^{L} or $_L$	appended to symbol, indicates left-flanking structure
^{R} or $_R$	appended to symbol, indicates right-flanking structure

APPENDIX A
COMPARISON OF FULL-BRIDGE AND OPTS ANALYSIS RESULTS

A parametric study was performed, in part, to compare the accuracy of one-pier two-span (OPTS) simplified models to full-bridge models using the coupled vessel impact analysis (CVIA) technique. Accordingly, CVIA analysis was conducted for one channel pier configuration, and one off-channel pier configuration for each of four different bridges for respective OPTS and full models. The data presented in this appendix compare the time-history results of these two levels of modeling complexity for multiple impact energy conditions applied to each bridge model. Additionally, the magnitude and location of the maximum displacement, shear, and moment are presented.

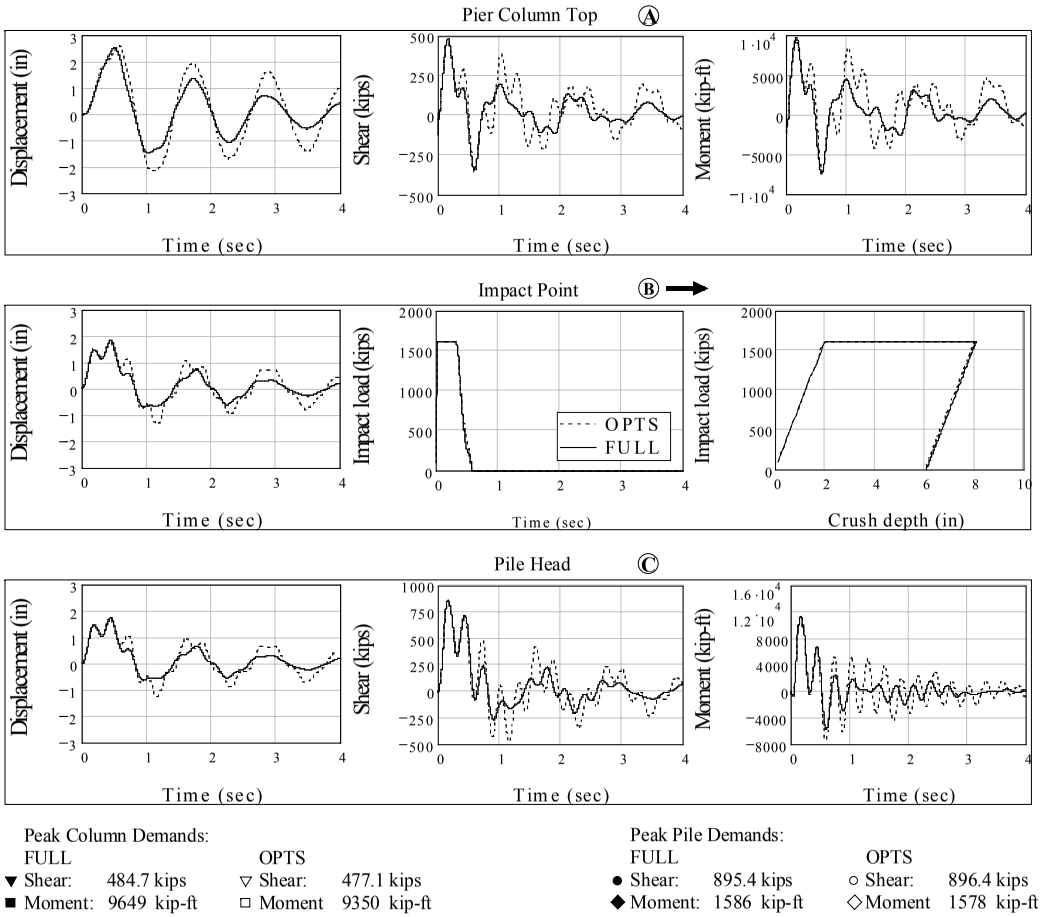

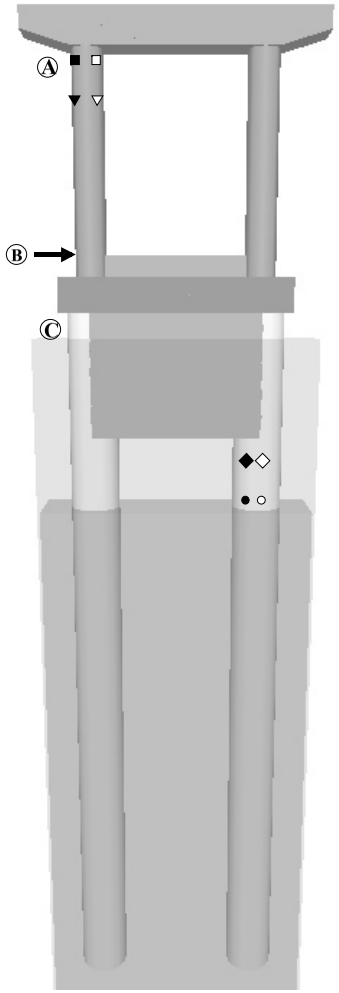

Figure A.1 Comparison of CVIA: Full vs. OPTS
Bridge: SR-20 at Blountstown (BLT) channel pier; Impact condition: 2030 tons at 2.5 knots

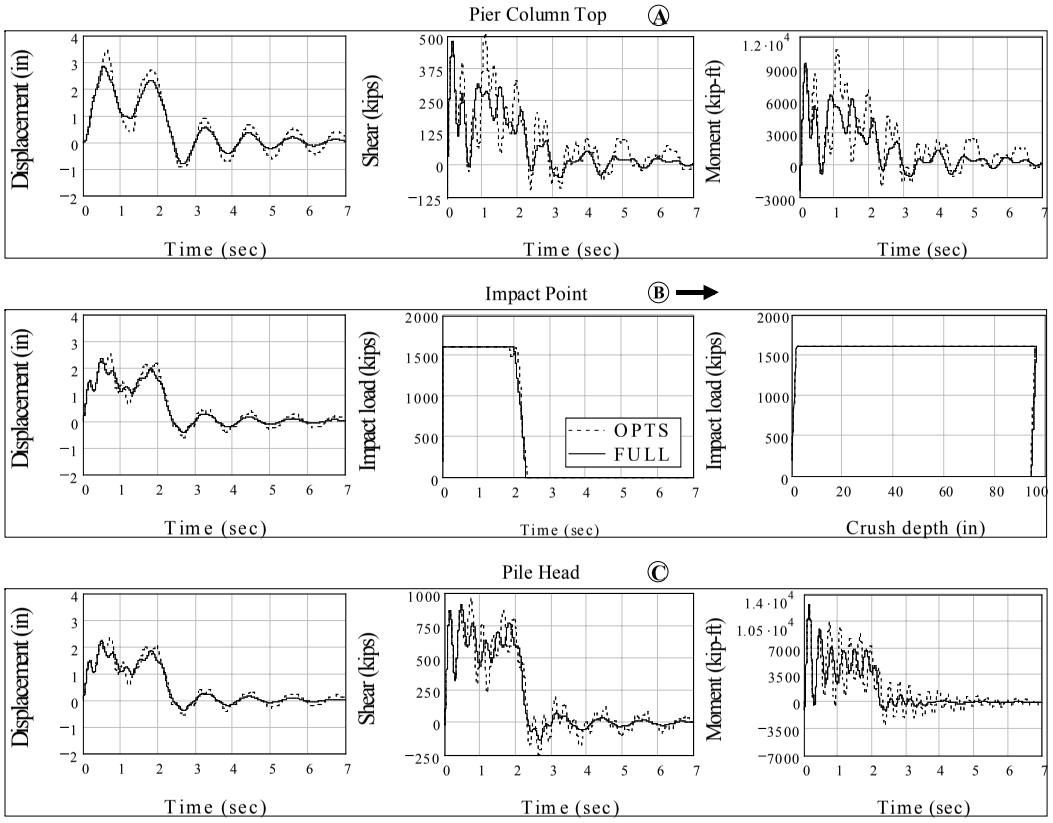

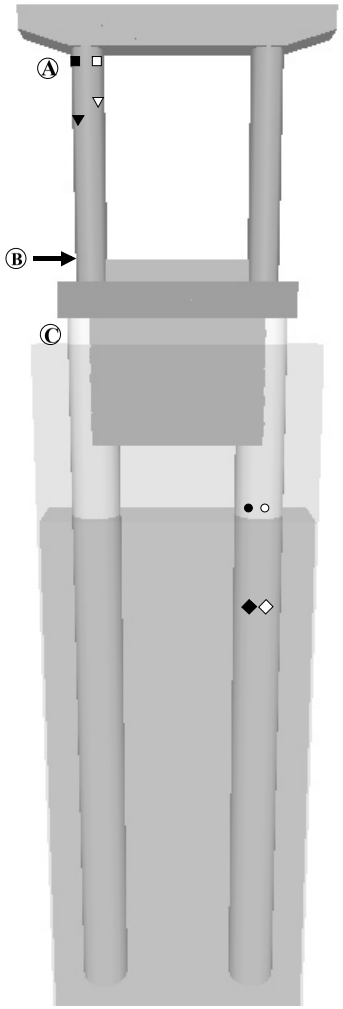

Figure A.2 Comparison of CVIA: Full vs. OPTS
Bridge: SR-20 at Blountstown (BLT) channel pier; Impact condition: 5920 tons at 5.0 knots

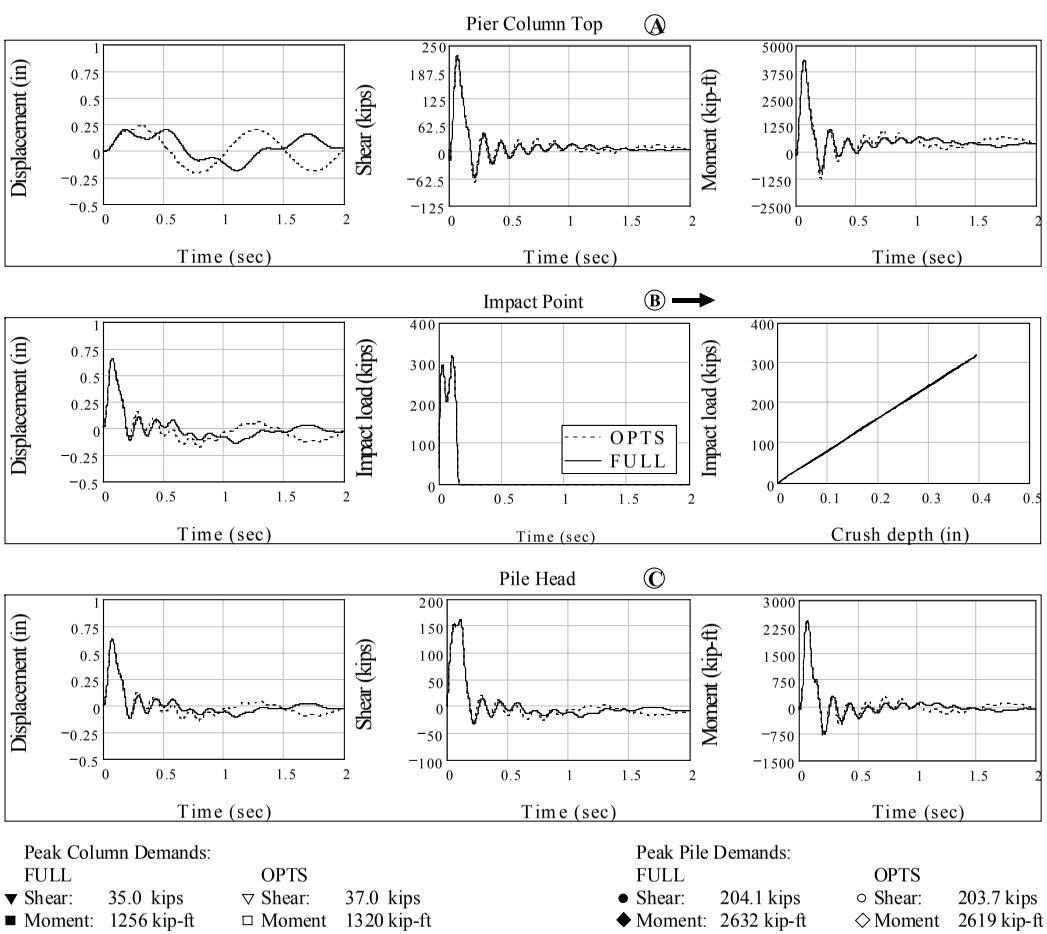

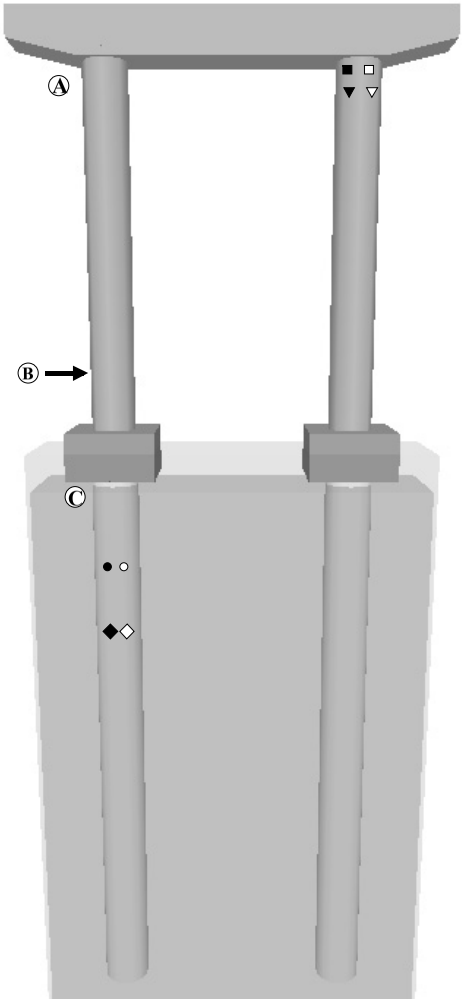

Figure A.3 Comparison of CVIA: Full vs. OPTS
Bridge: SR-20 at Blountstown (BLT) off-channel pier; Impact condition: 200 tons at 1.0 knots

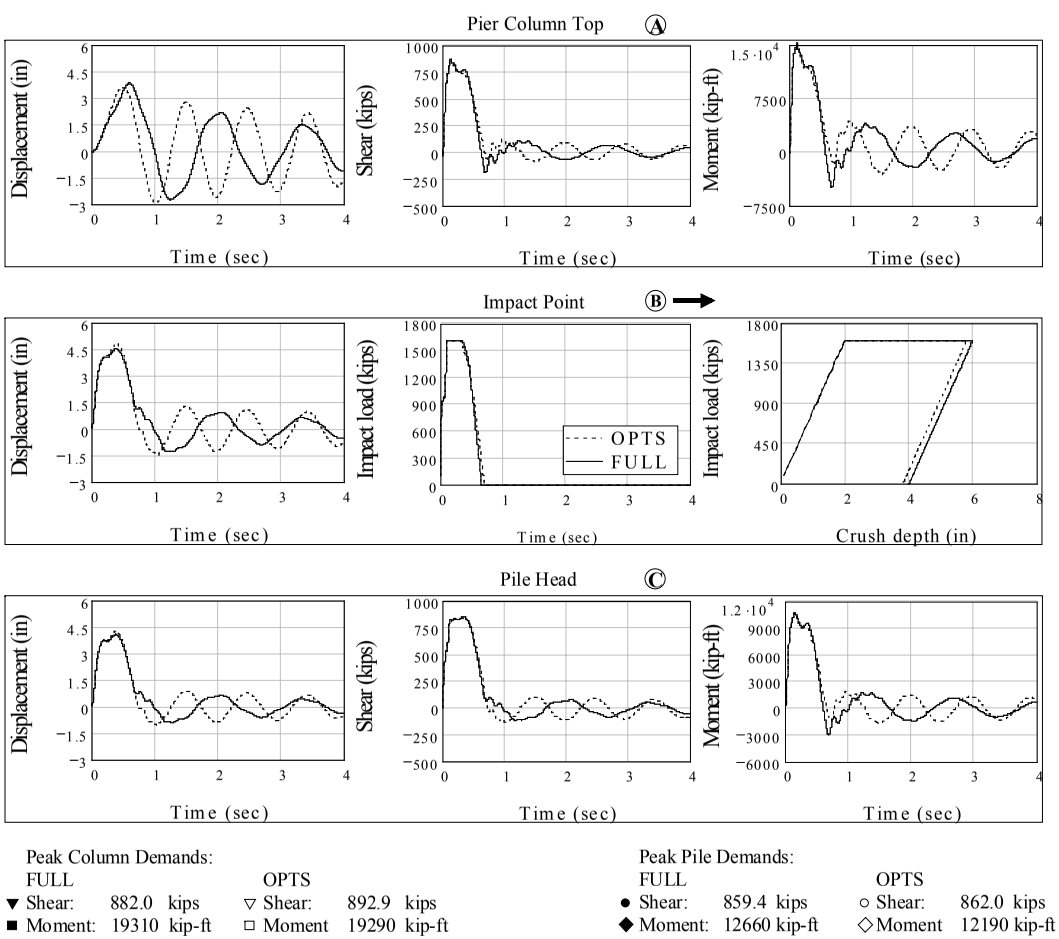

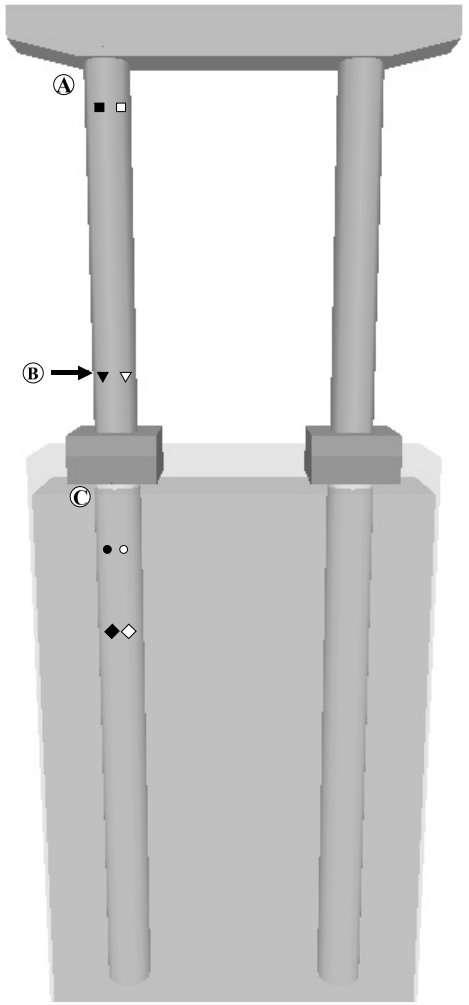

Figure A.4 Comparison of CVIA: Full vs. OPTS
Bridge: SR-20 at Blountstown (BLT) off-channel pier; Impact condition: 2030 tons at 2.5 knots

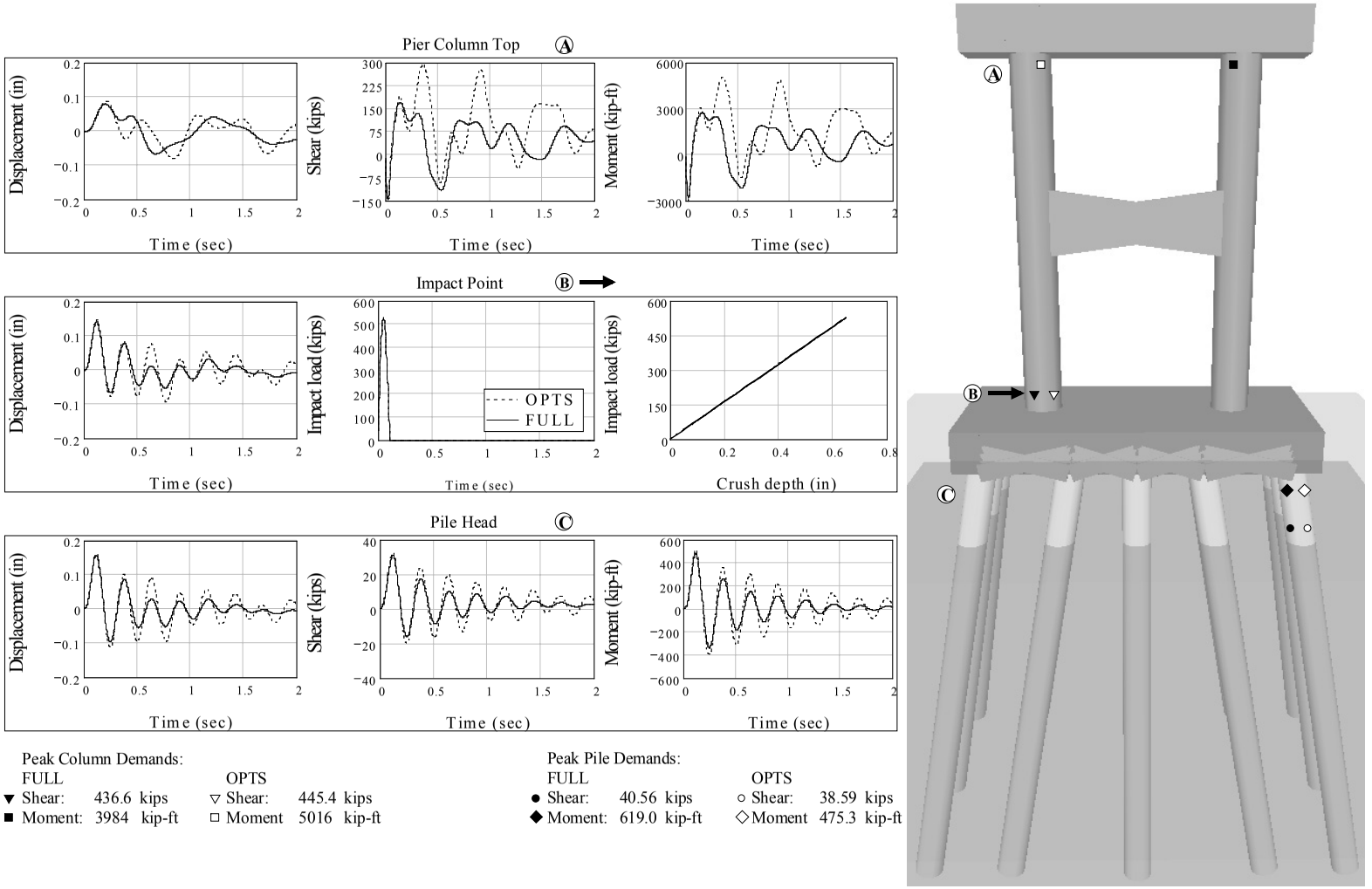

Figure A.5 Comparison of CVIA: Full vs. OPTS
Bridge: new St. George Island Causeway (NSG) channel pier; Impact condition: 200 tons at 1.0 knots

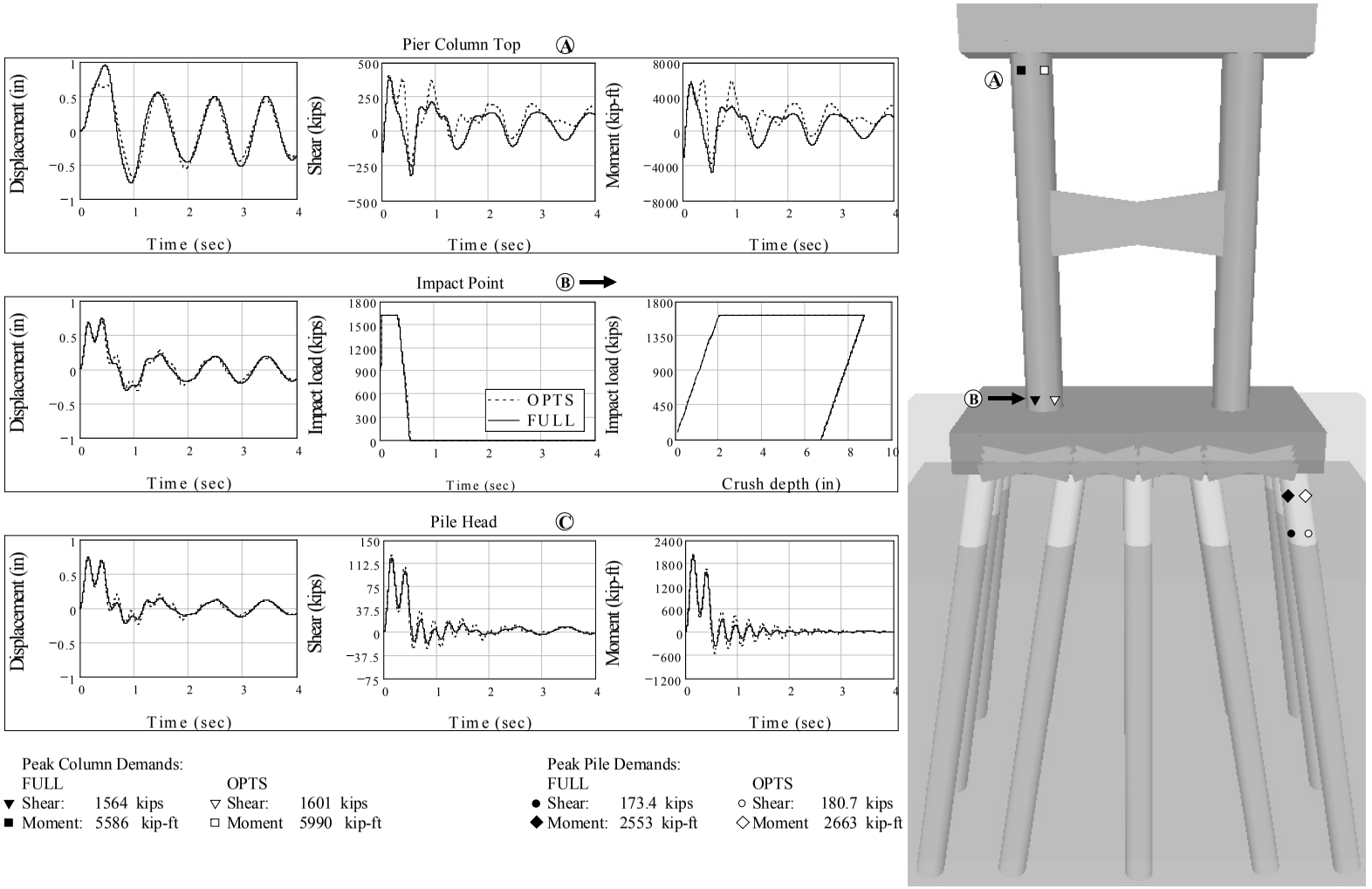

Figure A.6 Comparison of CVIA: Full vs. OPTS
Bridge: new St. George Island Causeway (NSG) channel pier; Impact condition: 2030 tons at 2.5 knots

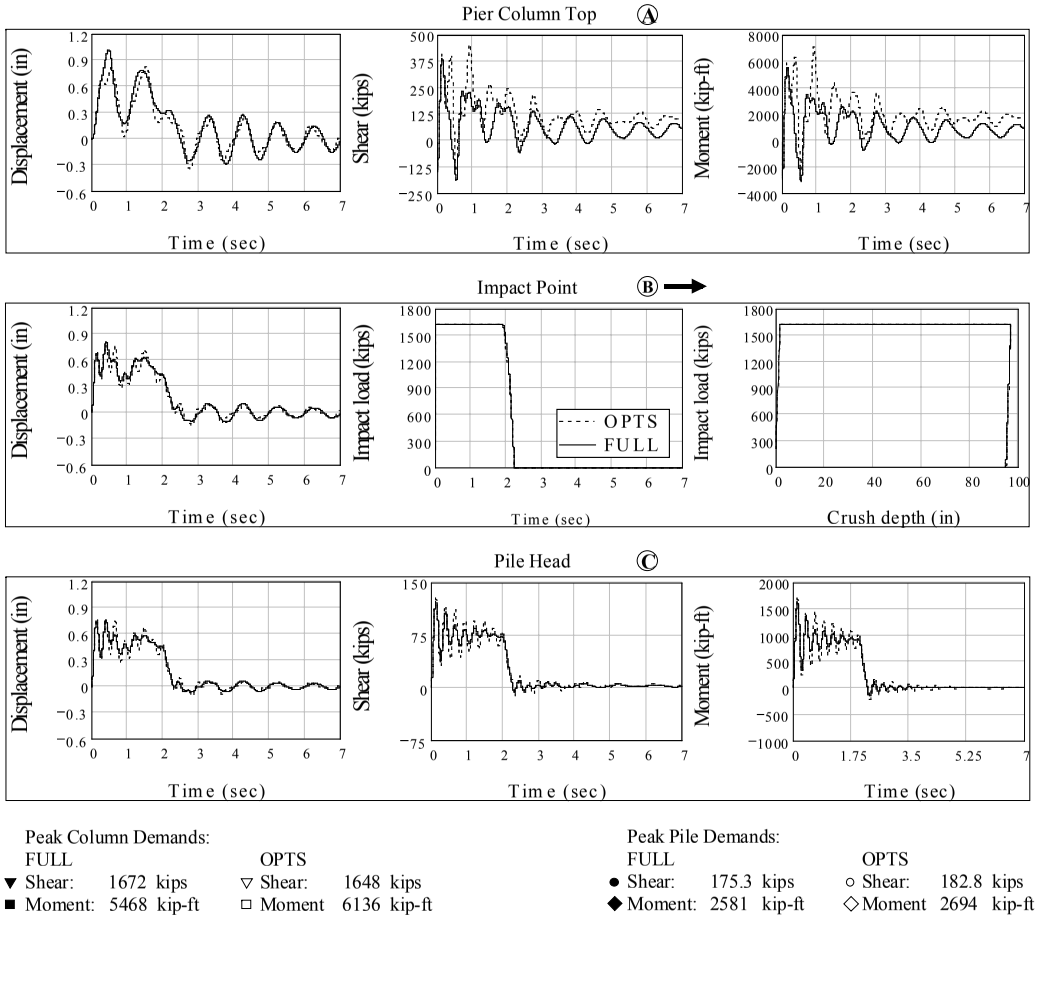

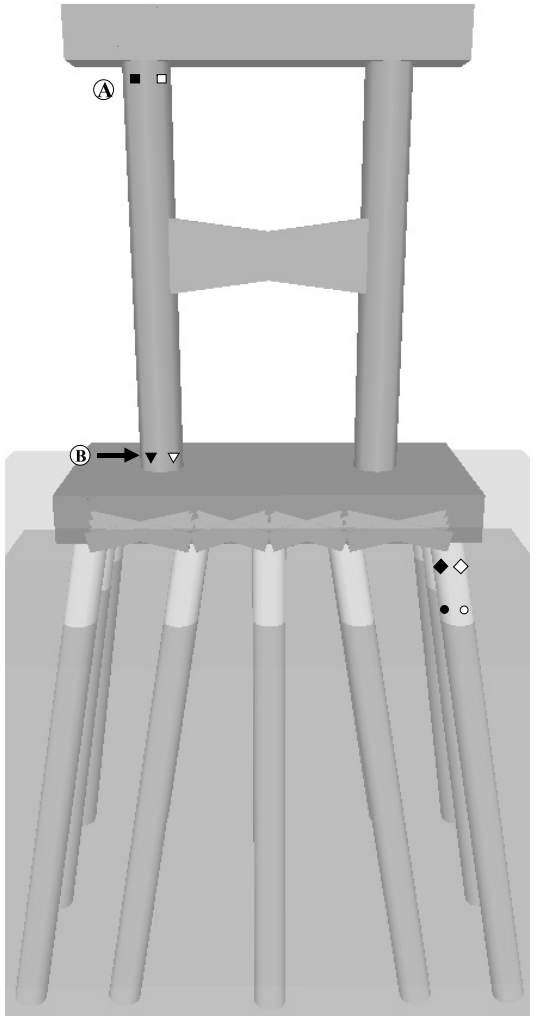

Figure A.7 Comparison of CVIA: Full vs. OPTS
Bridge: new St. George Island Causeway (NSG) channel pier; Impact condition: 5920 tons at 5.0 knots

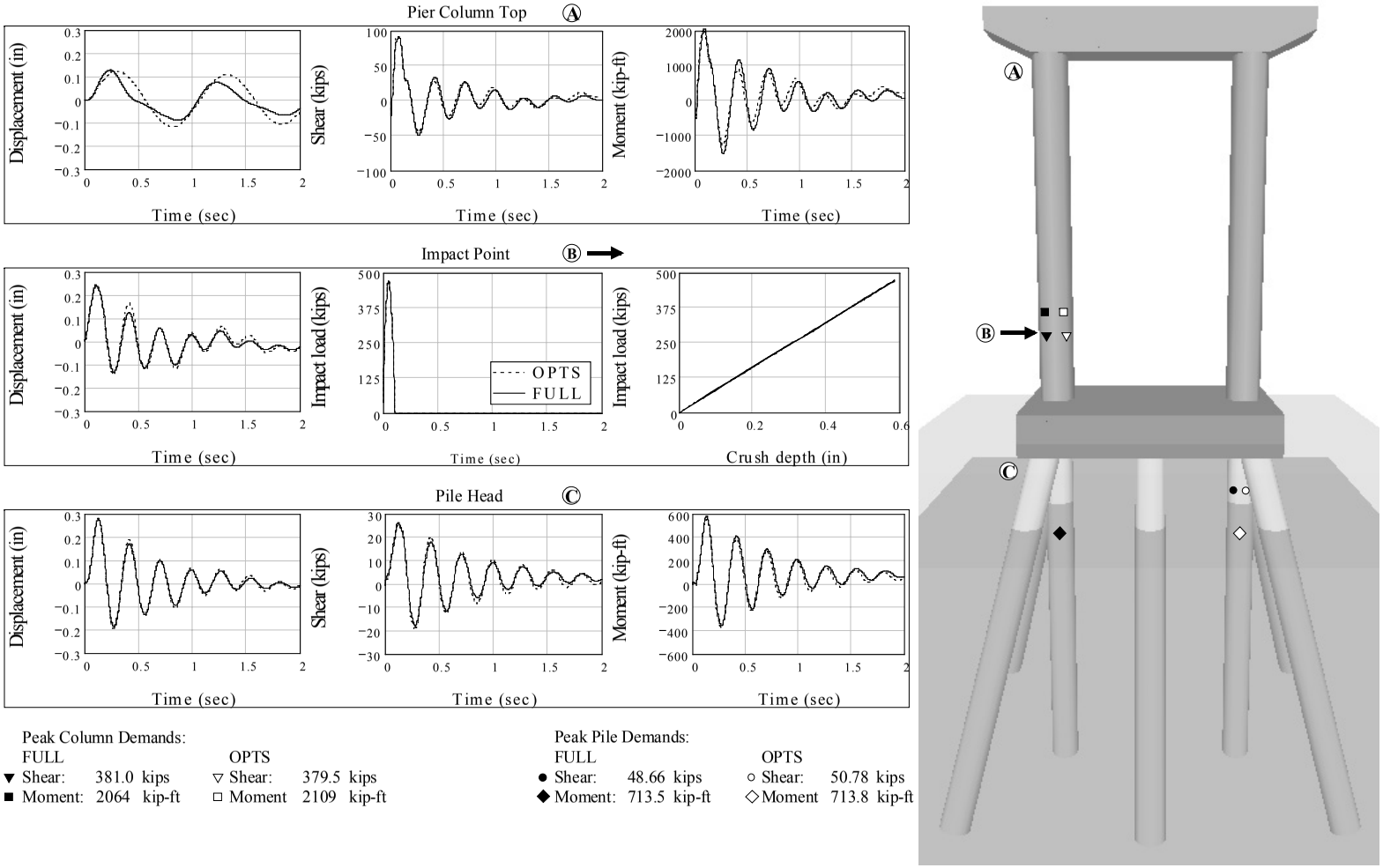

Figure A.8 Comparison of CVIA: Full vs. OPTS
Bridge: new St. George Island Causeway (NSG) off-channel pier; Impact condition: 200 tons at 1.0 knots

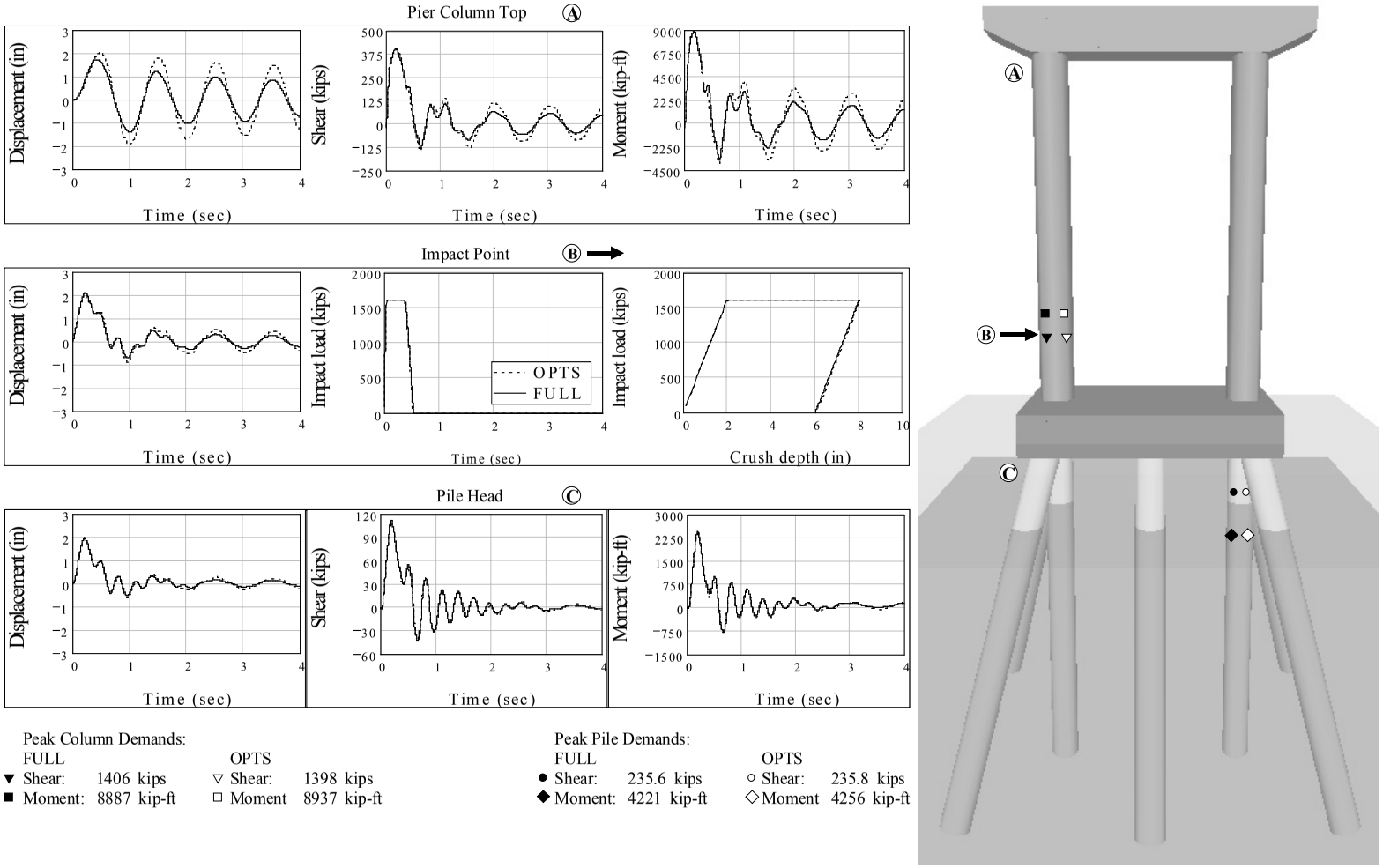

Figure A.9 Comparison of CVIA: Full vs. OPTS
Bridge: new St. George Island Causeway (NSG) off-channel pier; Impact condition: 2030 tons at 2.5 knots

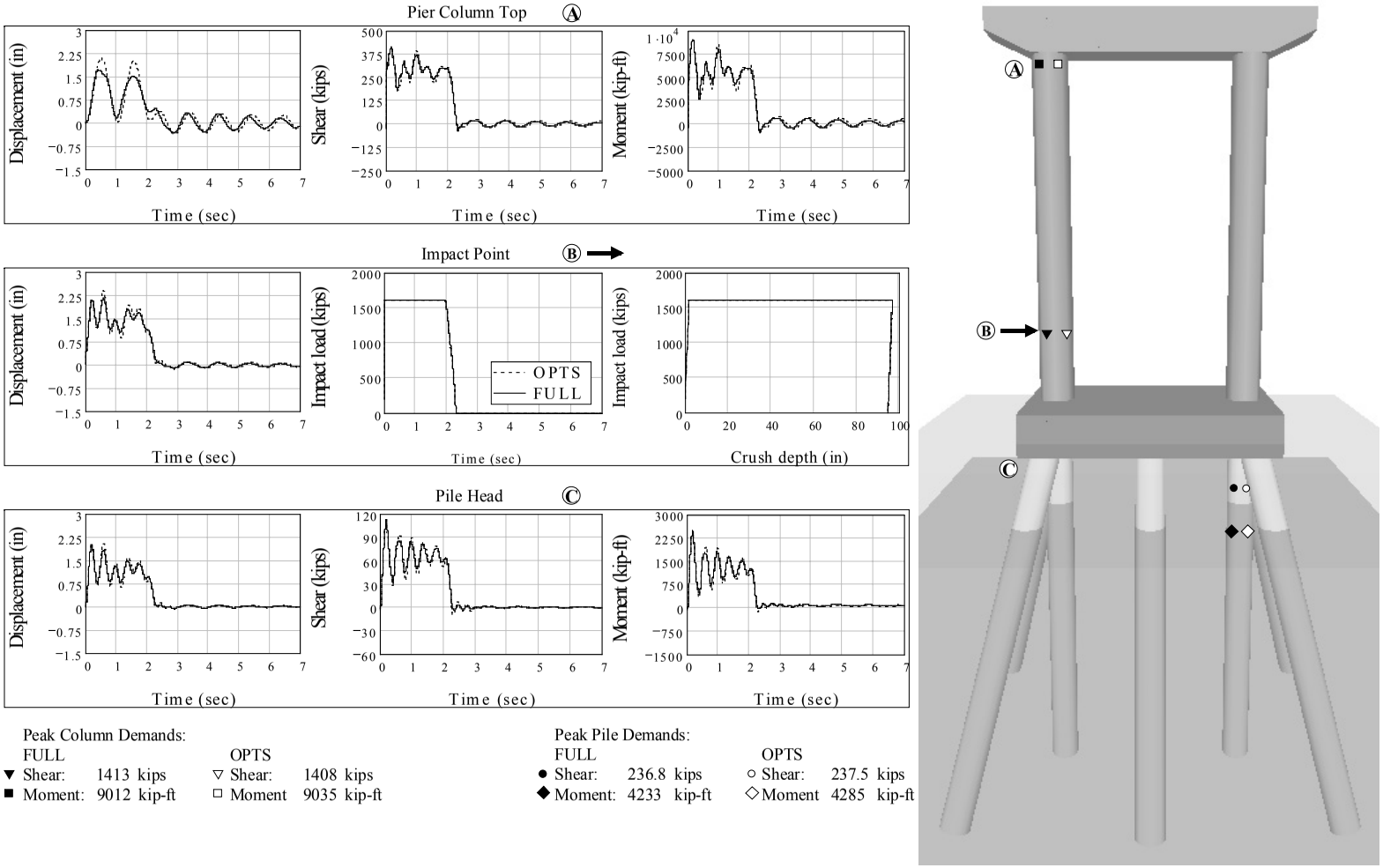

Figure A.10 Comparison of CVIA: Full vs. OPTS
Bridge: new St. George Island Causeway (NSG) off-channel pier; Impact condition: 5920 tons at 5.0 knots

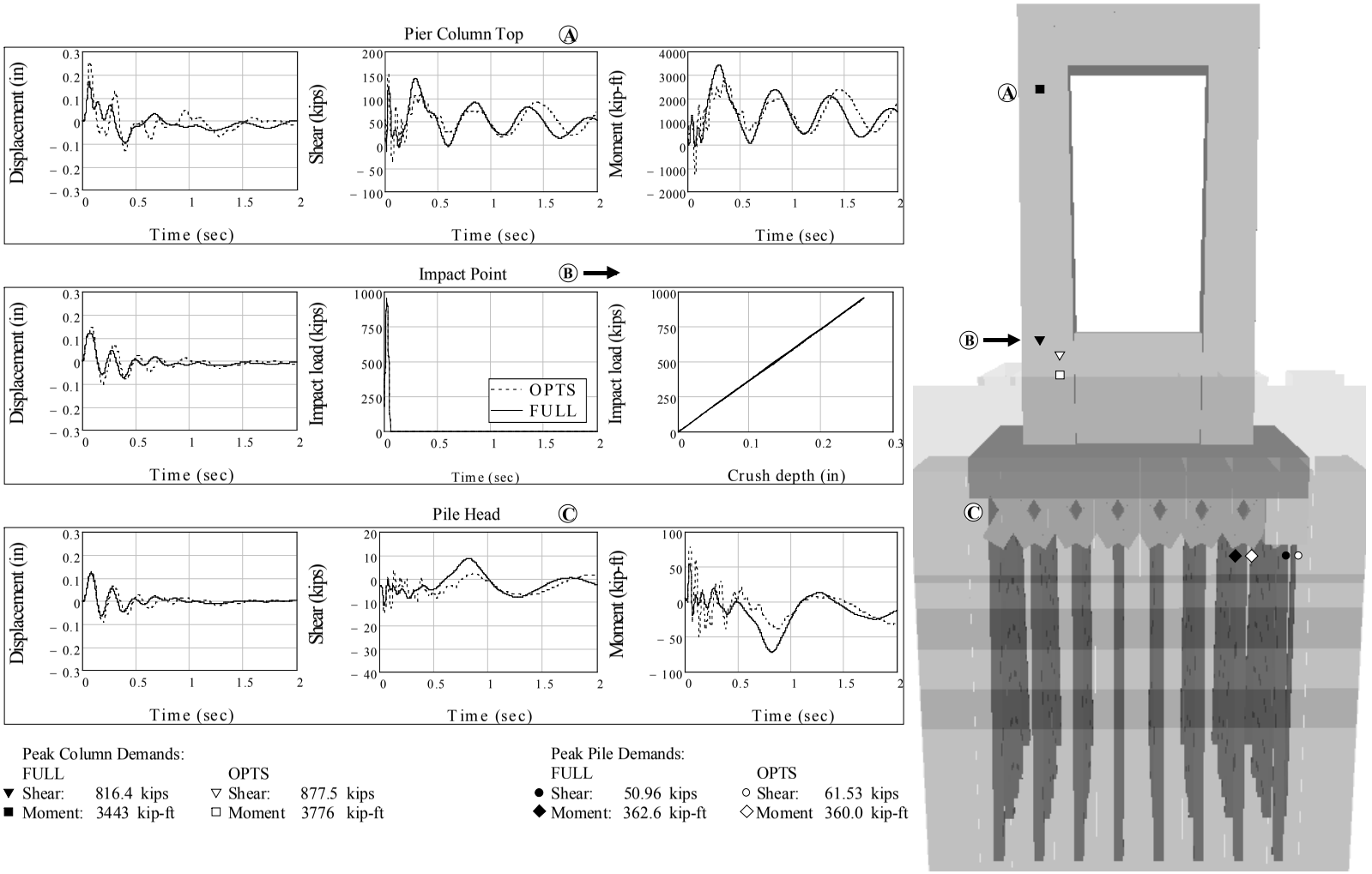

Figure A.11 Comparison of CVIA: Full vs. OPTS
Bridge: old St. George Island Causeway (OSG) channel pier; Impact condition: 200 tons at 1.0 knots

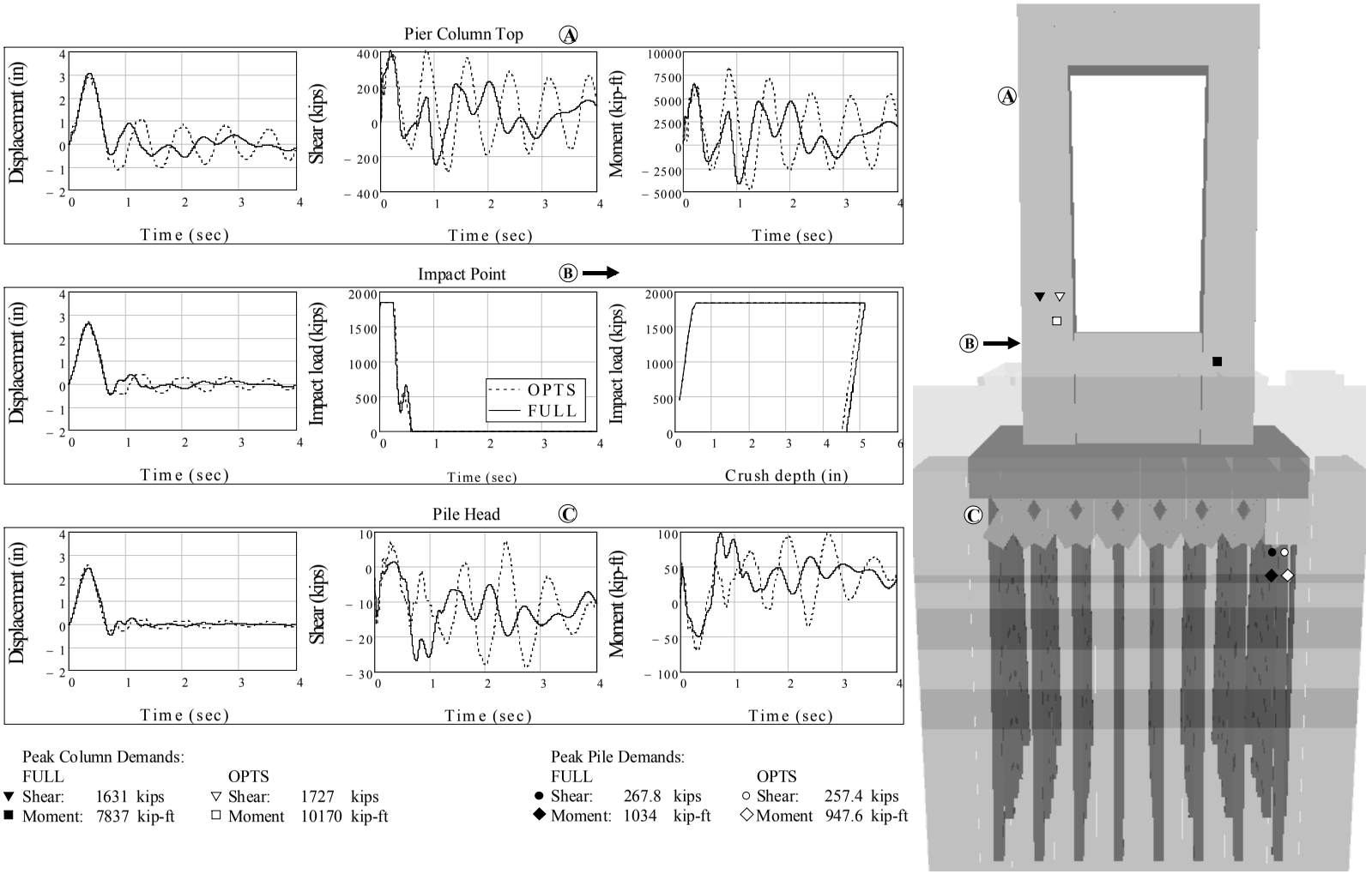

Figure A.12 Comparison of CVIA: Full vs. OPTS
Bridge: old St. George Island Causeway (OSG) channel pier; Impact condition: 2030 tons at 2.5 knots

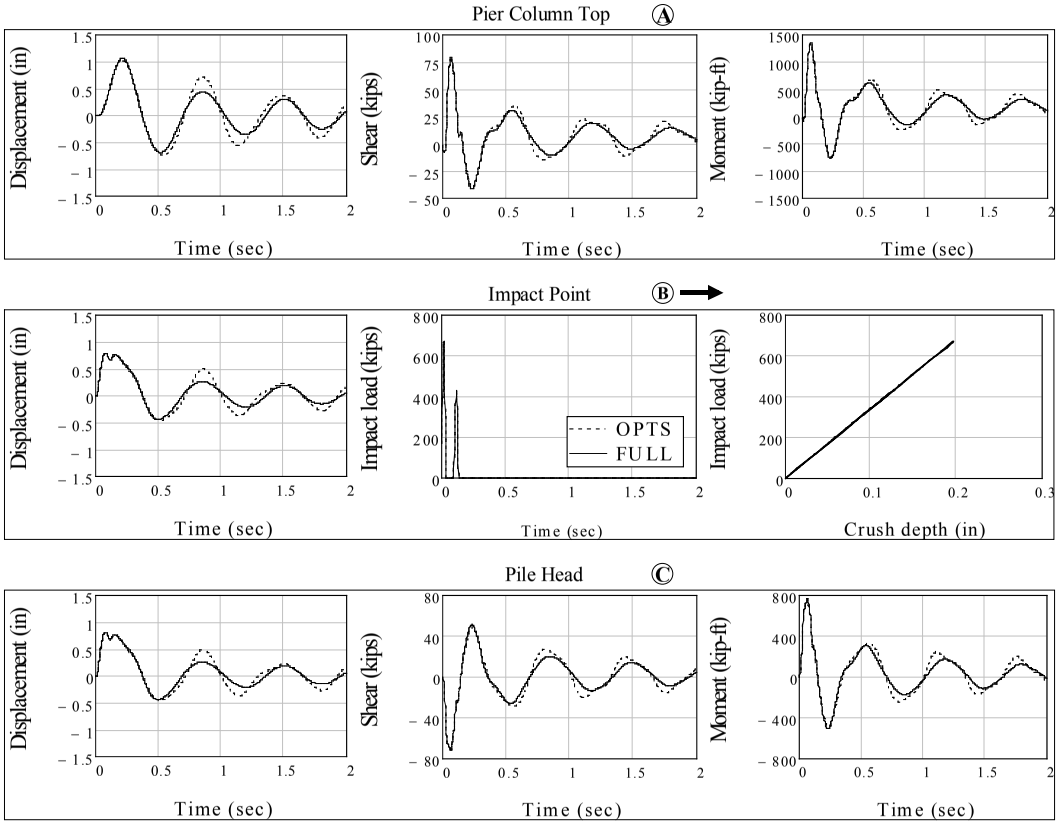

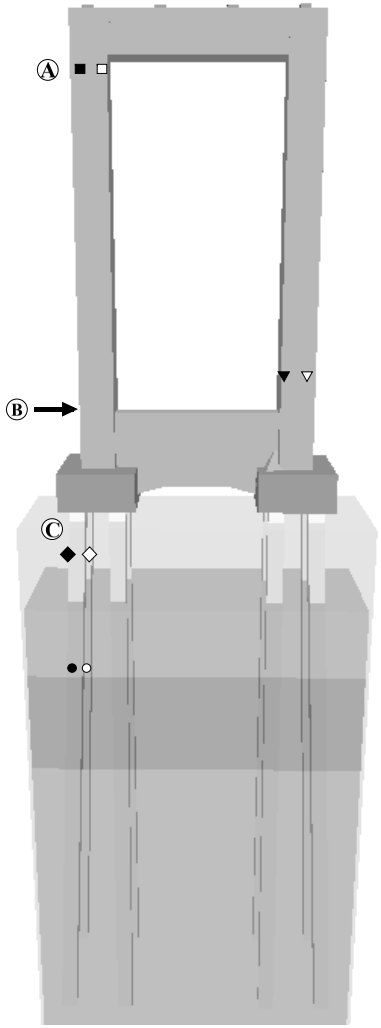

Figure A.13 Comparison of CVIA: Full vs. OPTS
Bridge: old St. George Island Causeway (OSG) off-channel pier; Impact condition: 200 tons at 1.0 knots

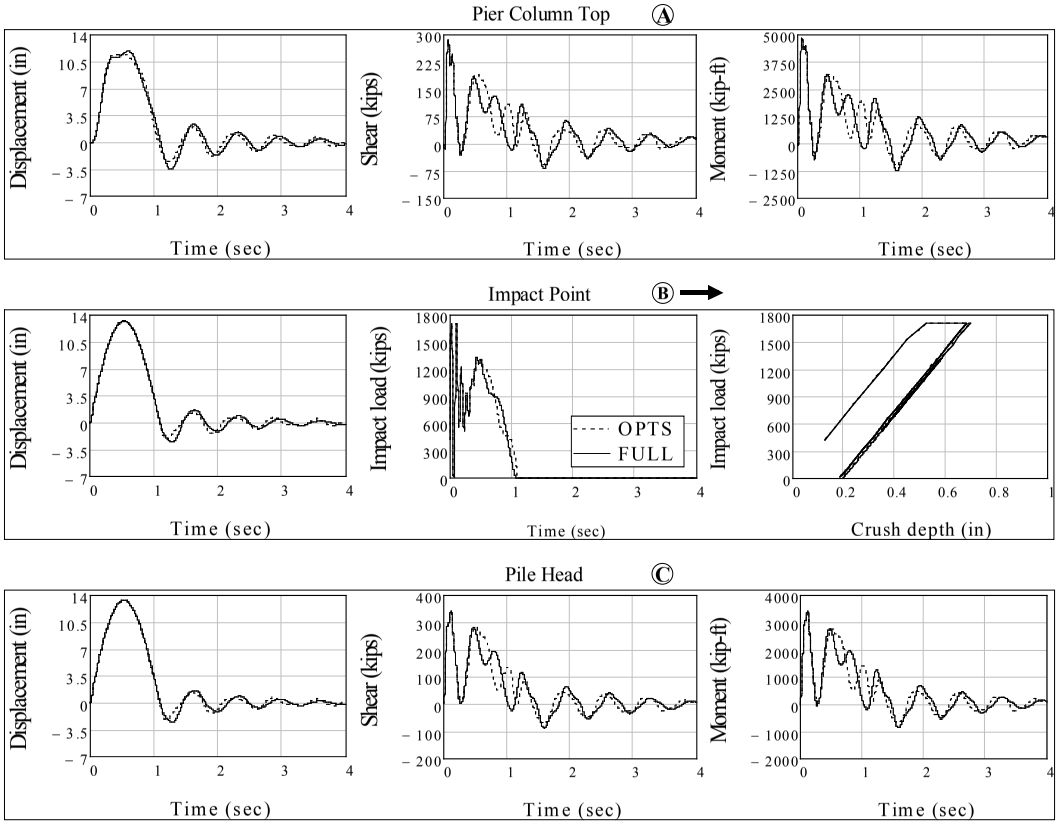

Peak Column Demands:

FULL			OPTS		
▼ Shear:	449.7	kips	▽ Shear:	432.0	kips
■ Moment:	5826	kip-ft	□ Moment	5690	kip-ft

Peak Pile Demands:

FULL			OPTS		
● Shear:	344.0	kips	○ Shear:	336.5	kips
◆ Moment:	3613	kip-ft	◇ Moment	3539	kip-ft

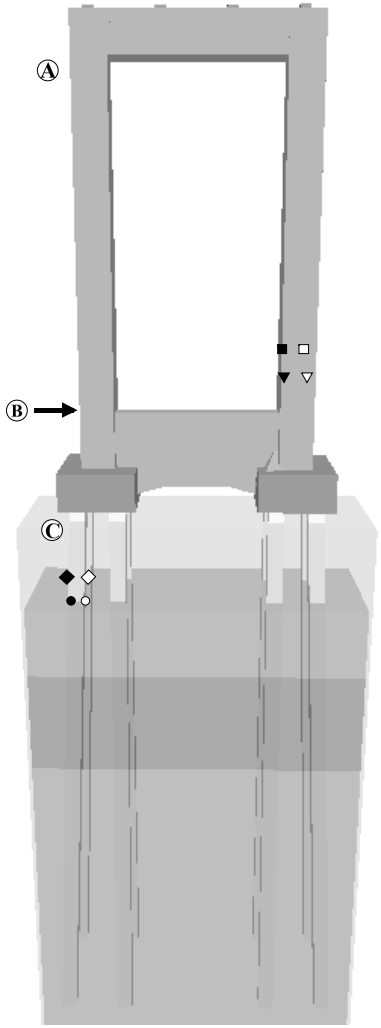

Figure A.14 Comparison of CVIA: Full vs. OPTS
Bridge: old St. George Island Causeway (OSG) off-channel pier; Impact condition: 2030 tons at 2.5 knots

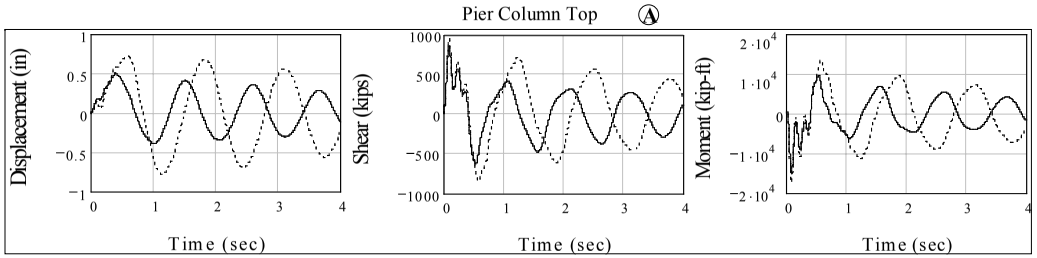

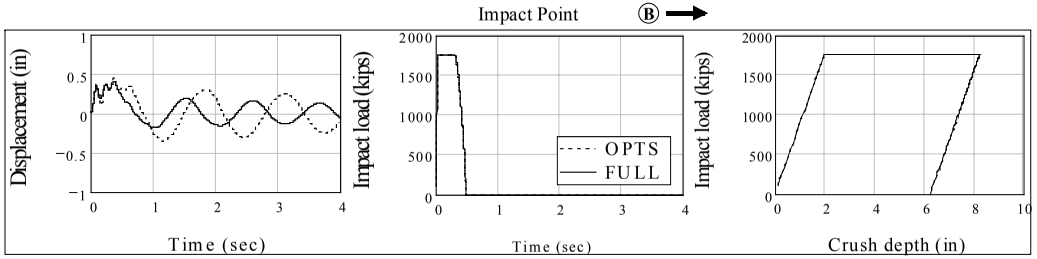

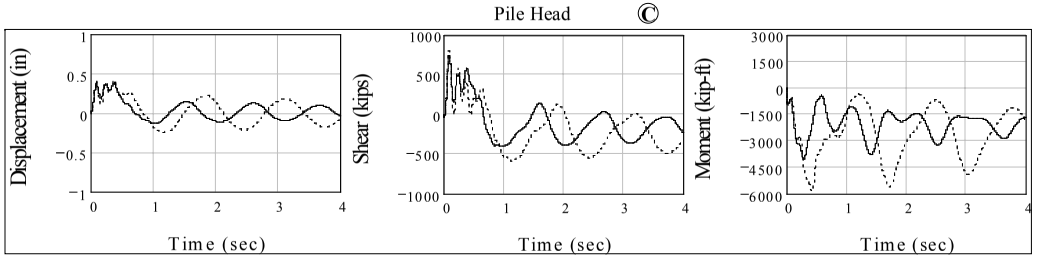

Peak Column Demands:

FULL		OPTS	
▼ Shear:	1417 kips	▽ Shear:	1401 kips
■ Moment:	45510 kip-ft	□ Moment	53860 kip-ft

Peak Pile Demands:

FULL		OPTS	
● Shear:	1153 kips	○ Shear:	1211 kips
◆ Moment:	9933 kip-ft	◇ Moment	14980 kip-ft

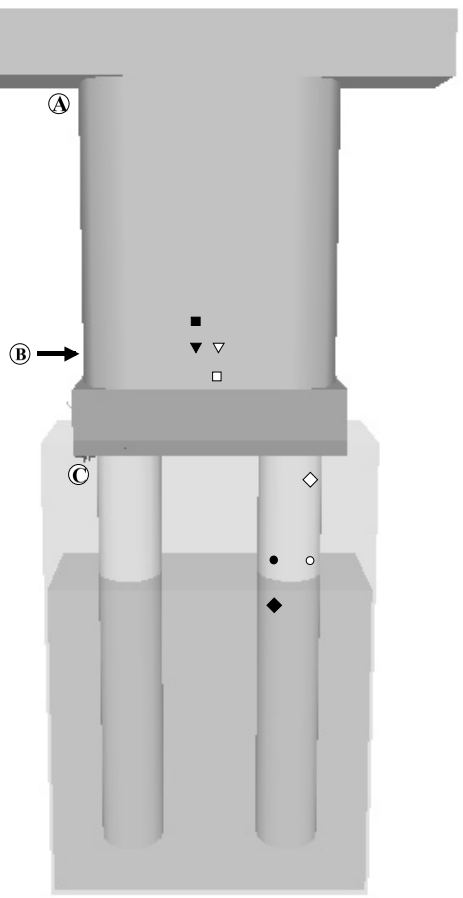

Figure A.15 Comparison of CVIA: Full vs. OPTS
Bridge: Ringling (RNG) channel pier; Impact condition: 2030 tons at 2.5 knots

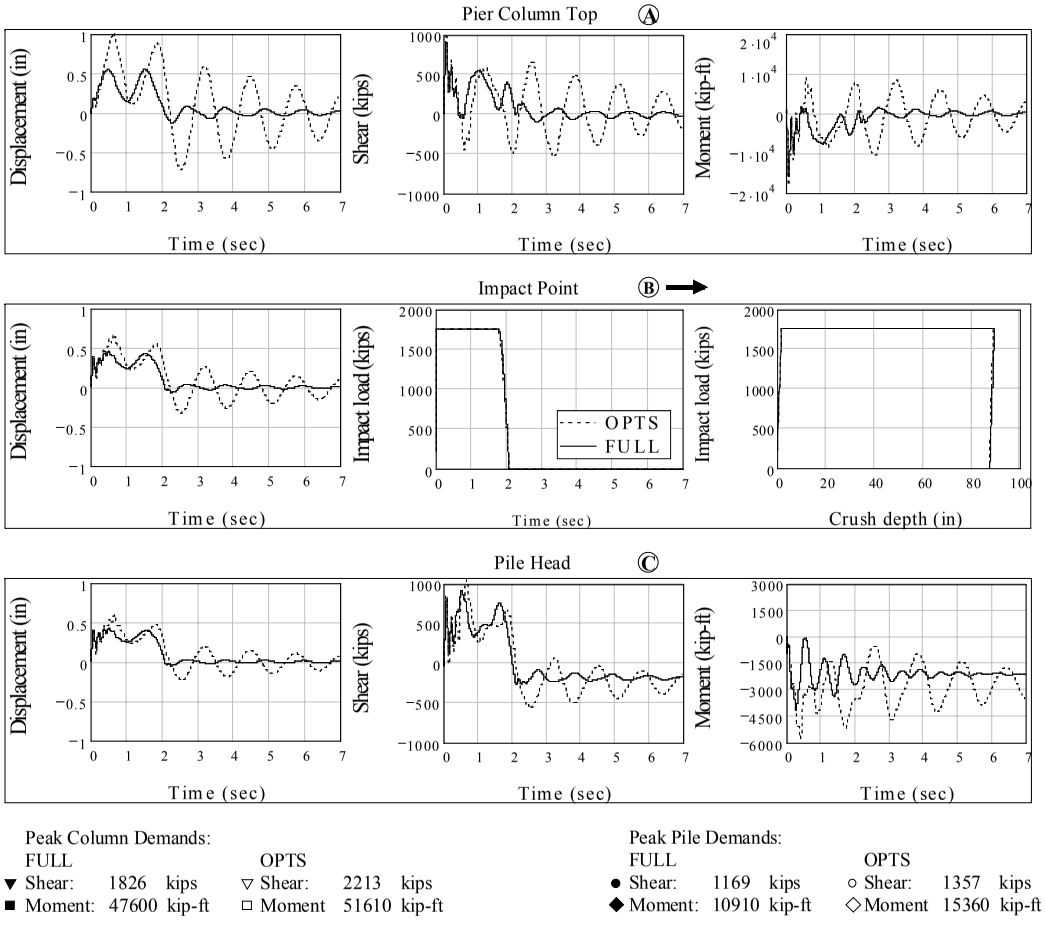

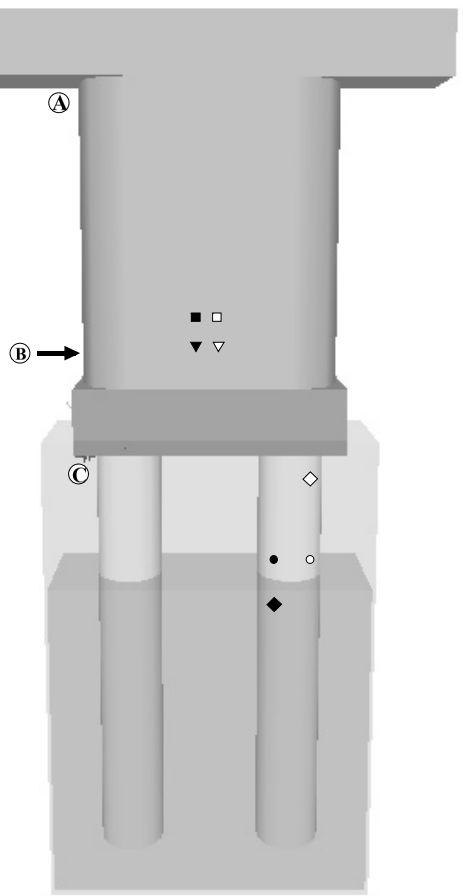

Figure A.16 Comparison of CVIA: Full vs. OPTS
Bridge: Ringling (RNG) channel pier; Impact condition: 5920 tons at 5.0 knots

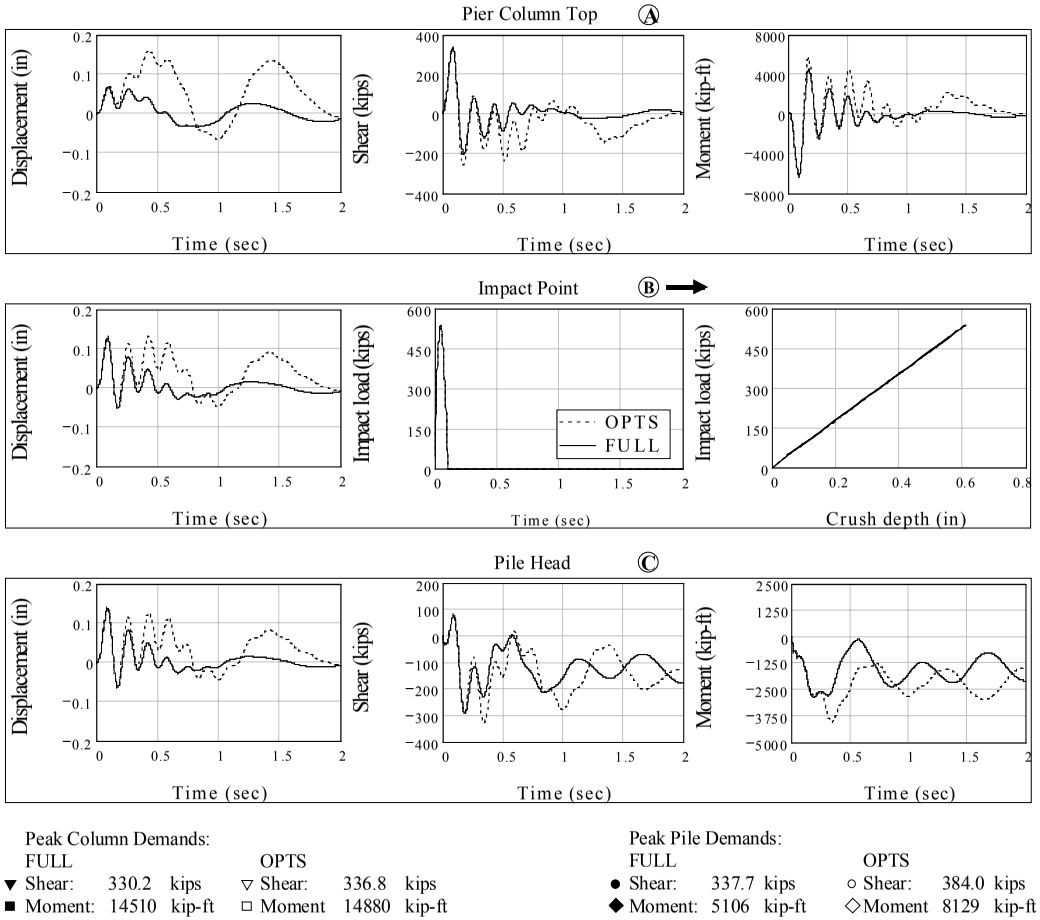

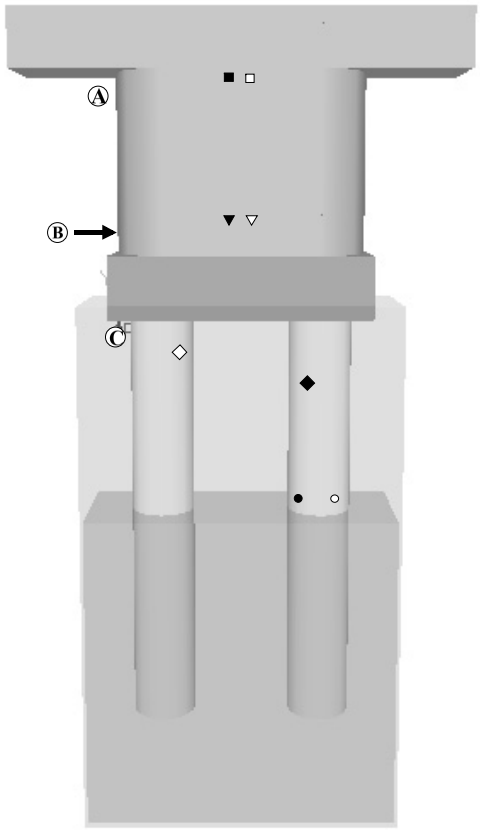

Figure A.17 Comparison of CVIA: Full vs. OPTS
Bridge: Ringling (RNG) off-channel pier; Impact condition: 200 tons at 1.0 knots

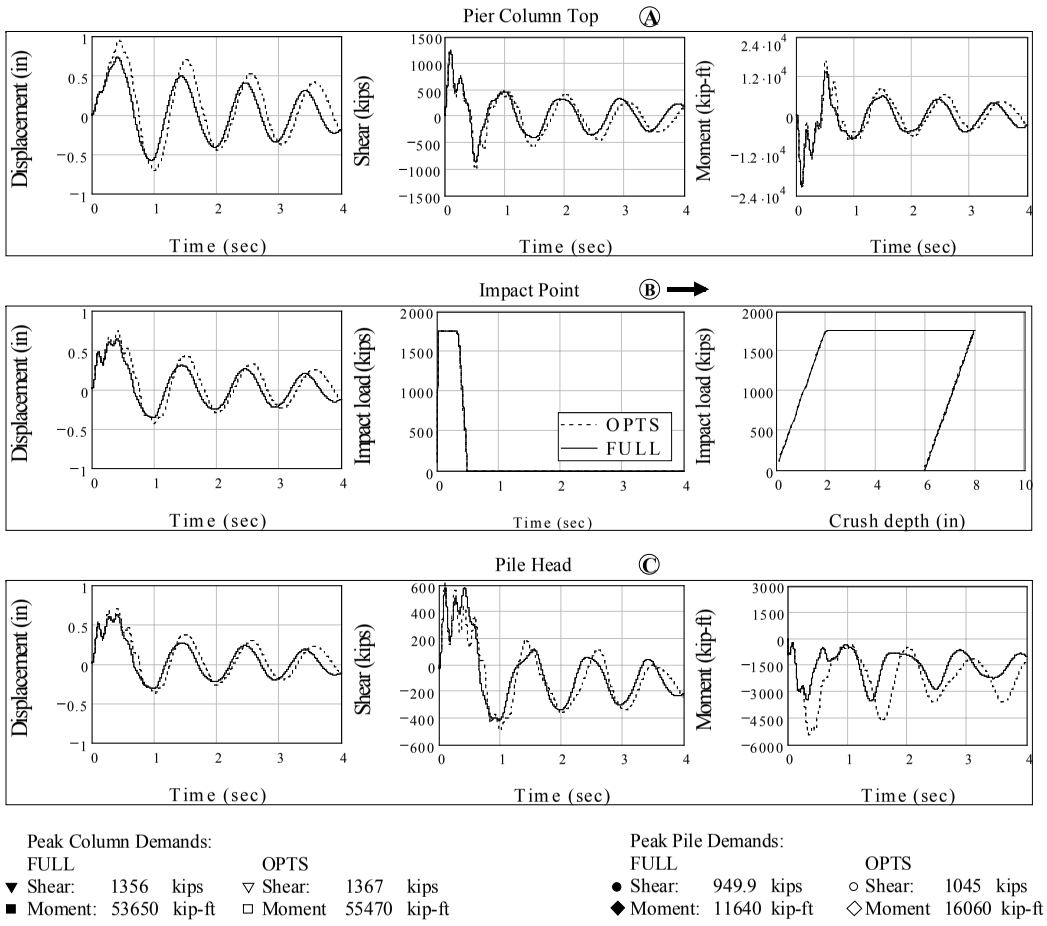

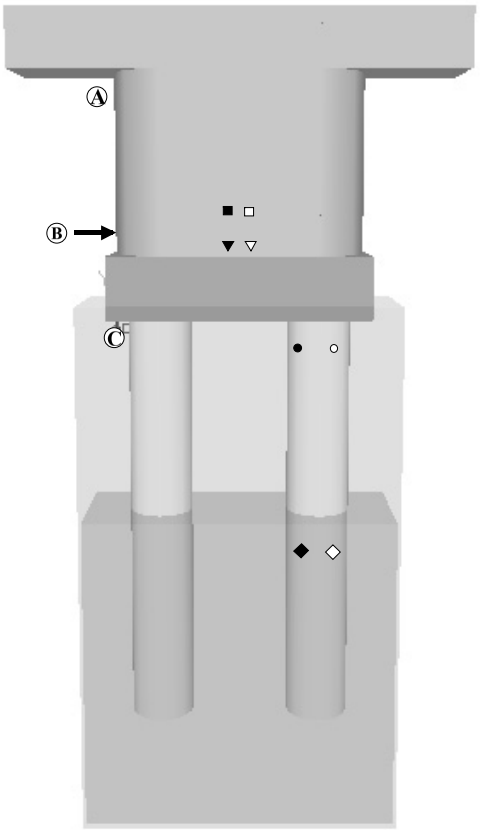

Figure A.18 Comparison of CVIA: Full vs. OPTSS
Bridge: Ringling (RNG) off-channel pier; Impact condition: 2030 tons at 2.5 knots

APPENDIX B
COMPARISON OF CVIA, IRSA, AND AASHTO RESULTS

The response of each of the bridge models that were investigated in the parametric study was determined using three analysis techniques: coupled vessel impact analysis (CVIA), impact response spectrum analysis (IRSA), and the static method prescribed by the American Association of State Highway and Transportation Officials (AASHTO). The data presented here provide a comparison of results obtained from these three analysis methods.

Figures presented in this appendix present the maximum magnitudes of displacement, shear force, and moment at each vertical elevation, for all three analysis methods. Elevation data have been adjusted such that the elevation datum (0 ft.) corresponds to the midplane elevation of the pile cap. In each figure, a gray rectangle is used to represent the pile cap vertical thickness. Each figure represents one impact energy condition applied to a respective bridge-pier configuration.

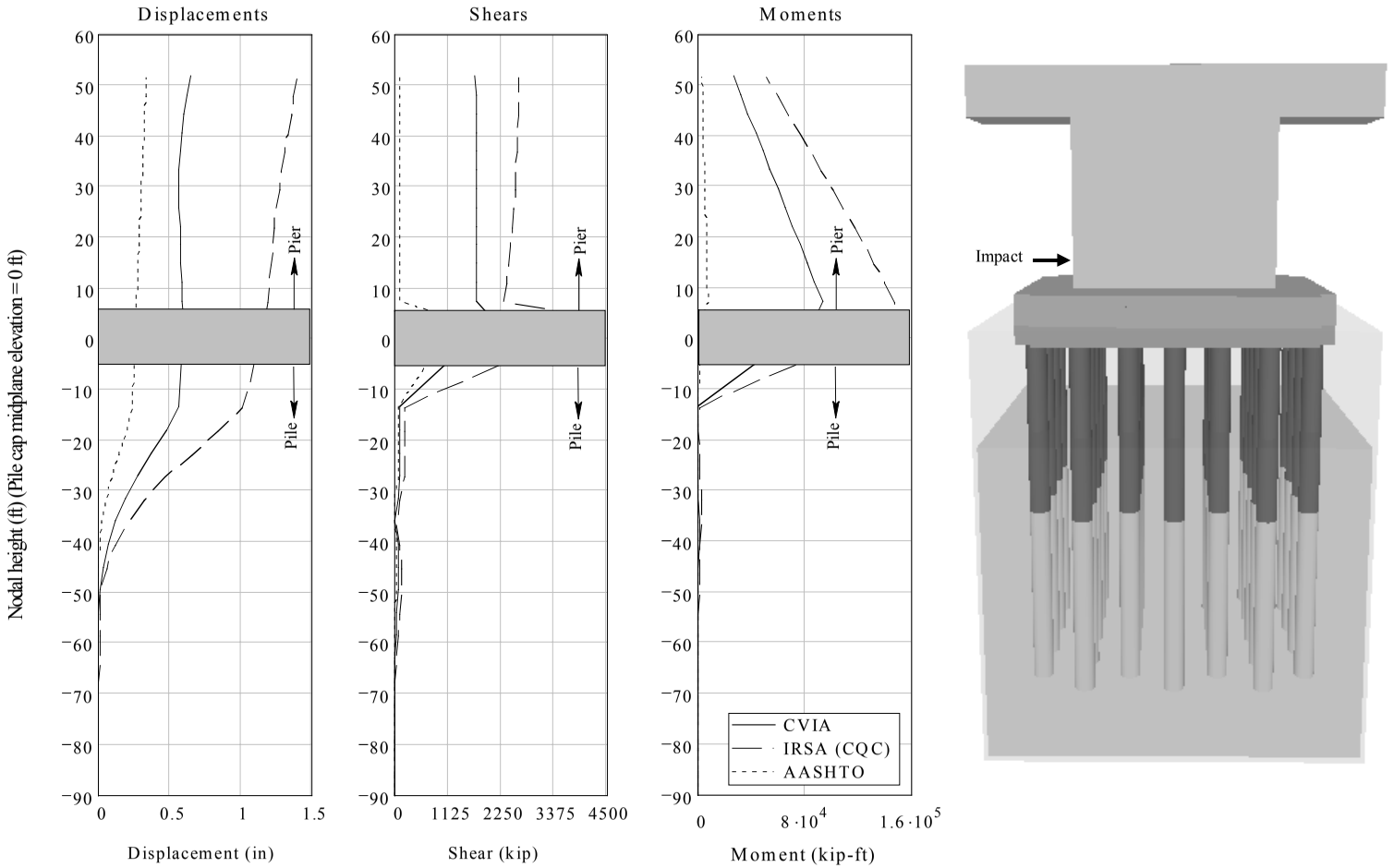

Figure B.1 Comparison of CVIA, IRSA, and AASHTO results
Bridge: Acosta Bridge (ACS) channel pier; Impact condition: 2030 tons at 2.5 knots

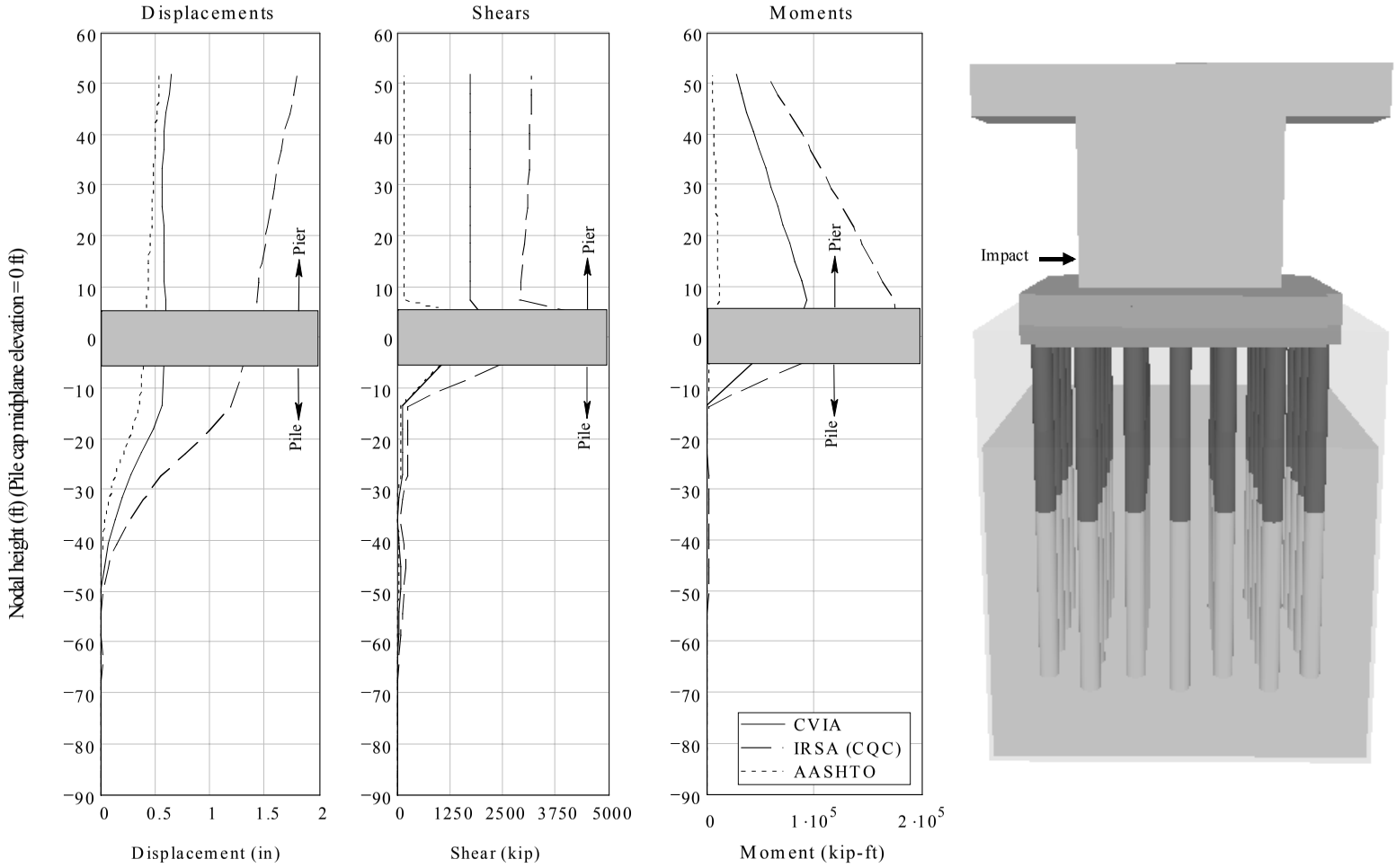

Figure B.2 Comparison of CVIA, IRSA, and AASHTO results
Bridge: Acosta Bridge (ACS) channel pier; Impact condition: 5920 tons at 5.0 knots

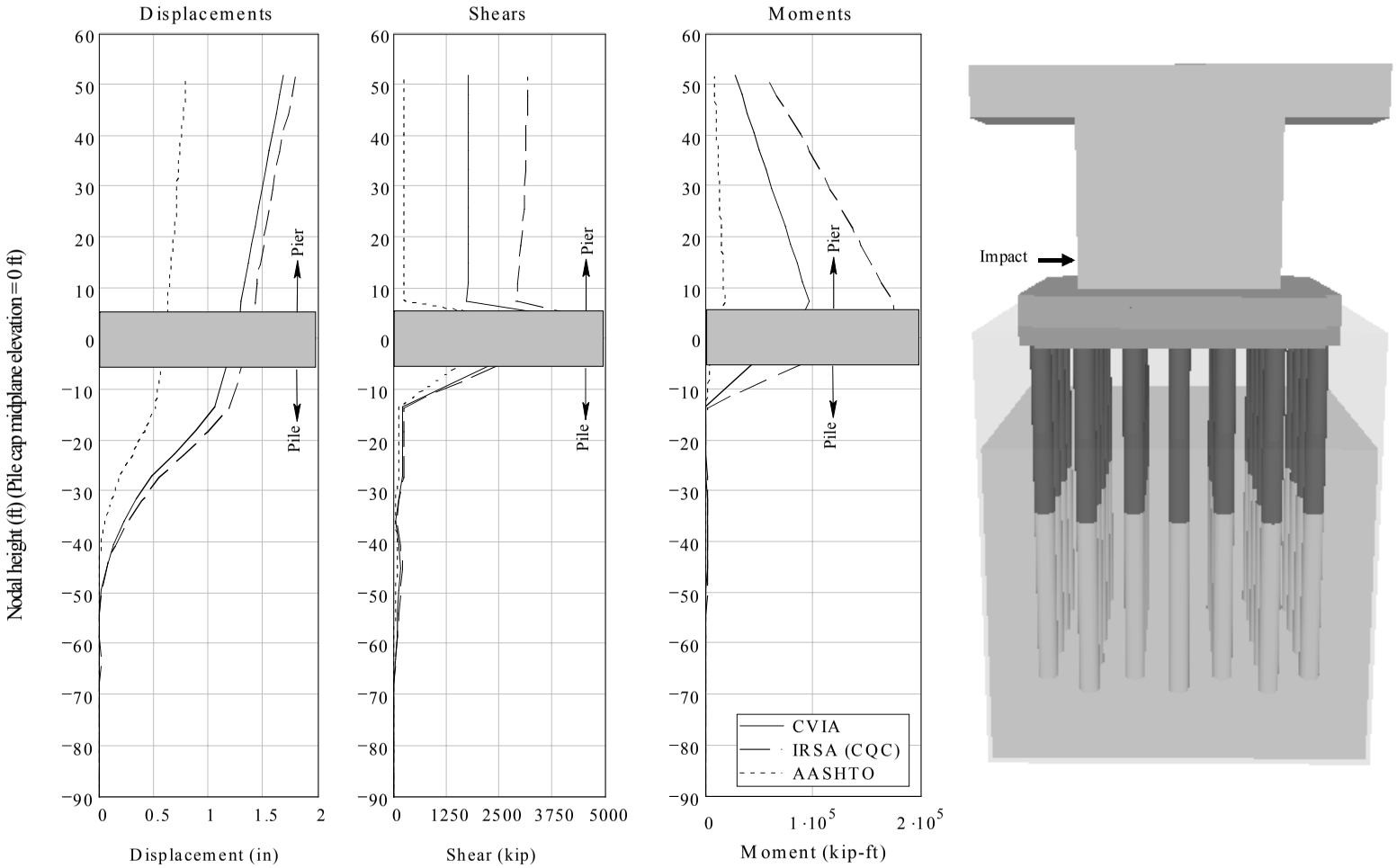

Figure B.3 Comparison of CVIA, IRSA, and AASHTO results
Bridge: Acosta Bridge (ACS) channel pier; Impact condition: 7820 tons at 5.0 knots

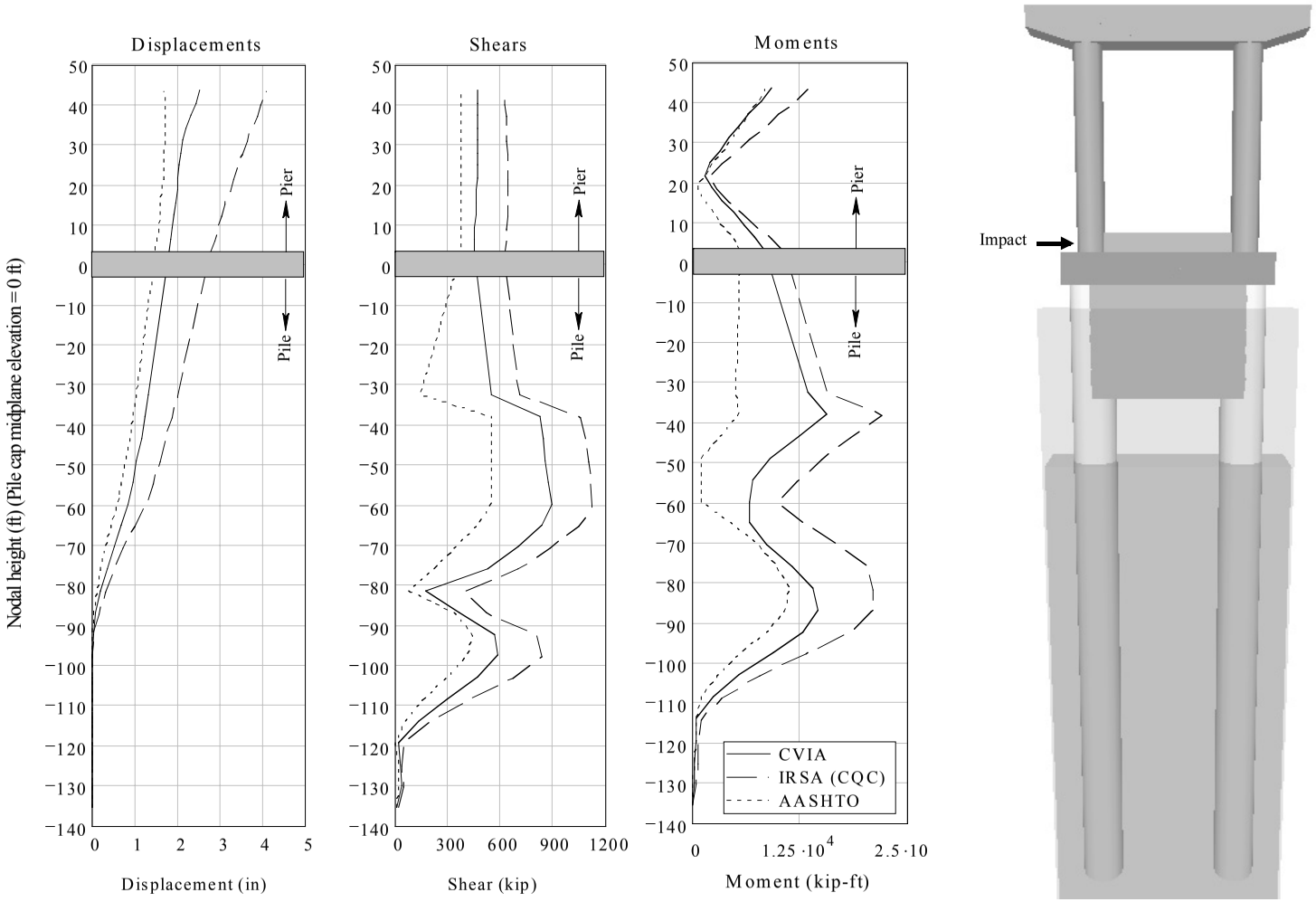

Figure B.4 Comparison of CVIA, IRSA, and AASHTO results
Bridge: SR-20 at Blountstown (BLT) channel pier; Impact condition: 2030 tons at 2.5 knots

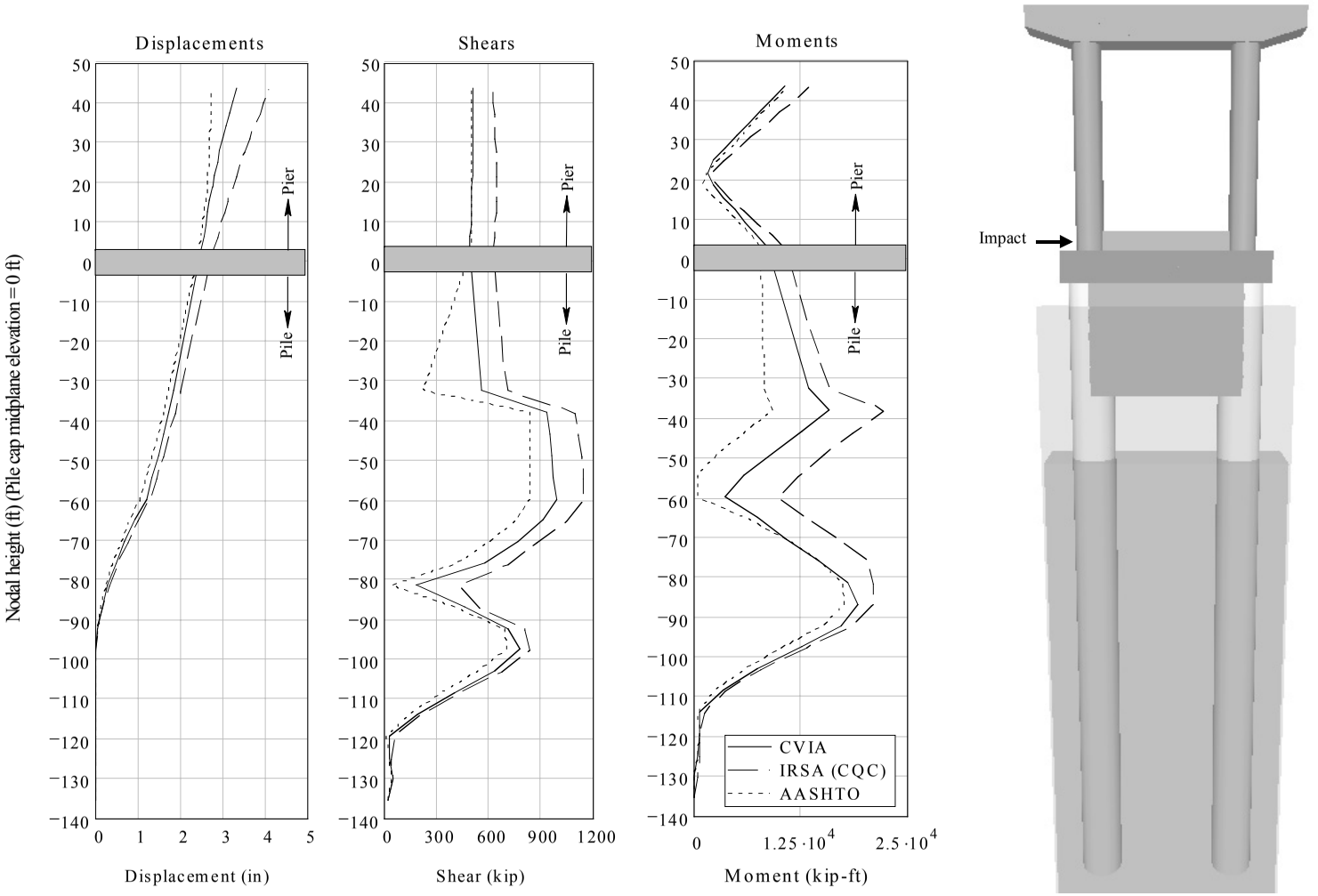

Figure B.5 Comparison of CVIA, IRSA, and AASHTO results
Bridge: SR-20 at Blountstown (BLT) channel pier; Impact condition: 5920 tons at 5.0 knots

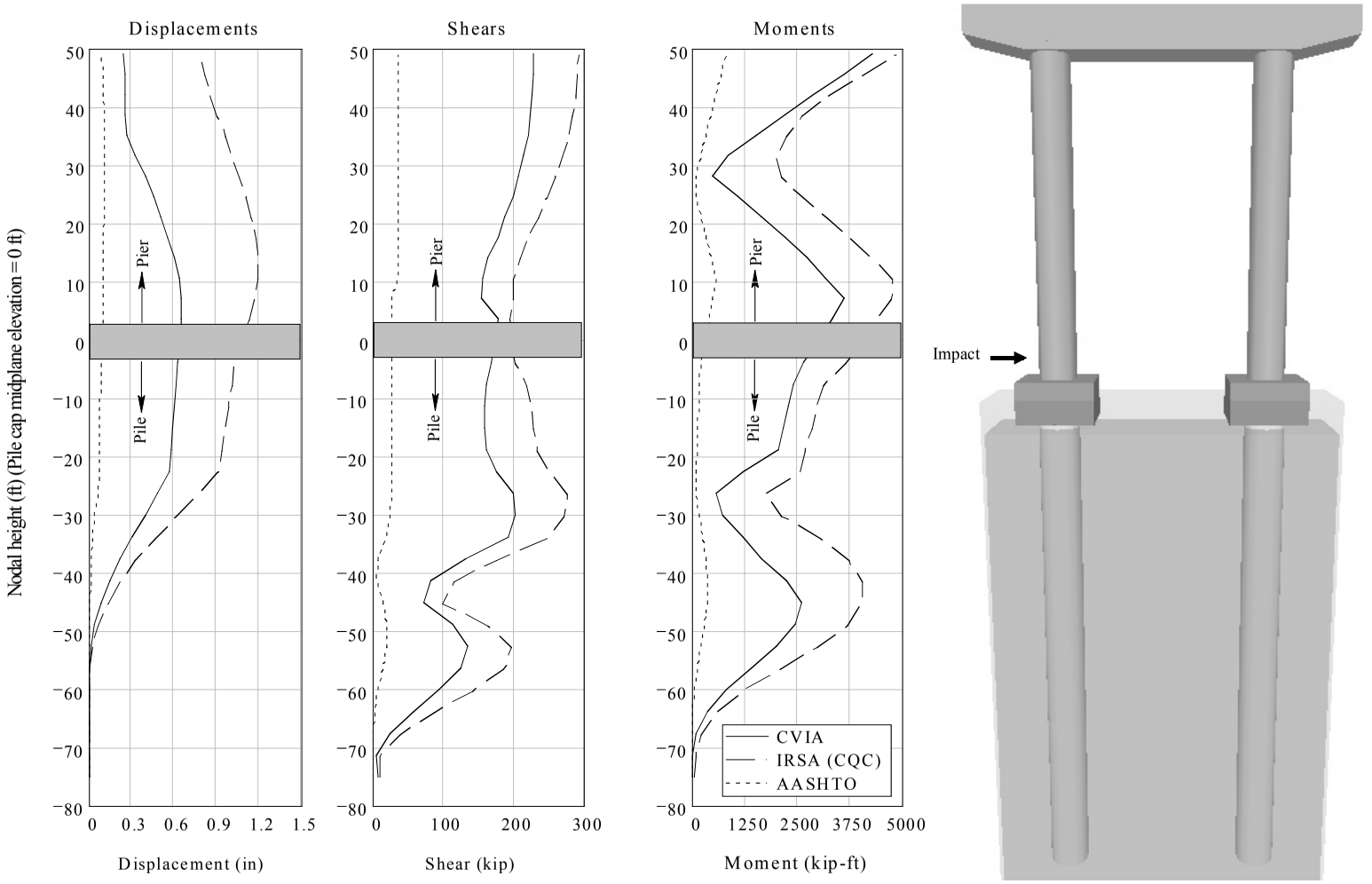

Figure B.6 Comparison of CVIA, IRSA, and AASHTO results
Bridge: SR-20 at Blountstown (BLT) off-channel pier; Impact condition: 200 tons at 1.0 knots

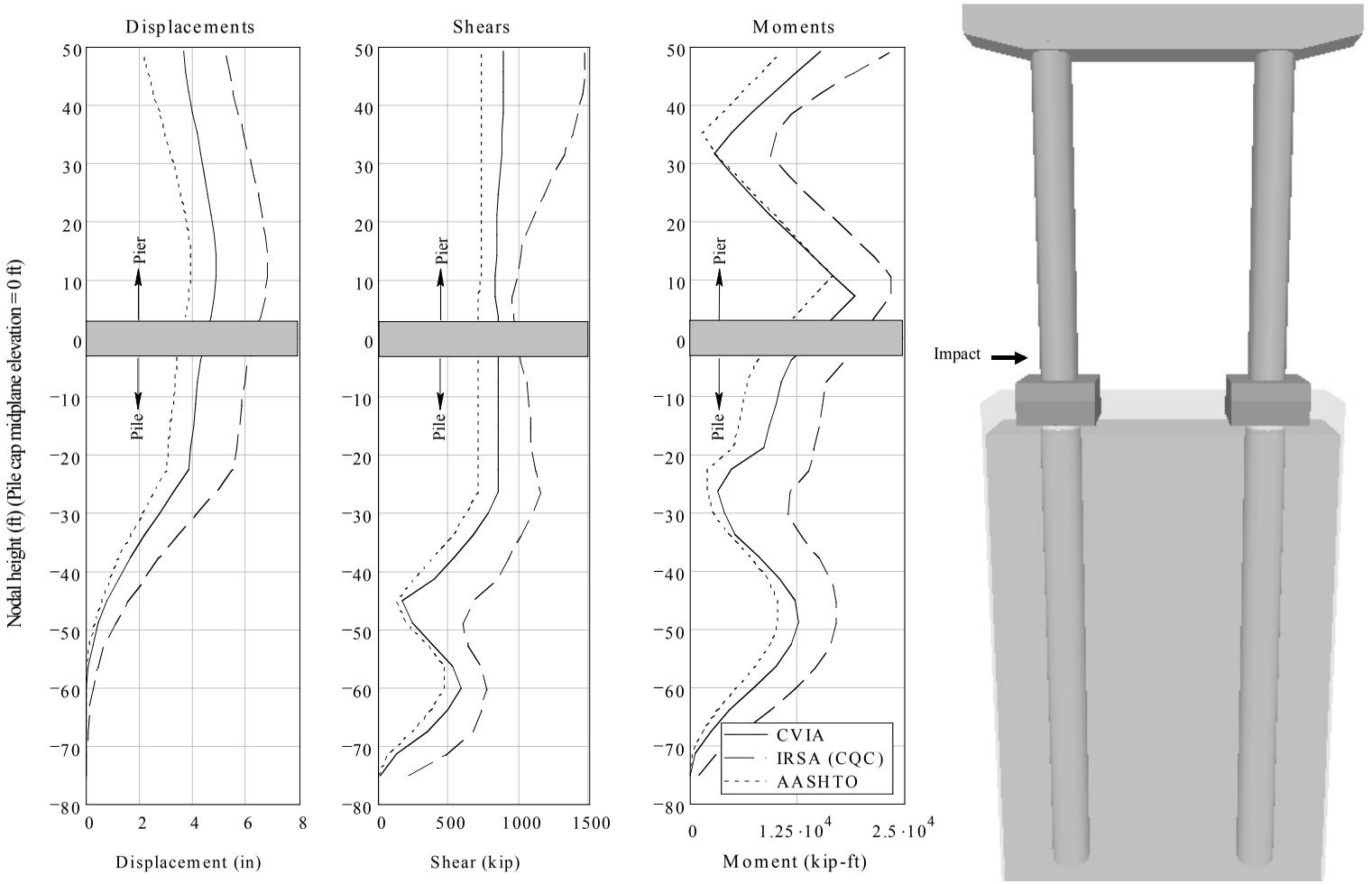

Figure B.7 Comparison of CVIA, IRSA, and AASHTO results
Bridge: SR-20 at Blountstown (BLT) off-channel pier; Impact condition: 2030 tons at 2.5 knots

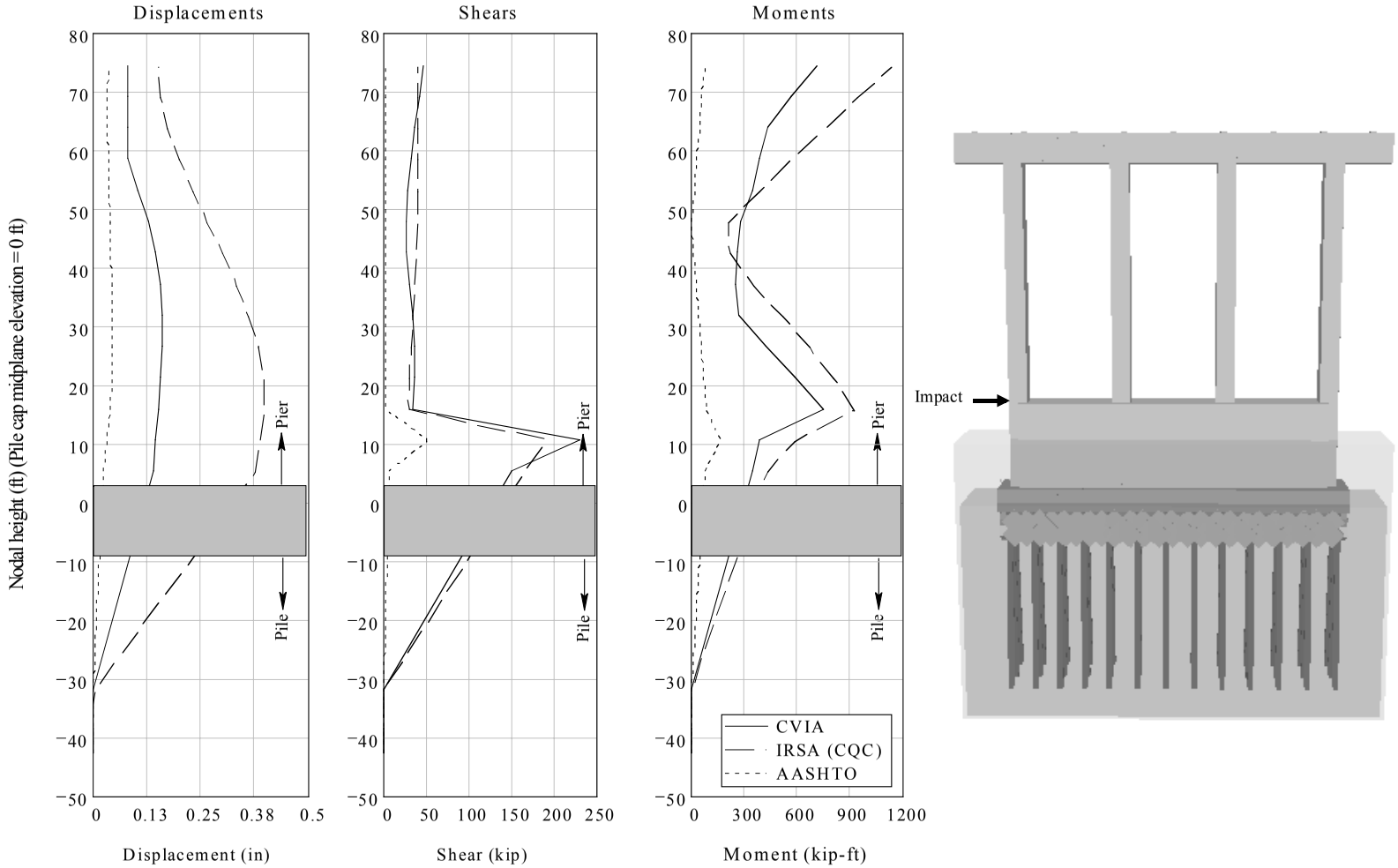

Figure B.8 Comparison of CVIA, IRSA, and AASHTO results
Bridge: Eau Gallie Bridge (EGB) channel pier; Impact condition: 200 tons at 1.0 knots

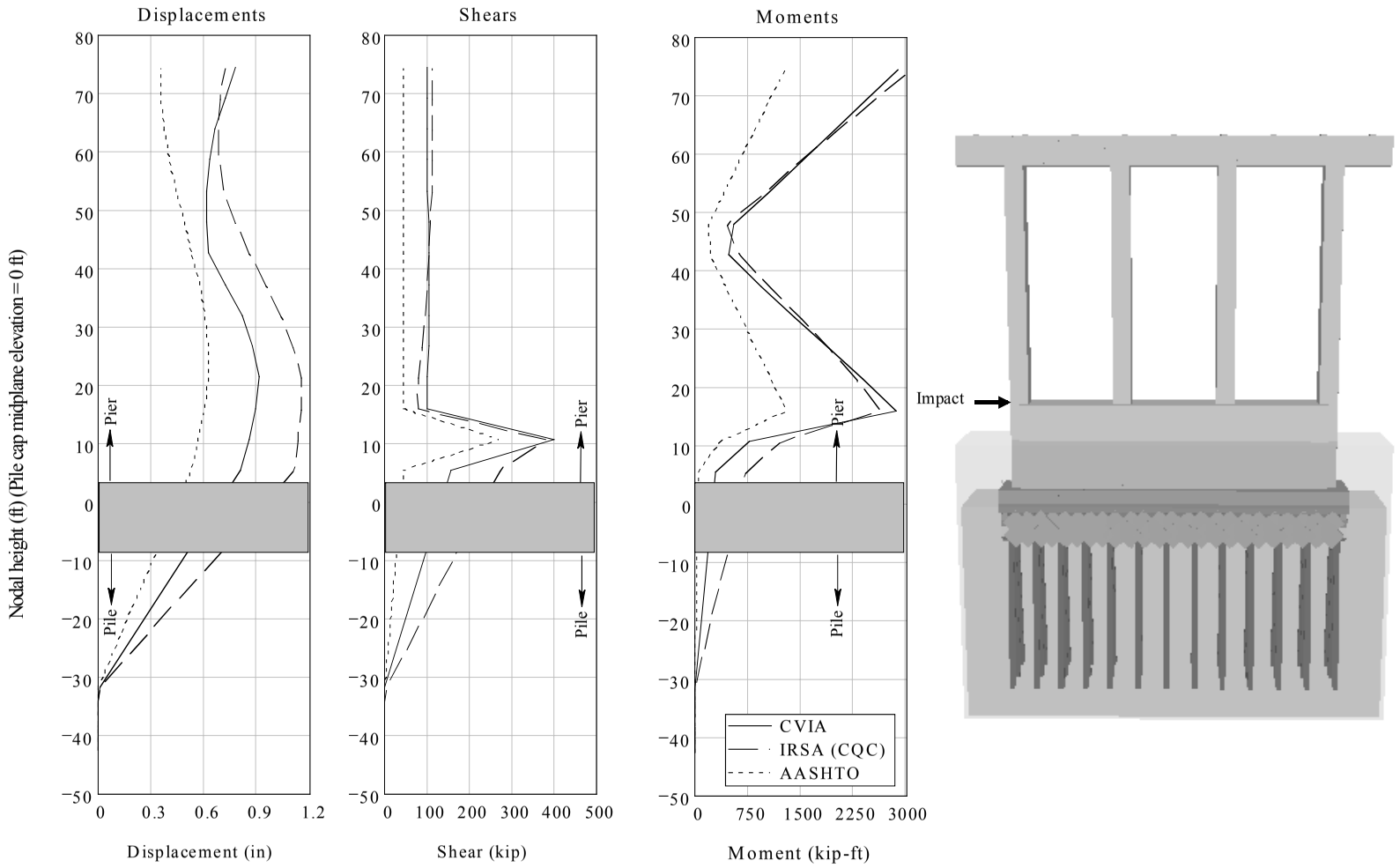

Figure B.9 Comparison of CVIA, IRSA, and AASHTO results
Bridge: Eau Gallie Bridge (EGB) channel pier; Impact condition: 2030 tons at 2.5 knots

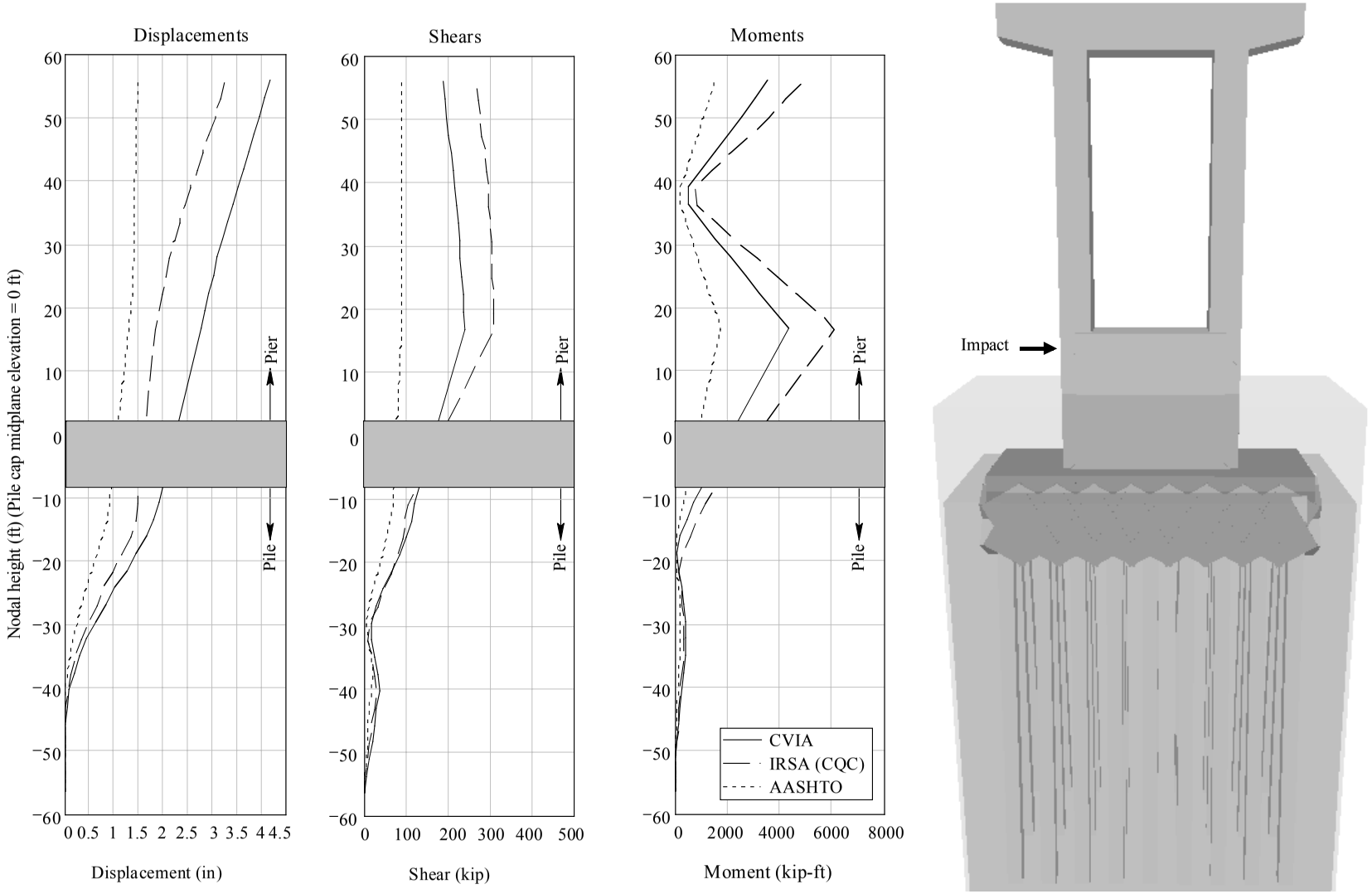

Figure B.10 Comparison of CVIA, IRSA, and AASHTO results
Bridge: I-10 over Escambia Bay (ESB) channel pier; Impact condition: 2030 tons at 2.5 knots

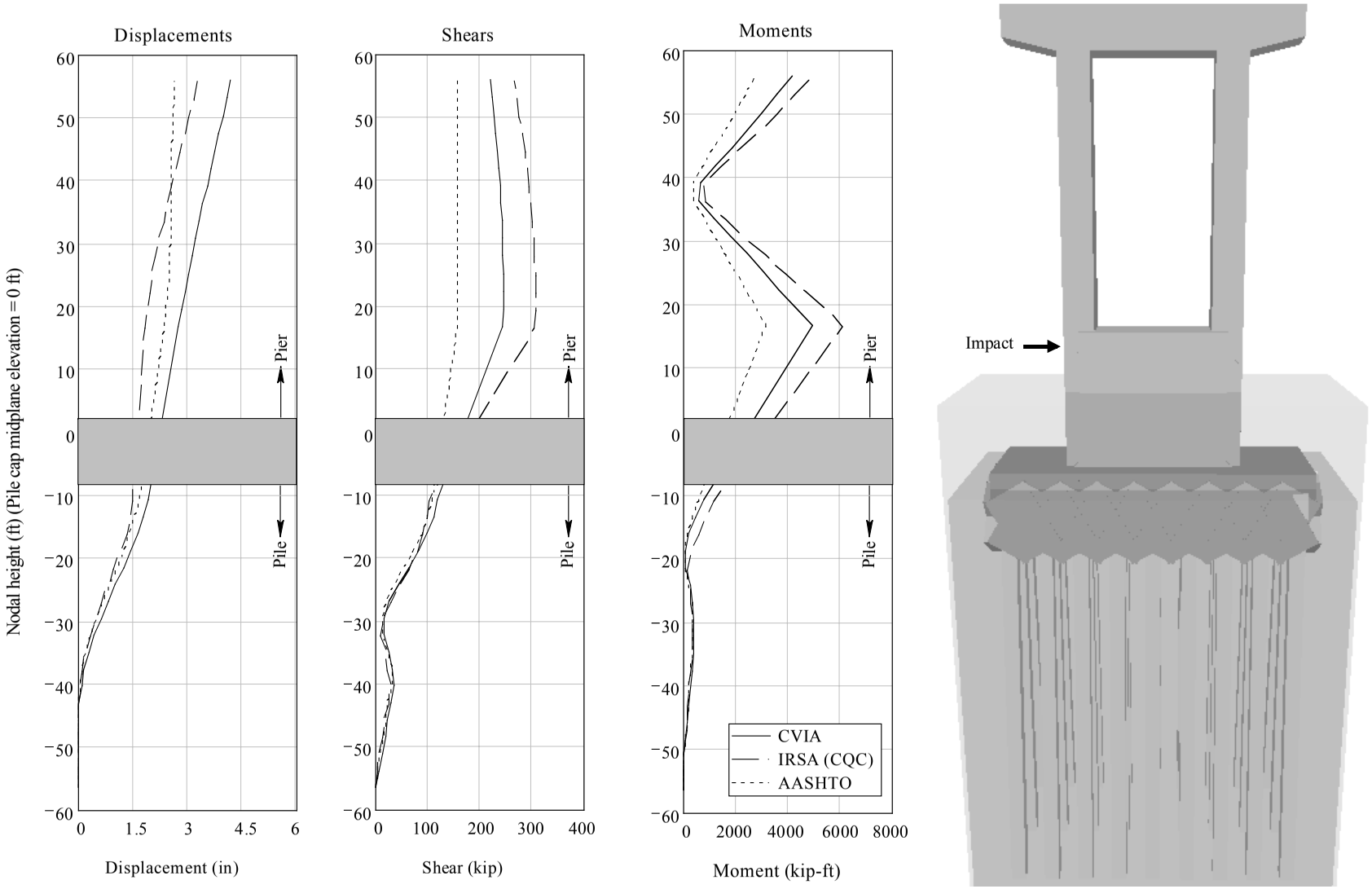

Figure B.11 Comparison of CVIA, IRSA, and AASHTO results
Bridge: I-10 over Escambia Bay (ESB) channel pier; Impact condition: 5920 tons at 5.0 knots

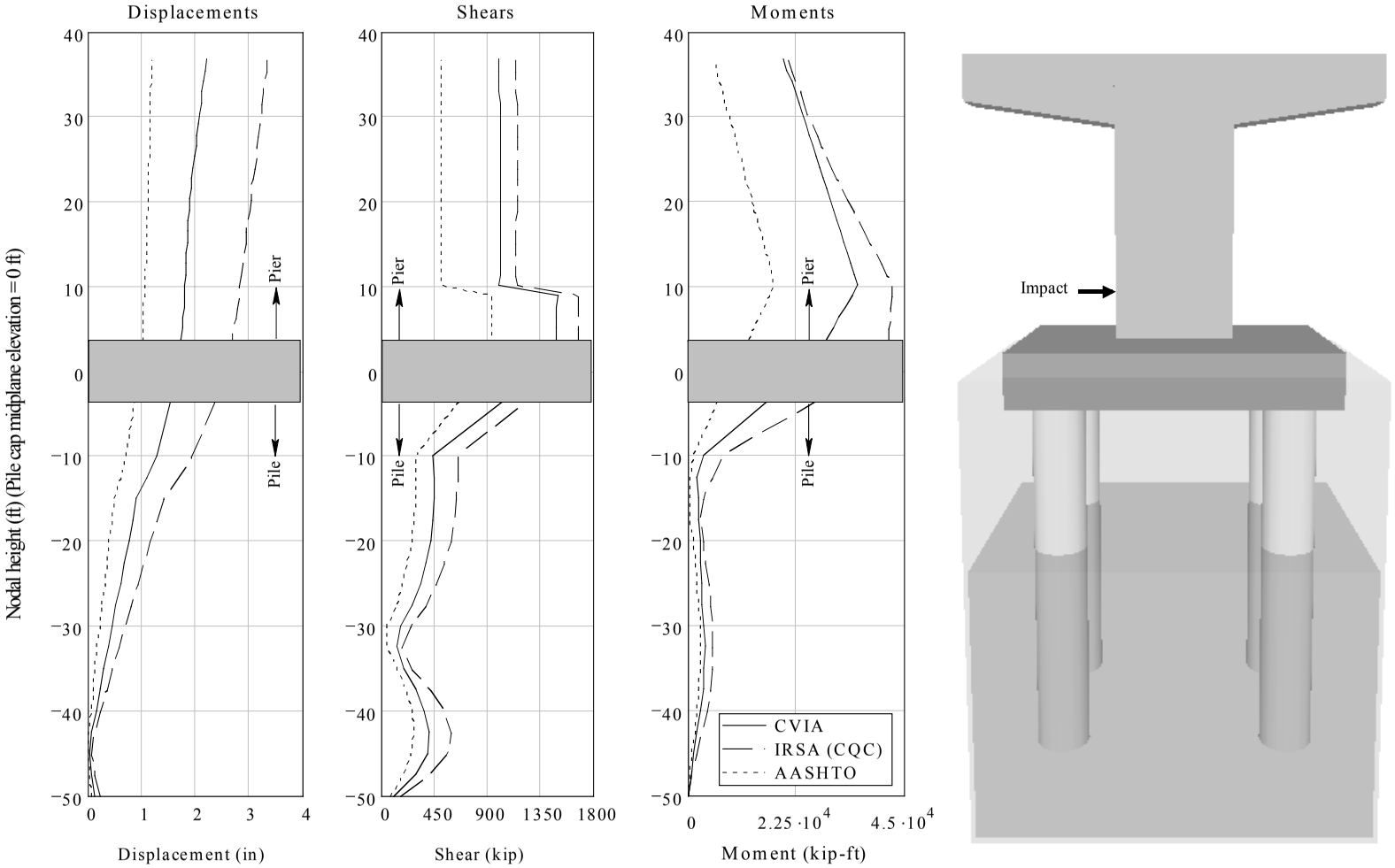

Figure B.12 Comparison of CVIA, IRSA, and AASHTO results
Bridge: Gandy Bridge (GND) channel pier; Impact condition: 2030 tons at 2.5 knots

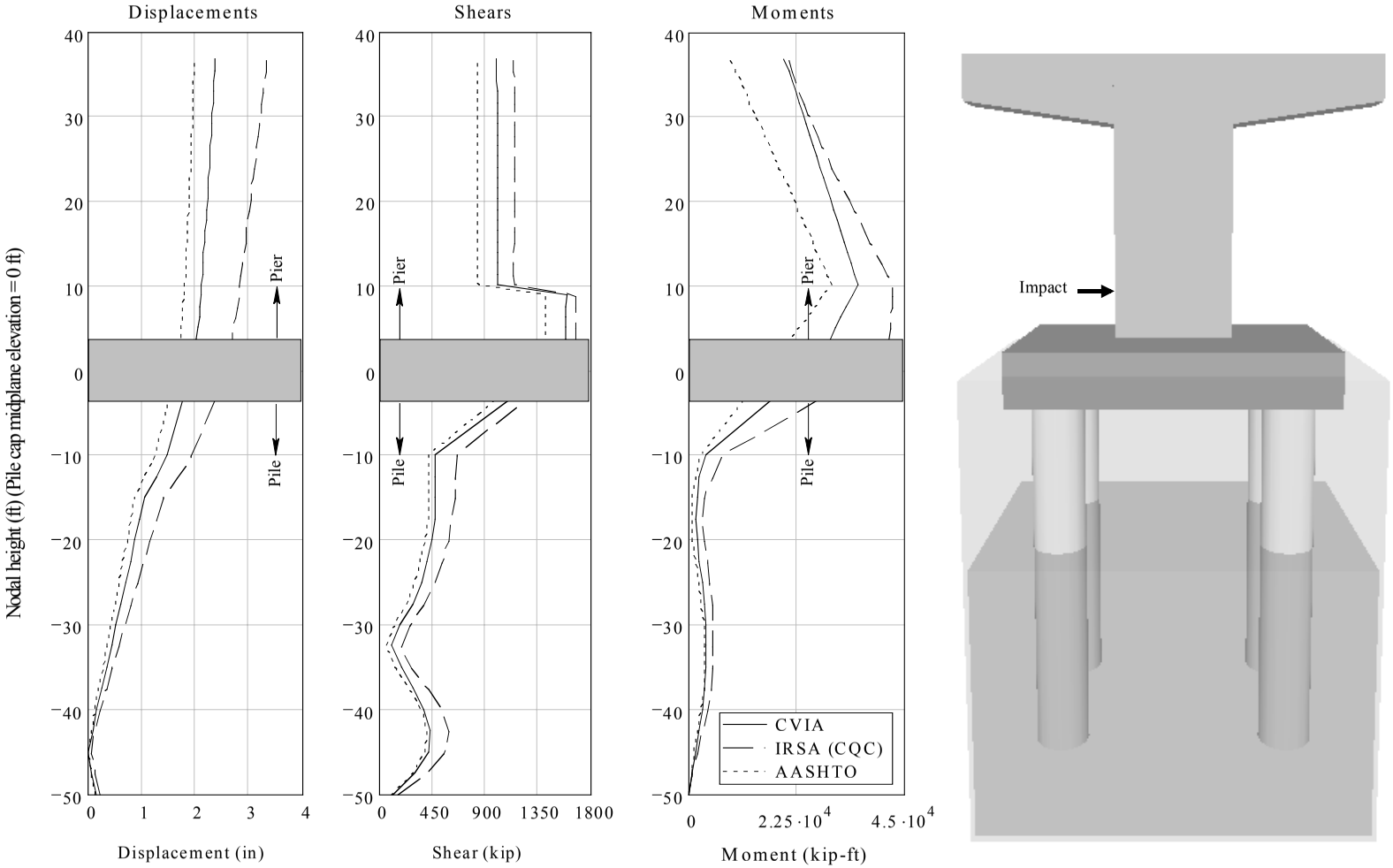

Figure B.13 Comparison of CVIA, IRSA, and AASHTO results
Bridge: Gandy Bridge (GND) channel pier; Impact condition: 5920 tons at 5.0 knots

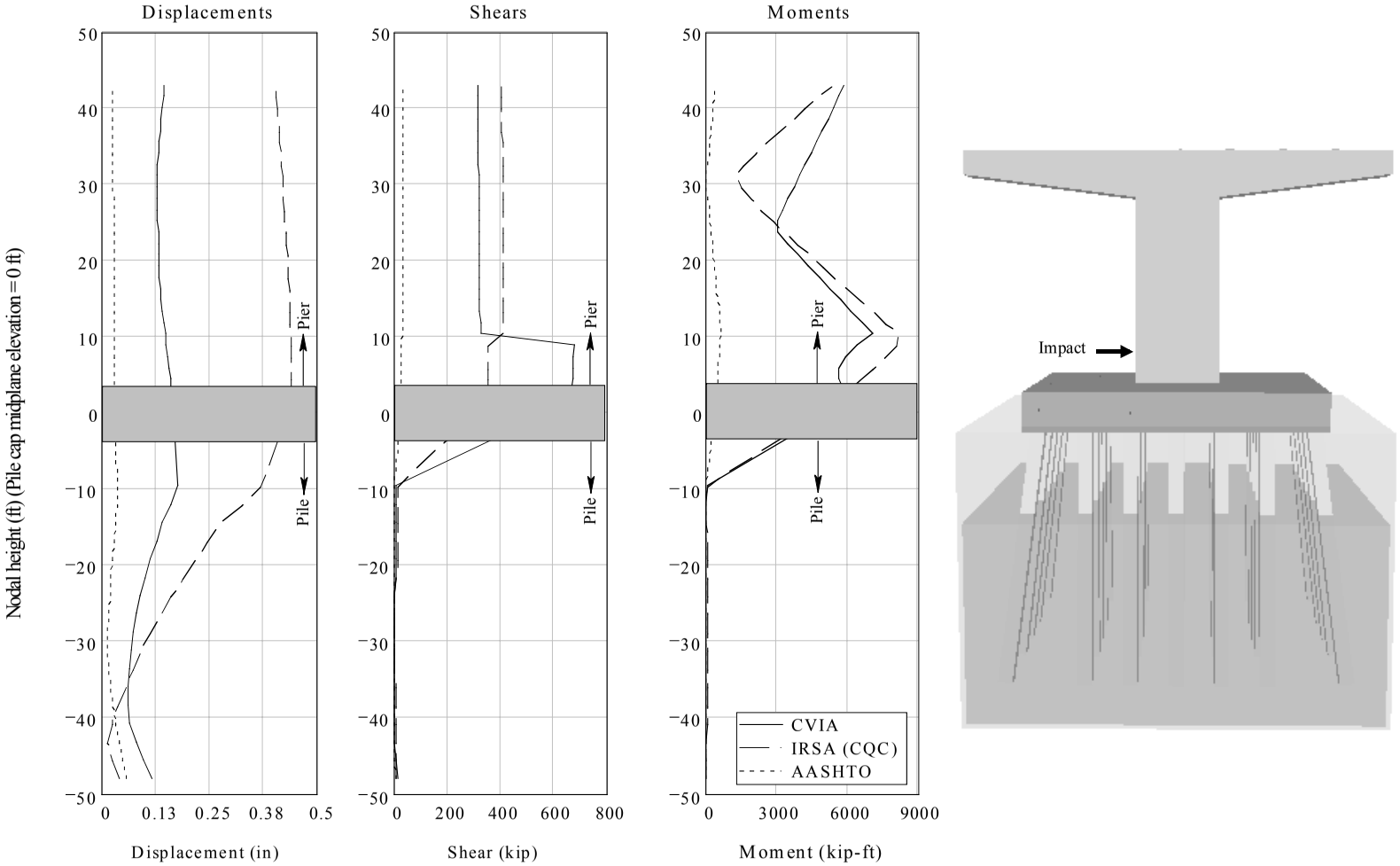

Figure B.14 Comparison of CVIA, IRSA, and AASHTO results
Bridge: Howard Frankland (HFK) channel pier; Impact condition: 200 tons at 1.0 knots

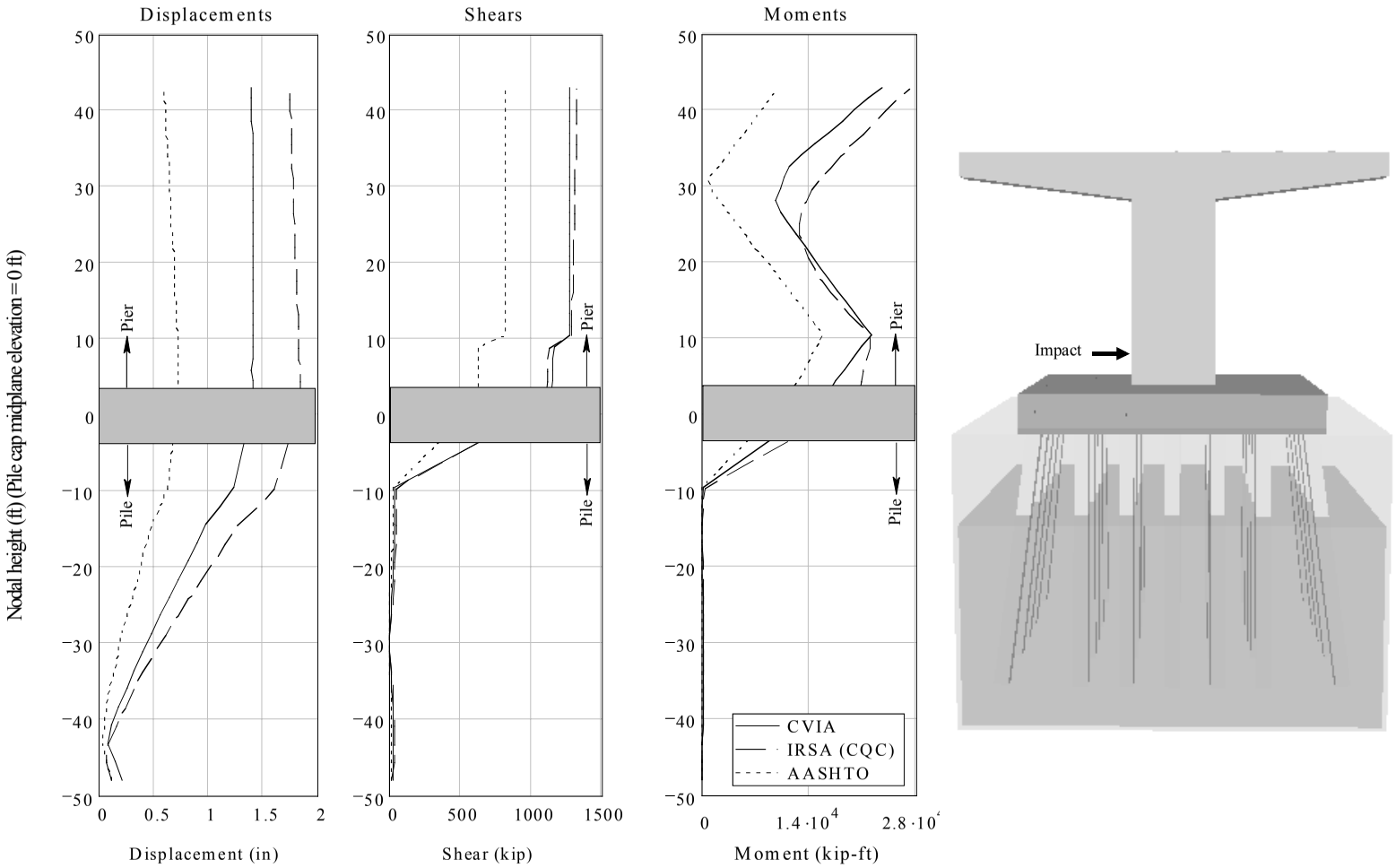

Figure B.15 Comparison of CVIA, IRSA, and AASHTO results
Bridge: Howard Frankland (HFK) channel pier; Impact condition: 2030 tons at 2.5 knots

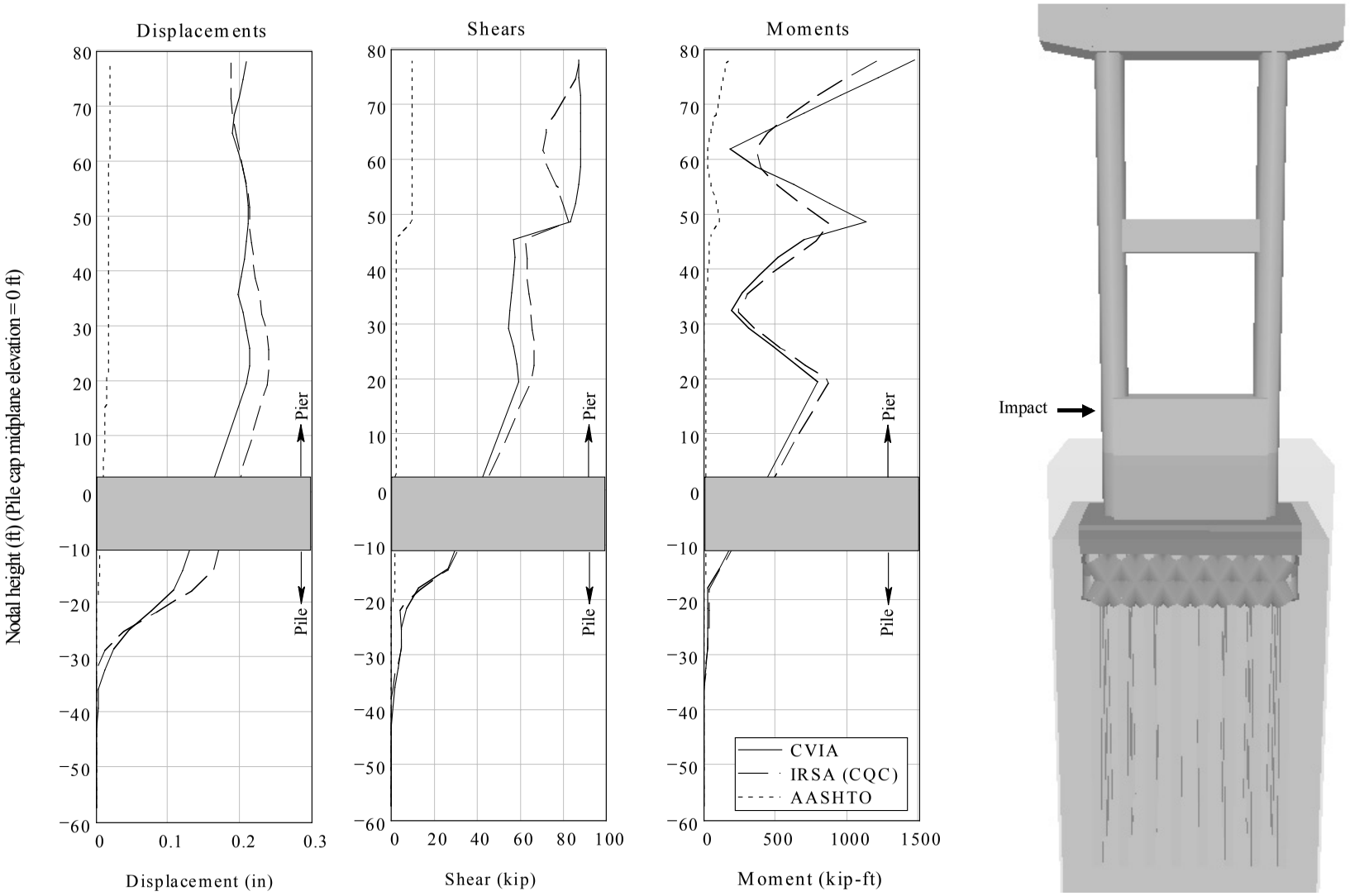

Figure B.16 Comparison of CVIA, IRSA, and AASHTO results
Bridge: Melbourne Causeway (MBC) channel pier; Impact condition: 200 tons at 1.0 knots

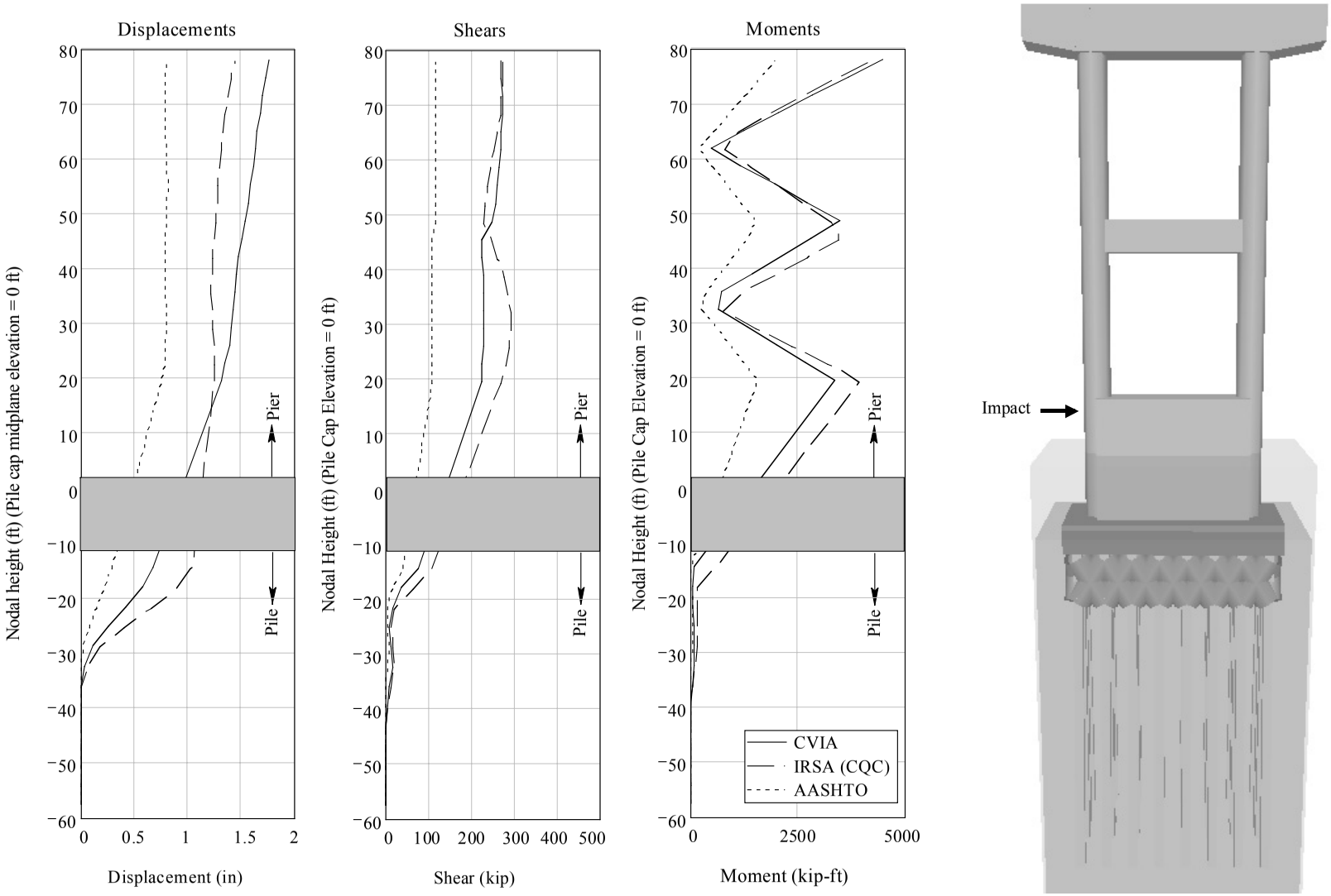

Figure B.17 Comparison of CVIA, IRSA, and AASHTO results
Bridge: Melbourne Causeway (MBC) channel pier; Impact condition: 2030 tons at 2.5 knots

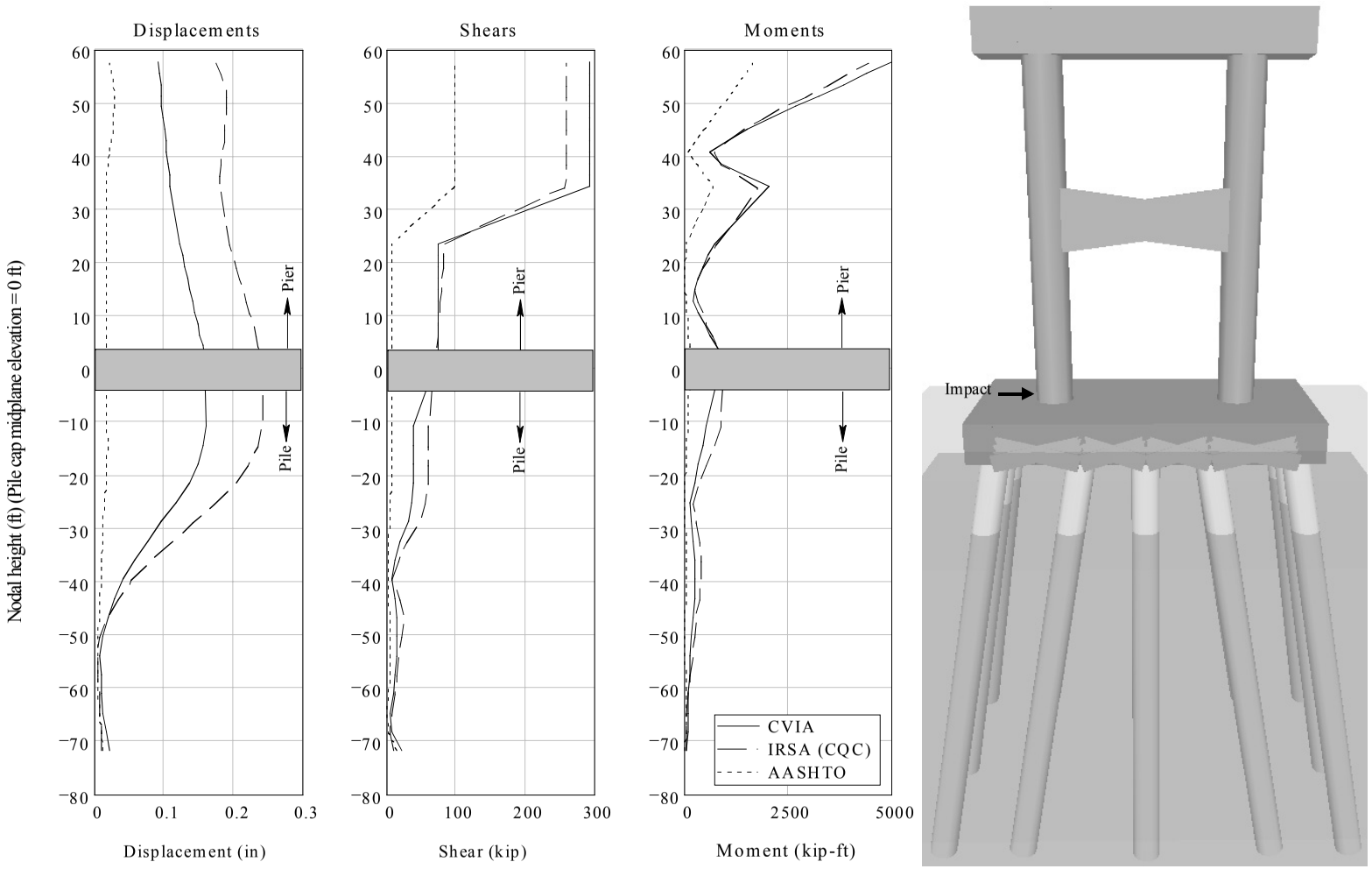

Figure B.18 Comparison of CVIA, IRSA, and AASHTO results
Bridge: new St. George Island (NSG) channel pier; Impact condition: 200 tons at 1.0 knots

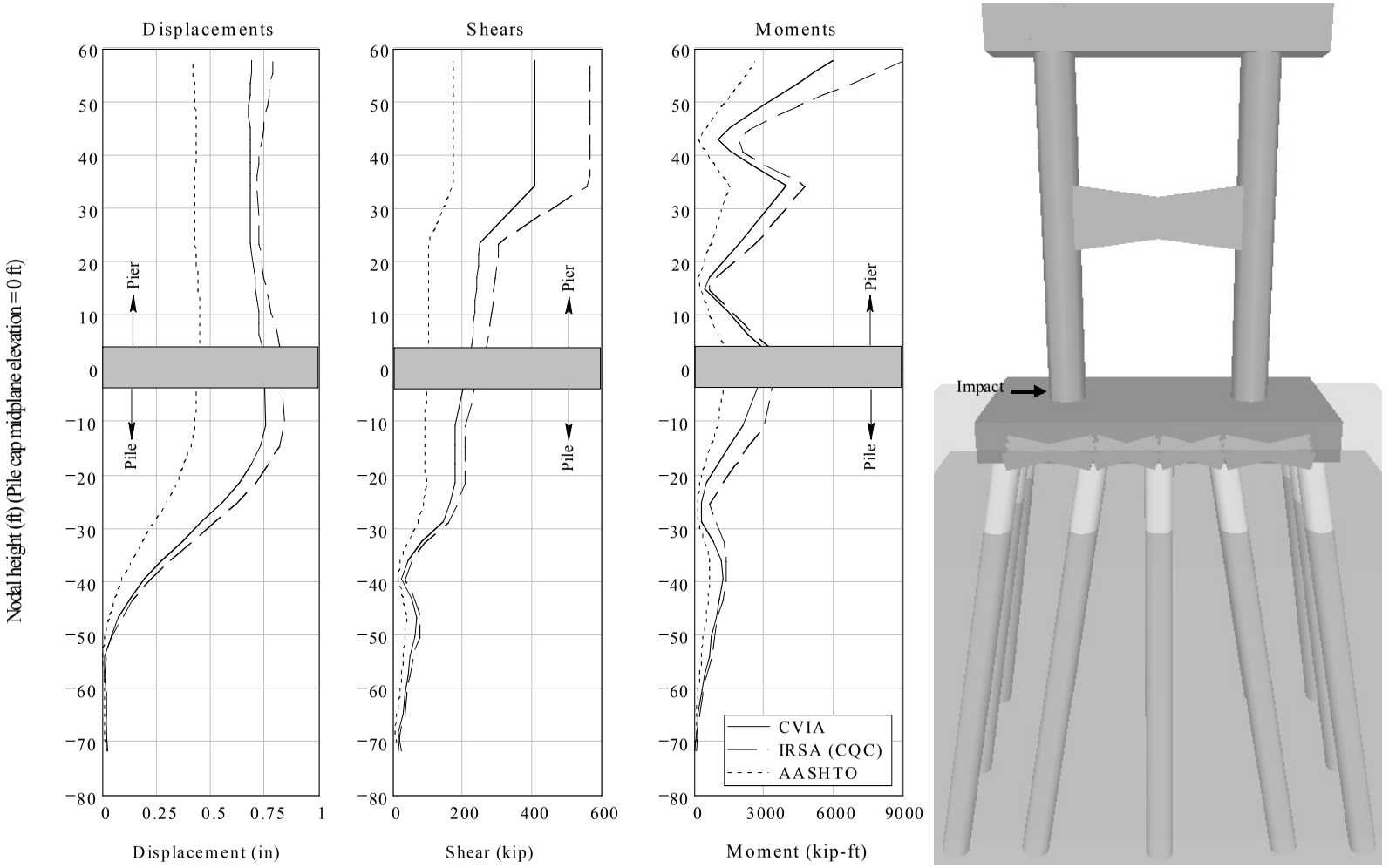

Figure B.19 Comparison of CVIA, IRSA, and AASHTO results
Bridge: new St. George Island (NSG) channel pier; Impact condition: 2030 tons at 2.5 knots

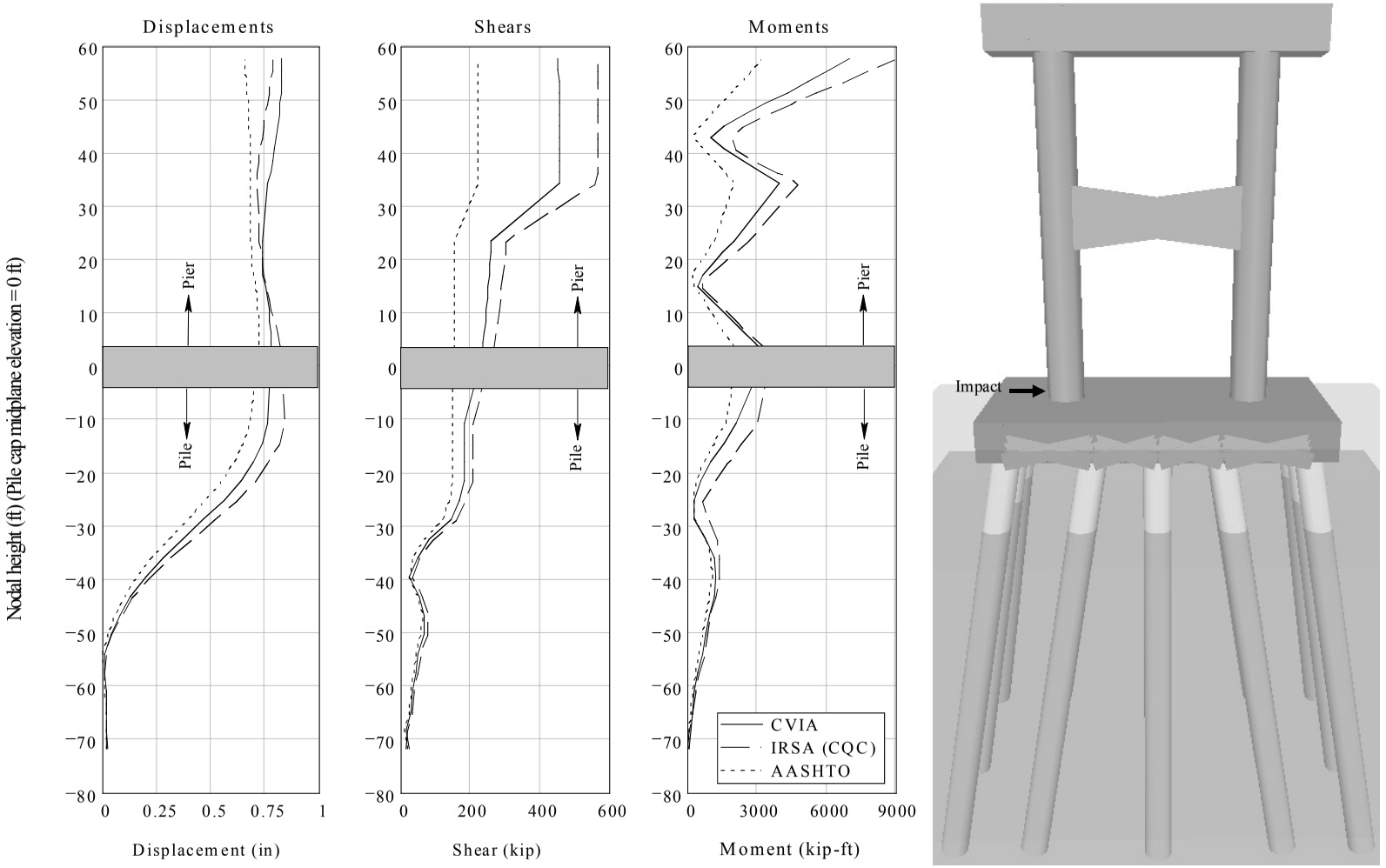

Figure B.20 Comparison of CVIA, IRSA, and AASHTO results
Bridge: new St. George Island (NSG) channel pier; Impact condition: 5920 tons at 5.0 knots

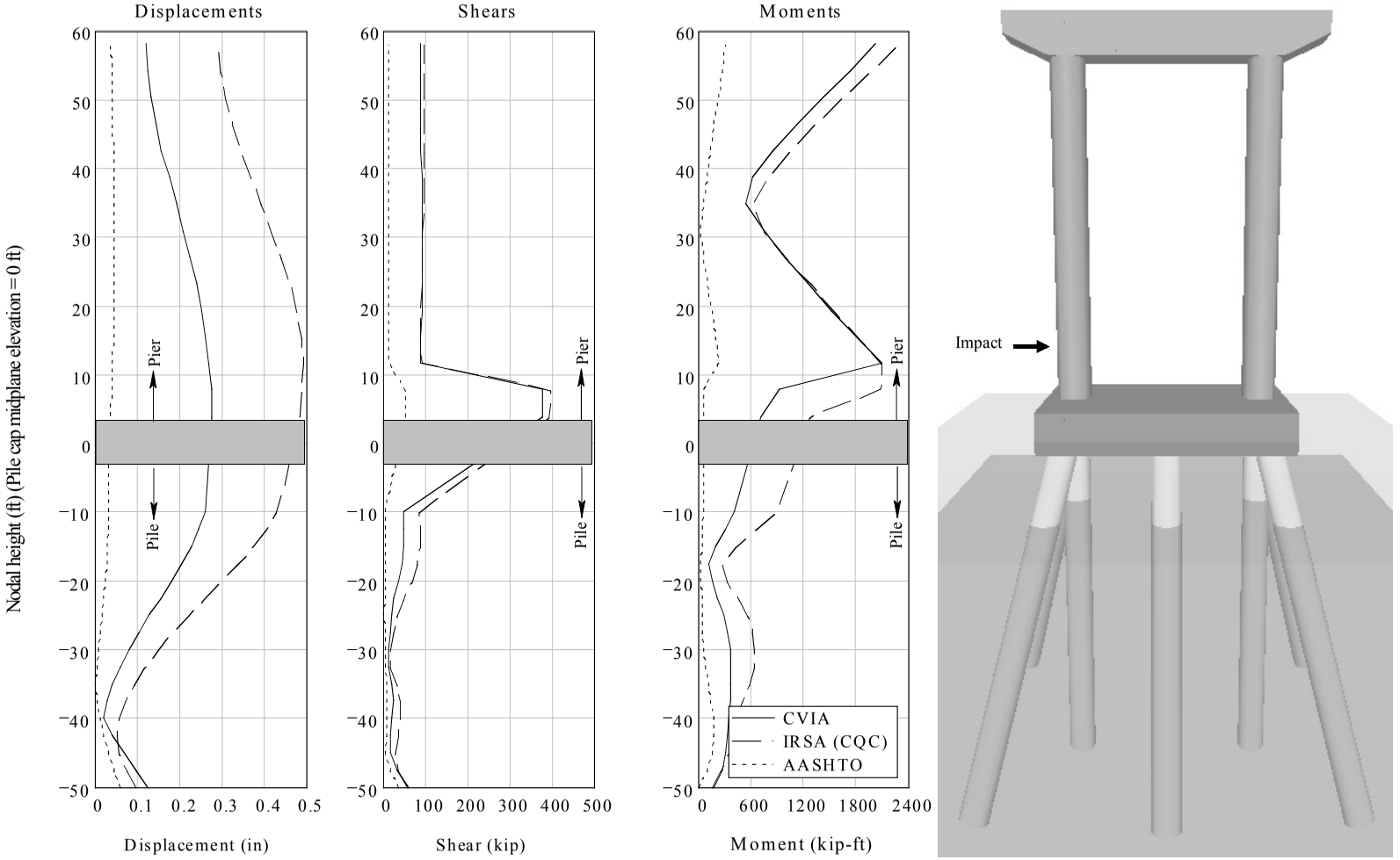

Figure B.21 Comparison of CVIA, IRSA, and AASHTO results
Bridge: new St. George Island (NSG) off-channel pier; Impact condition: 200 tons at 1.0 knots

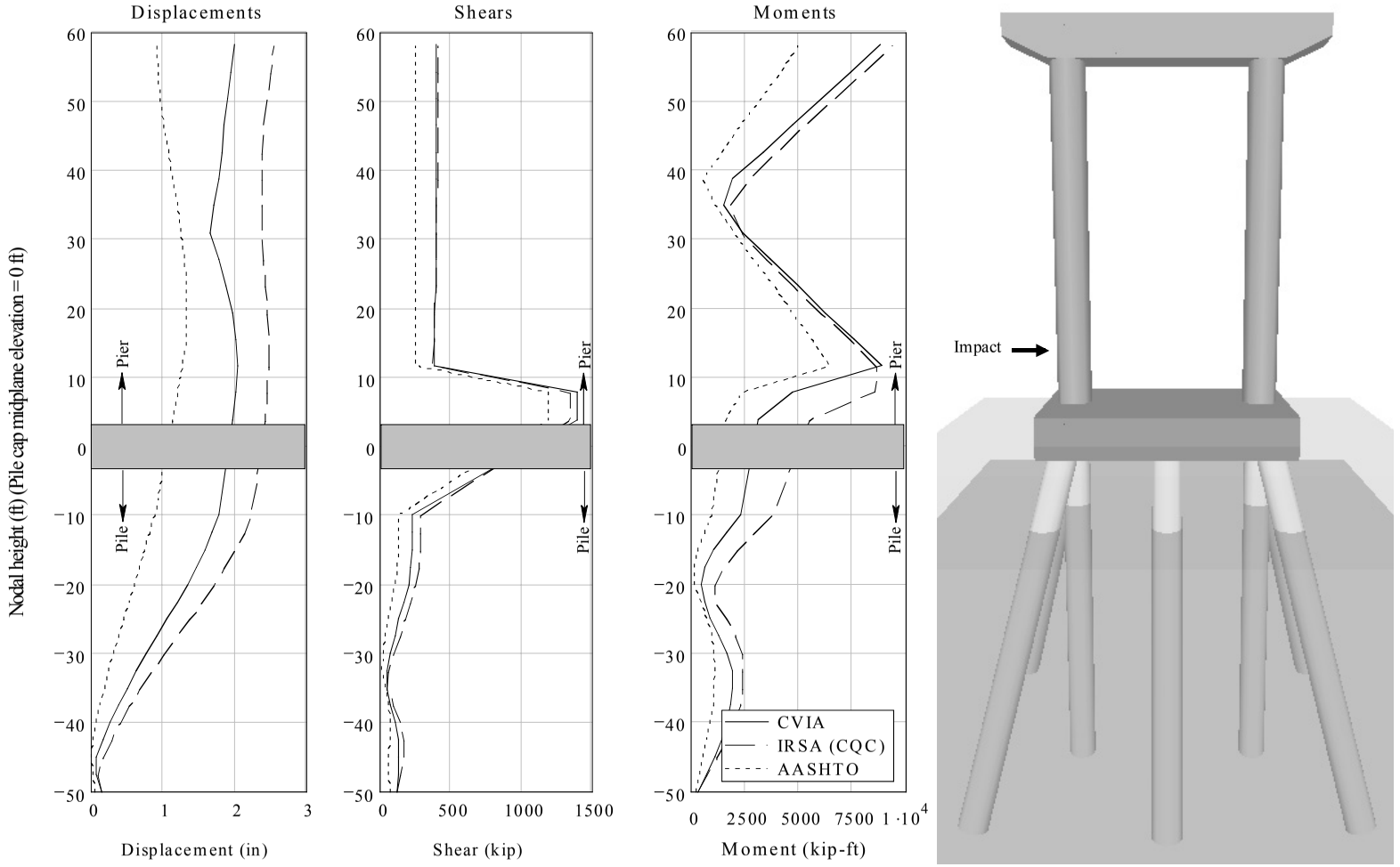

Figure B.22 Comparison of CVIA, IRSA, and AASHTO results
Bridge: new St. George Island (NSG) off-channel pier; Impact condition: 2030 tons at 2.5 knots

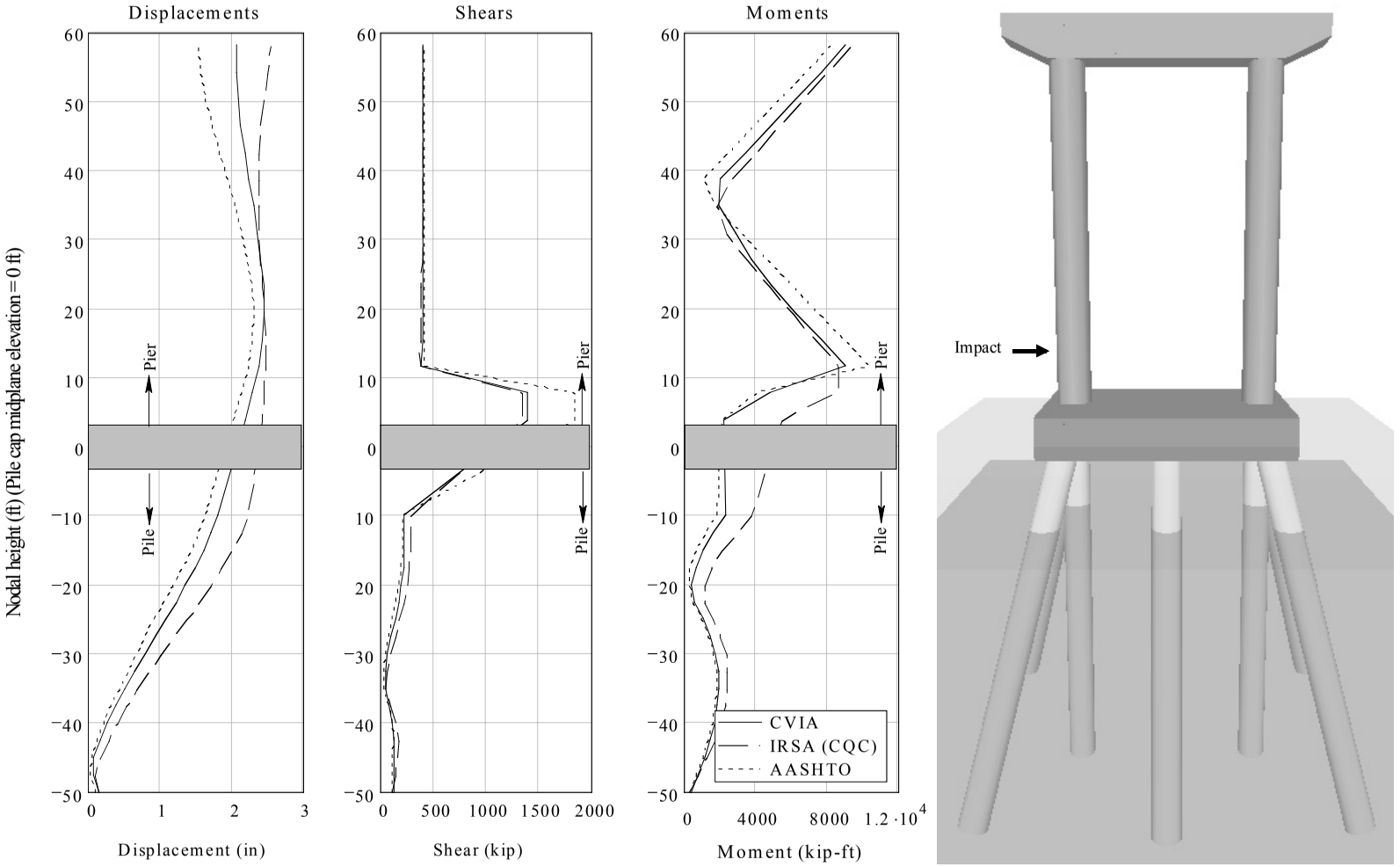

Figure B.23 Comparison of CVIA, IRSA, and AASHTO results
Bridge: new St. George Island (NSG) off-channel pier; Impact condition: 5920 tons at 5.0 knots

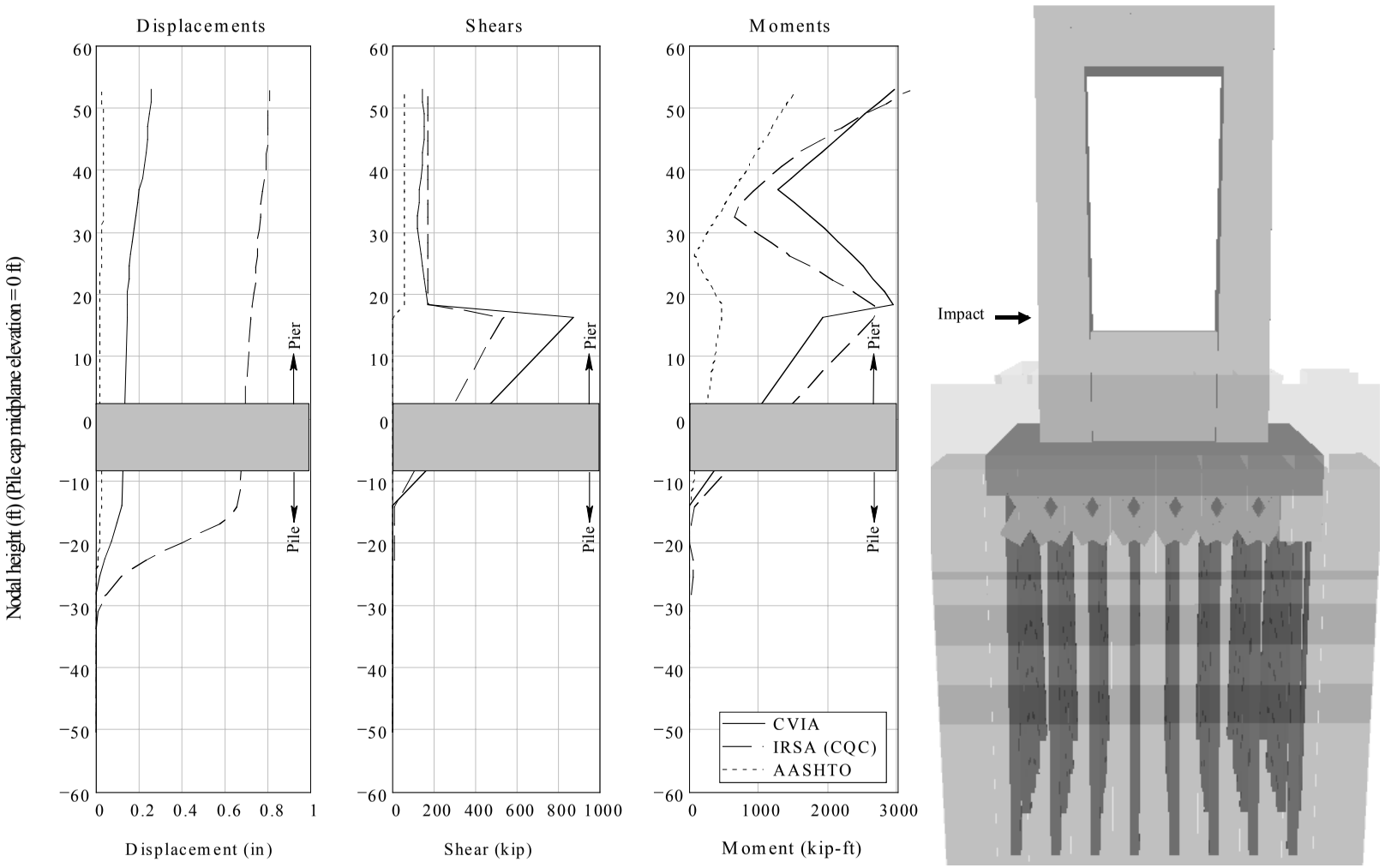

Figure B.24 Comparison of CVIA, IRSA, and AASHTO results
Bridge: old St. George Island (OSG) off-channel pier; Impact condition: 200 tons at 1.0 knots

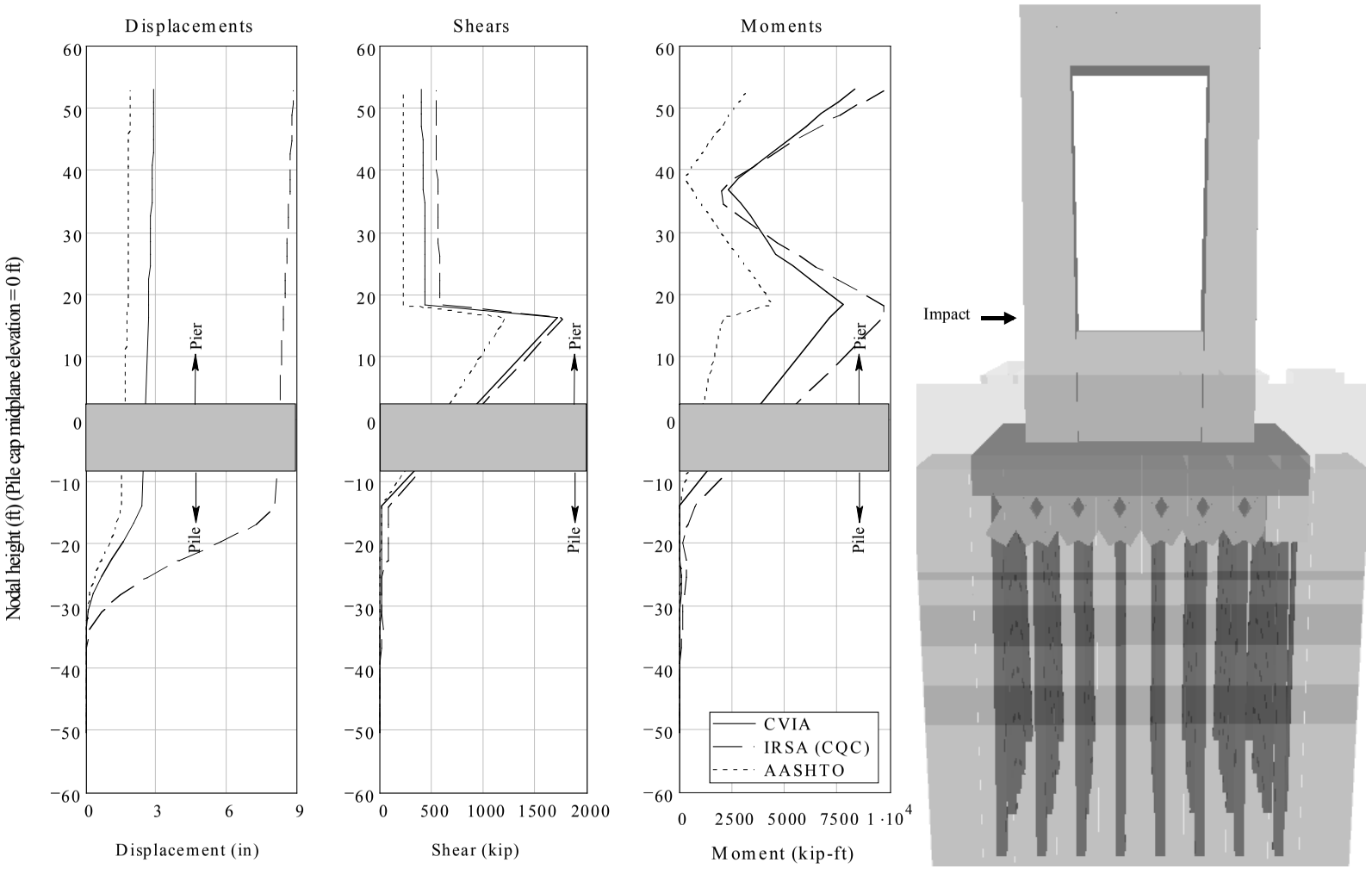

Figure B.25 Comparison of CVIA, IRSA, and AASHTO results
Bridge: old St. George Island (OSG) channel pier; Impact condition: 2030 tons at 2.5 knots

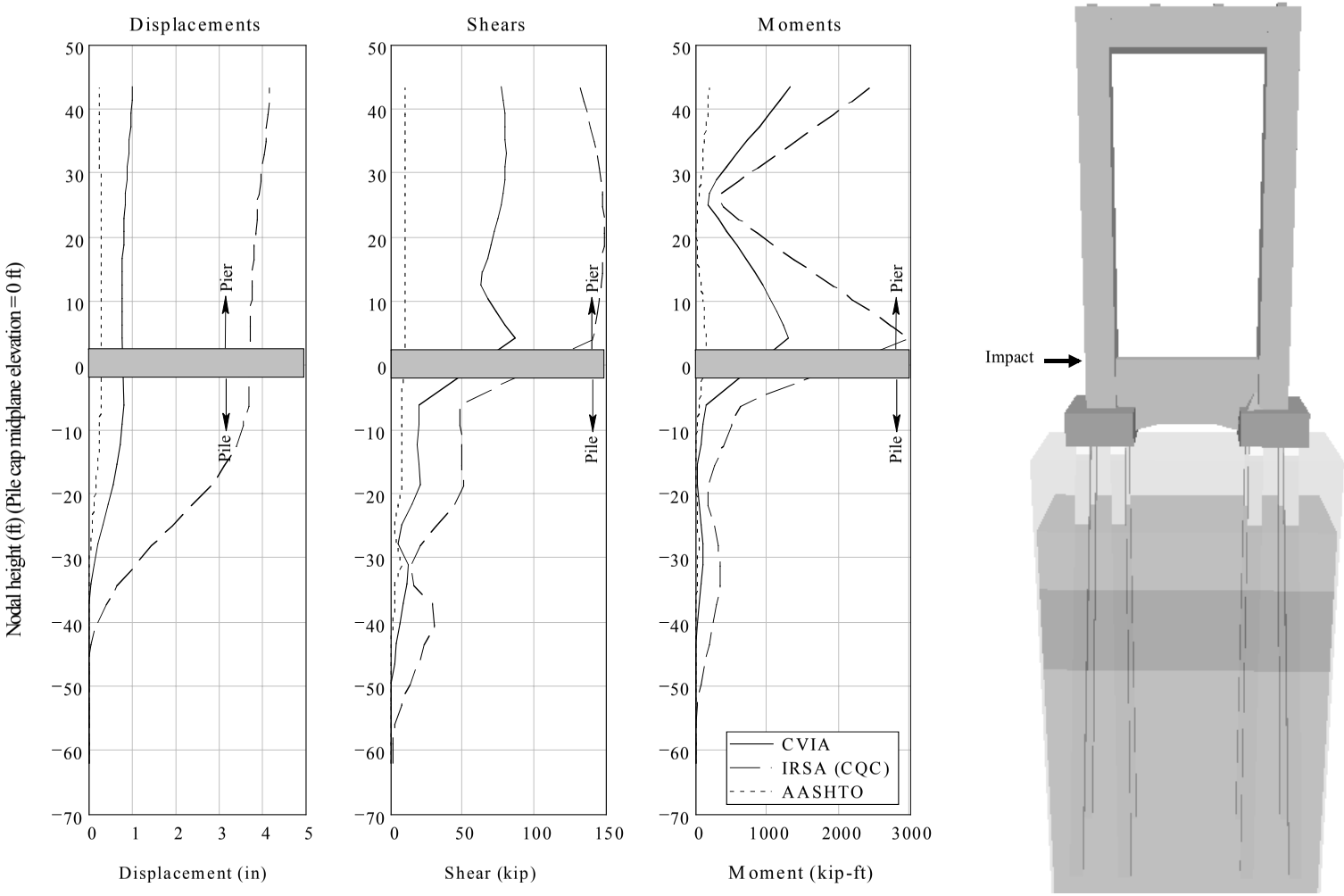

Figure B.26 Comparison of CVIA, IRSA, and AASHTO results
Bridge: old St. George Island (OSG) off-channel pier; Impact condition: 200 tons at 1.0 knots

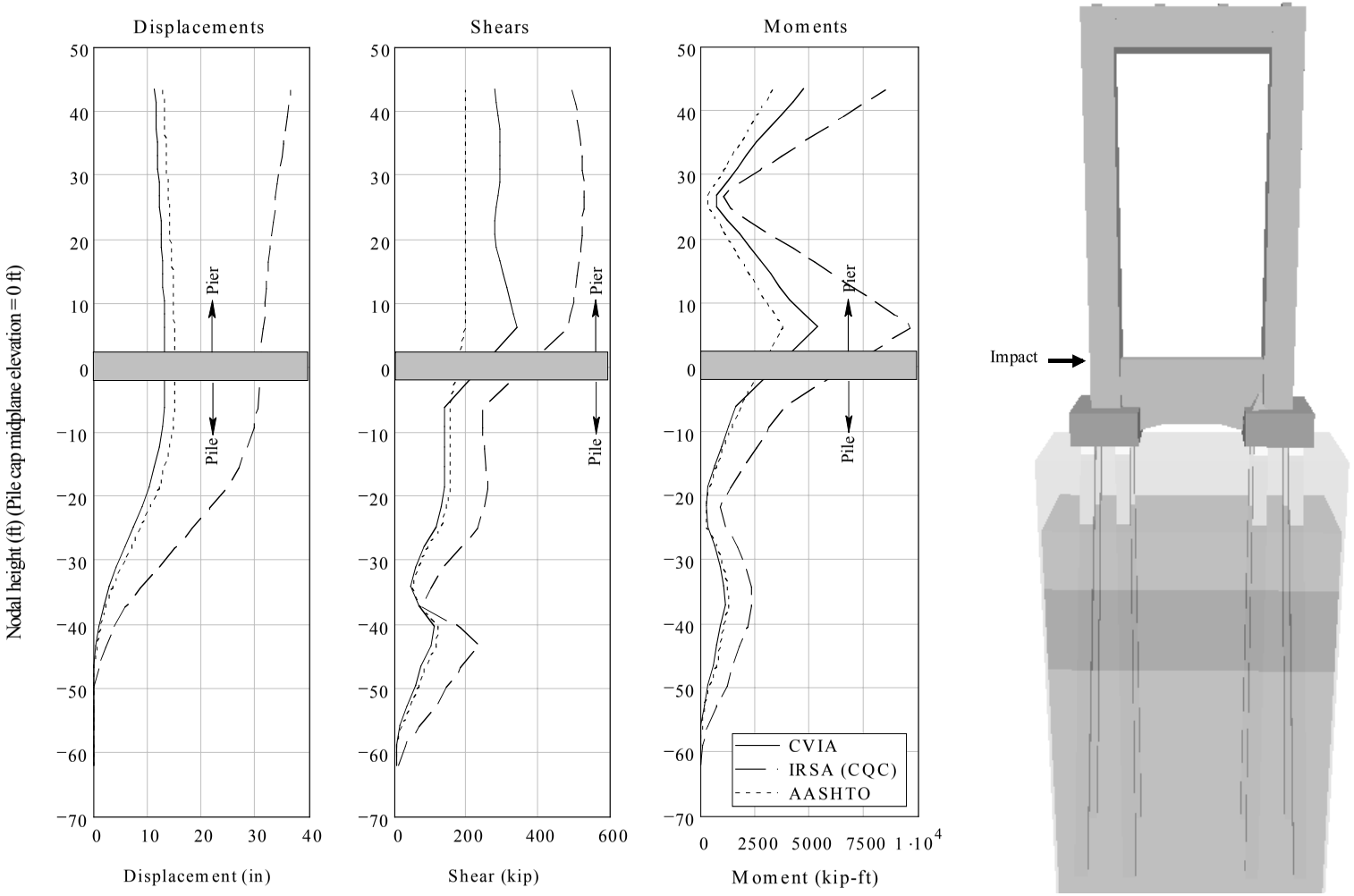

Figure B.27 Comparison of CVIA, IRSA, and AASHTO results
Bridge: old St. George Island (OSG) off-channel pier; Impact condition: 2030 tons at 2.5 knots

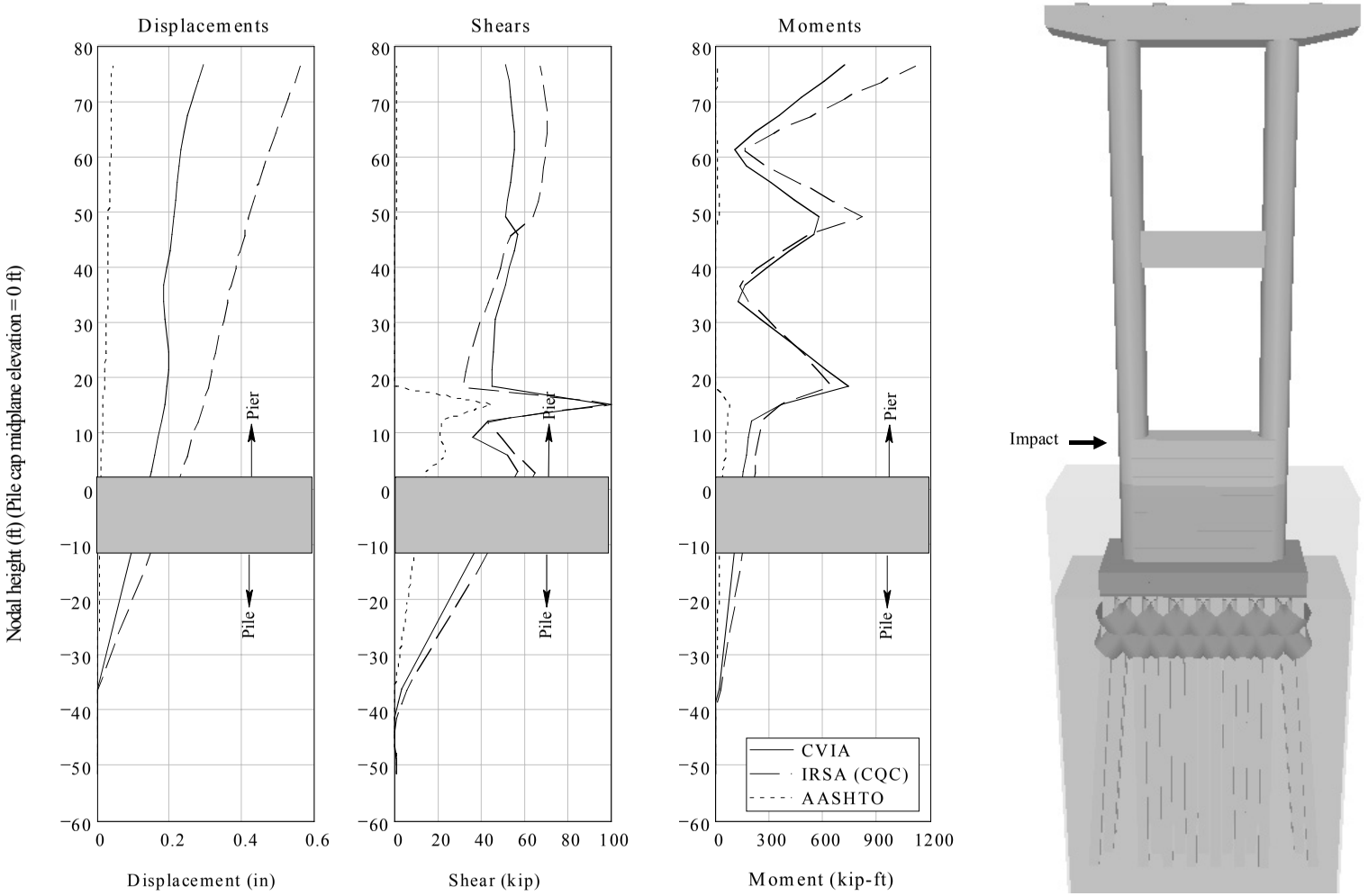

Figure B.28 Comparison of CVIA, IRSA, and AASHTO results
Bridge: Pineda Causeway (PNC) channel pier; Impact condition: 200 tons at 1.0 knots

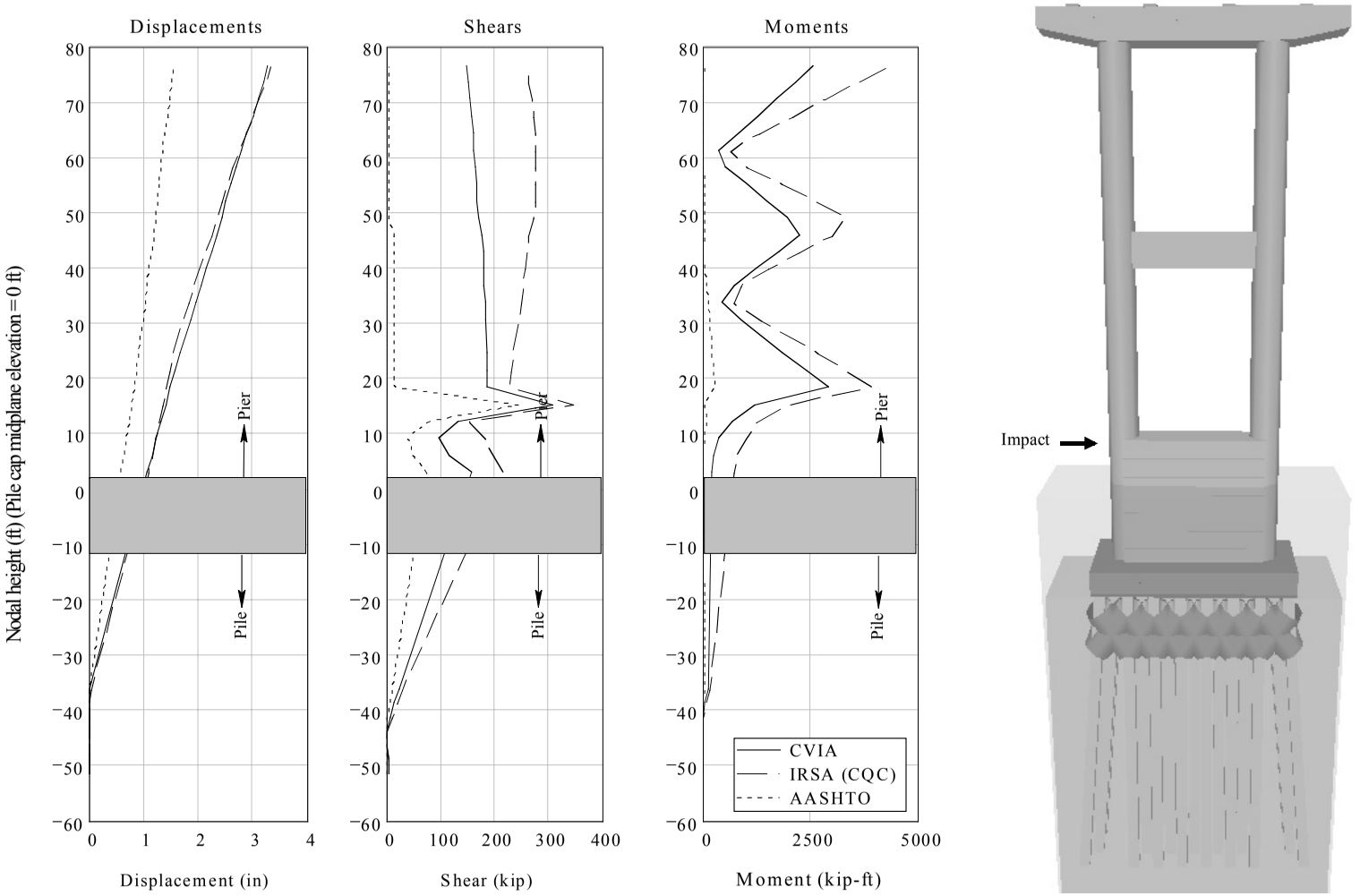

Figure B.29 Comparison of CVIA, IRSA, and AASHTO results
Bridge: Pineda Causeway (PNC) channel pier; Impact condition: 2030 tons at 2.5 knots

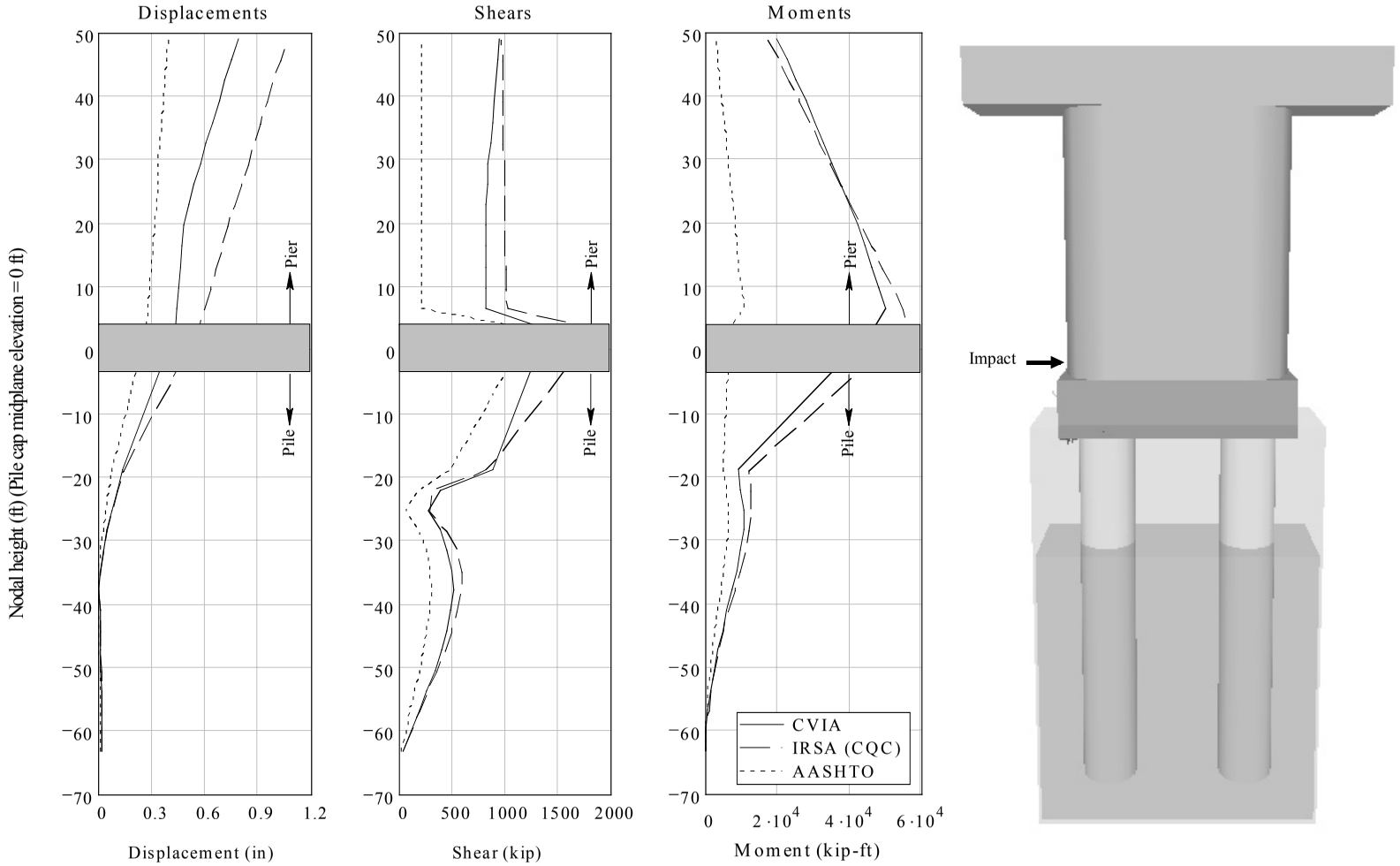

Figure B.30 Comparison of CVIA, IRSA, and AASHTO results
Bridge: Ringling (RNG) channel pier; Impact condition: 2030 tons at 2.5 knots

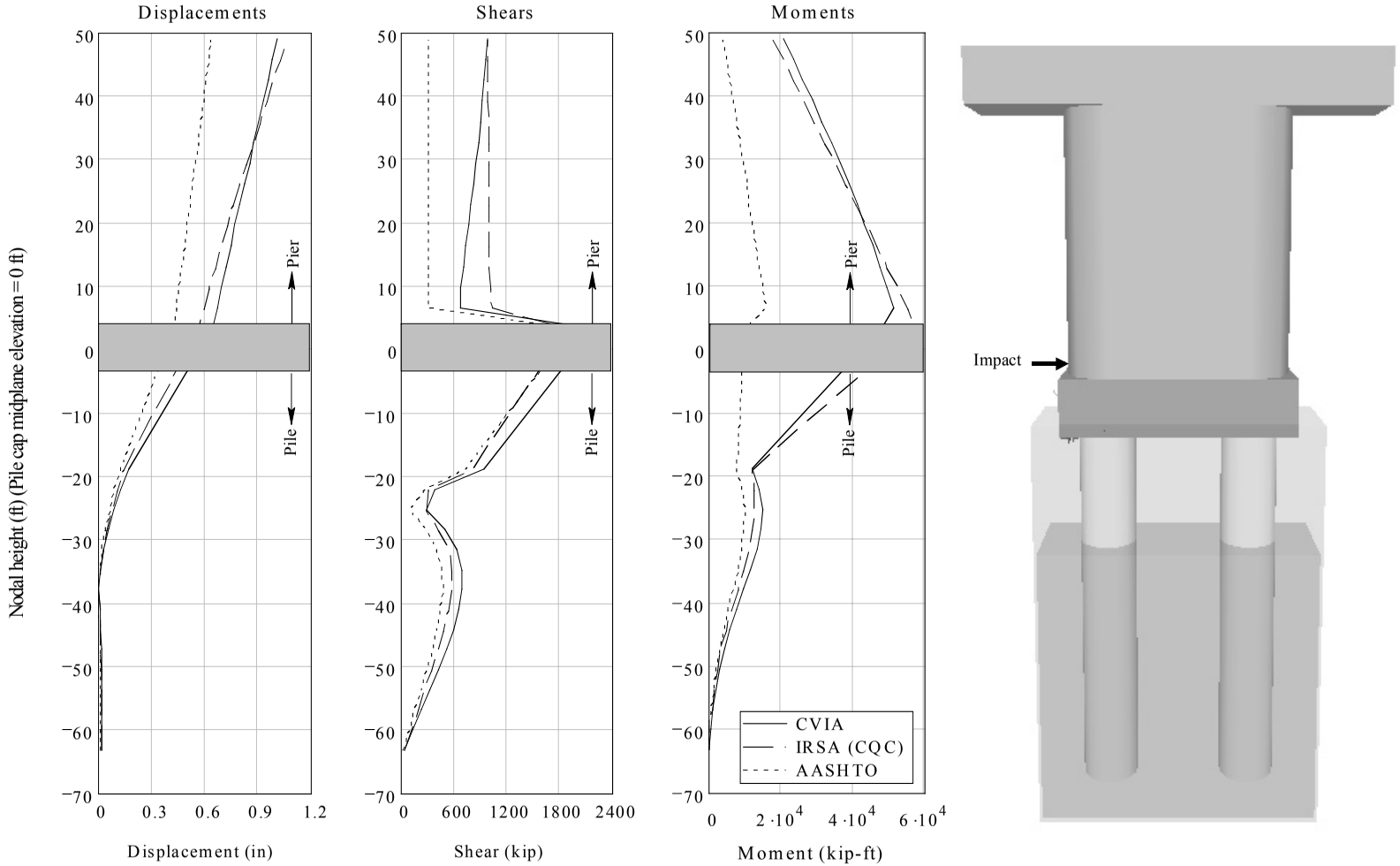

Figure B.31 Comparison of CVIA, IRSA, and AASHTO results
Bridge: Ringling (RNG) channel pier; Impact condition: 5920 tons at 5.0 knots

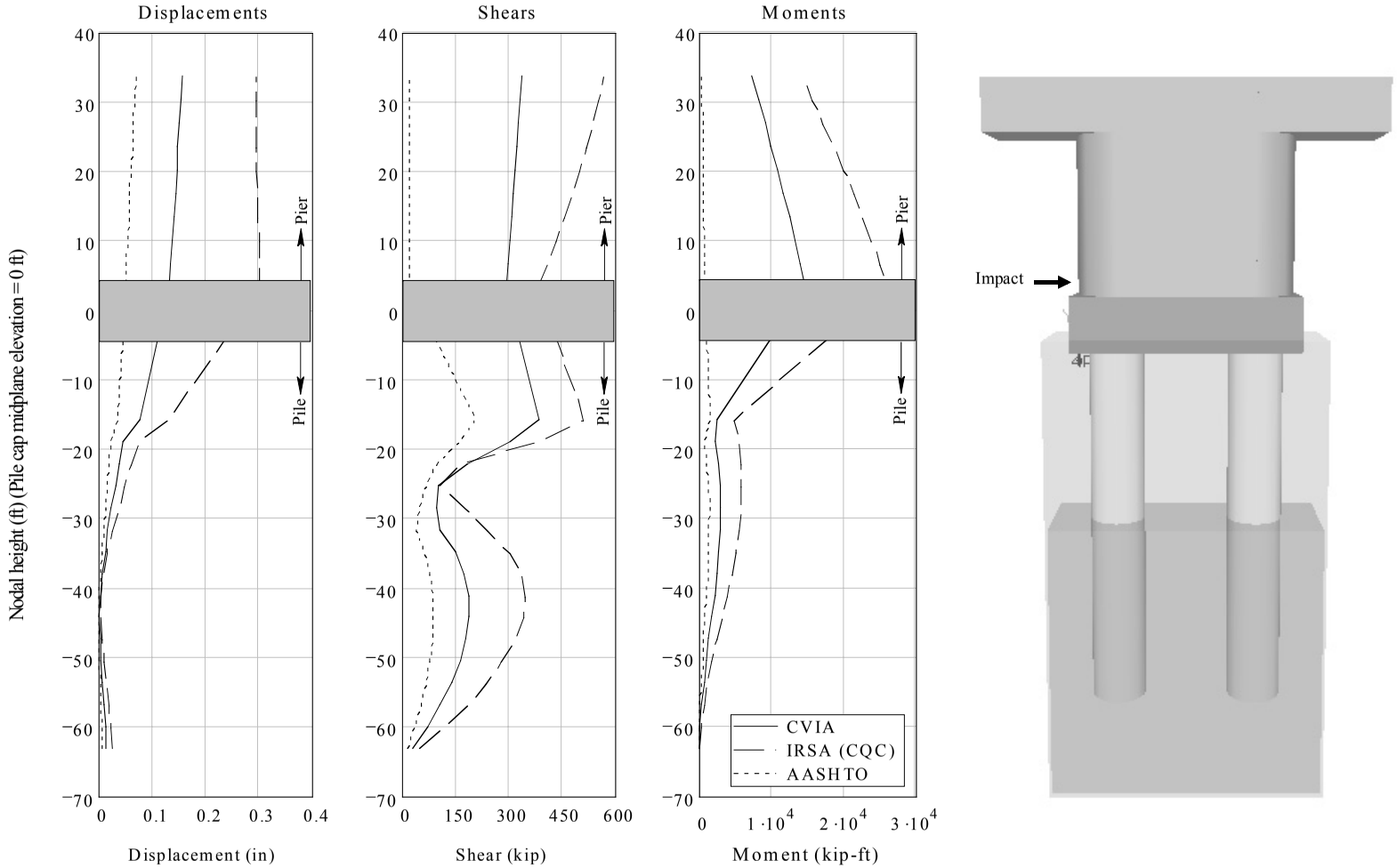

Figure B.32 Comparison of CVIA, IRSA, and AASHTO results
Bridge: Ringling (RNG) off-channel pier; Impact condition: 200 tons at 1.0 knots

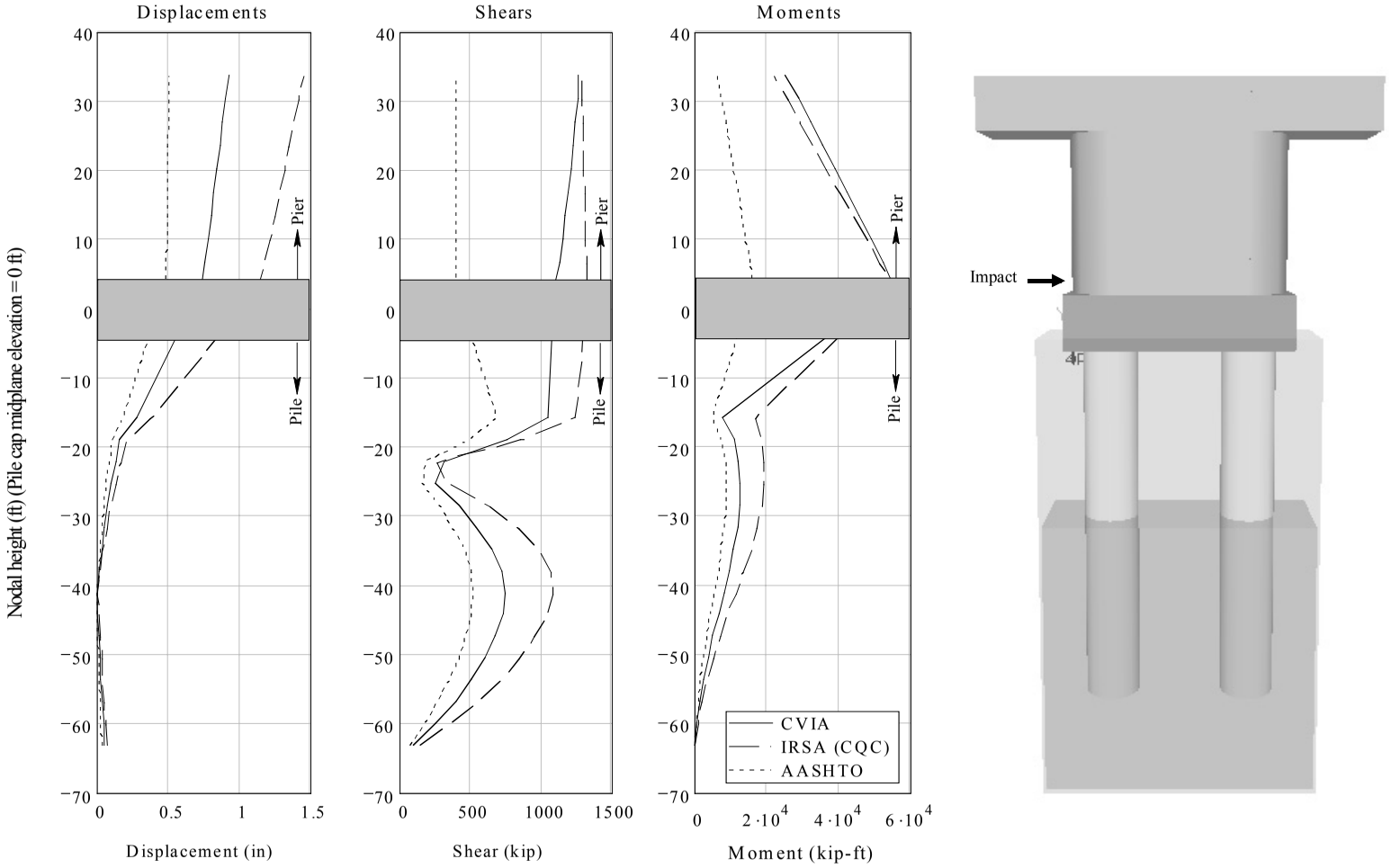

Figure B.33 Comparison of CVIA, IRSA, and AASHTO results
Bridge: Ringling (RNG) off-channel pier; Impact condition: 2030 tons at 2.5 knots

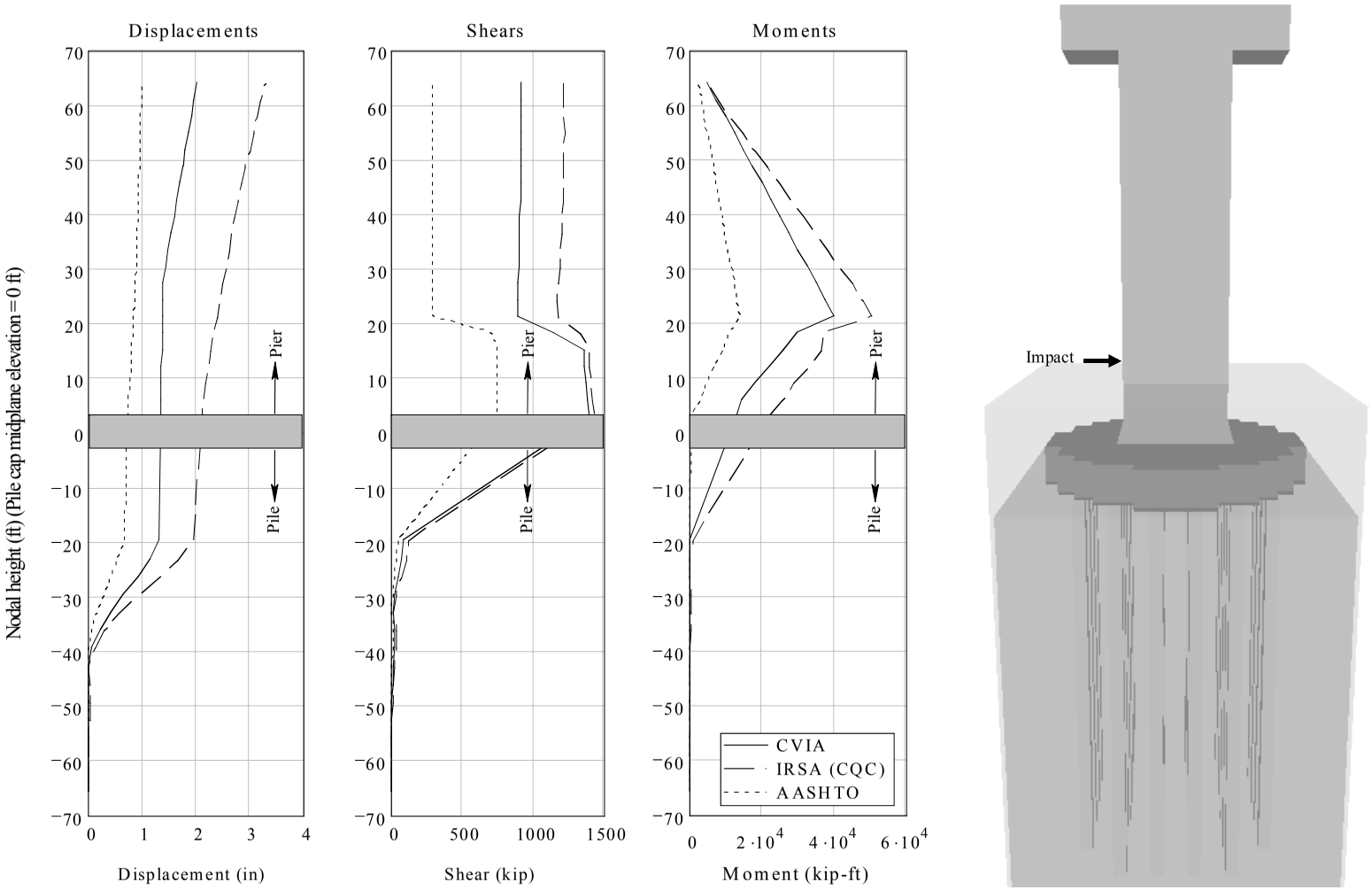

Figure B.34 Comparison of CVIA, IRSA, and AASHTO results
Bridge: Seabreeze (SBZ) channel pier; Impact condition: 2030 tons at 2.5 knots

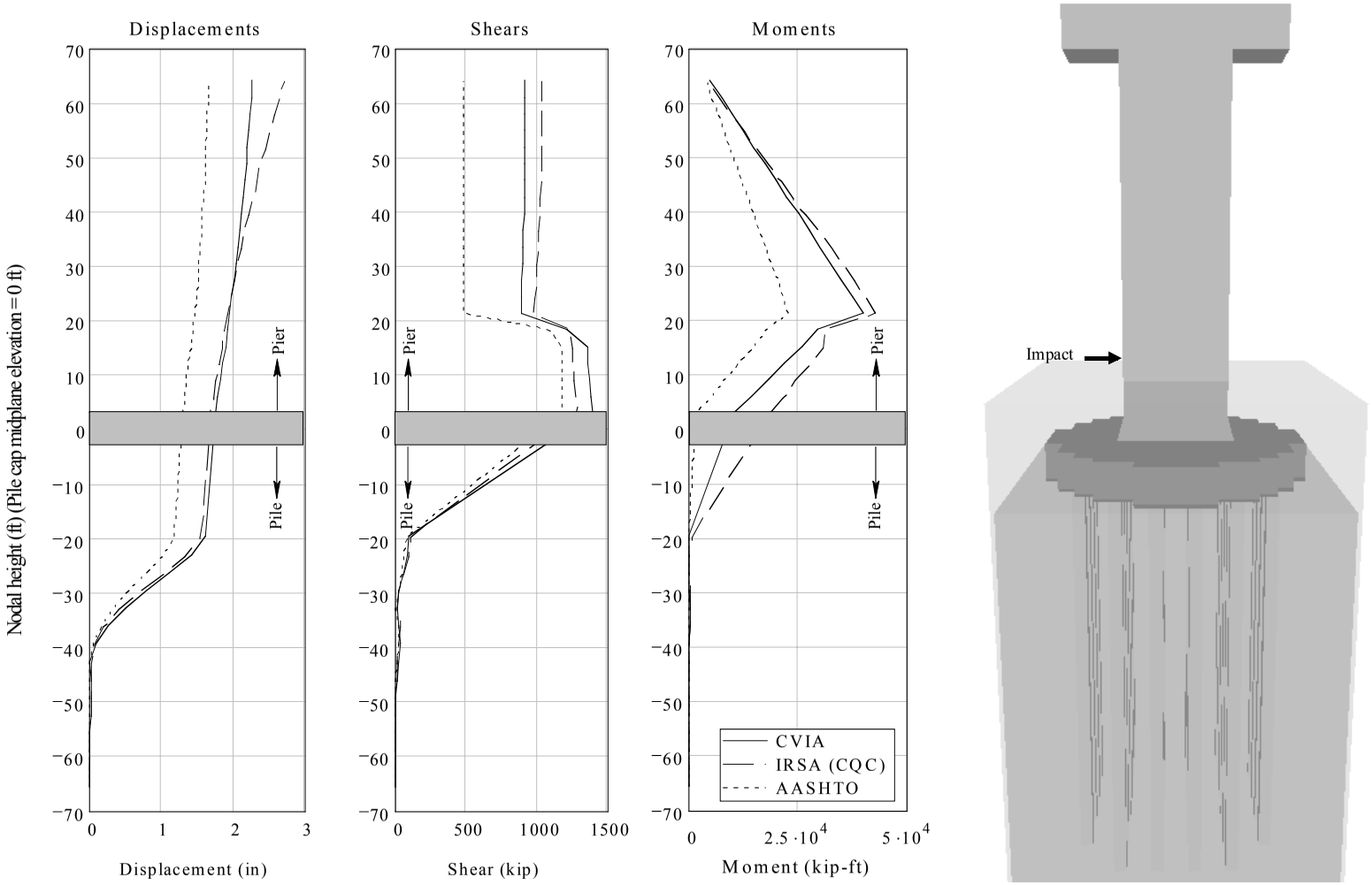

Figure B.35 Comparison of CVIA, IRSA, and AASHTO results
Bridge: Seabreeze (SBZ) channel pier; Impact condition: 5920 tons at 5.0 knots

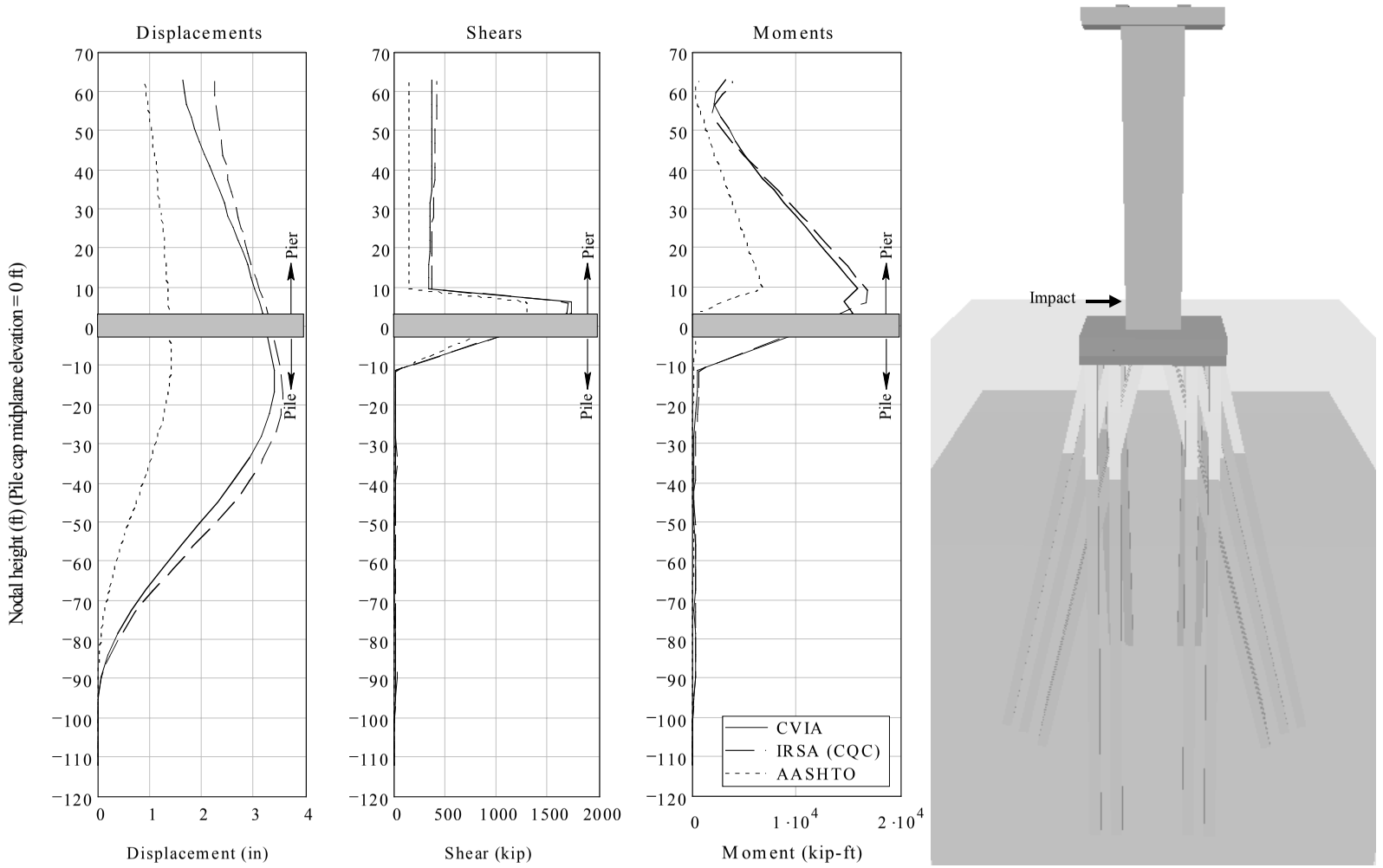

Figure B.36 Comparison of CVIA, IRSA, and AASHTO results
Bridge: Santa Rosa Bay (SRB) channel pier; Impact condition: 2030 tons at 2.5 knots

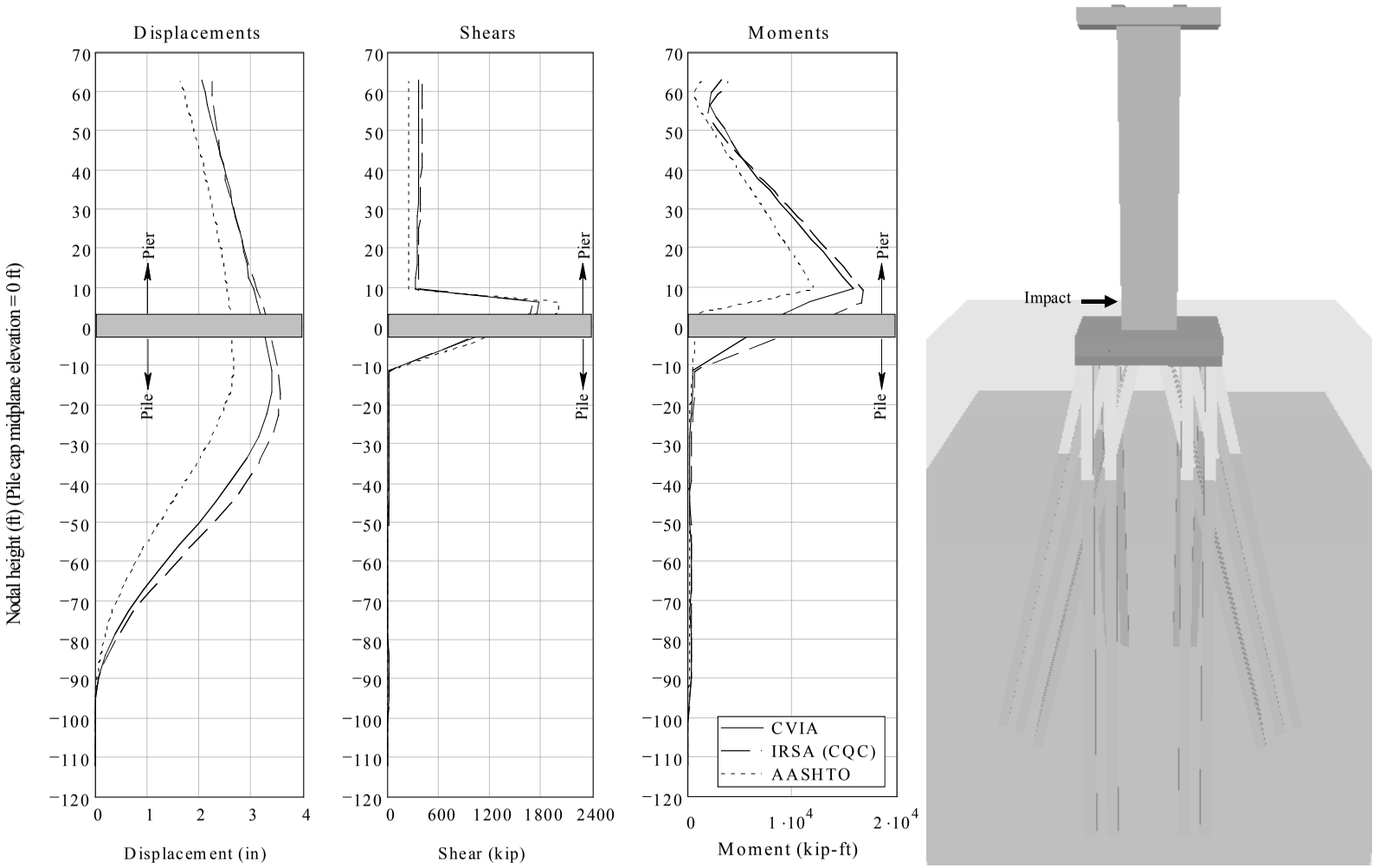

Figure B.37 Comparison of CVIA, IRSA, and AASHTO results
Bridge: Santa Rosa Bay (SRB) channel pier; Impact condition: 5920 tons at 5.0 knots